Provided by the author(s) and University of Galway in accordance with publisher policies. Please cite the published version when available.

Title	Synthetic investigations into discrete polynuclear cage formation and their subsequent incorporation into extended network materials
Author(s)	McDonald, Cecelia
Publication Date	2015-01-20
Item record	http://hdl.handle.net/10379/4910

Downloaded 2024-05-14T17:34:55Z

Some rights reserved. For more information, please see the item record link above.

Synthetic Investigations into Discrete Polynuclear Cage Formation and Their Subsequent Incorporation into Extended Network Materials

By

Cecelia McDonald

Supervisor: Dr. Leigh F. Jones

Head of School: Prof. Paul V. Murphy

Thesis for the degree of PhD

School of Chemistry

National University of Ireland, Galway

October 2014

Table of Contents

Chapter Four: Layered Cu(II) Cages Using Polydentate Ligands with Premeditated High Binding Site Concentrations 136

Declaration

I hereby declare that the work carried out in thesis is my own. No portion of the work referred to in this thesis has been submitted in support of an application of another degree or qualification, at this, or any other university or institute of higher learning.

Signature

Cecelia McDonald

Acknowledgements

Firstly, I would like to express my gratitude to my supervisor Dr. Leigh F. Jones for all his support and guidance throughout the four years of my PhD. A big thank you to Prof. Euan K. Brechin and the Brechin group at the University of Edinburgh for performing all the magnetic measurements carried out in this thesis and Dr. Gopalan Rajaraman and his research group at the Indian Institute of Technology in Mumbai for carrying out DFT calculations in Chapters 3 and 5. Also a huge thank you to Dr. Declan Gaynor for the synthesis of the hydroxamic acid ligand 2-(dimethylamino)phenylhydroxamic acid (L_1H_2). I would also like to thank Dr. Giannis S. Papaefstathiou (University of Athens) for all his help with the [Cu_2] 2D network and Dr. Mateusz Pitak (University of Southampton) for his help with crystallography in Chapter 4. Additionally, I would like to thank the College of Science for all their financial support. A big thank you to all the technical staff in the chemistry department for all the analysis carried out throughout the PhD.

A big thank you to Seán T. Meally, Nelly Berg and Edel Houton for all the craic inside and outside of the lab, to Nora, Deirdre and Rebecca for all the tea breaks and the chats throughout the years. A special thanks to all the gang in the inorganic chemistry department, including PhD students past and present, as well as all the lecturers for all their help throughout the years. Also I would like to thank all the fourth year undergraduate lab students we have had in the last four years especially Teresa Whyte for her contributions to Chapter 2.

A very special thank you to my mum Celia, my family and my partner Ross for all their support and help throughout the write up stage. This would not have been possible without your encouragement and motivation. Finally, I would like to dedicate this thesis to the loving memory of my dad Austin.

Abstract

This thesis details the synthesis and structural characterisation of thirty novel complexes via the utilisation of a variety of ligands (seven in total) including hydroxamic acids, Schiff base ligands and their hybrid analogues. In addition, a number of co-ligands have also been used in conjunction with one of the primary seven ligands.

In Chapter 2 we describe a family of planar pentanuclear Cu(II) 12-MC-4 metallacrowns constructed using the hydroxamic acid ligands 2-(dimethylamino)phenylhydroxamic acid (L_1H_2) or 2-(amino)phenylhydroxamic acid (L_2H_2). This family comprises four discrete complexes of formulae $[Cu(II)_5(L_1)_4(MeOH)_4](ClO_4)_2$ (**1**), $[Cu(II)_5(L_1)_4(pyr)_2](ClO_4)_2\cdot pyr$ (**2**), $[Cu(II)_5(L_1)_4(pyr)_6](ClO_4)_2$ (**3**), and $[Cu(II)_5(L_2)_4(MeOH)_4](ClO_4)_2\cdot H_2O$ (**7**), whereby the terminal methanol ligands in **1** and **7** have been exchanged in a controlled manner with N- donor pyridine ligands to give complexes **2** and **3**. The introduction of ditopic connector ligands such as 4,4'-bipyridine (4,4'-bipy), 4,4'-azopyridine (4,4'-azp), and pyrazine (pz) at the axial Cu(II) coordination sites within our discrete $[Cu_5]$ metallacrown units (**1**-**3**), results in the pre-meditated formation of the extended networks: $\{[Cu(II)_5(L_1)_4(4,4'\text{-bipy})_3](ClO_4)_2\cdot H_2O\}_n$ (**4**), $\{[Cu(II)_5(L_1)_4(4,4'\text{-azp})_2(MeOH)_2](ClO_4)_2\}_n$ (**5**) and $\{[Cu(II)_5(L_2)_4(pz)_2(MeOH)](ClO_4)_2\cdot 3MeOH\}_n$ (**6**). Electrospray mass spectrometry and UV-vis analysis indicate the solution stability of the $\{Cu_5(L_x)_4\}^{2+}$ (x = 1, 2) cores. Magnetic susceptibility studies carried out on **1**, **4** and **6** establish strong antiferromagnetic exchange interactions between the Cu(II) ions, resulting in isolated S = 1/2 ground spin values in all cases.

Chapter 3 presents the synthesis, structural and magnetic characterisation of a family of Ni(II) cages also constructed via the hydroxamate building blocks L_1H_2 or L_2H_2. This family comprises two pentanuclear 12-$MC_{Ni(II)}$-4 metallacrowns $[Ni(II)_5(L_1)_4(MeOH)_4](ClO_4)_2\cdot 2MeOH$ (**8**) and $[Ni(II)_5(L_1)_4(pyr)_5](ClO_4)_2\cdot 1H_2O$ (**9**). Both complexes share analogous near-planar $\{Ni(II)_5(L_1)_4\}^{2+}$ cores; however they differ in the number and nature of ligands positioned at the axial Ni(II) sites. The addition of pyridine ligands in **9** converts previous square planar Ni(II) centres to square-based pyramidal/octahedral geometries, thus deliberately introducing extra

paramagnetic centres and allowing us to magnetically 'switch on' diamagnetic square planar Ni(II) centres within our analogous [Ni_5] metallacrowns. Subtle alterations to the reaction scheme for complexes **8** and **9** results in a change in topology as well as an increase in nuclearity via the formation of the hepta- and nonanuclear complexes [$Ni(II)_7(L_1H)_8(L_1)_2(H_2O)_6](SO_4)\cdot 15H_2O$ (**10**), [$Ni(II)_9(\mu\text{-}H_2O)_2(L_2)_6(L_2H)_4(H_2O)_2](SO_4)\cdot 29H_2O$ (**11**) and [$Ni(II)_9(\mu\text{-}H_2O)_2(L_2)_6(L_2H)_4(H_2O)_2](ClO_4)_2\cdot 2MeOH\cdot 18H_2O$ (**12**). DFT calculations were performed on **8** and **9** to ascertain the ground spin configurations (s = 0 vs. s = 1) of all Ni(II) centres, yielding three and four paramagnetic (s = 1) Ni(II) centres in **8** and **9** respectively. Complementary DFT analysis and dc magnetic susceptibility measurements demonstrate dominant antiferromagnetic exchange pathways in **8** and **9**. Magnetic susceptibility measurements carried out on **11** and **12** also indicate dominant antiferromagnetic exchange interactions, while analysis of complex **10** suggest competing ferro- and antiferromagnetic exchange pathways.

Chapter 4 details the in-situ ligand formation and subsequent Cu(II) ligation of the polydentate ligands o-[(E)-(2-hydroxy-3-methoxyphenyl)methylideneamino]benzohydroxamic acid (L_3H_3), [[2-[(E)-(2-hydroxy-3-methoxy-phenyl)methyleneamino]benzoyl]amino]ethanimidate (L_4H_2) and o-[(E)-(o-hydroxyphenyl)methylideneamino]benzohydroxamic acid (L_5H_3), formed via the Schiff base condensation of 2-(amino)phenylhydroxamic acid and either 2-hydroxy-3-methoxybenzaldehyde (to give L_3H_3 and L_4H_2) or 2-hydroxybenzaldehyde (to give L_5H_3). The result is the synthesis of a family of discrete Cu(II) polynuclear cages of formulae: [$Cu(II)_{10}(L_3)_4(L_2)_2(H_2O)_2](ClO_4)_4\cdot 5MeOH\cdot H_2O$ (**13**), [$Cu(II)_{14}(L_3)_8(MeOH)_3(H_2O)_5](NO_3)_4\cdot 2MeOH\cdot 3H_2O$ (**15**), [$Cu(II)_{14}(L_5)_8(MeOH)_6(NO_3)_4(H_2O)_2]\cdot 6MeOH\cdot 10H_2O$ (**16**) and [$Cu(II)_{30}(O)_1(OH)_4(OMe)_2(L_3)_{16}(MeOH)_4(H_2O)_2](ClO_4)_4\cdot 2MeOH\cdot 27H_2O$ (**17**). Each member comprises a topology derived from off-set stacked near planar layers of polynuclear subunits connected through long Cu(II)-O contacts. The exact topology observed is dependent on the specific reaction conditions and methodologies employed. Furthermore, through simple modifications to the reaction scheme for **13** (namely the addition of acetonitrile), the topologies previously observed in our Cu(II) cage family (**13** and **15-17**) were completely transformed upon the construction of the

Cu(II) 1D coordination polymer $\{[Cu(II)(L_4)]\cdot H_2O\}_n$ (**14**) (where L_4^{2-} = [[2-[(E)-(2-hydroxy-3-methoxy-phenyl)methyleneamino]benzoyl]amino]ethanimidate).

Chapter 5 investigates the coordination chemistry of Ln(III) metal ions with the ligand 2,6-dimethoxyphenol (L_6H). L_6H is specifically selected to facilitate the formation of two oxophilic compartments, making it an ideal ligand for the strategic construction of $[Ln(III)_2]$ dimers. We were proved correct and present here the microwave assisted synthesis of the dimeric series: $[Ln(III)_2(L_6)_2(ROH)_x(H_2O)_y(NO_3)_4]\cdot z EtOH$; where Ln = La, R = Et, $x = 4$, $y = 0$, $z = 0$ (**18**); Ln = Ce, R = Et, $x = 4$, $y = 0$, $z = 0$ (**19**); Ln = Gd, $x = 0$, $y = 2$, $z = 2$ (**20**); Ln = Gd, R = Me, $x = 2$, $y = 0$, $z = 0$ (**21**); Ln = Tb, R = Et, $x = 2$, $y = 0$, $z = 1$ (**22**); Ln = Tb, R = Me, $x = 2$, $y = 0$, $z = 0$ (**23**); Ln = Dy, $x = 0$, $y = 2$, $z = 2$ (**24**). Simple solvent selection allowed us to control the number of $\{Ln(III)_2\}$ units observed in the asymmetric unit (i.e. 1 versus 2). Complementary dc magnetic susceptibility measurements and DFT analysis reveal the presence of weak antiferromagnetic exchange in all paramagnetic family members. DFT calculations were also performed towards elucidating the magnetic exchange mechanisms observed in our complexes.

In Chapter 6 we report the coordination chemistry of the Schiff base ligand 1-[(methylimino)methyl]-2-naphthol (L_7H), as well as continuing our investigations of the ligand 2,6-dimethoxyphenol (L_6H). In the first section of Chapter 6, we present the synthesis and structural analysis of a Mn(III) hydrogen bonded chain $[Mn(III)(L_7)_2(N_3)MeOH]$ (**25**) and two Mn(III) 1D coordination polymers $[Mn(III)(L_7)_2(Cl)]_n$ (**26**) and $[Mn(III)(L_7)_2(N_3)]_n$ (**27**) along with a dinuclear Cu(II) metal complex of formula $[Cu(II)_2(L_7)]$ (**28**).

Coordination polymers **25**-**27** are the first Mn(III) based chains to be synthesised using the L_7H ligand, as well as adding to a family of analogous $[Mn(III)(L)_2(X)]_n$ (where L = 2-iminomethyl-6-methoxyphenol or 1-[(methylimino)methyl]-2-naphthol and X = Cl^-, Br^-, OAc^-, N_3^-) chains, previously synthesised by the Jones group. The introduction of a linear ditopic secondary building unit (SBU) in the form of 4,4'-bipyridine to the reaction scheme for **28** resulted in the formation of a hydrogen bonded 2D extended network of formula $[Cu(II)_2(NO_3)_2(L_7)_2(MeOH)_2(4,4'\text{-bipy})]_n$ (**29**). In the last section of this chapter, we describe the synthesis of the tetranuclear Co(II) cubic complex $[Co(II)_4(OMe)_4(L_6)_4(MeOH)_4]$ (**30**). Magnetic susceptibility measurements performed on **30** display weak ferromagnetic intra-molecular interactions between Co(II) metal centres and are suggestive of an effective S' = 2 ground state.

Publications

1) Progressive decoration of pentanuclear Cu(II) 12-metallacrown-4 nodes towards targeted 1- and 2D extended networks

C. McDonald, T. Whyte, S. M. Taylor, S. Sanz, E. K. Brechin, D. Gaynor and L. F. Jones, *CrystEngComm*, 2013, 15, 6672-6681.

2) High nuclearity Ni(II) cages from hydroxamate ligands

C. McDonald, S. Sanz, E. K. Brechin, M. K. Singh, G. Rajaraman, D. Gaynor and L. F. Jones, *RSC Adv.*, 2014, 4, 38182-38191.

3) Sheet Metal: Layered Cu(II) cages using polydentate ligands with premeditated high binding site concentrations *(Manuscript in preparation)*

C. McDonald, P. Comar, M. B. Pitak, E. K. Brechin and L. F. Jones.

4) Microwave-Assisted Synthesis of a Family of Dinuclear $[Ln(III)_2(L)_2(ROH)_x(H_2O)_y(NO_3)_4]$ Complexes (Ln = La, Ce, Gd, Tb and Dy; R = Me, Et) *(Manuscript in preparation)*

C. McDonald, T. Gupta, S. T. Meally, A. Prescimone, E. K. Brechin, G. Rajaraman and L. F. Jones.

Chapter One

Introduction

1.1 A Brief History of Magnetism

Magnetism is a phenomenon that details the study of the properties and interactions of materials in response to an applied/external magnetic field. It dates back thousands of years to the ancient Greeks in a place called Magnesia, which is where modern Turkey stands today. Large black stones were observed to attract small pieces of iron containing substances and the ancient Greeks named them ‘Magnesian stone’ after the district of Magnesia.[1] These stones were pieces of the mineral magnetite (Fe_3O_4), which is the most magnetic of all naturally occurring substances on earth. According to historians, the Chinese were the first to discover that when small needle like pieces of magnetite were floated in water, one of the poles/ends of the magnetite would always spin until it pointed north. These first compasses were believed to be invented during the Hans Dynasty between the 2nd century BC and the 1st century AD.[2] Initially they were used to locate gems, but by the 11th century AD they were adapted by the Chinese for the use of navigational pointers.[3] However, there were no reports of compasses in western Europe until the 12th century. As a result of their navigational properties, these small pieces of magnetite became known as "Lodestones" which basically means ‘way-stone’ or ‘leading-stone’.

In 1600, William Gilbert published "De Magnete" also known as "On the Magnet", where he was the first to explain that the Earth itself is magnetic in nature and therefore has its own magnetic field. In response to the Earth's magnetic field the needle of a compass points north-south.[1] In 1820, Hans Christian Ørsted was the first scientist to demonstrate a relationship between electricity and magnetism. During a lecture he noticed that the needle of a compass deflected from magnetic north, this occurred when a wire carrying an electric current was brought within close proximity of the compass.[4] André-Marie Ampère was the first scientist to explain the electro-dynamic theory. This theory states that two parallel wires containing electric current are attracted if the current flows in the same direction and are repelled if the current flows in opposite directions. He formulated the laws which dictate the interaction of currents with magnetic fields in a circuit; hence the unit of electric current (amp) was named after him.[5] In 1831, Michael Faraday discovered electromagnetic induction, which is the production of a voltage across a conductor when exposed to a varying magnetic field.[5] In 1845, he demonstrated that all materials respond to an applied magnetic field in either a paramagnetic or diamagnetic fashion.

The origin of an electric current (and the electron) was first discovered in 1897 by J. J. Thomson and his colleagues while performing experiments on cathode rays.[6] Electrons are sub-atomic negatively charged moving particles, which are able to generate their own magnetic field and therefore have a dipole magnetic moment. Consequently, electrons are often described as tiny magnets and all magnetic materials are composed of unpaired electrons. The significance of electrons to magnetism will be discussed in more detail in Section 1.3.1.

1.2 The Importance of Magnetism in Today's World

Nowadays, magnetism and magnetic materials represents a multi-billion euro industry. People have come to rely on the use of magnetic materials in many areas of everyday life, from fridge magnets to the magnets in credit and identification cards. They have a variety of uses in different electronic and telecommunication devices such as computer storage devices, telephone receivers, as well as the operation of computer and television screens. Magnetic materials also have applications in medicine and are used in magnetic resonance imaging (MRI) scanners, in order to apply the required external magnetic field. Additionally, paramagnetic materials such as Gadolinum(III) chelates and iron oxide nanomaterials (e.g. ferumoxides) are used as MRI contrast agents.[7-10]

1.2.1 A Brief Introduction to Molecular Magnetism

Molecular magnetism is the study of magnetic properties of materials at the molecular level, as opposed to bulk solid materials. Traditional bulk magnets contain extended long range magnetic ordering while molecular magnets do not. In particular, molecular magnetism is the study of the magnetic properties of isolated molecules and assemblies of molecules.[11] These molecules may contain one or more metal centres comprising unpaired electrons. Academically, the field of molecular magnetism is multidisciplinary and covers synthetic and theoretical chemistry and chemical physics. It continues to be fundamental in the development of the theory of molecular and solid state chemistry and physics.[11, 12] Indeed, molecular magnetism offers a linkage between disciplines such as material science and the study of biological processes. For example, in the metalloenzyme cytochrome-c oxidase, magnetic behaviour is observed in the interactions occurring between the active sites of Fe(III) and Cu(II) centres (d^5 and d^9 ions respectively). This magnetic behaviour is comparable to the behaviour observed in a ferrimagnetic chain compound containing Mn(II) and Cu(II) ions, which display spontaneous magnetisation at low temperatures.[11, 13] Furthermore, molecular magnetism allows inorganic chemists to obtain important information about the physical and chemical traits of their complexes. For example, it is possible to differentiate between high and low spin complexes such as Fe(III) (high spin S = 5/2, low spin S = 1/2), as a variation in the number of unpaired electrons will produce a different magnetic reading (Figure 1).

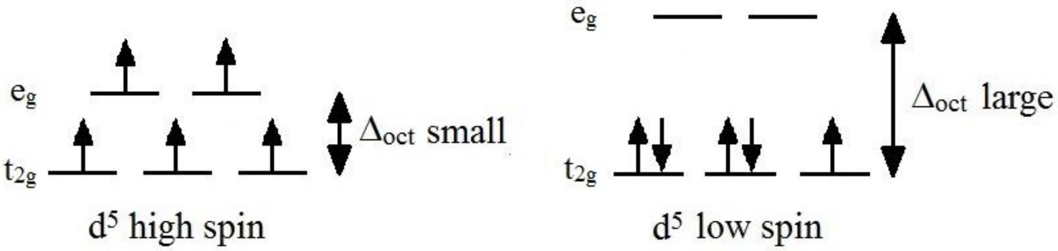

***Figure 1** - Crystal field diagram depicting a high spin (left) and a low spin (right) Fe(III) d^5 system. The symbol Δ_{oct} represents the crystal field splitting parameter, where Δ_{oct} is small for high spin systems and Δ_{oct} is large for low spin systems.*

More specific to the research carried out in this thesis, it is possible to differentiate between metal ions displaying different geometries within a complex. The magnetic measurements of Ni(II) species enable us to determine if a Ni(II) ion is square planar (s = 0, diamagnetic) or octahedral (s = 1, paramagnetic). In Chapter 3 we have carried out these particular measurements.

1.3 Some Fundamental Concepts of Magnetism

Before delving any further into the discipline of molecular magnetism, it is important to account for the basic concepts in this field of chemistry including the electron and micro spin states (M_S).

1.3.1 The Importance of the Electron

As stated previously, electrons are moving charged particles and have a magnetic moment and are therefore magnetic. The magnetic moment of an electron is generated by two possible sources:

1) ***Spin angular momentum*** - the intrinsic spin of an electron on its own axis generates the spin quantum number S. Only a free electron can possess spin angular momentum.

2) ***Orbital angular momentum*** - the orbit of an electron around the nucleus of the atom displays movement of charge, producing a magnetic field (magnetic moment) and is represented by the quantum number L.

The spin angular momentum and the orbital angular momentum combine to give the total angular momentum quantum number J (Equation 1.1).

$$J = S + L \quad \mathbf{(1.1)}$$

Each electron has a magnetic moment and spin quantum number (S) = 1/2. In the presence of an external magnetic field, an electron can either be ‘spin up’ with an M_s value of +1/2, or ‘spin down’ with an M_s value of -1/2 (Figure 2). The M_s states are known as spin microstates and the number of M_s states depends on the total spin quantum number (S). At zero magnetic field (H = 0), all the M_s states are degenerate and this is referred to as energy zero. The Zeeman effect refers to the splitting of S into M_s states upon an external magnetic field stimulus and is also known as Zeeman splitting. The spin multiplicity term (2S+1) determines the number of possible microstate orientations for a system. For instance in an S = 1 system, there are three possible M_s states taking values of Ms = -1, 0 and +1 (Figure 2). It can therefore be said that the possible M_s states range from +S to -S. Different M_s orientation states produce different energy values $E(M_s)$, which can be seen in Equation 1.2. $E(M_s)$ or $\Delta E(M_s)$ represents the change in energy of an M_s state brought about by the application of an external magnetic field (H), where g represents the electronic g-factor and β denotes the electron Bohr magneton (9.274×10^{-24} JT^{-1}).

$$E(M_s) = g\beta H M_s \quad \mathbf{(1.2)}$$

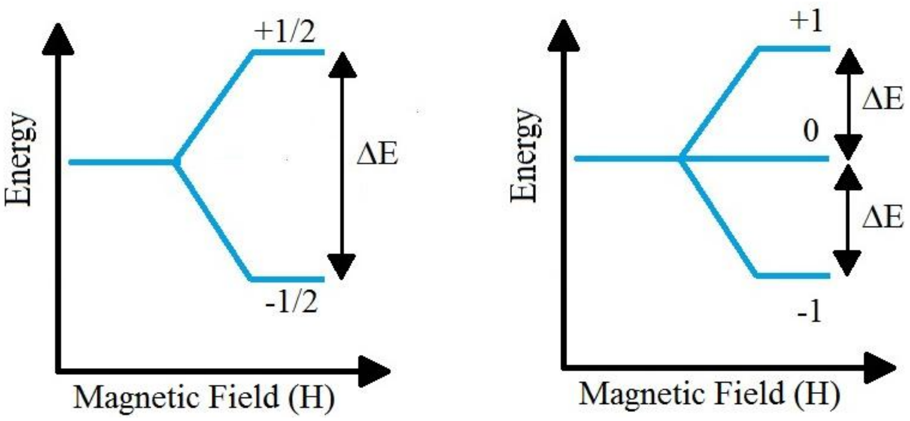

Figure 2 *- Illustration of the Zeeman splitting of microstates in an S = 1/2 (left) and an S = 1 system (right), where* $\Delta E = g\beta HM_s$.

The size of ΔE denotes the Zeeman effect and it is proportional to the applied magnetic field. Each M_s state has a different energy and therefore each M_s state is populated differently and the lowest lying energy states will be the most populated. The ΔE energy gaps tend to be quite small (in the order of microwave radiation GHz), therefore the difference in population of microstates such as $M_s = \pm 1/2$ is small. However, when carrying out magnetisation studies these small differences in M_s populations can be of great significance.

1.4 Quantifying Magnetic Properties

This section gives a brief introduction into some magnetism terminology including Magnetisation (M), magnetic susceptibility (χ) and magnetic moments per molecule (μ). We will also discuss the various types of magnetic behaviour regularly observed in magnetic materials, while introducing the related Curie and Curie-Weiss laws as well as the Van Vleck Equation.

1.4.1 Magnetisation and Magnetic Susceptibility

The volume magnetisation (M_v) of a paramagnetic sample is the magnetic dipole moment per unit volume upon application of a magnetic field. Likewise, the molar magnetisation (M_m; often referred to as M) quantifies the magnetic dipole moment per one mole of a sample. When a sample is exposed to an applied magnetic field the energy of the sample changes. The magnitude/intensity of the magnetisation of a sample is the rate of change of energy (E) of the sample in an applied magnetic field (H) (Equation 1.3). The units of an applied magnetic field are gauss (G) or oersted

(Oe) in the cgs system (where 1G = 1Oe). The units of tesla (T) are often used, where 1 tesla (T) = 10^4 G = 10^4 Oe. In the field of molecular magnetism, the most common units utilised for molar magnetisation (M) are cm^3 G mol^{-1}, which derives from the conversion of units for volume magnetisation (M_v) to molar magnetisation (M). Alternatively M can be expressed in Nβ units, N is Avogadro's number and β is the electronic Bohr magneton (1Nβ = 5585 cm^3 G mol^{-1}).

$$M = -\left[\frac{\delta E}{\delta H}\right] \quad \mathbf{(1.3)}$$

Magnetic susceptibility (χ) defines how attracted a sample is to a magnetic field. It is the rate of change of a samples magnetisation (M) in relation to the rate of change of an external magnetic field (H) (Equation 1.4).

$$\frac{\delta M}{\delta H} = \chi \quad \mathbf{(1.4)}$$

When the value for H is small, χ is considered to be independent of H and exists as a proportionality constant between M and H (Equation 1.5).

$$\chi = \frac{M}{H} \quad \mathbf{(1.5)}$$

χ is the experimentally obtained value; however in order to assess a samples true susceptibility the molar magnetic susceptibility (χ_M) must first be calculated. χ_M is the magnetic susceptibility per one mole of a sample and is calculated via Equation 1.6. Here, the molecular weight is denoted by Mwt and χ_g represents the magnetic susceptibility per gram (χ_g is obtained from χ by dividing by the samples density).

$$\chi_M = \chi_g \times Mwt(gmol^{-1}) \quad \text{(Units: cm}^3\text{ mol}^{-1}\text{)} \ \mathbf{(1.6)}$$

When determining the magnetic susceptibility of a paramagnetic compound the negative diamagnetic component (χ_{dia}) must first be calculated in order to obtain the true magnetic susceptibility value due to unpaired electrons (χ_{para}) (Equation 1.7). Diamagnetic susceptibilities of atoms are additive and can be estimated by summing the atomic susceptibilities known as Pascal's constants (Equation 1.8). Pascal's constants are a list of magnetic susceptibilities for all atoms, groups and bonds that make up a molecule. The letters A and B represent the atoms and bonds (including additional contributions such as π-bonds) respectively.

$$\chi_{obs} = \chi_{para} + \chi_{dia} \quad \textbf{(1.7)}$$

$$\chi_{dia} = \sum \chi_A + \sum \chi_B \quad \textbf{(1.8)}$$

Pascal's constants are not always accurate. Ideally the χ_{dia} value should be measured directly by measuring experimentally the χ_{obs} of a ligand in the absence of a paramagnetic metal, or by measuring the χ_{obs} of a diamagnetic analogue. However, in general for molecules of lower molecular weights the χ_{dia} value is very small, or even negligible, thus the inaccuracies of the Pascal's constants method are not hugely important. On the other hand, the accurate determination of χ_{dia} for molecules of larger molecular weights (such as proteins) is of greater importance. As χ is often highly temperature dependent, it is common to measure it as a function of temperature (i.e. $\chi_{\mathrm{M}}\mathrm{T}$). The room temperature value of $\chi_{\mathrm{M}}\mathrm{T}$ is useful in determining what type of magnetic exchange is occurring in a sample, as well as ensuring that a sample is of good purity. For example, if the $\chi_{\mathrm{M}}\mathrm{T}$ value at room temperature is too high it indicates the presence of impurities. In addition, antiferromagnetic samples tend to possess room temperature $\chi_{\mathrm{M}}\mathrm{T}$ values below their theoretical calculated values, while ferromagnetic samples tend to exhibit room temperature $\chi_{\mathrm{M}}\mathrm{T}$ products that are equal to, or greater than their theoretical values. The $\chi_{\mathrm{M}}\mathrm{T}$ product is related to the spin angular momentum (S) via Equations 1.9, where the electron g-factor (g) = 2 and Equation 1.10, where $g \neq 2$.

$$\chi_M T = \frac{S(S+1)}{2} \quad \text{(Units: cm}^3\text{ K mol}^{-1}\text{)} \ \textbf{(1.9)}$$

$$\chi_M T = \frac{g^2}{8} S(S+1) \quad \textbf{(1.10)}$$

1.4.2 Magnetic Moments Per Molecule

As M and χ_{M} are macroscopic properties, they refer to a bulk sample (i.e. per mole of a substance). The magnetic moment (μ) parameter allows for a measure of the spin quantum number (S) per molecule, where each electron has an S = 1/2 value. Therefore, the number of unpaired electrons in a metal complex may be calculated by measuring its magnetic moment. The intrinsic electron spin (S) and the electron orbit about the nucleus (L) combine to give what is known as the effective magnetic moment (μ_{eff}) parameter (Equation 1.11). This equation assumes that S and L are independent of each other.

$$\mu_{eff} = \sqrt{L(L+1) + 4S(S+1)} \quad \textbf{(1.11)}$$

When the orbital angular momentum (L) is quenched, only the electron spin quantum number (S) is responsible for the magnetic behaviour, resulting in the spin-only formula given below (Equation 1.12, where n = number of unpaired electrons). The most common unit used for magnetic moment is the Bohr magneton (BM), which is the natural unit for a single electron magnetic dipole moment (1 BM = 9.274×10^{-24} J T^{-1}) and is usually written as μ_B.

$$\mu_{S.O} = 2\sqrt{S(S+1)} = \sqrt{n(n+2)} \quad \textbf{(1.12)}$$

The magnetic susceptibility is directly related to the spin-only formula by:

$$\mu_{S.O} = 2.828\sqrt{\chi_M T} \quad \textbf{(1.13)}$$

1.4.3 Types of Magnetic Behaviour

Magnetisation (M) is the response of current loops to an applied magnetic field and for the most part the magnetic moments tend to orientate along the direction of the magnetic field, resulting in a positive M and χ value. However, negative M and χ values can also occur. The sign of M distinguishes between the main types of magnetic behaviour which are known as diamagnetism and paramagnetism. Other phenomena such as antiferromagnetism, ferromagnetism and ferrimagnetism all derive from paramagnetic behaviour.

1.4.3.1 Diamagnetism

A diamagnetic material is composed only of paired electrons and it is a property found in all matter. Upon application of an external magnetic field to a diamagnetic material, the diamagnetic substance opposes the lines of flux and are therefore repelled by the magnetic field (Figure 3). Negative magnetisation (M) and magnetic susceptibility (χ) values arise in response to the interaction of paired electrons and the applied homogenous magnetic field (H). The χ value of a diamagnetic substance is independent of temperature and the applied magnetic field. When M is negative (diamagnetic material), the energy (E) of the system is increasing with an increasing H value, resulting in a positive $\frac{\delta E}{\delta H}$ value. As a result, diamagnetic materials tend to move towards regions of lowest field strength, which decreases E and therefore the system is in a lower energy state which is more stable. Diamagnetism is a weak form of magnetism, which only exists while the magnetic field is applied.

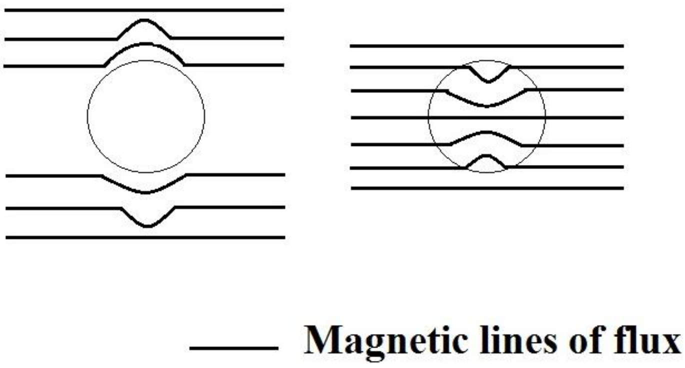

Figure 3 *- Illustration of the interaction of (left) diamagnetic substances and (right) paramagnetic substances with the magnetic lines of flux of an applied magnetic field.*

1.4.3.2 Paramagnetism

Paramagnetic materials comprise unpaired electrons as well as paired electrons and therefore they contain a diamagnetic component (from the paired electrons). Paramagnetic substances are drawn into the magnetic lines of flux upon application of an external magnetic field and hence they are attracted to the magnetic field (Figure 3). As a result, they have positive magnetisation (M) and magnetic susceptibility (χ) values. In the absence of an applied magnetic field, the individual magnetic moments of a paramagnetic sample remain unaffected by their neighbours, resulting in a completely randomised arrangement and a magnetic moment of zero (Figure 4a). Upon application of an external magnetic field, the individual magnetic moments align with one another in the direction of the magnetic field (Figure 4b and 4c). For true paramagnets this alignment is weak and once the applied magnetic field is removed the system reverts back to randomized magnetic moments.

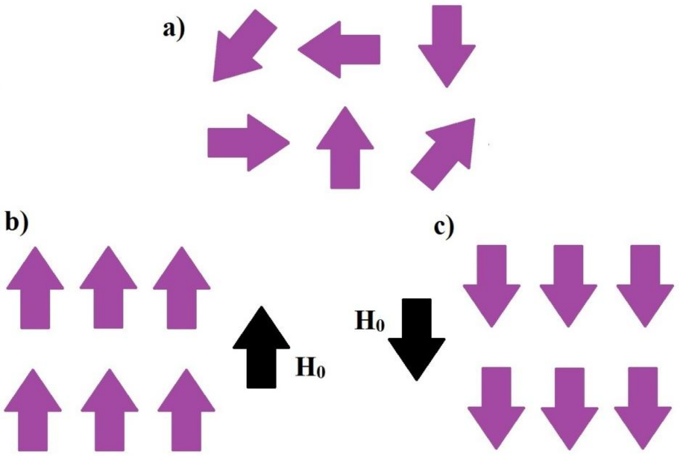

Figure 4 - *a) Schematic of the randomly orientated individual magnetic moments in a paramagnet. b) and c) Alignment of the individual magnetic moments in a paramagnetic sample with respect to the direction of an applied magnetic field.*

The magnetic susceptibility (χ) value of paramagnetic substances is temperature dependant and is usually independent of the applied field unless the H/T value is large. At lower temperatures, the unpaired electrons have less thermal energy and therefore they are more likely to align with the external magnetic field. Hence, as the temperature decreases the magnetic susceptibility of a material will increase. On the other hand, at higher temperatures, the thermal energy increases and therefore the magnetic susceptibility value decreases (Figure 5).

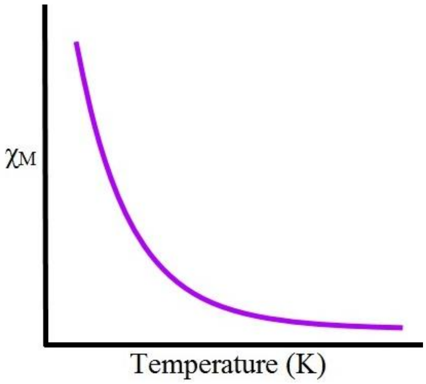

Figure 5 - *Illustration of molar magnetic susceptibility (χ_M) vs. temperature plot for a paramagnetic material. This type of behaviour is exhibited by ferro- and antiferromagnetic materials above their Curie (T_C) and Néel temperatures (T_N), respectively.*

1.4.3.3 Antiferromagnetism

In the presence of an applied magnetic field, the individual magnetic moments in an antiferromagnetic sample align anti-parallel to one another, cancelling each other out and resulting in a net magnetic moment of zero (Figure 6a).

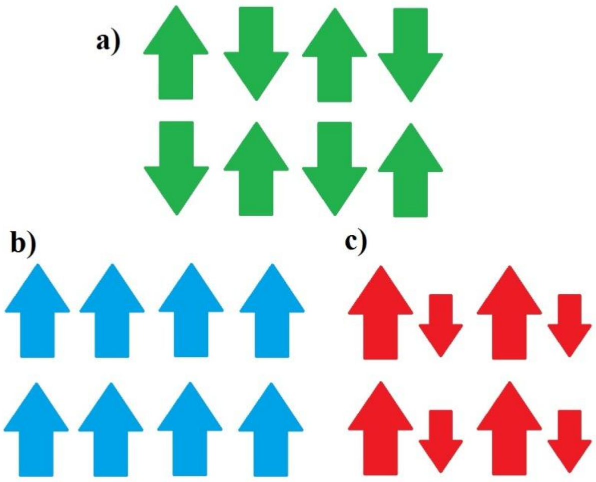

Figure 6 *- Diagram representing the alignment of individual magnetic moments in a) antiferromagnetic, b) ferromagnetic and c) ferrimagnetic systems.*

This type of magnetic ordering occurs at and below the critical temperature known as the Néel temperature (T_N). As the temperature rises, the magnetic susceptibility increases and thermal fluctuations increasingly disrupt the anti-parallel alignment of neighbouring magnetic moments. Above the T_N value antiferromagnetic behaviour declines abruptly and the sample becomes paramagnetic (i.e. the magnetic moments become randomised) (Figure 5 and 7).

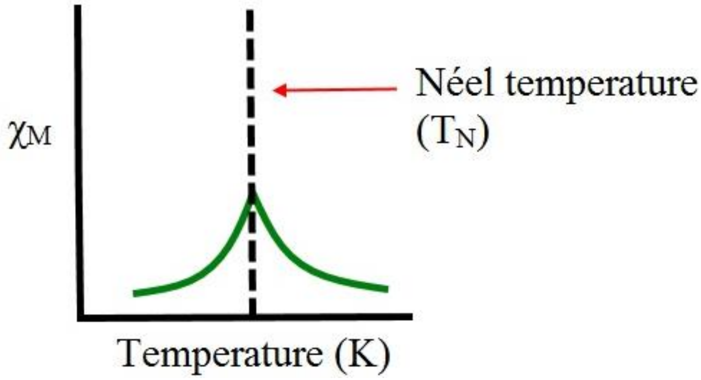

Figure 7 *- General representation of a molar magnetic susceptibility (χ_M) vs. temperature plot for an antiferromagnetic sample. The characteristic Néel temperature (T_N) is represented by a dashed line. An antiferromagnet behaves paramagnetically above T_N.*

1.4.3.4 Ferromagnetism

Ferromagnetism involves the parallel alignment of individual magnetic moments upon application of an applied magnetic field, resulting in a large net magnetic moment (Figure 6b). It is a much less common type of magnetism than antiferromagnetism and was originally named after metallic iron as it displays ferromagnetic properties. This type of magnetic ordering occurs below the Curie temperature (T_C). Above the

T_C value a ferromagnet loses its permanent magnetism and displays paramagnetic characteristics (i.e. the magnetic moments become randomised) (Figure 5 and 8).

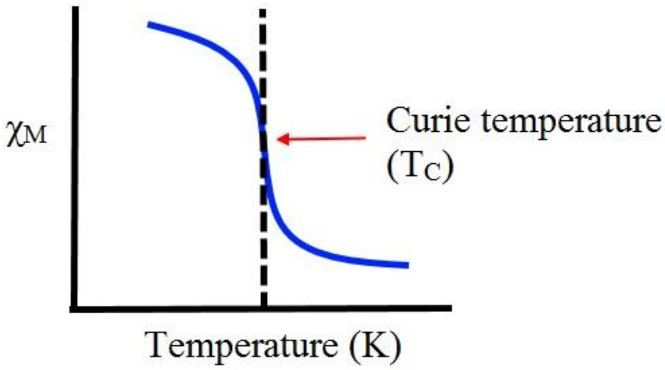

Figure 8 - *Schematic of typical ferromagnetic behaviour, where the Curie temperature (T_C) is represented by a dashed line.*

Bulk ferromagnets consist of regions of intense magnetic fields known as domains. Within each domain the spins are aligned, however the direction of the spins of individual domains are different. When an external magnetic field is applied all the domains line up and the sample is said to be magnetised (Figure 9). Unlike paramagnets, ferromagnets remain magnetised upon removal of an external magnetic field and are therefore often called permanent magnets.

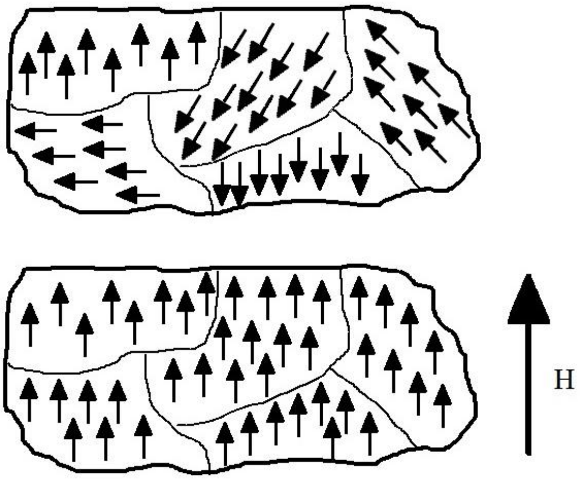

Figure 9 - *Schematic highlighting the spins within the individual domains of a bulk ferromagnetic material. (Top) In the absence of a magnetic field the direction of the net magnetisation of individual domains differ. (Bottom) When an external magnetic field (H) is applied the spins in all the individual domains align with the magnetic field.*

1.4.3.5 Ferrimagnetism

Ferrimagnetism is a type of antiferromagnetic behaviour, where the individual magnetic moments align in an anti-parallel arrangement, but the opposing adjacent moments are unequal in magnitude and hence produce a net magnetic moment (Figure 6c). The oldest known magnetic substance, magnetite ($Fe(II)Fe(III)_2O_4$) (Fe(II), S = 2, Fe(III), S = 5/2) is an example of a ferrimagnet. Other than ferromagnets, ferrimagnets are the only other magnetic materials thought of as permanent magnets. That is, they retain magnetisation when an applied magnetic field is removed. Below a temperature known as the ferrimagnetic Néel temperature (T_{fN}), these materials order in a ferrimagnetic arrangement.

1.4.3.6 Superparamagnetism

Superparamagnetism is a type of magnetic behaviour displayed in small single domain ferro- or ferrimagnetic nanoparticles (typical size of 10nm)[1] and more recently in Single-Molecule Magnets (SMMs) (see Section 1.9.1). These nanoparticles are composed of single magnetic domains, where the total magnetic moment of the nanoparticle can be thought of as one giant magnetic moment, consisting of all the individual magnetic moments of the atoms which make up the nanoparticle. Superparamagnetism is the ability of these nanoparticles to randomly flip the direction of magnetisation under the influence of temperature. If the nanoparticle is magnetically anisotropic (i.e. has a preferential direction for the alignment of its magnetic moment) (see Section 1.6), it will only possess two stable orientations anti-parallel to each other, separated by an energy barrier (ΔE). The so called *'easy axis'* is defined by these stable orientations. The average time between two flips is referred to as the Néel relaxation time (τ_N) and is given by the Néel-Arrhenius equation (Equation 1.14). τ_0 is a characteristic attempt time for spin reversal of a material (typically 10^{-9}-10^{-12} seconds),[14] k_B is the Boltzmann constant, T is the temperature, K is the magnetic anisotropy density, V is the volume and KV combined is equal to the energy barrier (ΔE).

$$\tau_N = \tau_0 \exp(\frac{KV}{k_B T}) \quad \textbf{(1.14)}$$

The blocking temperature (T_B) of a superparamagnet is the temperature at which the magnetisation does not flip during measurement, therefore the magnetisation is retained in one direction and is said to be blocked from flipping to the other direction.

1.4.4 Magnetic Hysteresis

Upon application of an external magnetic field, the atomic dipole moments of a magnetic sample align themselves with the magnetic field and the sample is said to be magnetised. Upon removal of the external magnetic field, part of the alignment of the sample can be retained and the sample remains magnetised. Once the sample is magnetised, it can potentially stay magnetised indefinitely. To demagnetise the sample, heat or a magnetic field in the opposite direction is required. This property is known as magnetic hysteresis and can be considered as a memory effect. A hysteresis loop is a plot of the response of magnetisation (M) in relation to an applied magnetic field for two opposing directions (+H and -H). Hence, hysteresis measurements determine a magnetic materials ability to remain magnetised in the absence of a magnetic field, as well as upon application of a magnetic field switch. Upon removal of a magnetic field, a pure paramagnet will lose its magnetisation almost instantly, due to thermal agitation, which randomises the orientation of the atomic dipoles so that they are no longer aligned with the external magnetic field. A soft ferro- or ferrimagnet will retain its memory for a short time (small energy barrier to magnetisation reorientation), while a hard ferro- or ferrimagnet will stay magnetised for a much longer time due to its significantly larger magnetisation reorientation energy barrier (Figure 10). For an ideal ferro- or ferrimagnet the *remnant magnetisation* equals the *saturation magnetisation* value. The *coercivity* is the value of the opposing applied magnetic field required to return the magnetisation to a value of zero. The *coercive field* is the area inside the hysteresis loop and its size is a good indication for the hardness of a magnetic material (i.e. the bigger the area the better the magnet). Figure 10 also shows that even though both the hard and soft magnets have approximately the same value for magnetisation saturation, their remnant magnetisation and coercivity values differ and are much lower for the soft magnet (i.e. it is much easier for the soft magnet to lose its magnetisation).

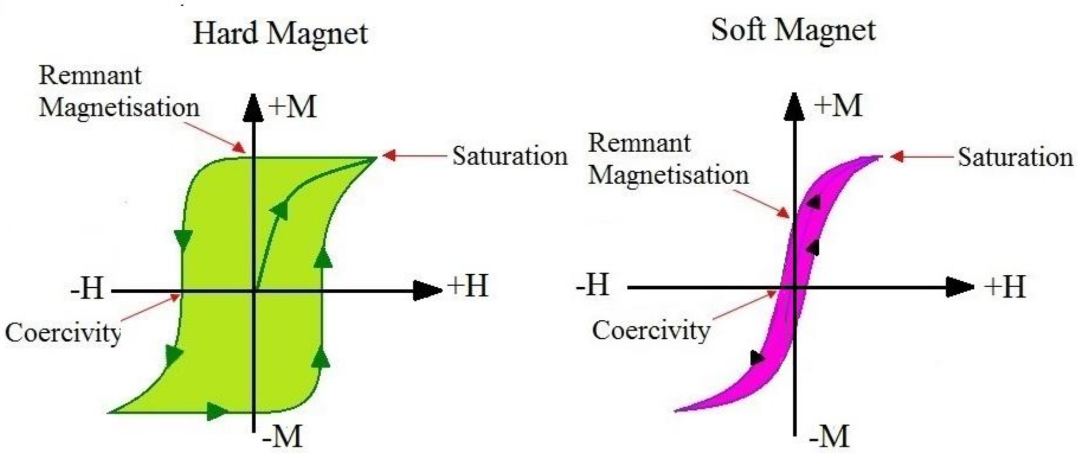

Figure 10 *- Schematic of Magnetisation (M) vs. Magnetic field (H) hysteresis plots for a hard (left) and soft magnet (right).*

1.4.5 The Curie and Curie-Weiss Laws

The Curie Law states that for a paramagnetic material the molar magnetic susceptibility (χ_M) of the particular material is inversely proportional to the temperature (Equation 1.15), thus χ_M increases as you lower the temperature. The value C is known as the Curie constant (units: $cm^3\ mol^{-1}\ K$), it relates a materials molar magnetic susceptibility to its temperature and is a material dependent property.

$$\chi_M = \frac{C}{T} \quad \textbf{(1.15)}$$

The Curie Law is only accurate for systems where the unpaired electrons do not communicate with each other (i.e. magnetically dilute materials). In such systems, the Curie constant (C) can be obtained by plotting $1/\chi_M$ vs. T to give a straight line where C^{-1} = slope (Figure 11). Generally the intercept of the straight line will not go through the origin. Traditionally, the Curie constant is converted into the magnetic moment (μ) (Equation 1.16).

$$\chi_M T = C = \frac{\mu^2}{8} \quad \textbf{(1.16)}$$

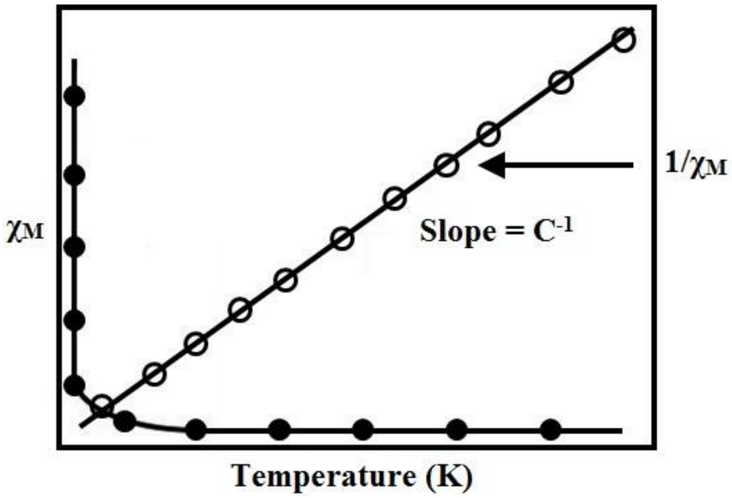

Figure 11 - *Plots of χ_M vs. T (black points) and $1/\chi_M$ vs. T (no fill points) of a system obeying the Curie Law. The slope of the graph is equal to C^{-1}.*

Quite often the observed molar magnetic susceptibility for magnetically non-dilute materials cannot be fitted using the Curie Law. In these situations, plotting of $1/\chi_M$ vs. T would not give a straight line and therefore a C parameter derived from the slope would be insignificant. In order to account for these magnetic interactions between neighbouring paramagnetic centres, a modified version known as the Curie-Weiss Law was proposed (Equation 1.17). An additional parameter θ (units: K) known as the Weiss constant is material specific and accounts for the weak inter-molecular interactions.

$$\chi_M = \frac{C}{(T-\theta)} \quad \textbf{(1.17)}$$

Plotting of $1/\chi_M$ vs. T gives a straight line, with θ as the intercept of the x axis (Figure 12). The sign of θ is a strong indication of the type of magnetic behaviour occurring within a particular system. For example, ferromagnetic systems tend to have a positive θ value, while antiferromagnetic systems usually have a negative θ value.

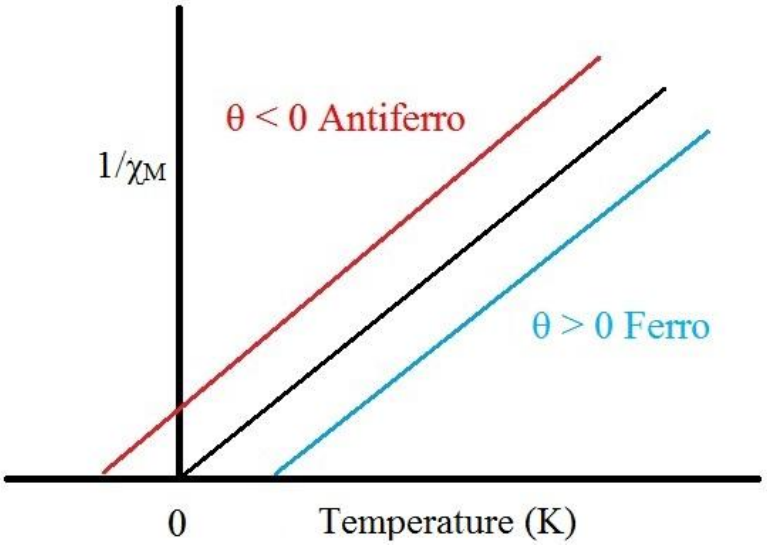

Figure 12 *- Curie-Weiss plot of 1/χ_M vs. T with Curie-Weiss constant (θ) at the intercept.*

It is quite common to present several other plots such as χ_MT vs. T, to show deviations from the Curie behaviour. This enables us to present a more detailed and informative picture of the magnetic behaviour occurring in our magnetic samples. For magnetically dilute materials, χ_MT does not vary as a function of temperature and obeys the Curie Law. However, the χ_MT product for a magnetically coupled system varies significantly with temperature, especially at low temperatures. Figures 13-15 illustrate the deviations from the Curie Law for real literature based antiferromagnetic and ferromagnetic materials, while deviations observed for ferrimagnetic materials can be seen in Figure 13.

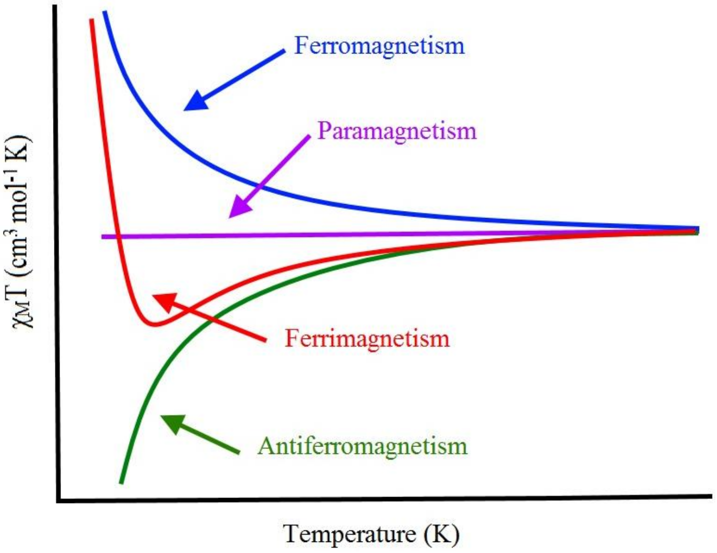

Figure 13 *- Schematics of the temperature dependence of χ_MT for paramagnets (purple), ferromagnets (blue), antiferromagnets (green) and ferrimagnets (red).*

Figures 14 and 15 have been removed due to copyright restrictions and can be seen in references 15 and 16 respectively.

1.4.6 The Van Vleck Equation

The Curie Law is only operational for a simple spin S system. It ignores a number of more complicated features including spin-orbit coupling, mixing into the ground state of excited states and zero-field splitting of excited states. Therefore, in order to accommodate for a variety of situations where these events are occurring, a more general equation is required for the calculation of χ_M. The Van Vleck Equation fulfils these requirements.

Firstly, the energy of state *n* (E_n) is calculated as a power series in terms of the applied field (H) via Equation 1.18, where $E_n^{(0)}$ is the energy of *n* at zero field, $E_n^{(1)}$ is the first-order Zeeman coefficient and $E_n^{(2)}$ is the second-order Zeeman coefficient. The interaction of state *n* with H and higher energy excited states (arising from field-induced mixing) results in energy changes $E_n^{(1)}H$ and $E_n^{(2)}H^2$ respectively.

$$E_n = E_n^{(0)} + E_n^{(1)}H + E_n^{(2)}H^2 + \dots \quad \textbf{(1.18)}$$

Therefore, the magnetic moment of state *n* or the microscopic magnetisation (μ_n) can be derived from Equation 1.19.

$$\mu_n = \frac{-\delta E_n}{\delta H} = -E_n^{(1)} - 2E_n^{(2)}H + \dots \quad \textbf{(1.19)}$$

The second approximation is that H/kT is small with respect to unity (i.e. H is not too large and T is not too small) resulting in Equation 1.20.

$$\exp(-E_n/kT) = \exp(-E_n^{(0)}/kT)(1 - E_n^{(1)}H/kT) \quad \textbf{(1.20)}$$

The two approximations combine to give the total macroscopic magnetisation (M) (Equation 1.21)

$$M = \frac{N\sum_n(-E_n^{(1)} - 2E_n^{(2)}H)(1 - E_n^{(1)}H/kT)\exp(-E_n^{(0)}/kT)}{\sum_n(1 - E_n^{(1)}H/kT)\exp(-E_n^{(0)}/kT)} \quad \textbf{(1.21)}$$

Under zero field, the magnetisation vanishes to give Equation 1.22.

$$\sum_n E_n^{(1)}\exp(-E_n^{(0)}/kT) = 0 \quad \textbf{(1.22)}$$

Substitution of Equation 1.22 into Equation 1.21 results in Equation 1.23.

$$M = \frac{NH\sum_{n}(E_n^{(1)^2}/kT - 2E_n^{(2)})\exp(-E_n^{(0)}/kT)}{\sum_{n}\exp(-E_n^{(0)}/kT)} \quad \mathbf{(1.23)}$$

From Equation 1.5 we know that $\chi = \frac{M}{H}$, therefore the molar magnetic susceptibility (χ_M) can be calculated via Equation 1.24. This formula describes the relationship between macroscopic magnetisation and the Boltzmann's population of contributing M_s states and is known as the *Van Vleck Equation* (after John Hasbrouck Van Vleck).

$$\chi_M = \frac{N\sum_{n}E_n^{(1)^2}/kT - 2E_n^{(2)})\exp(-E_n^{(0)}/kT)}{\sum_{n}\exp(-E_n^{(0)}/kT)} \quad \mathbf{(1.24)}$$

This equation can be utilised to derive the Curie Law (under Curie Law assumptions), as well as accounting for situations which the Curie/Curie-Weiss Law cannot be applied.

1.5 Measuring the Magnetic Susceptibility χ

There are two main methods for the measurement of the magnetic susceptibility parameter (χ): 1) ***Force Methods*** (e.g. Gouy Balance) and 2) ***Induction Methods*** via a Superconducting Quantum Interference Device (SQUID). The Gouy balance determines the magnetic susceptibility (χ) by measuring the change in weight of a sample when placed in a homogenous magnetic field. A sample is placed in a cylindrical quartz tube, suspended at a height (h) from a sensitive balance, which is located between the two poles of a magnet. The bottom end of the sample (X in Figure 16) is positioned centrally between the two poles (i.e. in a strong applied magnetic field), while the top end of the sample (Y) is kept at zero field (Figure 16). Upon application of the magnetic field a displacement force is exerted on the sample and a change in weight occurs which is then related to χ. SQUID measurements (see below) offer a much greater sensitive technique and are therefore more commonly used in magnetic studies.

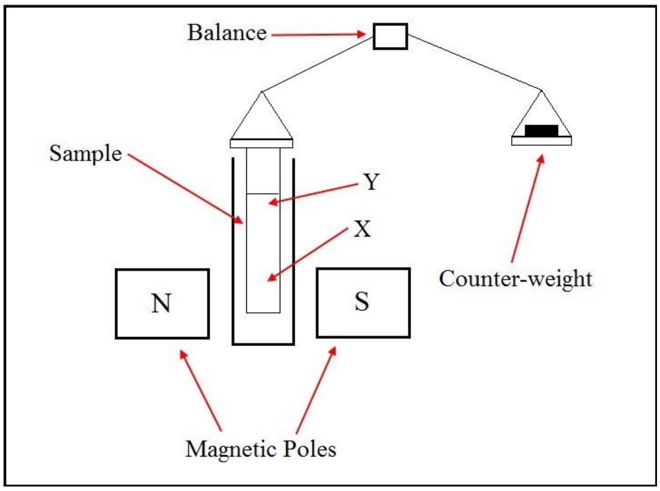

Figure 16 *- Schematic for a simple Gouy Balance.*

1.5.1 Induction Methods via SQUID Measurements

SQUID measurements offer a highly sensitive (>10^{-12} emu vs. 10^{-6}-10^{-8} emu for Gouy method) approach to the measurement of magnetic susceptibility, resulting in a superior technology when compared to previously employed force methods. As well as offering an easy variable temperature control, this method only requires a small amount of powdered sample (~20 mg) as it can detect very small magnetic field changes, while single crystals are also easily measured. SQUID technology has been utilised since the 1960's and there are two types of SQUID magnetometers: 1) *direct current (DC)* and 2) *radio frequency (RF),* both of which were developed at Ford Scientific Labs.[17, 18] A DC SQUID is based on the Josephson effect[19] and has two Josephson junctions connected in a parallel arrangement within the superconducting loop (Figure 17).[20] Each Josephson junction is composed of two superconductors that are weakly connected by a superconductor-insulator-superconductor junction. The RF SQUID comprises one Josephson junction, therefore it is cheaper than a DC SQUID but it is less sensitive. The SQUID technique utilises an electromagnetic induction process, where a superconducting magnet generates a magnetic field. The sample is mixed with a low melting point wax (eicosane) to avoid movement of the material (a.k.a. torqueing of the crystallites) and it is placed in the SQUID machine. Here, it is surrounded by a superconducting (S_c) sensing coil which is coupled to a second loop within the SQUID. As the magnetised sample moves through the S_c coil, a current is generated which then induces a voltage in the second S_c loop. These S_c loops have zero resistance and therefore no damping or loss of signal occurs. The magnitude of the induced voltage is proportional to the magnetic susceptibility (χ) of the sample.

The one major disadvantage of the SQUID method is the complexity and expensive equipment which is required. For instance, a basic SQUID model can cost in between €400,000-500,000, while liquid He and general maintenance costs can also be prohibitively expensive.

Figure 17 has been removed due to copyright restrictions and can viewed in reference 20.

1.6 Magnetic Anisotropy

Up until now, it has been assumed that the magnetic susceptibility (χ) of a material is independent of molecular orientation in an applied magnetic field and is therefore isotropic. However, this is not usually the case, as the majority of magnetic materials are anisotropic in nature. This means that a molecule or compound preferentially aligns its magnetic moments along a certain direction in a magnetic field (H). This is known as the easy axis, as it is more energetically favoured and is usually defined as the z axis. Therefore, a materials magnetic properties differ depending on which axis you measure along (x, y, z). Isotropic behaviour tends only to be observed in systems displaying pure O_h and T_d (cubic) symmetries, where the symmetry around a metal ion is quenched via the ligands. The magnetic susceptibility is a tensor quality and is described by a 3 x 3 matrix (Equation 1.25).

$$\begin{pmatrix} \chi_{xx} & \chi_{xy} & \chi_{xz} \\ \chi_{yx} & \chi_{yy} & \chi_{yz} \\ \chi_{zx} & \chi_{zy} & \chi_{zz} \end{pmatrix} \quad \textbf{(1.25)}$$

The average susceptibility $\overline{\chi}$ is described in Equation 1.26.

$$\overline{\chi} = \frac{\chi_{xx} + \chi_{yy} + \chi_{zz}}{3} \quad \textbf{(1.26)}$$

If $\chi_{xx} = \chi_{yy} = \chi_{zz}$ then the χ value for the material is said to be isotropic. On the other hand, if $\chi_{xx} = \chi_{yy} \neq \chi_{zz}$ then the χ parameter is said to be axial.

1.6.1 Types of Magnetic Anisotropy

1.6.1.1 g-anisotropy

The g-value characterises a particles magnetic moment (μ) and is an assessment of the orbital angular momentum of the electron. The g-value links a particles magnetic moment with its angular momentum quantum number (M_l), producing a real value of μ_B (units of Bohr magnetons) and sequentially χ. Furthermore, the energy gap between M_s states and the applied magnetic field (H) are linked by the g-value as can be seen in Equation 1.27.

$$\Delta E(M_s) = g\beta M_s H \quad \textbf{(1.27)}$$

In isotropic systems g is often quoted as ~ 2; however when there is significant spin-orbit coupling, the g-value deviates from 2 and indicates an anisotropic system. A free electron has a g-value of 2.0023 and is referred to as g_e. The g-value is dependent on the energy gap between ground state (E_{gs}) and excited state (E_{es}), where $\Delta g = g - g_e$ (Equation 1.28). The orientation of the orbital containing the unpaired electron (in terms of the applied field) determines which excited state can couple with the ground state (i.e. the g-value is anisotropic). If an unpaired electron couples to an empty orbital i.e. d^1 systems then $g < g_e$, whereas if an unpaired electron couples to an occupied orbital i.e. d^9 system then $g > g_e$. The symbol λ represents the spin-orbit coupling (SOC) constant and the magnitude of this parameter is dependent on angular momentum, which varies from ion to ion.

$$\Delta g = n\lambda / (E_{es} - E_{gs}) \quad \textbf{(1.28)}$$

1.6.1.2 Zero-Field Splitting

Zero-field splitting (ZFS) is the removal of spin microstate degeneracy for S > 1/2 systems in the absence of a magnetic field (H). The ZFS phenomenon arises from the spin-orbit coupling (SOC) (Section 1.7) of empty excited states into the ground state, as a result of the lowering of symmetry around the metal centre. ZFS is often referred to as single-ion anisotropy in magnetism. For an S = 1 system, ZFS splits the microstates into the $M_s = 0$ and $M_s = +/-1$ energy levels in the absence of an applied magnetic field and the energy separation between the two states is the zero-field splitting parameter (D). If $M_s = \pm 1$ is the lowest energy state, this means that the magnetisation is preferentially aligned along the '*easy axis*' and results in a negative

D value.[21] If the $M_s = 0$ is the lowest energy state, this means that the magnetisation lies along an '*easy plane*' and results in a positive D value (Figure 18). In addition, illustrations of S = 3/2 and S = 2 systems can be seen in Figure 18.

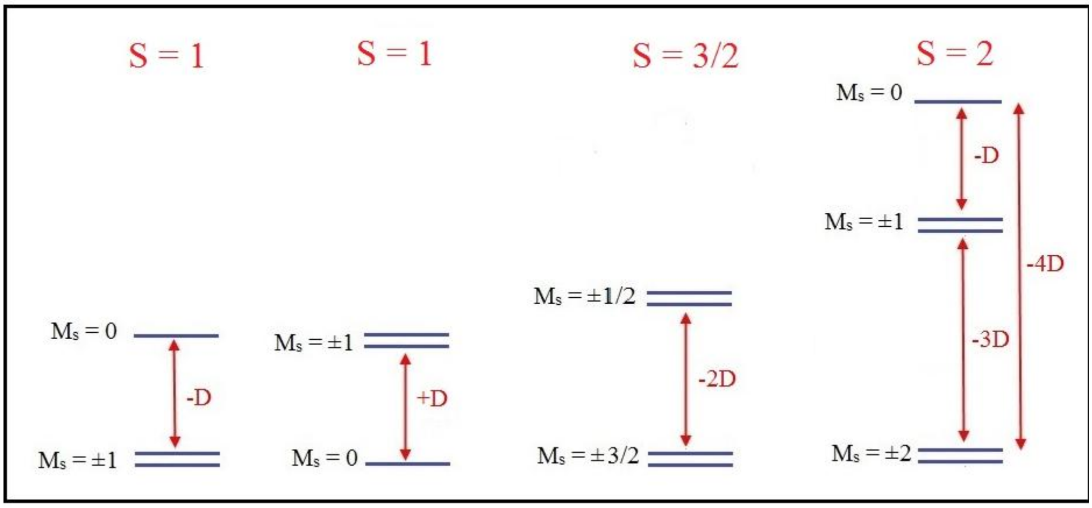

***Figure 18** - Schematic representing the zero-field splitting of systems where S = 1 (for both positive and negative D parameters), S = 3/2 and S = 2. Here, S = 3/2 and S = 2 systems display negative D parameters.*

Sometimes the spin-orbital contribution is quenched and therefore no ZFS occurs. For example, an S = 3/2 system such as an octahedral Cr(III) (d^3) ion in a CrL_6 complex (where L = ligand) displays no ZFS and the magnetic moment of this material is given by the spin-only formula: $\mu_{S.O} = 2\sqrt{S(S+1)}$ (Equation 1.12). Zero-field splitting can be impinged on this CrL_6 system by simply lowering its symmetry by replacing two axial ligands with two different trans ligands (X), resulting in an axially distorted tetragonal CrL_4X_2 D_{4h} system. The energies of these now separated M_s states may be calculated using the equation:

$$E(M_s) = M_s{}^2 D \quad \textbf{(1.29)}$$

1.7 Spin-Orbit Coupling

Sometimes the magnetic moment (μ) differs from the spin-only value $\mu_{s.o}$, resulting in a larger effective moment given as μ_{eff}. In these situations (i.e. $\mu_{eff} > \mu_{s.o}$), the orbital angular momentum (L) is not quenched and therefore spin-orbit coupling (SOC) contributes to the overall magnetic moment. SOC is the interaction of an electrons orbital angular momentum (L) and its spin angular momentum (S), resulting in a magnetic moment. There are two main requirements to be satisfied before SOC can take place:

1) There must be a half-filled or empty orbital of similar energy and symmetry to the orbital carrying the unpaired electron.

2) The nearby energy and symmetry related orbital cannot contain an electron that has the same spin as the first electron, in order to fulfil Hund's rule and the Pauli exclusion principle. d_z^2

For SOC to occur, the electron residing within a given orbital will move into a nearby vacant orbital via a transformation process. Here, the electron circulates around the centre of the complex and generates an orbital momentum (μ_L), which adds to the total magnetic moment and therefore results in a deviation from the $\mu_{s.o}$ value. For a free transition metal ion (M^{x+}), all the d-orbitals are degenerate and therefore a variety of potential transformations are available (e.g. $d_{xz} \rightarrow d_{yz}$; 90° rotation about the z axis and $d_{yz} \rightarrow d_{xy}$; 90° rotation about the y axis) (see Figure 19).

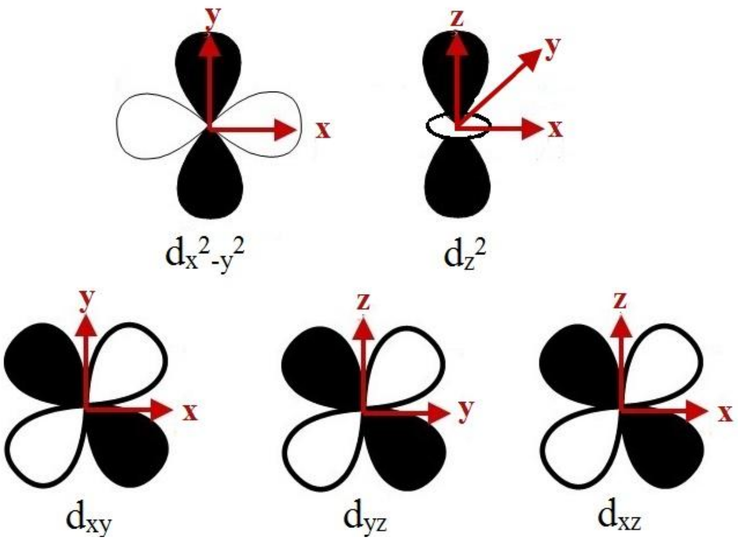

Figure 19 *- Illustration of the five d-orbitals.*

Orbital contributions of free ions should occur for anything other than d^5 and d^{10} systems. However, in reality, bound ligands tend to remove the 5-fold d-orbital degeneracy via crystal field splitting and therefore significant quenching of orbital contributions may occur (Figure 20). The orbital component (L) of the angular momentum is said to be quenched when there is an energy cost associated with the transformation from one orbital to another degenerate orbital. Examples of energy costs include a large ligand field splitting (Δ_{oct}) and electron-electron repulsion (i.e. two electrons with the same spin in the same orbital).

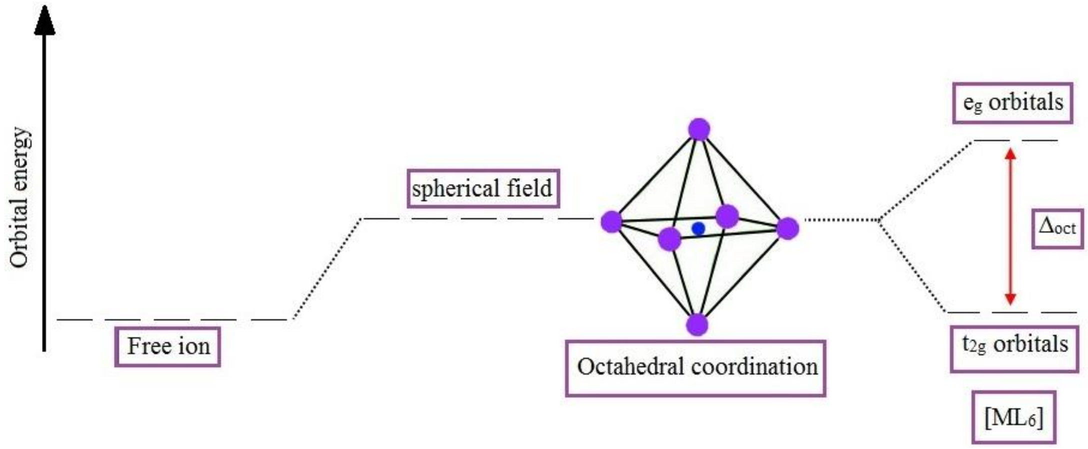

Figure 20 *- Representation of crystal field splitting in an octahedral complex $[ML_6]$. The blue and purple spheres denote the metal centre (M) and ligands (L) respectively.*

The aforementioned conditions are fulfilled when one or two of the three t_{2g} orbitals (d_{xy}, d_{yz}, d_{xz}) contain an odd number of electrons. Therefore, large deviations from spin-only values can be seen for low spin d^5 systems (e.g. Fe(III)), high spin d^6 systems (e.g. Fe(II)) and high spin d^7 systems (e.g. Co(II)).[22-24] For example, the d_{xy} orbital of a low spin d^5 Fe(III) system is related to the $d_{x^2-y^2}$ orbital by symmetry. Thus, the unpaired electron can move from the d_{xy} orbital to the $d_{x^2-y^2}$ orbital by rotating 45° about the z axis (Figure 21).

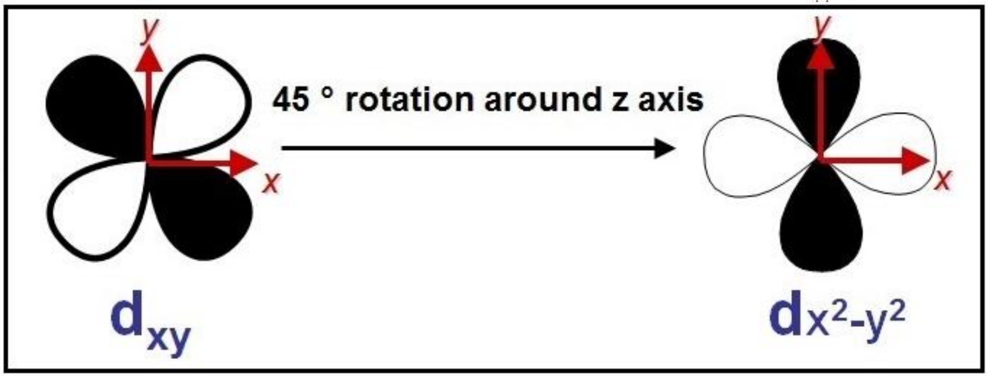

Figure 21 *- Schematic for spin-orbit coupling (SOC) via orbital transformation. An unpaired electron can transform from a d_{xy} to a $d_{x^2-y^2}$ orbital through a 45° rotation about the z axis.*

We previously reported the formula for the effective magnetic moment (μ_{eff}) in Equation 1.11 in Section 1.4.2. This describes the spin angular momentum (S) and the orbital angular momentum (L) as independent processes contributing to the total μ_{eff}.

$$\mu_{eff} = \sqrt{L(L+1) + 4S(S+1)} \quad \textbf{(1.11)}$$

In reality this is not the case as S and L are not independent and in fact are able to interact with one another. If the coupling is strong, S and L are no longer good quantum numbers and are replaced with J. J is the total angular quantum number and it takes the absolute values from $|L+S|$ to $|L-S|$. For example, a d^3 Cr(III) ion has an S value of 3/2 and an L value of 3, yielding J values of 9/2, 7/2, 5/2, 3/2. For d^1-d^4 systems (i.e. less than half full shells), the ground state is equal to the minimum J value (J = 3/2). For more than half full valence shells (i.e. d^6-d^9 systems) the ground state is equivalent to the maximum J value (J = 9/2). In the case of a high spin d^5 system only one J value exists as L = 0 and therefore J = S. If SOC is included in the contribution for μ_{eff}, Equation 1.30 is used. For spin-only (i.e. L = 0 and J = S) the g-value is ~ 2; however if SOC is present this is not always the case. The value for g is related to the quantum numbers S, L and J as described below (Equation 1.31).

$$\mu_{eff} = g\sqrt{[J(J+1)]} \quad \textbf{(1.30)}$$

$$g = 1 + \frac{S(S+1) - L(L+1) + J(J+1)}{2J(J+1)} \quad \textbf{(1.31)}$$

For lanthanide systems, the unpaired electrons lie in the f-orbitals, which are lower in energy than the frontier orbitals, therefore they are unaffected by ligands and thus remain degenerate. Therefore, any first-order orbital angular momentum remains unquenched with $\mu_{eff} > \mu_{s.o}$ and thus SOC is very important here. SOC strength (λ) can be particularly large for lanthanide systems in comparison to that for transition metals. As a result the spin-only formula gives very poor agreement for μ_{eff} experimental values for Ln(III) ions, but in general excellent agreement is obtained if μ_{eff} is calculated via Equation 1.30. This is of relevance to the work described in Chapter 5, where it will be discussed again.

1.8 Magnetic Exchange

So far, this introduction to molecular magnetism has mainly focused on mononuclear metal complexes. For polynuclear systems, the individual paramagnetic ions are able to interact and therefore magnetically couple to their neighbours via a process known as magnetic exchange. The two main mechanisms for magnetic exchange are *1) Direct exchange* and *2) Superexchange*. Firstly, it is necessary to mention the *J* value, which describes the magnetic exchange between two metal centres and should not be confused with the spin-orbit coupling parameter J. If we consider a Cu(II) dimeric complex, each Cu(II) centre is d^9 with one unpaired electron. The magnetic moments of the unpaired electrons can either align anti-parallel (antiferromagnetic) to give S = 0, or parallel (ferromagnetic) to give S = 1. If the two unpaired electrons interact antiferromagnetically, S' = 0 is the ground state, while if they interact ferromagnetically, S' = 1 is the ground state (Figure 22). S_A and S_B represent the local spin on CuA and CuB respectively. If *J* is negative and large then the magnetic coupling is strongly antiferromagnetic, whereas a positive and large *J* value indicates strongly ferromagnetic exchange coupling. The spin-Hamiltonian that describes the interaction between the two metal centres is given by Equation 1.32, where $\hat{S}_A$ and $\hat{S}_B$ denote the spin-operators for S_A and S_B.

$$\hat{H} = -2J\hat{S}_A \bullet \hat{S}_B \quad \textbf{(1.32)}$$

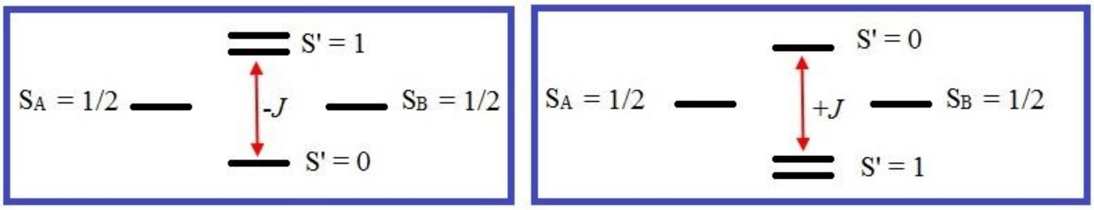

Figure 22 *- Schematic for antiferromagnetic (left) and ferromagnetic exchange (right) for a Cu(II) dimeric complex. The energy difference between the ground state and the excited state is equal to the J value.*

1.8.1 Direct Exchange

The direct exchange mechanism involves the direct overlap of two magnetic orbitals (i.e. the orbitals which contain the unpaired electrons) and is often thought of as analogous to a weak metal-metal bond formation. This results in the formation of two molecular orbitals (MOs), one bonding (symmetric) and one anti-bonding (anti-symmetric). There are two possible energy states available for the formation of a ‘metal-metal bonded’ molecule; however the excited state is very high in energy and therefore only the ground state is occupied at room temperature (Figure 23). However, if the direct overlap is weak, ΔE will be small enough to allow the excited state to be thermally populated. For example, overlap of orbitals with δ symmetry tend to be weak, due to their side-on nature. The direct exchange mechanism involves the thermal population of the anti-bonding (σ^*) excited state.

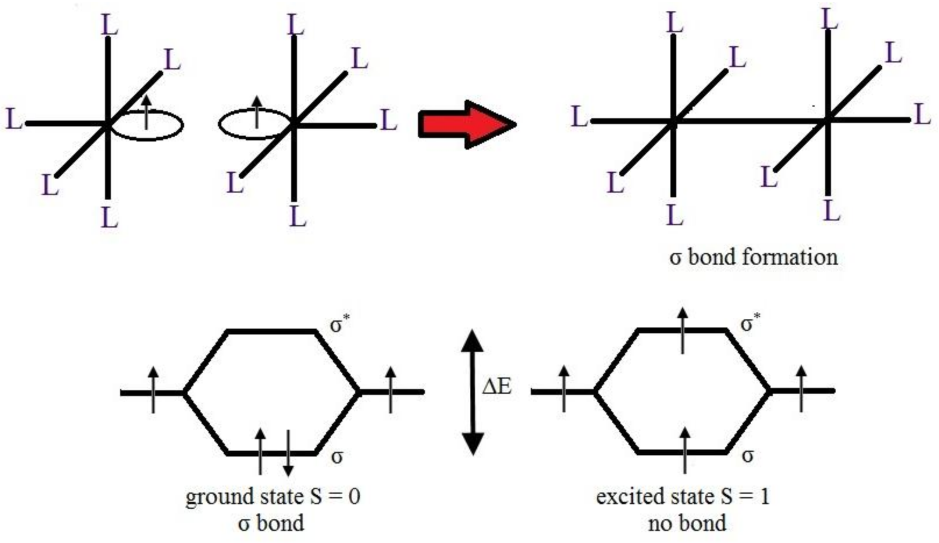

***Figure 23** - (Top) Representation of the formation of a 'metal-metal' bond via two ML_5 fragments carrying one unpaired electron each. (Bottom) Two possible energy states for 'metal-metal' bond formation.*

1.8.2 Superexchange

The magnetic orbitals do not directly overlap via the superexchange pathway. Instead the filled orbitals of a diamagnetic ligand participates in the orbital overlap. Magneto-structural correlation studies enable magneto-chemists to investigate links between a change in structure (e.g. $M\cdots M$ distance, M-L-M angle and M-L-L-M torsion angles; where L is a bridging ligand) and a change in magnetic properties (i.e. anti- or ferromagnetic). The first magneto-structural correlation studies for Cu(II) dinuclear compounds was carried out by Hatfield et al, where hydroxide bridges act as the diamagnetic ligands.[25] They demonstrated that the J value is dependent on the Cu-O-Cu angle, where an angle < 97.5° results in ferromagnetic behaviour ($J > 0$), while an angle > 97.5° produces antiferromagnetic exchange ($J < 0$). For example, in a $[Cu_2(OH)_2(L)_4]$ (L represents an organic ligand) dimeric complex, where Cu-O-Cu = 90°, an $S = 1$ ground state is achieved and ferromagnetic exchange is displayed (Figure 24). Here, the single unpaired electron of each Cu(II) is located in the $d_{x^2-y^2}$ orbital. The O atom of the hydroxide ligand bonds to one Cu(II) centre via its p_x orbital and the other Cu(II) centre via its p_y orbital. On the other hand, if the Cu-O-Cu angle is approximately 180°, the O atom of the bridging ligand bonds to both Cu(II) centres via the p_y orbital, yielding an $S = 0$ ground state and antiferromagnetic exchange is exhibited (Figure 25). If the unpaired electrons are in orthogonal magnetic orbitals then they cannot overlap with each other and thus ferromagnetic exchange is observed. This is known as the *orthogonality principle* and in general, the more obtuse an angle the stronger the observed antiferromagnetic interaction.

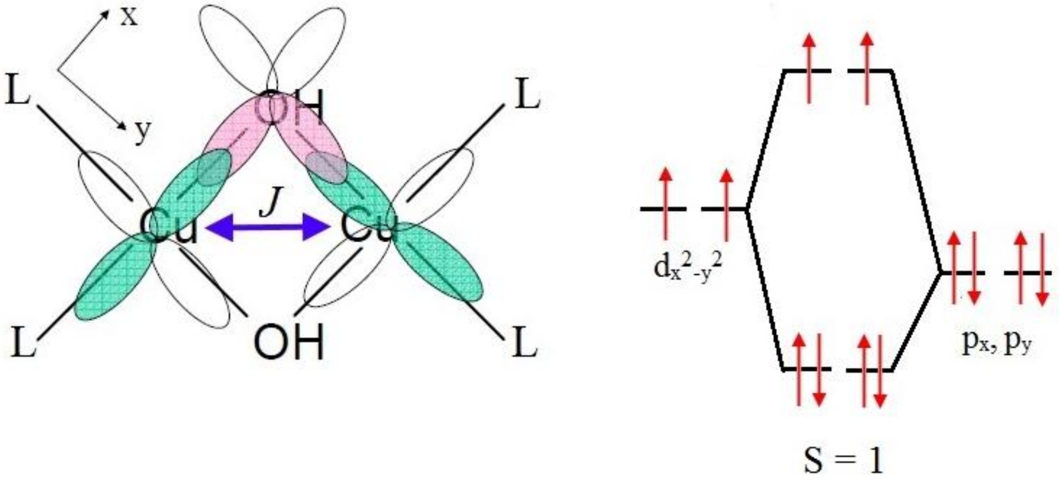

Figure 24 - *(Left) Schematic of the hydroxide bridged mediated orbital overlap in $[Cu(II)_2(OH)_2(L)_4]$, where Cu-O-Cu = 90°. (Right) Molecular orbital (MO) diagram for the [Cu(II)] dimer, with bonding and antibonding orbitals. Two unpaired electrons arise in ferromagnetic exchange.*

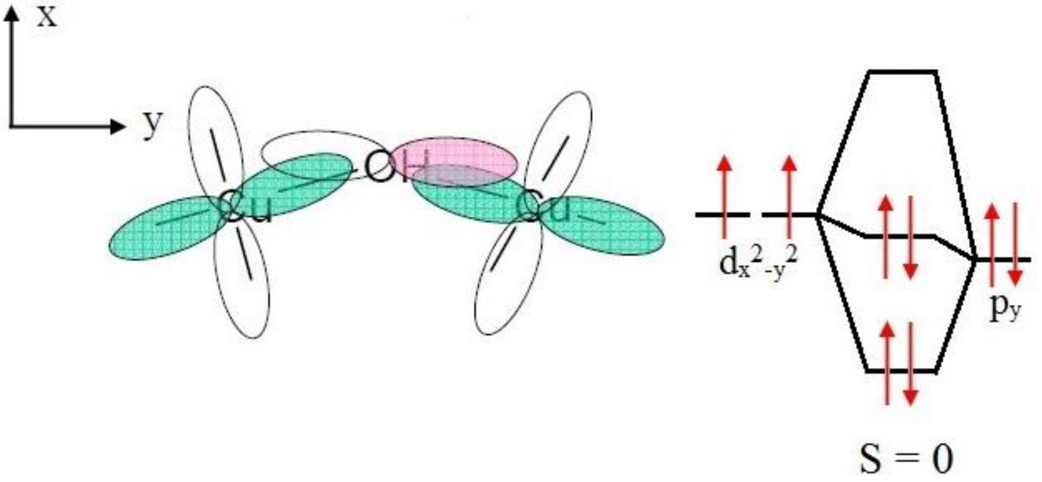

Figure 25 - *(Left) Illustration of a hydroxide bridged $[Cu(II)_2]$ complex, where the oxygen atom uses only one p orbital to bridge the two centres. Here, the Cu-O-Cu angle ≈ 180°. (Right) MO diagram for the [Cu(II)] dimer, where all electrons are paired and therefore antiferromagnetic exchange is observed.*

For bigger clusters the magnetic properties are more complicated, involving more than one exchange pathway and as a result more than one J value. For example, Figure 26 illustrates a model utilised for the magnetic susceptibility measurements of a $[Ni(II)_7]$ complex reported in this thesis (see Chapter 3 for more details). There are two exchange pathways, J_1 represents a Ni-O-Ni pathway, while J_2 denotes a Ni-O-N-

Ni interaction. The best fit parameters are J_1 = +0.64 and J_2 = -8.94 cm^3 mol^{-1} K, emphasising that both ferromagnetic and antiferromagnetic exchange reactions are occurring. Overall, antiferromagnetic exchange interactions dominate in this particular complex.

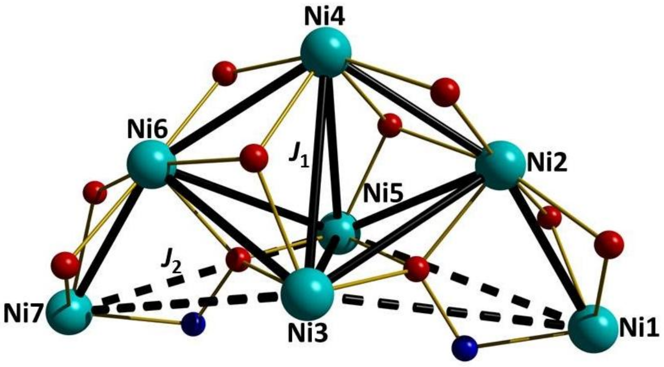

Figure 26 *- Illustration of a model used in the magnetic susceptibility measurements of a [Ni_7] complex. See Chapter 3 for a detailed account.*

Magneto-structural correlations studies have also been carried out on larger complexes such as a large family of salicylaldoxime based [Mn_3] and [Mn_6] complexes.[26] Here, it was discovered that twisting of the Mn-O-N-Mn unit was the dominant factor for magnetic exchange and this could be controlled with relative ease by substituting the H atom on the oximic C atom for more steric R groups (i.e. R = Me, Et). Furthermore, these studies showed that the $[Mn(III)_3O(R\text{-}sao)_3]^+$ building block is magnetically tuneable, adept to ligand substitution, allowing for a broad scope in terms of the design of analogous clusters. This is advantageous, as if we know how magnetic properties are linked to molecular structure, it is possible to deliberately synthesise compounds and tune magnetic properties towards future applications such as molecular spintronics (spin transport electronics) and information storage devices.

1.9 Applications of Magnetic Materials

1.9.1 Single-Molecule Magnets

Single-Molecule Magnets (SMMs) are discrete polynuclear molecules that exhibit slow magnetisation reorientation and therefore magnetic hysteresis (see Section 1.4.4). As stated previously, magnetic hysteresis is the ability to remain magnetised after the applied magnetic field has been switched off (i.e. it is a memory effect). It is important to note that the fundamental difference between SMMs and traditional magnets (i.e. bulk magnetic materials) is the source of their magnetic hysteresis. For SMMs magnetic hysteresis is of purely molecular origin and governed by local interactions of finite clusters. On the other hand, magnetic hysteresis for bulk magnetic materials is brought about by regional interactions within magnetic domains resulting in 1, 2 or 3-D long range ordering and magnetic hysteretic behaviour.

SMMs are members of a class of compounds known as exchange coupled clusters and have been synthesised from a variety of transition metal ion complexes of varying oxidation state distributions including Mn(II)/Mn(III),[27, 28] Mn(III),[26, 29] Mn(III)/Mn(IV),[30] Fe(III),[31, 32] Fe(II),[33] Ni(II),[34, 35] and Co(II) centres.[36, 37] The metallic core of these clusters are surrounded by organic ligand moieties which protect the core from inter-molecular exchange interactions, while primarily connecting the metal ions into architectures of various nuclearities and topologies. SMMs display superparamagnetic behaviour below a characteristic temperature known as their blocking temperature, T_B (see Section 1.4.3.6). There are two main prerequisites for SMM behaviour in a polynuclear complex. The complex must have *1)* a large ground spin state (S) and *2)* a large and negative magnetoanisotropic parameter (D) arising from zero-field splitting (ZFS) (see Section 1.6.1.2). The value for the energy barrier to magnetisation reorientation (given as ΔE or ΔU) is directly proportional to the combined values for S and D (i.e. large S and D values result in a large ΔE term). Equation 1.33 and Equation 1.34 represent the relationship between the ΔE, S and D terms for systems with integer values and half integer values of S respectively. It is important to note that in addition to the above two requirements, inter-molecular interactions must be kept to a minimum in order for SMM behaviour to occur.

$$\Delta E = S^2 |D| \quad (\mathbf{1.33})$$

$$\Delta E = (S^2 - 1/4)|D| \quad (\mathbf{1.34})$$

In order to calculate the energy barrier to magnetisation (ΔE) we must first work out the ground spin state. In the S = 2 system from Section 1.6.1.2, M_s states = 0, +/-1, +/-2 arise upon zero-field splitting. As seen previously, the energy separations of M_s states in zero field is calculated via Equation 1.29 (Section 1.6.1.2), resulting in negative D values of -1D between $M_s = 0$ and $M_s = +/-1$, -3D between $M_s = +/-1$ and $M_s = +/-2$ and -4D between $M_s = 0$ and $M_s = +/-2$ (Figure 27).

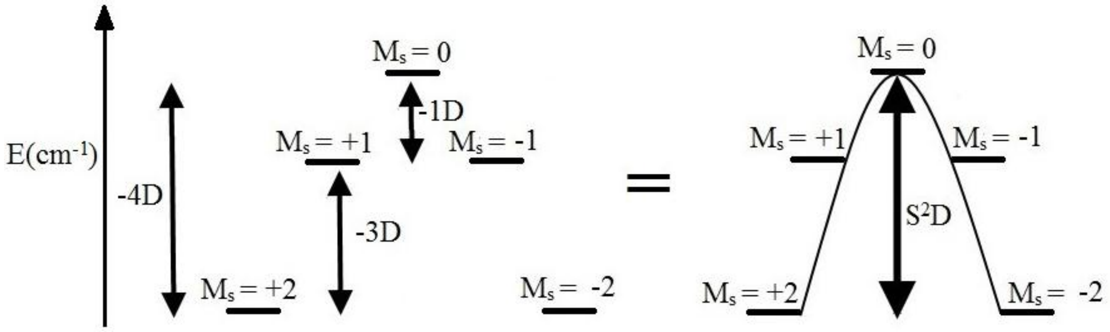

Figure 27 - *Schematic of zero-field splitting of an S = 2 system, highlighting the energy separations of the M_s states and the energy barrier (S^2D) to magnetisation at zero field i.e. H = 0.*

Quite often, the separation of the M_s states and the barrier to magnetisation reorientation is represented by a double well (Figure 28). At zero field (H = 0), the ± M_s states are degenerate, however upon application of the magnetic field the microstates split and we see a shift in energy levels and the removal of the degeneracy of the microstates. The $M_s = +2$ level is the lowest in energy and therefore the most stable, which leads to electron population of its microstate. Therefore, the Ms = +2 microstate is the ground spin state and this is (thereafter) more commonly referred to as an S = 2 ground spin state.

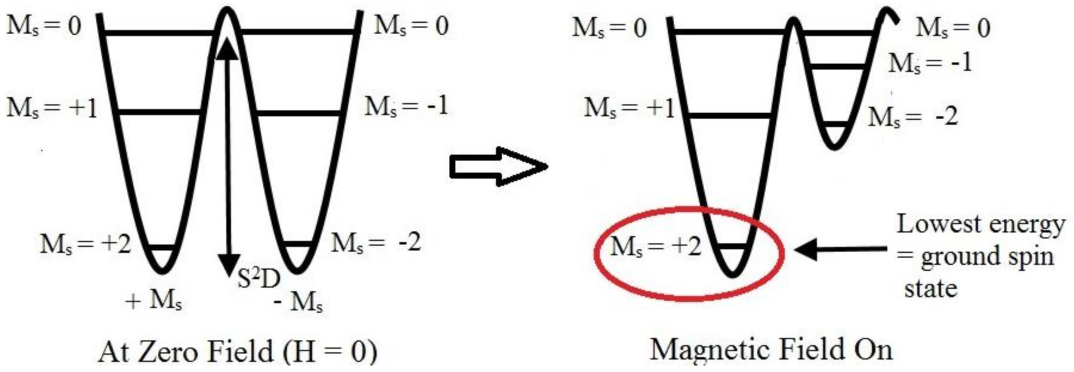

Figure 28 - *Double well representation of the separation of the M_s states in an S = 2 system at zero field (left) and with an applied magnetic field (right). Please note the ground spin state is circled in red.*

1.9.1.1 Single-Molecule Magnets: Past and Present

The first polynuclear complex to display SMM behaviour was the dodecahedral [Mn_{12}] prototype complex [$Mn(III)_8Mn(IV)_4O_{12}(OAc)_{16}(H_2O)_4$], more commonly known as [$Mn_{12}OAc$], which was discovered in 1993 by Gatteschi et al,[30, 38] although it was rather surprisingly first synthesised in 1980 by Lis et al.[39] The crystal structure and magnetic hysteresis plot of the SMM prototype can be seen in Figure 29 and Figure 30 respectively. A few years after the discovery that [Mn_{12}OAc] exhibited magnetic hysteresis properties (purely of molecular origin), the term Single-Molecule Magnet came in to existence.[40]

Figures 29 and 30 have been removed due to copyright restrictions and can be viewed in references 41 and 30 respectively.

The [Mn_{12}OAc] complex is composed of an inner cubane core of four ferromagnetically coupled S = 3/2 Mn(IV) ions (green spheres). This is surrounded by an outer ring of eight ferromagnetically coupled S = 2 Mn(III) ions (blue spheres). The Mn(III) and Mn(IV) ions are coordinated to each other via triply bridging oxo O atoms and by bridging acetate ions. The outer ring couples antiferromagnetically to the central cubane core, resulting in an overall ground spin state of S = 10 (S = 16 – 6 = 10). The Mn(III) ions display a near parallel alignment of their Jahn-Teller axes along the easy axis and therefore each Mn(III) exhibits a significant single ion anisotropy. As there are eight Mn(III) ions, the combined anisotropic D parameter is significantly large and negative, yielding a value of ≈ -0.5 cm^{-1}.[41]

The synthesis of the SMM prototype [Mn_{12}OAc] initiated a huge growth in the field of molecular magnetism. Even after almost 15 years of intense research, [Mn_{12}OAc] and its various carboxylate substituted derivates continued to hold the highest blocking temperature of ≈ 3.5 K and an effective energy barrier to magnetisation reversal (U_{eff}) of up to 74 K.[42] However in 2007, the long record held by the [Mn_{12}] family was finally broken. By targeting specific structural distortion in a known [$Mn(III)_6$] complex of formula [$Mn(III)_6O_2(sao)_6(O_2CPh)_2(EtOH)_4$][43] (where $saoH_2$ = salicylaldoxime), Brechin et al demonstrated the ability to tune and improve SMM behaviour in the above complex. This was achieved by switching the dominant exchange interactions within the cluster from antiferromagnetic to ferromagnetic, resulting in the synthesis of the complex of formula [$Mn(III)_6O_2(Etsao)_6(O_2CPh(Me)_2)_2(EtOH)_6$] (where Et-$saoH_2$ = 2-hydroxyphenylpropanone oxime).[44] This [$Mn(III)_6$] cluster possesses a ground spin state of S = 12, D value of -0.43 cm^{-1}, blocking temperature (T_B) of 4.5 K and a U_{eff} value of 86.4 K. The crystal structure and hysteresis curve of which can be seen in Figure 31.

Figure 31 has been removed due to copyright restrictions and can be viewed in reference 44.

Lanthanide elements offer promising candidates towards the synthesis of SMMs due to their highly anisotropic nature. Therefore, it is no surprise to see that in more recent advances in the production of SMMs, lanthanide elements have played a significant role. In 2011, a new record holder was reported by Rinehart et al via the synthesis of a N_2^{3-} bridged dinuclear complex of formula $[K(18\text{-crown-}6)(THF)_2]\{[(Me_3Si)_2N]_2(THF)Dy\}_2(\mu\text{-}\eta^2\text{:}\eta^2\text{-}N_2)$.[45] The crystal structure and magnetic hysteresis plot for $[Dy(III)_2]$ is given in Figure 32, displaying a blocking temperature of 8.3 K. In the same year, Rinehart et al broke their own record via the synthesis of a $[Tb(III)_2]$ analogue to the above mentioned $[Dy(III)_2]$ complex.[46] To date, this is the current record holder, possessing a blocking temperature of 13.9 K and a U_{eff} of 326.62 K. The magnetic hysteresis plot for $[Tb(III)_2]$ can be seen in Figure 33.

Figures 32 and 33 has been removed due to copyright restrictions and can be seen in references 45 and 46 respectively.

1.9.1.2 Applications of Single-Molecule Magnets

The potential applications of SMMs arise from their ability to exhibit magnetic hysteresis at the molecular level. An overview of some of these applications is given in the following sections.

1.9.1.2.1 Information Storage Devices

SMMs show magnetic hysteresis below their characteristic blocking temperature (T_B) and can therefore be considered as magnetically bi-stable.[30] If we think back to the hysteresis loop in Section 1.4.4, the magnetisation direction of a particular material may be considered as 'spin up' (Point A) or 'spin down' (Point B) at zero field, depending on the direction of the original applied magnetic field and may therefore be described as bi-stable (Figure 34-left). In order to switch from one spin state to another the energy barrier to magnetisation reversal (ΔE or $\Delta U = S^2D$) must first be overcome ($\Delta E = S^2D$) (Equations 1.33, Section 1.9.1) (Figure 34-right). In addition, molecules can switch from one state to another by tunnelling through the energy barrier via a phenomenon known as quantum tunnelling of magnetisation (QTM) (see Section 1.9.1.2.2). This bi-stable nature is analogous to the (0, 1) binary units used in information storage devices, for example 'spin up' and 'spin down' could be represented by ‘1’ and ‘0’ respectively. Therefore, SMMs offer promising candidates for information storage devices.[47] Home computers store information via magnetic regions known as magnetic domains, where each domain consists of hundreds of magnetic grains and each magnetic grain is typically ~10 nm in size. SMMs are several orders of magnitude smaller than these magnetic domains and therefore their use in information storage would theoretically lead to miniaturisation of storage devices. However, the current working temperatures of SMM materials are very low and therefore at the moment they are not practical for application in information storage. The temperatures at which SMM behaviour occurs would need to increase drastically before their application as information storage devices may be achieved.

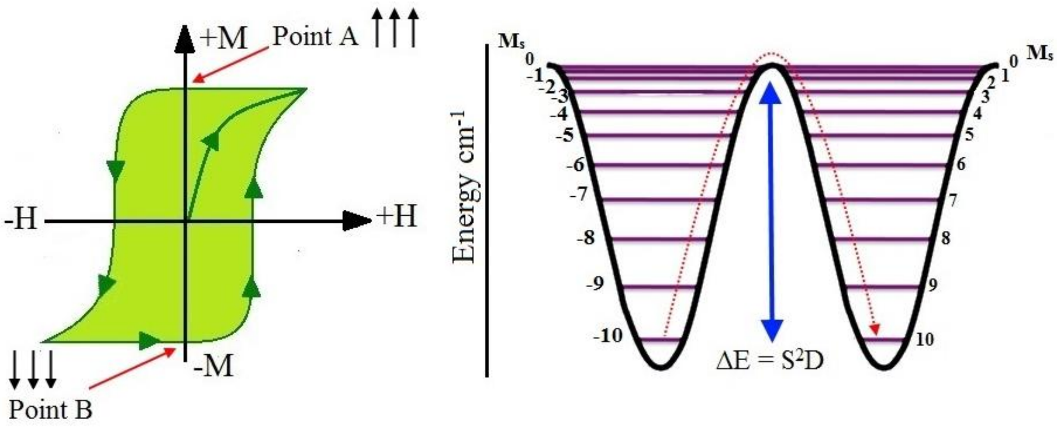

Figure 34 *- (Left) Magnetic hysteresis plot highlighting ‘spin up’ (Point A) and ‘spin down’ (Point B). (Right) Schematic representing the energy barrier for magnetisation reversal (ΔE) of an S = 10 ground spin state system. The* $M_s = +10$ *and* $M_s = -10$ *microstates could represent ‘spin up’ and ‘spin down’ states respectively in terms of a binary information storage model.*

1.9.1.2.2 Quantum Computing

In 1995, it was reported by Novak et al, that the magnetic hysteresis plot for the original SMM [Mn_{12}OAc] displayed steps at regular intervals.[48] At certain fields the magnetisation relaxes faster and this phenomenon is now known as Quantum Tunnelling Magnetisation (QTM).[49] An example of a stepped hysteresis plot for [Mn_{12}-*t*BuAc] (where *t*BuAc = tert-butyl acetate), a member of the prototype SMM family, can be seen in Figure 35-left.[50] QTM bypasses the energy barrier to magnetisation reversal by tunnelling through the barrier from one M_s state to another, provided the M_s states are in resonance with one another (represented by blue arrows in Figure 35-right).[51]

Figure 35 (left and right) has been removed due to copyright restrictions and can be viewed in references 50 and 51 respectively.

A classical computer can only process bits that are in one state at a time, whereas quantum computers process quantum bits known as qubits. These ‘quantum bits’ can exist as a superposition of two different states (i.e. ‘spin up’ and ‘spin down’ and a superposition of both). QTM allows for the superposition of two states at a time, allowing for a much more powerful computer than classical computers and thus indicating that SMMs would theoretically offer ideal candidates for quantum information processing (QIP) (or quantum computing).[52, 53] It should be noted that quantum tunnelling would be a disadvantage in certain applications, such as information storage applications for classical computers, as it would lead to loss of data. Certain operations carried out by quantum computers require multi-qubits to be performed, thus the controlled switchable coupling and decoupling interconnection of molecular nanomagnets is of the utmost importance to allow for these operations to be carried out.[54] In 2002, Christou and co-workers reported the first controlled coupling between two [Mn_4] molecular nanomagnets, resulting in different quantum behaviour than those previously observed for a SMM and thus suggesting the possibility of tuning quantum tunnelling in SMMs (Figure 36).[55] Studies of QTM have been carried out by Ardavan et al on a [Cr_7NiF_8] cluster, previously synthesised by Larsen et al (Figure 37).[56, 57] More recently, the occurrence of QTM on a chemically grafted SMM monolayer of formula [$Fe_4(L)_2(DPM)_6$] (where L = 7-(acetylthio)-2,2-bis(hydroxymethyl)heptan-1-ol and DPM denotes dipivaloylmethane) was reported by Mannini et al. This is of great significance towards potential applications for SMMs, as it would allow for the controlled orientation of molecules.[58]

Figure 36 and 37 have been removed due to copyright restrictions, both of which can viewed in reference 54.

1.9.1.2.3 Molecular Spintronic Devices

The area of spintronics (Spin Transport Electronics) aims to exploit an electrons intrinsic spin along with its ability to carry an electron charge towards the production of miniaturised solid-state devices (i.e. electronic circuit components such as semiconductors and transistors). The prototype device for spintronics is the giant magnetoresistance (GMR) structure in hard disks, comprising alternating layers of ferromagnetic (F) and non-magnetic metal (NM) materials (Figure 38).[59, 60] One of the ferromagnetic layers is permanently magnetised in one direction, commonly referred to as the pinned layer and is often composed of cobalt. The other ferromagnetic layer is known as the free layer, it has the ability to switch its magnetisation and typically consists of a Ni/Fe alloy. The non-metallic layer often consists of copper and acts as a buffer between the two magnetic layers. As the read head in a hard disk passes over a specific ‘bit’, the magnetic orientation of the free layer adjusts to match the ‘bit’. Therefore, sometimes the free layer is aligned parallel with the pinned layer and sometimes it is aligned anti-parallel. The orientation of the magnetisation (magnetic field) controls the electronic resistance of the device, parallel arrangements of the ferromagnetic layers produce a low resistance, while anti-parallel arrangements leads to high resistance. In GMR devices, alterations in resistance (commonly referred to as magneto-resistance) are interpreted, where high resistance is read as ‘0’ and low resistance represents ‘1’.

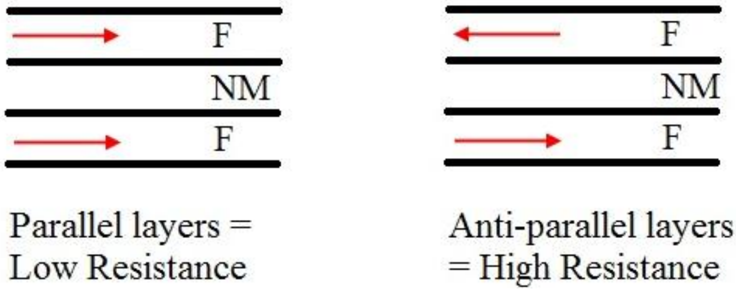

Figure 38 *- Schematic of the alternating layers within a material with Giant Magneto-resistance properties (GMR). In the absence of an applied magnetic field the layers align anti-parallel (right), to give a high resistance reading, while in the presence of a magnetic field the layers align parallel (left), producing a low resistance reading.*

1.9.2 Molecular Coolants

The phenomenon known as the magneto-caloric effect (MCE) was first observed in iron in 1881 by Warburg.[61] It is based on the change in disorder and consequently magnetic entropy (ΔS_M) of a material as a result of the application and subsequent removal of a magnetic field by a process known as adiabatic demagnetisation.[62] Initially, the magnetic moments of the magnetic material are randomly orientated. Upon application of an external magnetic field the magnetic moments of the material align with the magnetic field, producing a more ordered state and thus the magnetic entropy (S_M) is lowered. If the magnetic field is applied under adiabatic conditions (where the total entropy of the system remains constant), the magnetic entropy must be compensated for by an equal but opposite change of the entropy associated with the lattice. This results in the system heating up and therefore an increase in temperature of the material. As the external magnetic field is removed (demagnetisation), the magnetic moments of the material absorb the heat and thus return to random orientation. This leads to a decrease in order of the magnetic material and an increase in S_M and therefore lowering of the temperature of the material. All magnetic materials exhibit MCE but the intensity of the effect varies depending on the properties of the materials. MCE is of great significance in terms of cooling applications such as magnetic coolants (a.k.a. molecular refrigerants). In order for a molecule to be a good molecular coolant, it must have a large ground spin state (S), negligible magnetic exchange between magnetic centres and negligible magnetic anisotropy (D).[63] The coupling of transition metal ions with Gd(III) ions have proven to display weakly ferromagnetic interactions.[64] Therefore, it is no surprise that the majority of molecular coolants are 3d-4f mixed metal complexes, including Mn-Gd,[65] Cu-Gd,[66, 67] Ni-Gd,[67] Co-Gd[68] and Zn-Gd complexes.[67, 69] The crystal structure and magnetic susceptibility data of the ferrimagnetic $[Cu(II)_{15}Gd(III)_7]$ magnetic refrigerant is displayed in Figure 39.[66] This technology utilises ultra low temperatures which minimises cost and provides a cheaper, more efficient and environmentally friendly alternative to helium-3.

Figure 39 has been removed due to copyright restrictions and can be seen in reference 66.

1.9.3 Metal-Organic Frameworks

Metal-Organic Frameworks (MOFs)[70] (a.k.a coordination polymers) are inorganic-organic hybrid compounds, comprising organic linker ligands and metal connector ions which form infinite 1-, 2-, 3-dimensional structures. Generally, the organic linker ligands consist of at least one oxygen and/or nitrogen donor centre. Influential research by Hoskins and Robson carried out in the late 1980's to the mid 1990's resulted in an accelerated interest in MOFs.[71-73] This increase in interest is due to the large choice of building blocks available when synthesising MOFs, allowing for tuneable surface area and pore size. Therefore, they are promising candidates for a broad range of applications in areas such as gas storage, catalysis, luminescence and non-linear optics (NLO).[74-77] Much thought and consideration is required when choosing starting materials for MOFs, as this will determine the type of molecular polymer assembled. For example, the use of Ln(III) and Zn(II) / Cd(II) ions can often yield fluorescent materials, which may be used for the production of structures with photoactive properties, which may be tuned towards luminescent switches.[78-80] Moreover, the use of single or multiple paramagnetic metal ions may often result in magnetically interesting materials such as Single-Chain Magnets (SCMs) (Figure 40).[81]

Figure 40 has been removed due to copyright restrictions and can be viewed in reference 81.

Examples of coordination polymers synthesised as part of the research in this thesis include a 2-D $[Cu(II)_5]$ extended network of formula $\{[Cu(II)_5(L_1)_4(4,4'\text{-bipy})_3](ClO_4)_2\cdot H_2O\}_n$ (where L_1H_2 = 2-(dimethylamino)phenylhydroxamic acid) (**4**) and a 1-D [Mn(III)] chain complex of formula $[Mn(III)(L_7)_2(Cl)]_n$ (L_7H = 1-[(methylimino)methyl]-2-naphthol) (**26**), which are reported in Chapters 2 and 6 respectively (Figure 41).

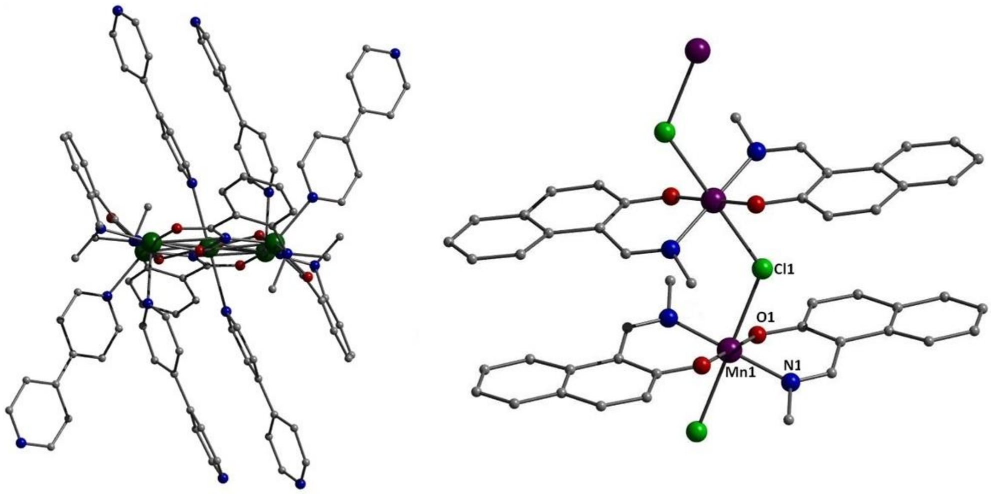

Figure 41 *- Crystal structures of coordination polymers (left)* $\{[Cu(II)_5(L_1)_4(4,4'\text{-bipy})_3](ClO_4)_2\cdot H_2O\}_n$ ***(4)*** *(where* L_1H_2 *= 2-(dimethylamino)phenylhydroxamic acid) and (right)* $[Mn(III)(L_7)_2(Cl)]_n$ ***(26)*** *(*L_7H *= 1-[(methylimino)methyl]-2-naphthol).*

1.10 Synthesis of Magnetic Clusters and MOFs

1.10.1 Ligand Choice

A ligand is essentially a molecule comprising one or more donor atoms that can bond to one or more metal ions, resulting in the formation of a coordination compound. There are three main types of ligands: *1)* monodentate ligands which possess only one donor atom, *2)* bidentate ligands which consist of two donor atoms and *3)* polydentate ligands which comprise many donor atoms. A ligand can be considered as a building block for the synthesis of discrete complexes and coordination polymers. Choosing the correct ligand type is imperative when attempting to design and synthesise cluster complexes or MOFs. For example, some ligands act as bridging or connector units, linking the metal ions together to form structures with infinite arrays (i.e. MOFs). Other ligands act as terminal units, preventing the formation of infinite networks and therefore are unsuitable in the synthesis of MOFs, but could be very useful in terms of the synthesis of cluster complexes.

1.11 Aims of the Project

The general aims of this thesis were to investigate the role of the hydroxamic acids 2-(dimethylamino)phenylhydroxamic acid (L_1H_2) and 2-(amino)phenylhydroxamic acid (L_2H_2) towards the formation of polynuclear complexes, in particular metallacrown topologies. In addition, we aimed to rationalise the transformation away from metallacrown topologies via the utilisation of the above mentioned ligands, as well as the Schiff base hydroxamic acid ligand building blocks L_xH_3 (where x = 3 or 5) and L_4H_2. We also were interested in the investigation of the controlled synthesis of pre-mediated MOFs using polynuclear nodes. Furthermore, we also wanted to research alternative synthetic methods towards the construction of new polynuclear [Ln(III)] complexes via the utilisation of the 2,6-dimethoxyphenol (L_6H) building block.

1.11.1 Ligands Used

1.11.1.1 Hydroxamic Acids

As part of this research, we have investigated the coordination chemistry of two hydroxamic acid ligands 2-(dimethylamino)phenylhydroxamic acid (L_1H_2) and 2-(amino)phenylhydroxamic acid (L_2H_2) (Figure 42). Previous research carried out utilising L_1H_2 resulted in the formation of a heptanuclear [Ni_7] ferrimagnet which exhibits four hydroxamate ligand binding modes.[82] While prior research with L_2H_2 produced a clam shaped metallacrown[83] dimer [$Cu(II)_5$] with 12-MC-4 conformation.[84] Hydroxamic acid ligands have proven to be valuable building blocks towards the synthesis of metallacrowns. Examples of hydroxamic acid ligands used in the synthesis of metallacrowns can be seen in Figure 43.

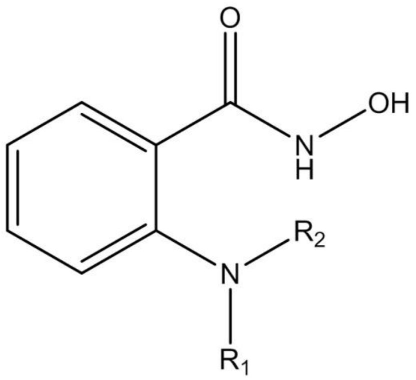

Figure 42 - Hydroxamic acid ligands utilised in this research where $R_1 = R_2 = Me$; L_1H_2 and $R_1 = R_2 = H$; L_2H_2.

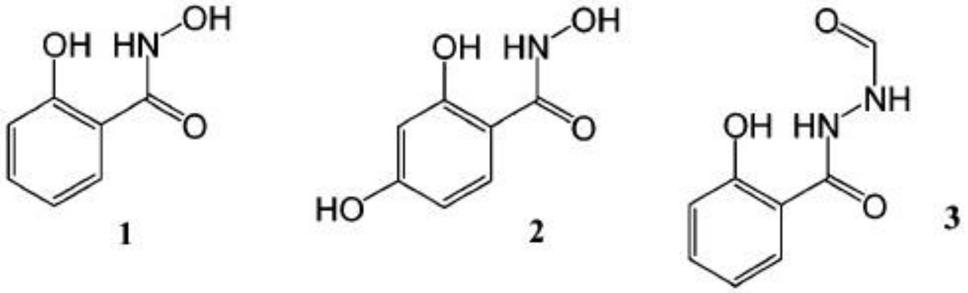

Figure 43 - Examples of hydroxamic acids used in the synthesis of metallacrowns. 1 = Salicylhydroxamic acid, 2 = 2,4-dihydroxybenzohydroxamic acid and 3 = N-formylsalicylhydrazide.[83]

1.11.1.2 In-situ Ligand Formation of Schiff Base Hydroxamic Ligands

In-situ ligand synthesis led to the formation of o-[(E)-(2-hydroxy-3-methoxyphenyl)methylideneamino]benzohydroxamic acid (L_3H_3), [[2-[(E)-(2-hydroxy-3-methoxy-phenyl)methyleneamino]benzoyl]amino]ethanimidate (L_4H_2) and o-[(E)-(o-hydroxyphenyl)methylideneamino]benzohydroxamic acid (L_5H_3) via the reaction of 2-(amino)phenylhydroxamic acid (L_2H_2) with 2-hydroxy-3-methoxybenzaldehyde (to give L_3H_3 and L_4H_2) or 2-hydroxybenzaldehyde respectively (to give L_5H_3) (Figure 44 and 45). To the best of our knowledge no previous research in terms of the synthesis of coordination complexes has been carried out with these ligands.

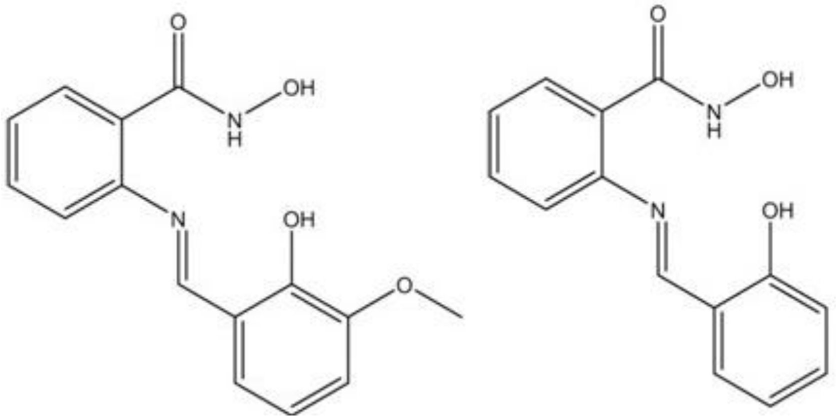

Figure 44 *- Schematic representations of ligands (left) L_3H_3 and (right) L_5H_3.*

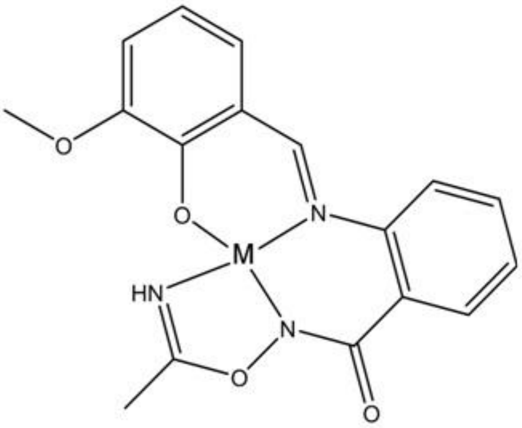

Figure 45 *- Structure representation of the metal ligated L_4^{2-} moiety.*

1.11.1.3 2,6-dimethoxyphenol and 1-[(methylimino)methyl]-2-naphthol

Previous research in our group involved the synthesis of a family of heptanuclear [M_7] (M = Co, Ni, Zn) pseudo metallocalix[6]arene complexes via the incorporation of the Schiff base ligand (2-imino-6-methoxyphenol) (Figure 46 and 47).[85-87] Therefore, we were immediately interested in the analogous ligands 2,6-dimethoxyphenol (L_6H) and 1-[(methylimino)methyl]-2-naphthol (L_7H) (Figure 46). Prior to our research, very little work had been carried out on the integration of L_6H into metal coordination compounds. L_6H was utilised in alkene polymerization catalyst studies[88] as well as in the synthesis of poly(aryl)silane and heterometallic aluminium-lithium compounds.[89, 90] L_7H has previously been incorporated into a relatively small number of coordination complexes including a number of Cu(II) monomers, as well as dimeric Mn(IV) and Cu(II) complexes of formula $[Mn(IV)(L_7)_2(\mu\text{-}O)]_2$ and $[Cu(II)(L_7)_2]_2$ respectively.[91-94]

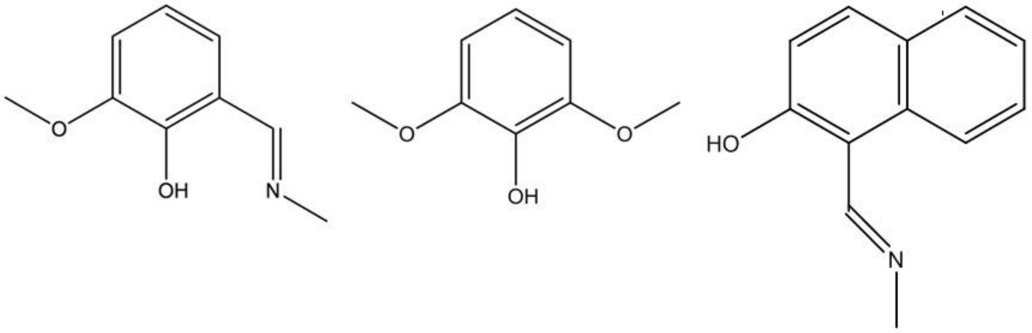

Figure 46 - *(Left) Structure of Schiff base ligand 2-imino-6-methoxyphenol used in earlier research in our group. (Middle) Structure of the bridging ligand (L_6H) used in Chapter 5 and (right) structure of naphthol ligand (L_7H) used in Chapter 6.*

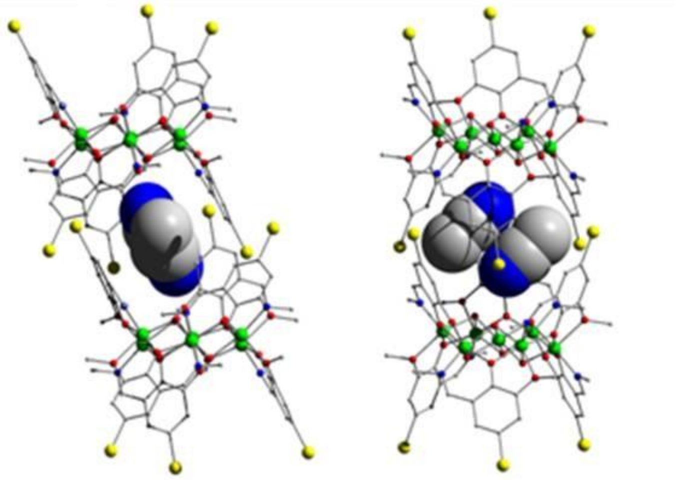

Figure 47 - *Schematic representing the hydrogen bonding of individual units of [Ni_7], which are stacked into 1-D columns within the unit cell. Guest MeCN molecules are space-fill represented.*

1.11.2 Use of Co-ligands

Throughout these studies a number of co-ligands have been utilised towards the synthesis of discrete clusters and coordination polymers. A co-ligand can operate in conjunction with the original ligand in the construction of discrete polynuclear cages, as well as acting as a connector ligand towards the synthesis of coordination polymers. In addition, a co-ligand completes coordination around a metal ion and can alter the geometry (and magnetic properties) of metal ions. Figure 48 highlights some of the co-ligands successfully utilised in this thesis.

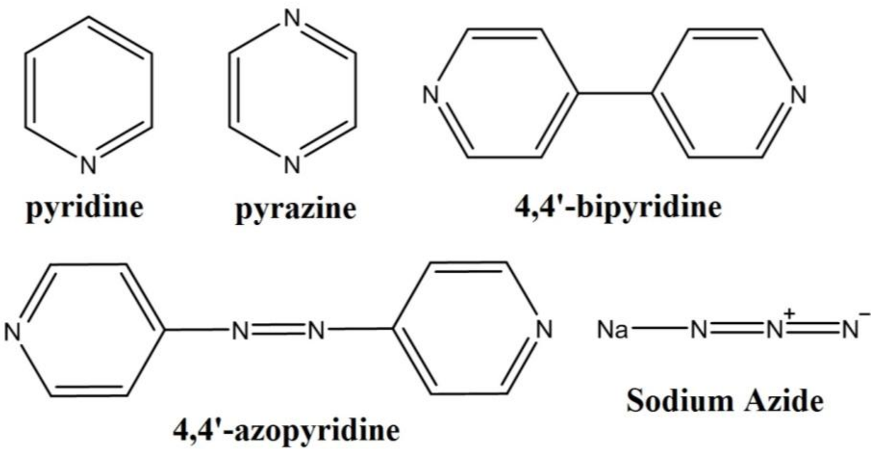

Figure 48 - *A selection of co-ligands utilised in the work carried out in this thesis.*

1.12 Bibliography

1. A. F. Orchard, *Magnetochemistry*, Oxford University Press, New York, 2003.
2. R. T. Merrill, *The earth's magnetic field : its history, origin, and planetary perspective / Ronald T. Merrill, Michael W. McElhinny*, Academic Press, London ; New York, 1983.
3. W. Lowrie, *Fundamentals of geophysics*, Cambridge University Press, 2007.
4. K. Jelved, A. D. Jackson and O. Knudsen, *Selected Scientific Works of Hans Christian Ørsted*, Princeton University Press, 1998.
5. D. C. Giancoli, *Physics for scientists and engineers with modern physics*, Pearson Education, 2008.
6. J. J. Thomson, *Philosophical Magazine Series 5*, 1897, 44, 293-316.
7. P. Caravan, J. J. Ellison, T. J. McMurry and R. B. Lauffer, *Chem. Rev.*, 1999, 99, 2293-2352.
8. P. Caravan, *Chem. Soc. Rev.*, 2006, 35, 512-523.
9. R. C. Semelka and T. K. G. Helmberger, *Radiology*, 2001, 218, 27-38.
10. H. B. Na, I. C. Song and T. Hyeon, *Adv. Mater.*, 2009, 21, 2133-2148.
11. O. Kahn, *Molecular Magnetism*, Wiley, 1993.
12. R. L. Carlin, *Magnetochemistry*, Springer Berlin et al., 1986.
13. H. O. Stumpf, Y. Pei, O. Kahn, J. Sletten and J. P. Renard, *J. Am. Chem. Soc.*, 1993, 115, 6738-6745.
14. G. C. Papaefthymiou, *Nano Today*, 2009, 4, 438-447.
15. Y.-Z. Zhang and O. Sato, *Inorg. Chem.*, 2009, 49, 1271-1273.
16. R. Inglis, S. M. Taylor, L. F. Jones, G. S. Papaefstathiou, S. P. Perlepes, S. Datta, S. Hill, W. Wernsdorfer and E. K. Brechin, *Dalton Trans.*, 2009, 9157-9168.
17. R. C. Jaklevic, J. Lambe, A. H. Silver and J. E. Mercereau, *Phys. Rev. Lett.*, 1964, 12, 159-160.
18. J. E. Zimmerman, P. Thiene and J. T. Harding, *J. Appl. Phys.*, 1970, 41, 1572-1580.
19. B. D. Josephson, *Phys. Lett.*, 1962, 1, 251-253.
20. S. Magure-Boyle and A. Barron, Theory of A Superconducting Quantum Interference Device (SQUID), http://cnx.org/content/m22750/1.3/, Accessed 9/08/2014.
21. J. Cirera, E. Ruiz, S. Alvarez, F. Neese and J. Kortus, *Chem. Eur. J.*, 2009, 15, 4078-4087.
22. P.-H. Lin, N. C. Smythe, S. I. Gorelsky, S. Maguire, N. J. Henson, I. Korobkov, B. L. Scott, J. C. Gordon, R. T. Baker and M. Murugesu, *J. Am. Chem. Soc.*, 2011, 133, 15806-15809.
23. A. M. Bryan, W. A. Merrill, W. M. Reiff, J. C. Fettinger and P. P. Power, *Inorg. Chem.*, 2012, 51, 3366-3373.
24. R. Stoyanova, A. L. Barra, E. Zhecheva, R. Alcántara, G. Ortiz and J. L. Tirado, *Inorg. Chem.*, 2009, 48, 4798-4805.
25. V. H. Crawford, H. W. Richardson, J. R. Wasson, D. J. Hodgson and W. E. Hatfield, *Inorg. Chem.*, 1976, 15, 2107-2110.
26. R. Inglis, C. J. Milios, L. F. Jones, S. Piligkos and E. K. Brechin, *Chem. Commun.*, 2012, 48, 181-190.
27. R. T. W. Scott, S. Parsons, M. Murugesu, W. Wernsdorfer, G. Christou and E. K. Brechin, *Chem. Commun.*, 2005, 2083-2085.
28. S. M. Taylor, R. D. McIntosh, C. M. Beavers, S. J. Teat, S. Piligkos, S. J. Dalgarno and E. K. Brechin, *Chem. Commun.*, 2011, 47, 1440-1442.
29. C. J. Milios, A. Vinslava, A. G. Whittaker, S. Parsons, W. Wernsdorfer, G. Christou, S. P. Perlepes and E. K. Brechin, *Inorg. Chem.*, 2006, 45, 5272-5274.
30. R. Sessoli, D. Gatteschi, A. Caneschi and M. A. Novak, *Nature*, 1993, 365, 141-143.
31. D. Gatteschi, R. Sessoli and A. Cornia, *Chem. Commun.*, 2000, 725-732.

32. A. Cornia, L. Gregoli, C. Danieli, A. Caneschi, R. Sessoli, L. Sorace, A.-L. Barra and W. Wernsdorfer, *Inorg. Chim. Acta*, 2008, 361, 3481-3488.
33. A. K. Boudalis, B. Donnadieu, V. Nastopoulos, J. M. Clemente-Juan, A. Mari, Y. Sanakis, J.-P. Tuchagues and S. P. Perlepes, *Angew. Chem.*, 2004, 116, 2316-2320.
34. C. Cadiou, M. Murrie, C. Paulsen, V. Villar, W. Wernsdorfer and R. E. P. Winpenny, *Chem. Commun.*, 2001, 2666-2667.
35. R. Biswas, Y. Ida, M. L. Baker, S. Biswas, P. Kar, H. Nojiri, T. Ishida and A. Ghosh, *Chem. Eur. J.*, 2013, 19, 3943-3953.
36. R. Boča, J. Miklovič and J. Titiš, *Inorg. Chem.*, 2014, 53, 2367-2369.
37. E.-C. Yang, D. N. Hendrickson, W. Wernsdorfer, M. Nakano, L. N. Zakharov, R. D. Sommer, A. L. Rheingold, M. Ledezma-Gairaud and G. Christou, *J. Appl. Phys.*, 2002, 91, 7382-7384.
38. R. Sessoli, H. L. Tsai, A. R. Schake, S. Wang, J. B. Vincent, K. Folting, D. Gatteschi, G. Christou and D. N. Hendrickson, *J. Am. Chem. Soc.*, 1993, 115, 1804-1816.
39. T. Lis, *Acta Crystallogr. Sect. B*, 1980, 36, 2042-2046.
40. S. M. J. Aubin, M. W. Wemple, D. M. Adams, H.-L. Tsai, G. Christou and D. N. Hendrickson, *J. Am. Chem. Soc.*, 1996, 118, 7746-7754.
41. R. Bagai and G. Christou, *Chem. Soc. Rev.*, 2009, 38, 1011-1026.
42. N. E. Chakov, S.-C. Lee, A. G. Harter, P. L. Kuhns, A. P. Reyes, S. O. Hill, N. S. Dalal, W. Wernsdorfer, K. A. Abboud and G. Christou, *J. Am. Chem. Soc.*, 2006, 128, 6975-6989.
43. C. J. Milios, C. P. Raptopoulou, A. Terzis, F. Lloret, R. Vicente, S. P. Perlepes and A. Escuer, *Angew. Chem.*, 2004, 116, 212-214.
44. C. J. Milios, A. Vinslava, W. Wernsdorfer, S. Moggach, S. Parsons, S. P. Perlepes, G. Christou and E. K. Brechin, *J. Am. Chem. Soc.*, 2007, 129, 2754-2755.
45. J. D. Rinehart, M. Fang, W. J. Evans and J. R. Long, *Nature Chem.*, 2011, 3, 538-542.
46. J. D. Rinehart, M. Fang, W. J. Evans and J. R. Long, *J. Am. Chem. Soc.*, 2011, 133, 14236-14239.
47. M. Mannini, F. Pineider, P. Sainctavit, C. Danieli, E. Otero, C. Sciancalepore, A. M. Talarico, M.-A. Arrio, A. Cornia, D. Gatteschi and R. Sessoli, *Nature Mater.*, 2009, 8, 194-197.
48. M. A. Novak, R. Sessoli, A. Caneschi and D. Gatteschi, *J. Magn. Magn. Mater.*, 1995, 146, 211-213.
49. D. Gatteschi and R. Sessoli, *Angew. Chem. Int. Ed.*, 2003, 42, 268-297.
50. W. Wernsdorfer, M. Murugesu and G. Christou, *Phys. Rev. Lett.*, 2006, 96, 057208.
51. L. Bogani and W. Wernsdorfer, *Nature Mater.*, 2008, 7, 179-186.
52. M. N. Leuenberger and D. Loss, *Nature*, 2001, 410, 789-793.
53. R. E. P. Winpenny, *Angew. Chem. Int. Ed.*, 2008, 47, 7992-7994.
54. W. Wernsdorfer, *Nature Mater.*, 2007, 6, 174-176.
55. W. Wernsdorfer, N. Aliaga-Alcalde, D. N. Hendrickson and G. Christou, *Nature*, 2002, 416, 406-409.
56. A. Ardavan, O. Rival, J. J. L. Morton, S. J. Blundell, A. M. Tyryshkin, G. A. Timco and R. E. P. Winpenny, *Phys. Rev. Lett.*, 2007, 98, 057201.
57. F. K. Larsen, J. Overgaard, S. Parsons, E. Rentschler, A. A. Smith, G. A. Timco and R. E. P. Winpenny, *Angew. Chem.*, 2003, 115, 6160-6163.
58. M. Mannini, F. Pineider, C. Danieli, F. Totti, L. Sorace, P. Sainctavit, M. A. Arrio, E. Otero, L. Joly, J. C. Cezar, A. Cornia and R. Sessoli, *Nature*, 2010, 468, 417-421.
59. M. N. Baibich, J. M. Broto, A. Fert, F. N. Van Dau, F. Petroff, P. Etienne, G. Creuzet, A. Friederich and J. Chazelas, *Phys. Rev. Lett.*, 1988, 61, 2472-2475.
60. G. Binasch, P. Grünberg, F. Saurenbach and W. Zinn, *Phys. Rev. B*, 1989, 39, 4828-4830.
61. A. M. Tishin and Y. I. Spichkin, *The Magnetocaloric Effect and its Applications*, Taylor & Francis, 2003.
62. P. Debye, *Ann. Phys. (Berlin)*, 1926, 81, 1154-1160.

63. M. Evangelisti and E. K. Brechin, *Dalton Trans.*, 2010, 39, 4672-4676.
64. A. Bencini, C. Benelli, A. Caneschi, R. L. Carlin, A. Dei and D. Gatteschi, *J. Am. Chem. Soc.*, 1985, 107, 8128-8136.
65. G. Karotsis, M. Evangelisti, S. J. Dalgarno and E. K. Brechin, *Angew. Chem.*, 2009, 121, 10112-10115.
66. D. Dermitzaki, G. Lorusso, C. P. Raptopoulou, V. Psycharis, A. Escuer, M. Evangelisti, S. P. Perlepes and T. C. Stamatatos, *Inorg. Chem.*, 2013, 52, 10235-10237.
67. T. N. Hooper, J. Schnack, S. Piligkos, M. Evangelisti and E. K. Brechin, *Angew. Chem. Int. Ed.*, 2012, 51, 4633-4636.
68. Y.-Z. Zheng, M. Evangelisti, F. Tuna and R. E. P. Winpenny, *J. Am. Chem. Soc.*, 2011, 134, 1057-1065.
69. J. Ruiz, G. Lorusso, M. Evangelisti, E. K. Brechin, S. J. A. Pope and E. Colacio, *Inorg. Chem.*, 2014, 53, 3586-3594.
70. C. Janiak and J. K. Vieth, *New J. Chem.*, 2010, 34, 2366-2388.
71. B. F. Hoskins and R. Robson, *J. Am. Chem. Soc.*, 1989, 111, 5962-5964.
72. B. F. Hoskins and R. Robson, *J. Am. Chem. Soc.*, 1990, 112, 1546-1554.
73. S. R. Batten, B. F. Hoskins and R. Robson, *J. Am. Chem. Soc.*, 1995, 117, 5385-5386.
74. S. Ma and H.-C. Zhou, *Chem. Commun.*, 2010, 46, 44-53.
75. K. Na, K. M. Choi, O. M. Yaghi and G. A. Somorjai, *Nano Lett.*, 2014.
76. M. D. Allendorf, C. A. Bauer, R. K. Bhakta and R. J. T. Houk, *Chem. Soc. Rev.*, 2009, 38, 1330-1352.
77. C. Wang, T. Zhang and W. Lin, *Chem. Rev.*, 2011, 112, 1084-1104.
78. J. Rocha, L. D. Carlos, F. A. A. Paz and D. Ananias, *Chem. Soc. Rev.*, 2011, 40, 926-940.
79. Q.-K. Liu, J.-P. Ma and Y.-B. Dong, *Chem. Commun.*, 2011, 47, 7185-7187.
80. Y. Cui, Y. Yue, G. Qian and B. Chen, *Chem. Rev.*, 2011, 112, 1126-1162.
81. J. Boeckmann and C. Nather, *Chem. Commun.*, 2011, 47, 7104-7106.
82. D. Gaynor, Z. A. Starikova, S. Ostrovsky, W. Haase and K. B. Nolan, *Chem. Commun.*, 2002, 506-507.
83. G. Mezei, C. M. Zaleski and V. L. Pecoraro, *Chem. Rev.*, 2007, 107, 4933-5003.
84. D. Gaynor, Z. A. Starikova, W. Haase and K. B. Nolan, *J. Chem. Soc., Dalton Trans.*, 2001, 1578-1581.
85. S. T. Meally, G. Karotsis, E. K. Brechin, G. S. Papaefstathiou, P. W. Dunne, P. McArdle and L. F. Jones, *CrystEngComm*, 2010, 12, 59-63.
86. S. T. Meally, C. McDonald, G. Karotsis, G. S. Papaefstathiou, E. K. Brechin, P. W. Dunne, P. McArdle, N. P. Power and L. F. Jones, *Dalton Trans.*, 2010, 39, 4809-4816.
87. S. T. Meally, C. McDonald, P. Kealy, S. M. Taylor, E. K. Brechin and L. F. Jones, *Dalton Trans.*, 2012, 41, 5610-5616.
88. T. A. Manz, J. M. Caruthers, S. Sharma, K. Phomphrai, K. T. Thomson, W. N. Delgass and M. M. Abu-Omar, *Organometallics*, 2012, 31, 602-618.
89. Y. Obora and M. Tanaka, *J. Organomet. Chem.*, 2000, 595, 1-11.
90. M. A. T. Munoz, C. Urbaneja, M. Temprado, M. E. G. Mosquera and T. Cuenca, *Chem. Commun.*, 2011, 47, 11757-11759.
91. H. Torayama, H. Asada, M. Fujiwara and T. Matsushita, *Polyhedron*, 1998, 17, 3859-3874.
92. G. R. Clark, J. M. Waters, T. N. Waters and G. J. Williams, *J. Inorg. Nucl. Chem.*, 1977, 39, 1971-1975.
93. D. W. Martin and T. N. Waters, *J. Chem. Soc., Dalton Trans.*, 1973, 2440-2443.
94. M. Shiotsuka, Y. Okaue, N. Matsumoto, H. Okawa and T. Isobe, *J. Chem. Soc., Dalton Trans.*, 1994, 2065-2070.

Chapter Two

Progressive Decoration of Pentanuclear Cu(II) 12-Metallacrown-4 Nodes Towards Targeted 1- and 2D Extended Networks

2.1 Introduction

Hydroxamic acids are a group of weak organic acids of general formula RCONHOH, which were first discovered in 1869 by Lossen.[1] However, it was not until the early 1980's that research into their synthesis, chemistry, bioactivity, and their metal complexation commenced. They exist in two tautomeric forms, the enol tautomer which is prominent in alkaline conditions and the keto tautomer which is the primary form under acidic conditions, where it behaves as a monobasic acid (Figure 49).[2] Furthermore, nuclear magnetic resonance (NMR) studies have proven the existence of E and Z isomers of each tautomer.[3] The pK_a values of hydroxamic acids tend towards a value of 9, but can exhibit a range of values based on variation in the electronic properties of their substituents. For example, ortho-nitrobenzohydroxamic acid has a value of 7.05, while N-phenyl-n-butyrohydroxamic acid has a value of 11.33.[4]

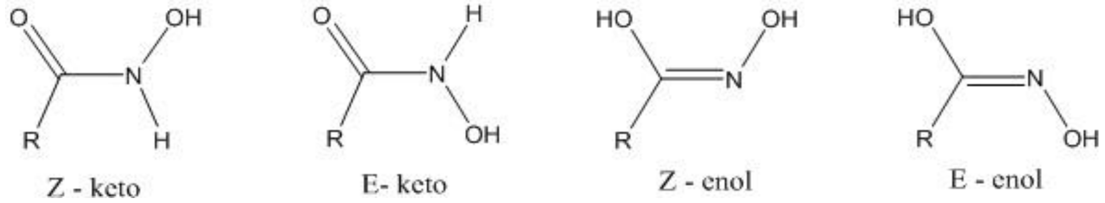

Figure 49 *- The keto and enol tautomeric forms of hydroxamic acids along with their corresponding E/Z isomers.*

Hydroxamic acids have a strong ability to bind to numerous metal ions, the most common mode of binding is via the carbonyl and deprotonated hydroxyl oxygen atoms, resulting in a singly deprotonated hydroxamato species (Figure 50). The chelation of metal ions via these oxygen atoms, in conjunction with a deprotonated nitrogen atom produces a doubly deprotonated hydroximato species (Figure 50).[5, 6]

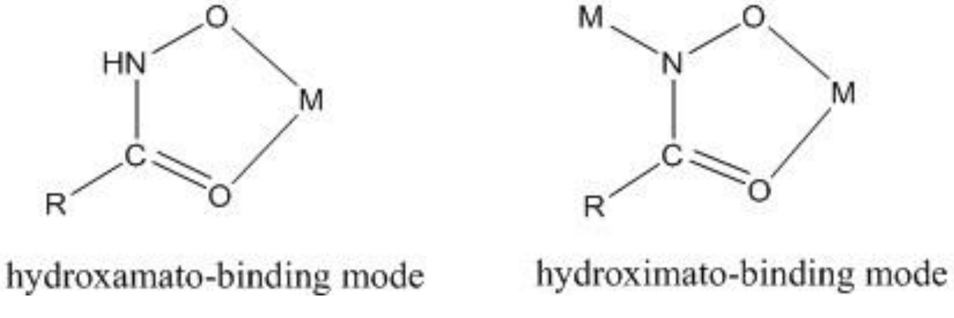

Figure 50 *- Single deprotonated (left) versus doubly deprotonated (right) binding modes exhibited by hydroxamate ligands.*

Due to their affinity for metal ions, it is no surprise that hydroxamic acids were primarily used as siderophores.[7] Siderophores are a class of low molecular weight Fe(III) chelating agents produced by bacteria for the uptake and transport of iron. Iron is essential for many life sustaining processes and even though it is one of the most plentiful elements on earth, it is in short supply due to its poor solubility in water. In addition, hydroxamic acids have an important role as enzyme inhibitors for ureases,[2, 8] matrix metalloproteases (MMP's),[2, 9] histone deacetylases (HDAC's),[2, 10] and prostaglandin H_2 synthases (PGHS's).[2, 11] This has led to their potential therapeutic applications as anti-fungal, anti-cancer, anti-hypertension, anti-osteoarthritis, and anti-tuberculosis agents.[2, 12, 13] Indeed, their ability to chelate to metals has allowed hydroxamic acids to be valuable ligands in the field of coordination chemistry.[14] Furthermore, they have industrial applications in the extraction and recovery of a variety of transition metals including Fe, Co, Ni, Cu, Zn, and Cd.[15, 16]

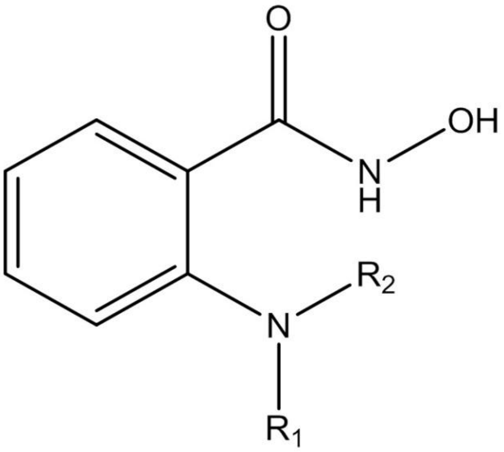

Figure 51 *- Hydroxamic acid ligands used in this research, where* $R_1 = R_2 = Me$; L_1H_2 *and* $R_1 = R_2 = H$; L_2H_2.

Our research involves the use of the two hydroxamic acid ligands 2-(dimethylamino)phenylhydroxamic acid (L_1H_2) and 2-(amino)phenylhydroxamic acid (L_2H_2) (Figure 51). Previous studies utilising L_1H_2 resulted in the formation of a heptanuclear [Ni_7] complex, which exhibits four hydroxamate ligand binding modes.[6] Prior research with L_2H_2 is of greater relevance to the work described in this chapter and details a clam shaped dimer of [$Cu(II)_5$] 12-MC-4 metallacrowns.[17] Metallacrowns[18] are inorganic analogues of crown ethers with a repeating -$[M\text{-}N\text{-}O]_n$- unit, where a ring metal and a nitrogen atom replace the methylene carbon atoms of a crown ether (Figure 52). The nomenclature for metallacrowns is derived from the naming system used for crown ethers. That is, they are named according to the ring size and the number of donating oxygen atoms they contain. For example, a 12-MC-4 metallacrown is a twelve membered metallacrown ring with four repeating [M-N-O] units and four oxygen donating atoms. MX[Ring size-MC$_{M'Z(L)}$-ring oxygens]Y is the typical nomenclature used for metallacrowns, where M stands for the bound central metal and its oxidation state, X is any bound anions, M′ is the ring metal and its oxidation state, Z is the third heteroatom of the ring (usually N), L is the organic ligand used in the complex, and Y is any unbound anions. For example, Mn(II)(OAc)$_2$(DMF)$_6$[12-MC$_{Mn(III)N(shi)}$-4] was the first metallacrown to be synthesised in 1989.[19] Since their discovery, a large amount of metallacrowns have been synthesised from a variety of metal ions (Cu(II), Mn(II/III), Fe(III), Co(II), Ni(II), Zn(II), Ln(III) etc.), with a plethora of topologies (currently ranging from 9-MC-3 to 60-MC-20), using a variety of organic ligands, in particular hydroxamic acids.[18, 20, 21] In addition, these complexes have proven to be viable target molecules due to their solution stability, selective cation and anion binding, ligand exchange capabilities and their use as building blocks towards extended architectures. Therefore, they have potential applications for a variety of functions including molecular recognition,[22] catalysis,[23, 24] selective substrate sorption,[25, 26] luminescent,[20] and magnetic materials.[27-29]

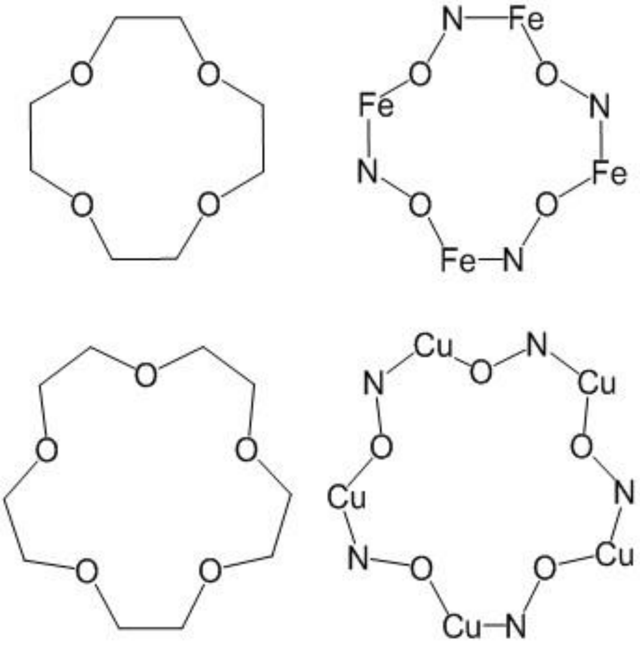

***Figure 52 -** Illustration comparing crown ethers and metallacrowns. Please note ligand substituents have been omitted for clarity. (Top left) 12-crown-4, (top right) 12-MC$_{Fe(III)N(shi)}$-4, (bottom left) 15-crown-5 and (bottom right) 15-MC$_{Cu(II)N(picHA)}$-5.*[18]

This chapter describes the synthesis, structure and magnetic characterisation of a family of planar pentanuclear Cu(II) 12-MC-4 metallacrowns, utilising the hydroxamic acid ligands 2-(dimethylamino)phenylhydroxamic acid (L_1H_2) or 2-(amino)phenylhydroxamic acid (L_2H_2). This family includes four discrete complexes of formulae $[Cu(II)_5(L_1)_4(MeOH)_4](ClO_4)_2$ (**1**), $[Cu(II)_5(L_1)_4(pyr)_2](ClO_4)_2 \cdot pyr$ (**2**), $[Cu(II)_5(L_1)_4(pyr)_6](ClO_4)_2$ (**3**), and $[Cu(II)_5(L_2)_4(MeOH)_4](ClO_4)_2 \cdot H_2O$ (**7**), where the terminal (i.e. MeOH in **1** and **7**) ligands have been exchanged in a controlled manner. The introduction of ditopic connector ligands such as 4,4'-bipyridine (4,4'-bipy), 4,4'-azopyridine (4,4'-azp), and pyrazine (pz) at the axial Cu(II) coordination sites within our discrete [Cu_5] metallacrown units in **1**-**3**, represents a controlled and progressive approach to the self-assembly of the 1-2D extended networks of formulae $\{[Cu(II)_5(L_1)_4(4,4'\text{-bipy})_3](ClO_4)_2 \cdot H_2O\}_n$ (**4**), $\{[Cu(II)_5(L_1)_4(4,4'\text{-azp})_2(MeOH)_2](ClO_4)_2\}_n$ (**5**) and $\{[Cu(II)_5(L_2)_4(pz)_2(MeOH)](ClO_4)_2 \cdot 3MeOH\}_n$ (**6**).

2.2 Results and Discussion

2.2.1 Structural Descriptions

2.2.1.1 Founding Member of the 12-MC$_{Cu(II)}$-4 Family

The first complex synthesised from this work was the 12-MC$_{Cu(II)}$-4 pentanuclear metallacrown $[Cu(II)_5(L_1)_4(MeOH)_4](ClO_4)_2$ (**1**) (Figure 53). This founding member was obtained via the methanolic reaction of $Cu(ClO_4)_2 \cdot 6H_2O$, 2-(dimethylamino)phenylhydroxamic acid (L_1H_2) (Figure 51) and NaOH. Upon filtration and slow evaporation of the mother liquor, dark green crystals of **1** were formed with a yield of ~10%. Complex **1** crystallises in the monoclinic *C*2/*c* space group with unit cell parameters: a = 17.9896(7) Å, b = 12.2939(4) Å, c = 23.8922(9) Å, α = 90°, β = 107.805(4)°, γ = 90°. Complete single crystal X-ray diffraction data for **1** is given in Table 1 (Section 2.2.1.6).

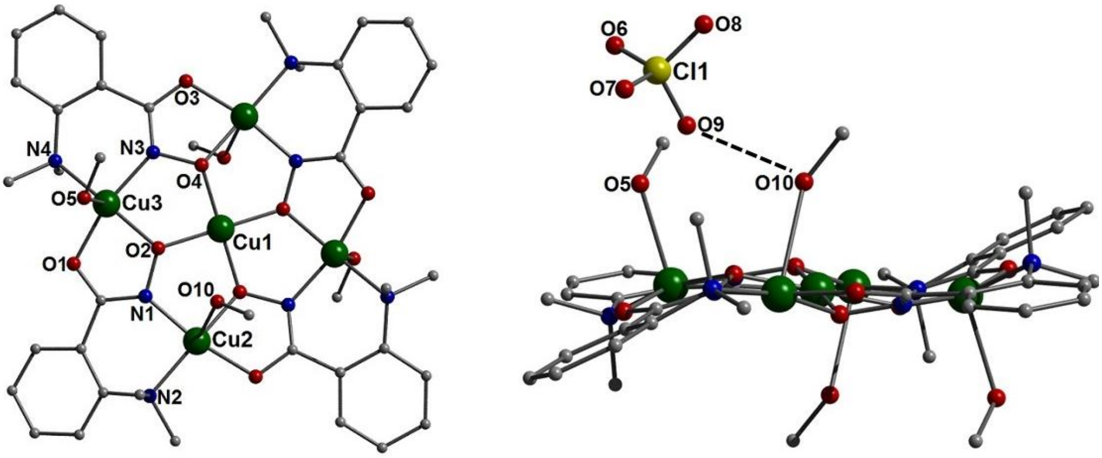

Figure 53 *- Crystal structure of* ***1*** *as viewed perpendicular (left) and parallel (right) to the [Cu$_5$] plane. The dashed lines (right) represent hydrogen bonding in* ***1****. Colour code: green (Cu), red (O), blue (N), grey (C). Hydrogen atoms have been omitted for clarity.*

The structure of **1** consists of a planar core, whereby a central distorted square planar Cu(II) ion (labelled Cu1) is surrounded by four other Cu(II) ions. Each of the peripheral Cu(II) ions are five-coordinate (labelled Cu2, Cu3) and possess almost perfect square-based pyramidal geometries (τ values of 0.004 for Cu2 and 0.07 for Cu3).[30] The four 2-(dimethyl)aminophenylhydroxamic acid ligands are doubly deprotonated (L_1^{2-}) and utilise a $\eta^1:\eta^1:\eta^2:\eta^1\text{-}\mu_3$ coordination mode to bridge the Cu(II) ions in **1** (Figure 54).

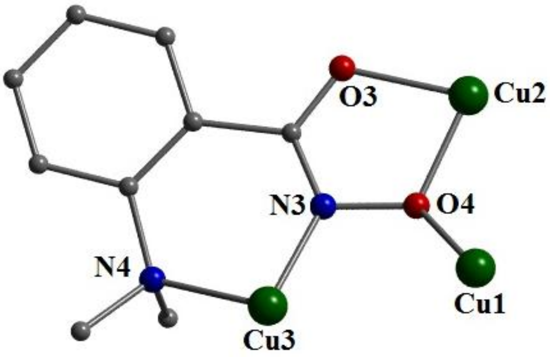

Figure 54 *- Schematic showing the $\eta^1:\eta^1:\eta^2:\eta^1\text{-}\mu_3$ coordination mode of L_1^{2-} in relation to the Cu(II) metal ions in* ***1****.*

The outer Cu(II) ions coordinate to L_1^{2-} via the oxime group oxygen atoms (O2 and O4) with bond lengths of 1.932(3) Å (Cu2-O4) and 1.934(3) Å (Cu3-O2), which bind the peripheral Cu(II) ions to the central Cu(II) ion establishing the pentanuclear planar core. The central Cu(II) ion is coordinated to all four L_1^{2-} ligands with Cu-O bond lengths of 1.892(3) Å (Cu1-O2) and 1.896(2) Å (Cu1-O4). In addition, the oximic nitrogens (N1 and N3) of the L_1^{2-} ligands bond to the outer Cu(II) ions with bond lengths of 1.913(3) Å (Cu2-N1) and 1.933(3) Å (Cu3-N3). Coordination of the peripheral Cu(II) ions is completed at the axial position via a terminal methanol ligand with expected long distances of 2.558(3) Å (Cu2-O10) and 2.303(3) Å (Cu3-O5). The $\{Cu(II)_5(L_1)_4(MeOH)_4\}^{2+}$ cations are charged balanced by two ClO_4^- counter anions, sitting above and below the $[Cu_5]$ plane at a distance of approximately 4.8 Å. Furthermore, these counter anions participate in inter-molecular hydrogen bonding with the aforementioned terminal methanol ligands (O5(H5)$\cdots$O9 = 2.515 Å, O10(H10)$\cdots$O9 = 2.235 Å; Figure 53). Linkage of the $[Cu_5]$ units via these hydrogen bonds, results in the formation of zig-zag rows which propagate along the *c* axis of the unit cell. These individual rows then arrange along the *a* axis with alternating wave-like phases (Figure 55).

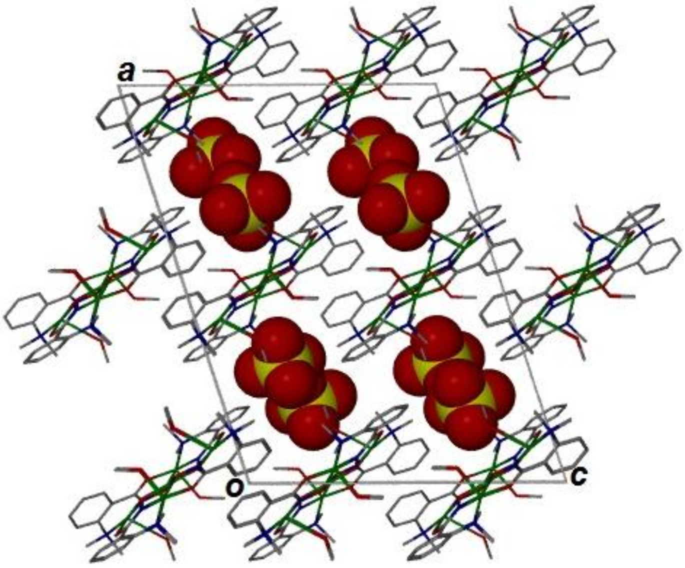

Figure 55 *- Crystal packing arrangement in* ***1*** *as viewed along the b axis of the unit cell. The* ClO_4^- *counter anions are space-fill represented and hydrogen atoms have been removed for clarity. Colour scheme as in Figure 53 and used throughout this chapter.*

2.2.1.2 Manipulation of Primary Co-ordination Spheres at Cu(II) Centres

Examination of complex **1** showed several opportunities for the exploitation of the flexible coordination sites of the Cu(II) ions. Firstly, the potential introduction of specific ligands at the vacant sites of some Cu(II) ions and secondly, the substitution of the terminal methanol ligands at the axial positions of Cu2 and Cu3. Indeed, this proved to be successful with the formation of the analogous metallacrown $[Cu(II)_5(L_1)_4(pyr)_2](ClO_4)_2\cdot pyr$ (**2**), which was synthesised by the addition of 1 cm^3 (12.4 mmol) of pyridine to the experimental procedure for **1** (Figure 56). Complex **2** crystallises in the triclinic *P*-1 space group with unit cell parameters: *a* = 11.283(2) Å, *b* = 11.482(2) Å, *c* = 13.688(3) Å, α = 72.42(3)°, β = 80.58(3)°, γ = 61.80(3)°. Complete single crystal X-ray diffraction data for **2** is given in Table 1 (Section 2.2.1.6).

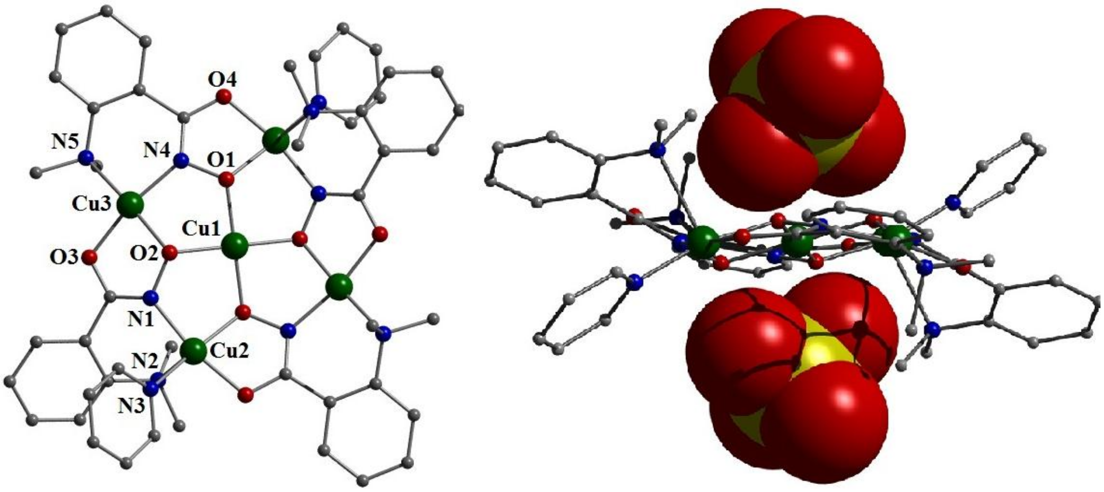

Figure 56 *- Crystal structure of* ***2*** *as viewed perpendicular (left) and parallel (right) to the [Cu$_5$] plane. The ClO_4^- counter anions are space-fill represented. The pyridine solvent of crystallisation and hydrogen atoms have been omitted for clarity.*

The core in **2** closely resembles that of **1**; however it differs in two significant ways. Firstly, the central Cu(II) ion (Cu1) once again possesses four equatorial Cu-O$_{\text{oxime}}$ bonds (Cu1-O1 = 1.914(3) Å, Cu1-O2 = 1.933(3) Å), but also exhibits two long axial close contacts with the two symmetry equivalent (s.e.), charge balancing, ClO_4^- anions (Cu1-O5 = 2.681 Å), which sit above and below the distorted [Cu$_5$] core, respectively. The second major difference is the puckering of the [Cu$_5$] core in **2** compared to that of **1** (Figure 53 *cf*. Figure 56). This is due to the presence of the two terminally bound pyridine ligands attached to Cu2 (and s.e.) (Cu2-N3 = 2.006(3) Å). More interestingly, although the additional (or addition of) pyridine in **2** does not alter the distorted square-based pyramidal coordination geometry of Cu2 and its symmetry equivalents ($\tau = 0.024$),[30] the pyridine ligands force the hydroxamate ligands (L_1^{2-}) to distort away from the [Cu$_5$] plane. This results in the ligands -NMe$_2$ moiety forming a Cu-N bond at the axial position at a distance of Cu2-N2 = 2.438(3) Å. The Cu3 (and its s.e.) ion is distorted square planar in **2** (unlike in **1**) presumably due to the steric constraints enforced by the nearby ClO_4^- anions. Indeed, the perchlorate O5 atom lies at a distance of 2.861 Å from Cu3, which would represent a fifth close contact around this metal ion. The [Cu$_5$] moieties in **2** form rows along the *a* axis with a large inter-cluster separation of ~11.2 Å (Cu1···Cu1'). These individual rows are linked by $\pi_{\text{centroid}} \cdots \pi_{\text{centroid}}$ stacking of their terminal and symmetry equivalent pyridine ligands

([C10-C14-N3]···[C10′-C14′-N3′] = 3.644 Å). These individual rows then pack in the common brickwork motif and the 3D connectivity in **2** is completed via H bonding through the ClO_4^- anions and pyridine molecules of crystallisation (Cl1(O6)···(H33)C33 = 2.673 Å and Cl1(O8)···(H13)C13 = 2.508 Å; Figure 57).

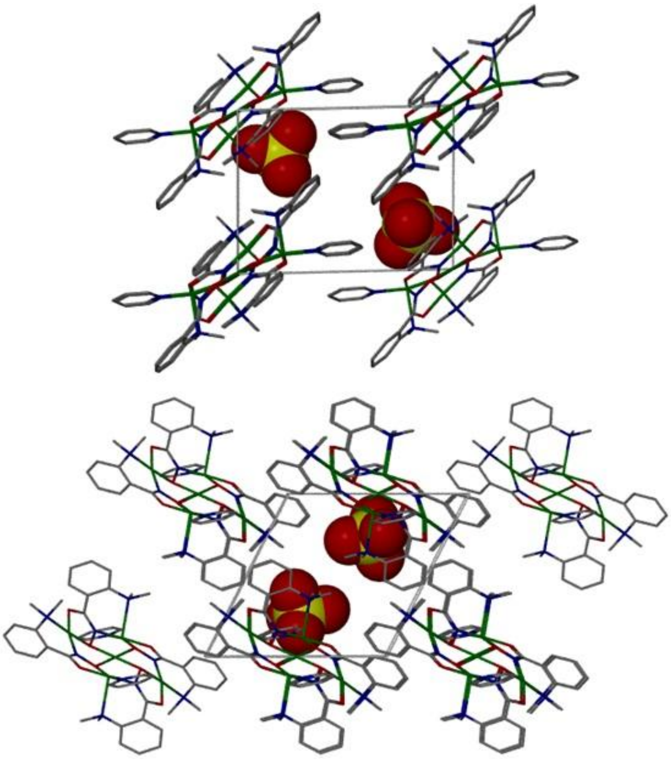

Figure 57 *- Crystal packing arrangement of **2** as viewed along the b axis (top) and a axis (bottom) of the unit cell. The pyridine solvent of crystallisation and all hydrogen atoms have been removed for clarity. The ClO_4^- counter anions are shown in space-fill mode.*

By simple addition of an even greater excess of pyridine to the synthetic procedure for **1** (5 cm^3, 62 mmol), it was possible to occupy more Cu(II) ion sites by taking advantage of the coordinatively unsaturated Cu(II) ions previously observed in **2**. This resulted in the introduction of an additional four pyridine ligands within the [Cu_5] metallacrown in **2**, producing the analogue [$Cu(II)_5(L_1)_4(pyr)_6](ClO_4)_2$ (**3**) (Figure 58). This complex crystallises in the triclinic *P*-1 space group with unit cell parameters: *a* = 11.3067(3) Å, *b* = 12.7372(5) Å, *c* = 13.2511(4) Å, *α* = 97.753(3)°, *β* = 104.385(3)°, *γ* = 103.130(3)°. Complete single crystal X-ray diffraction data for **3** is given in Table 1 (Section 2.2.1.6).

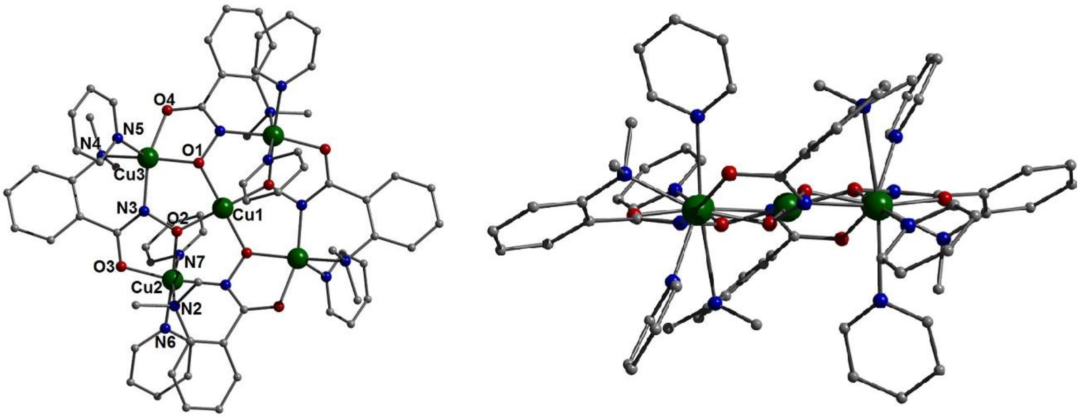

Figure 58 *- Crystal structure of* ***3*** *as viewed perpendicular (left) and parallel (right) to the [Cu_5] plane. Hydrogen atoms and ClO_4^- counter anions have been omitted for clarity.*

Upon close inspection of crystal structures **2** and **3** several structural differences are observed. Firstly, the introduction of the four extra pyridine ligands in **3** has pushed the ClO_4^- counter anions away from the primary coordination sphere of the central Cu1 ion, resulting in a distorted square planar geometry. The ClO_4^- counter anions are now located 5 Å away from the [Cu_5] planar core. Here, they are held in place by hydrogen bonds to two neighbouring pyridine ligands and two neighbouring L^{2-} units via aromatic and aliphatic protons (C32(H32)···O5 = 2.698 Å, C21(H21)···O6 = 2.661 Å, C12(H12)···O8 = 2.544 Å and C9(H9C)···O7 = 2.452 Å). In addition, the Cu2 ion and its symmetric equivalent now display distorted octahedral geometries in **3** (as opposed to square-based pyramidal geometries in **2**). Elongated axial bonds to a pyridine ligand (N7) and an NMe_2 functional group (N2) exist at two of these positions with bond distances of 2.532(19) Å (Cu2-N7) and 2.666(19) Å (Cu2-N2). The bonding at Cu3 (and its s.e.) is also different to that in **2**. Cu3 exhibits a distorted square-based pyramidal geometry, whereby a pyridine ligand occupies the axial position (Cu3-N5 = 2.211(18) Å) (τ = 0.11).[30] The individual [Cu_5] units in **3** are connected in all directions via numerous inter-molecular interactions involving the perchlorate counter anions. Each of their O atoms (O5-O8 and s.e.) partake in H bonding interactions with either aromatic (H12, H21) or aliphatic (H8B, H9C) protons belonging to nearby L_1^{2-} or terminal pyridine ligands (C8(H8B)···O5 = 2.589 Å; C21(H21)···O6 = 2.661 Å; C9(H9C)···O7 = 2.452 Å and C12(H12)···O8 = 2.554 Å) (Figure 59).

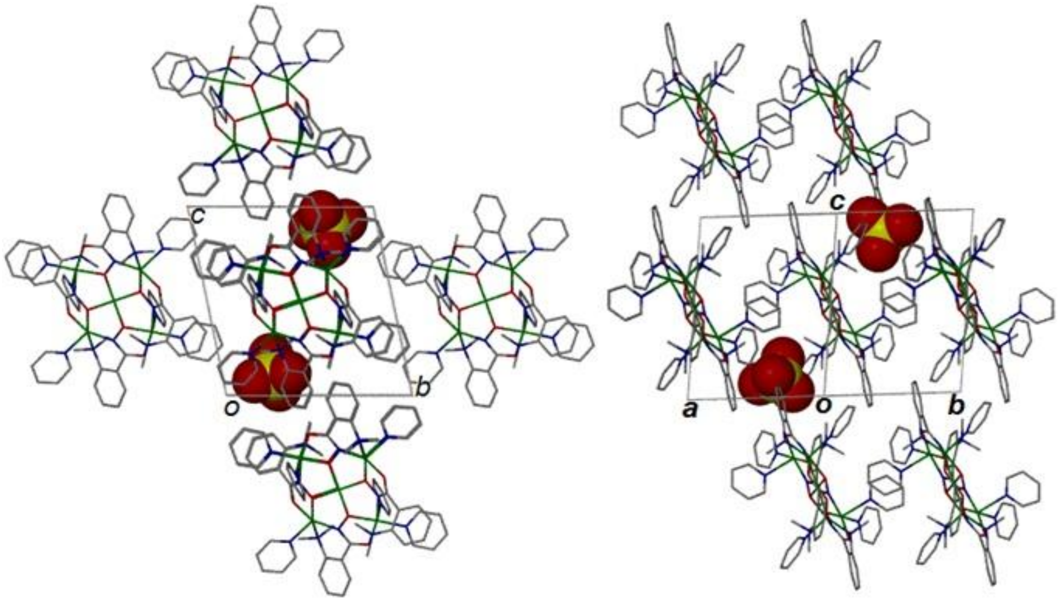

Figure 59 *- Crystal packing arrangement of* ***3*** *as viewed along the a (left) and ab (right) cell direction. Hydrogen atoms have been omitted for clarity. The* ClO_4^- *counter anions are shown in space-fill mode.*

It should be noted that the preservation of the 12-$MC_{Cu(II)}$-4 topology upon addition of pyridine to give complexes **2** and **3** was by no means an expected event. For example, addition of pyridine to the 12-MC-4 complex $[Cu_5(picha)_4](NO_3)_2$ (where picha = 2-picolinehydroxamic acid) resulted in the transformation of a $[Cu_5]$ to a $[Cu_3]$ core.[31]

2.2.1.3 Self Assembly of Larger Extended Architectures

The success in the synthesis of complexes **1**-**3** proved that it was possible to influence the coordination numbers of the Cu(II) ions via facile axial ligand addition or substitution (i.e. replacing alcohol with pyridine), thus in turn altering their resultant coordination geometries (e.g. square-based pyramidal vs. distorted octahedral). All of the above hinted at the potential for self assembly of a larger extended architecture via the incorporation of linear linker ligands. This was first achieved through a one pot synthesis via the addition of the linear ditopic linker ligand 4,4'-bipyridine (4,4'-bipy), producing the 2D coordination polymer $\{[Cu(II)_5(L_1)_4(4,4'\text{-bipy})_3](ClO_4)_2\cdot H_2O\}_n$ (**4**) (Figure 60). To date, there are only a small number of extended networks containing $[Cu_5]$ metallacrown nodes, all of which comprise a carboxylate based or alkali metal linker unit and these $[Cu_5]$ nodes possess different internal bridging ligands to those used in the synthesis of **4**.[26, 32, 33] Prior to the synthesis of **4**, there were no $[Cu_5]$ metallacrown extended networks prepared with a pyridyl connector ligand. Incorporation of structurally related metallacyclic complexes into extended architectures is known in the literature and includes two examples involving pyridyl connector ligands.[34, 35] Complex **4** crystallises in the triclinic *P*-1 space group with unit cell parameters: a = 11.3776(7) Å, b = 12.6211(9) Å, c = 12.6793(8) Å, α = 90.229(6)°, β = 107.558(6)°, γ = 104.589(6)°. Complete single crystal X-ray diffraction data for **4** is given in Table 1 (Section 2.2.1.6).

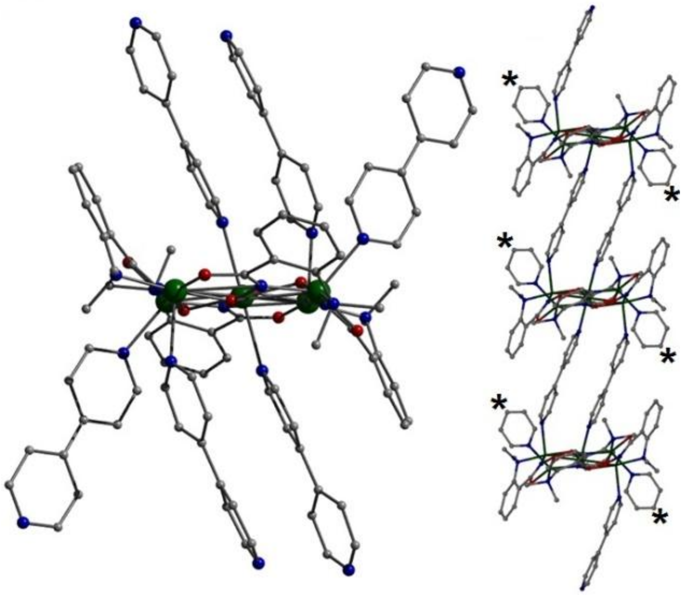

***Figure 60** - (Left) Crystal structure of one [Cu_5] unit within the extended network of **4**. (Right) Structure of three [Cu_5] units linked by 4,4'-bipy to form 1D arrays. The * symbol represents the position whereby the 4,4'-bipy connects the 1D rows to form 2D sheets in **4**. Hydrogen atoms, H_2O solvents of crystallisation, and ClO_4^- counter anions have been removed for clarity.*

The extended network of **4** consists of superimposable 1D rows of [Cu_5] units propagating along the a direction of the unit cell. Each [Cu_5] unit maintains the $\{Cu(II)_5(L_1)_4\}^{2+}$ core and is connected via two out of the three 4,4'-bipy ligands (and s.e.) resulting in the formation of 1D chains. These dipyridyl ligands are axially bonded to the central Cu(II) ions (Cu1 and s.e.) at N4 and the outer Cu2 ions (N3) respectively, with rather long bond lengths of Cu1-N4 = 2.495 Å and Cu2-N3 = 2.294(5) Å. A third dipyridyl ligand in **4** acts as a connector in between these 1D chains to form covalent 2D sheets, giving rise to a [4,4] grid topology (Figure 61 and 62).

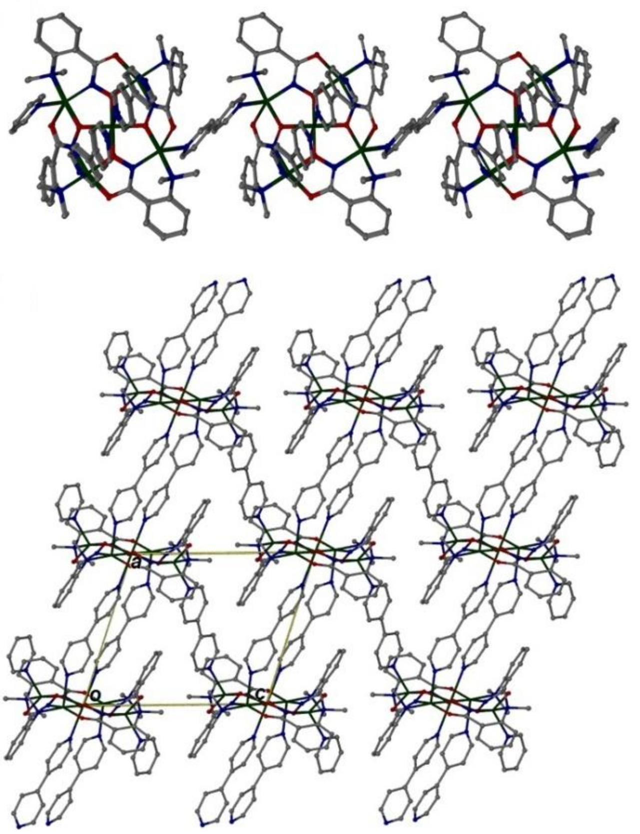

Figure 61 *- Aerial (top) and perpendicular (bottom) view of one 2D sheet of [Cu_5] nodes linked into the [4,4] grid topology in* ***4****. Hydrogen atoms, H_2O solvents of crystallisation, and ClO_4^- counter anions have been omitted for clarity.*

These 2D nets in **4** stack in parallel staggered layers along the *b* direction of the unit cell with an inter-nodal distance of 12.62 Å (Cu1···Cu1′). The ClO_4^- counter anions connect the separate 2D sheets in **4** and are held in position through H bonding with aromatic protons of nearby 4,4'-bipy (H20, H33) and L_1^{2-} ligands (H14) with distances of C20(H20)···O7 = 2.359 Å; C33(H33)···O8 = 2.397 Å and C14(H14)···O5 = 2.614 Å (Figure 61). A water of crystallisation is also present within these 2D planes and was modelled isotropically as disordered over two sites (50:50 occupancy).

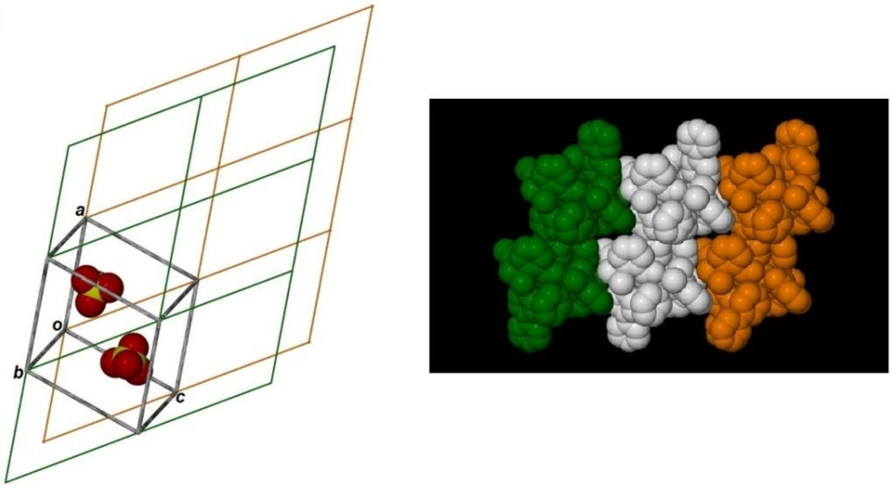

Figure 62 *- (Left) Schematic diagram (obtained from crystal data) showing two parallel 2D grid-like sheets in **4** represented as different colours for clarity (green and orange). Each node represents one {Cu_5} building block in **4** (taken as the central Cu1 ion). The unit cell location and its contents (ClO_4^- anions) are also shown. (Right) Three colour coded 2D sheets of **4** standing parallel to one another along the b cell direction.*

A 1D coordination polymer {[$Cu(II)_5(L_1)_4$(4,4'-azp)$_2$(MeOH)$_2$](ClO_4)$_2$}$_n$ (**5**) was obtained via the introduction of the ditopic ligand 4,4'-azopyridine (4,4'-azp) to the general {Cu_5} synthetic procedure employed in this work (Figure 63). Complex **5** crystallises in the monoclinic $P2_1/n$ space group with unit cell parameters: a = 12.6809(3) Å, b = 10.7919(3) Å, c = 20.7122(5) Å, α = 90°, β = 100.018(2)°, γ = 90°. Complete single crystal X-ray diffraction data for **5** is given in Table 2 (Section 2.2.1.6).

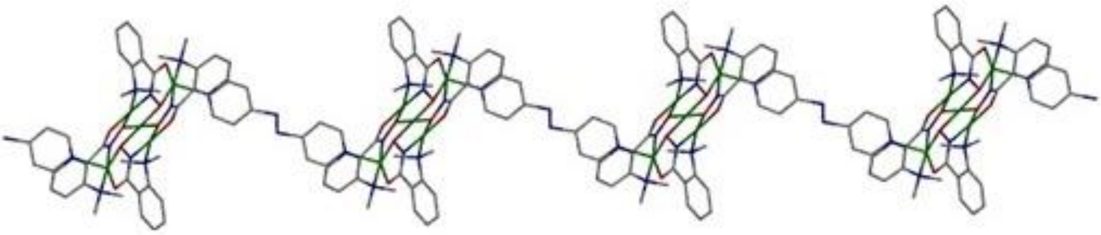

Figure 63 *- Schematic of the zig-zag chains in **5**. Hydrogen atoms and perchlorate counter anions have been removed for clarity.*

The {$Cu(II)_5(L_1)_4$}$^{2+}$ core is once again maintained in **5**. Similarly to **2**, Cu1 possesses two long axial close contacts with the two charge balancing ClO_4^- anions, sitting above and below the distorted [Cu_5] plane with bond lengths of 2.670 Å (Cu1-$O5_{perchlorate}$). These counter anions hydrogen bond to pyridyl and MeOH protons with bond lengths of 3.171 Å (C19(H19)$\cdots$O8) and 2.905 Å (O9(H9)$\cdots$O6). The 4,4'-azopyridine ligands bond to Cu2 (and s.e.) with a Cu2-N5 distance of 2.277(3) Å and display distorted square-based pyramidal geometries (τ = 0.093).[30] The change in connectivity from 2D (**4**) to 1D (**5**) is presumably due to these -N=N- bridges which give *trans* conformations in the crystal structure and leads to a zig-zag chain arrangement. The individual 1D rows in **5** are superimposable and propagate across the *ab* plane of the cell, while stacking on top of one another in the *b* direction in an offset manner (Figure 64). The [Cu_5] nodes of adjacent chains are close enough to partake in C-H$\cdots\pi_{centroid}$ interactions (C5(H5)$\cdots$[C11'-C16'] = 3.767 Å). The direction of these chains alternate (along *a* versus along *b* direction) as viewed along the *c* direction of the cell (Figure 64).

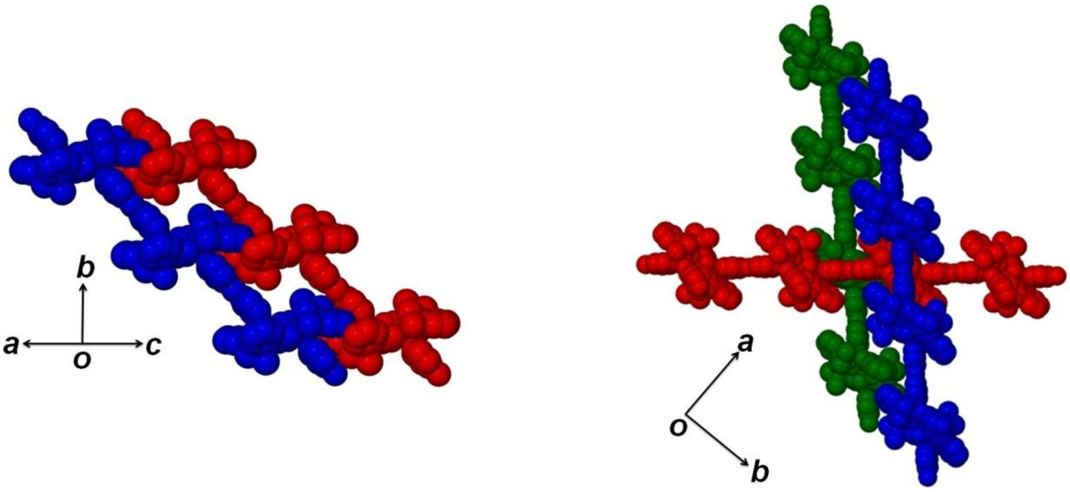

Figure 64 - *(Left) Schematic showing stacking of two colour coded, space filled represented, zig-zag, 1D chains of **5** along the ab plane. (Right) Space-fill represented schematic of three colour coded, 1D chains of **5** running in alternate directions, lying almost perpendicular to each other along the c direction of the unit cell.*

The next step was to attempt to bring the individual [Cu_5] nodes closer together and this proved successful via the use of the shorter connector ligand pyrazine, in conjunction with the ligand 2-(amino)phenylhydroxamic acid (L_2H_2) (Figure 51). By using a similar reaction procedure to those previously described, the 1D coordination polymer $\{[Cu(II)_5(L_2)_4(pz)_2(MeOH)](ClO_4)_2\cdot 3MeOH\}_n$ (**6**) was obtained (Figure 65). Complex **6** crystallises in the monoclinic $P2_1$ space group with unit cell parameters: a = 9.3958(19) Å, b = 26.777(5) Å, c = 10.690(2) Å, α = 90°, β = 100.54(3)°, γ = 90°. Complete single crystal X-ray diffraction data for **6** is given in Table 2 (Section 2.2.1.6). It must be noted that we were unable to isolate any crystalline products when using the 2-(dimethylamino)phenylhydroxamic acid ligand (L_1H_2) in the above reaction procedure. This is presumably due to the steric effects of the more bulky -NMe_2 moiety in L_1H_2 as opposed to the less bulky -NH_2 functional group in L_2H_2.

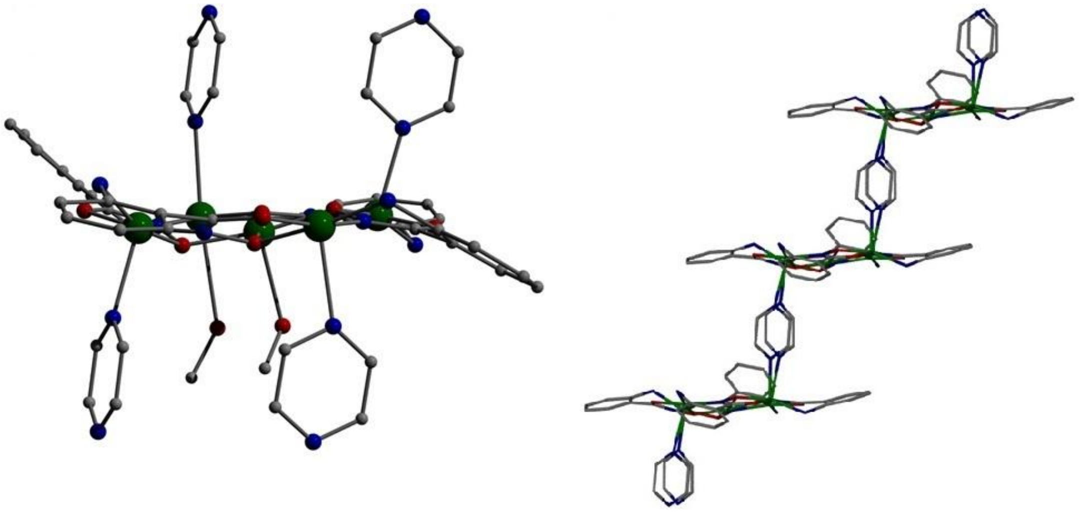

***Figure 65* - (**(*Left) Crystal structure of **6** showing a single [Cu_5] node and (right) schematic showing 1D chains of **6**. Hydrogen atoms, solvents of crystallisation, and ClO_4^- counter anions have been omitted for clarity.*

Complex **6** contains a $\{Cu(II)_5(L_2)_4\}^{2+}$ core, whereby the central Cu(II) ion (Cu1) exhibits almost perfect square-based pyramidal geometry ($\tau = 0.0072$),[30] with completed coordination at the axial position via a MeOH ligand. Three of the four peripheral Cu(II) ions (Cu2, Cu4 and Cu5) display square-based pyramidal geometries ($\tau = 0.051$, 0.077 and 0.098 respectively).[30] Each of the peripheral Cu(II) ions (Cu2-5) are bound to one pyrazine ligand (N9-N12) giving bond distances of 2.292(6) Å (Cu2-N10), 2.471(6) Å (Cu3-N9), 2.289(5) Å (Cu4-N11) and 2.418(6) Å (Cu5-N12). The coordination of the pyrazine ligands form 1D rows along the *a* direction resulting in a step like conformation (Figure 65). These individual rows stack in parallel interlocking layers along the *c* axis, held in place by inter-molecular hydrogen bonds (N6(H6B)···[C9'-C14']$_{centroid}$ = 3.802 Å) to form 2D sheets, which stack parallel along the *b* cell direction (Figure 66). The distance between the 2D sheets in **6** (measured as the Cu1···Cu1' distance) is approximately 9.40 Å which is considerably smaller in comparison to **4** (12.62 Å). The $\{Cu(II)_5(L_2)_4(pz)_2(MeOH)\}^{2+}$ cations in **6** are charge balanced by two crystallographically unique ClO_4^- counter anions. The octahedral geometry of Cu3 is completed via a close contact with one ClO_4^- counter anion at a distance of 2.782 Å (Cu3-O11). The second ClO_4^- anion is positioned at the periphery of the [Cu_5] unit and is held in position by H bonding interactions with: *1)* aliphatic hydroxamate protons (N8(H8B)···O13 = 2.198 Å), *2)* MeOH solvents of crystallisation (C37(H37A)···O15 = 2.485 Å), *3)* MeOH ligands (O19(H19A)···O13 = 1.984 Å) and *4)* aromatic hydroxamate protons (C29(H29)···O16 = 2.833 Å).

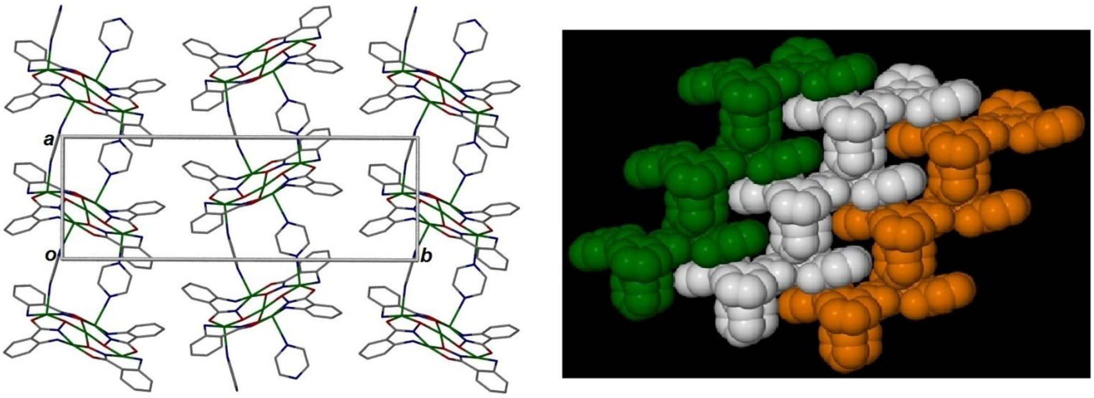

***Figure 66** - (Left) Crystal packing in **6** depicting alternating [Cu_5] tilt angles along the b direction of the unit cell. (Right) Space-fill representation of three colour coded 1D chains, highlighting the step like conformation in **6**. Hydrogen atoms, solvent molecules, and ClO_4^- counter anions have been removed for clarity.*

2.2.1.4 Further Investigations of the Less Bulky -NH_2 Functional Group

We decided it would be pertinent to further investigate the less bulky nature of the 2-(amino)phenylhydroxamic acid ligand (L_2H_2) and its involvement in the synthesis of a less puckered [Cu_5] metallacrown (**6**). This led to the production of a discrete [Cu_5] metallacrown $[Cu(II)_5(L_2)_4(MeOH)_4](ClO_4)_2 \cdot H_2O$ (**7**) (analogue to **1**-**3**). Complex **7** crystallises in the triclinic *P*-1 space group with the unit cell parameters: a = 11.0640(3) Å, b = 12.2750(4) Å, c = 17.2399(6) Å, α = 110.321(3)°, β = 96.075(3)°, γ = 96.316(2)° and the asymmetric unit contains two whole [Cu_5] cages (labelled Cu1-3 and Cu4-6 respectively). Complete single X-ray crystal diffraction data for **7** is given in Table 2 (Section 2.2.1.6). All peripheral Cu(II) ions (Cu2-3 and Cu5-6) display distorted square-based pyramidal geometries (τ = 0.235, 0.232, 0.039, 0.131 respectively)[30] with coordination capped via a terminal MeOH ligand at the axial position at Cu2, Cu3 and Cu5 (Cu2-O6 = 2.32(3) Å, Cu3-O5 = 2.35(3) Å, Cu5-O11 = 2.433(3) Å). Coordination is completed at the Cu6 centre via a close contact with a ClO_4^- counter anion (Cu6-O16 = 2.504 Å). In addition, the same ClO_4^- counter anion forms close contacts to Cu4 (octahedral geometry) with bond length of 2.646 Å (Cu4-O17). This perchlorate anion positions itself directly above one of the [Cu_5] units (labelled Cu4-Cu6), while the other ClO_4^- counter anion (Cl1) is situated in between the two [Cu_5] units and is held in place by H-bond interactions with *1)* MeOH ligands (C16(H16B)···O12 = 2.507 Å), *2)* aliphatic hydroxamate protons (N5(H5B)···O13 = 2.557 Å) and *3)* aromatic hydroxamate protons (C12(H12)···O15 = 2.685 Å). As anticipated these units lie in close proximity to one another, with $\pi_{centroid} \cdots \pi_{centroid}$ interactions between adjacent hydroxamate aromatic rings at distances of 4.724 Å

([C1-C6]···[C17'-C22']) and 4.799 Å ([C8-C13]···[C24'-C29']) (Figure 67). The MeOH solvent molecule of crystallisation in **7** lies in between the two [Cu_5] units and simultaneously hydrogen bonds (via O20 and H20A) to the aliphatic $-NH_2$ proton (H7A) and a second hydroxamate ligand via its bridging carbonyl O atom (O1) with distances of 2.066 Å (N7(H7A)···O20) and 1.891 Å (O20(H20A)···O1). The [Cu_5] units in **7** pack along the *a* cell direction in superimposable columns, which then arrange themselves into the space efficient brickwork motif.

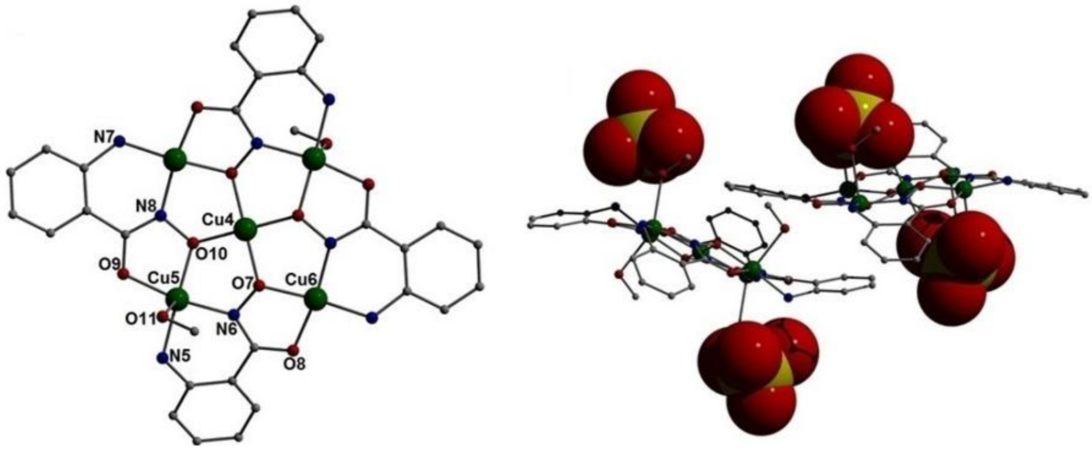

Figure 67 *- (Left) Crystal structure of one of the [Cu_5] units in* ***7*** *(ClO_4^- counter anions omitted for clarity). (Right) Illustration of the asymmetric unit in* ***7*** *depicting the close proximity of the two [Cu_5] units with space fill representation of the ClO_4^- counter anions. Hydrogen atoms, MeOH and H_2O solvents of crystallisation have been removed from both figures for clarity.*

2.2.1.5 The Influence of Solvent Ligands on the Position of ClO_4^- Counter Anions

Upon closer inspection, we discovered that the hydrogen bonding and coordination ability of MeOH and pyridyl containing ligands in complexes **1**-**7** influence the position of the ClO_4^- counter anions in relation to their proximity to the [Cu_5] metallacrowns. For example, in **1**, **3** and **4** the ClO_4^- counter anions position themselves at the periphery of the structures, which is to be expected due to their weak coordination ability. However, in siblings **2** and **5** the ClO_4^- counter anions locate above and below the [Cu_5] units, creating weak close contacts to the central Cu(II) ions and hydrogen bond to adjacent metal bound ligands ($-NMe_2$ protons in **2**; MeOH and 4,4'-azp protons in **5**). Furthermore, in **6** and **7** one of the ClO_4^- counter anions acts as a close contact, while the other sits on the periphery of the structure. These observations highlight how the solvent ligands in **1**-**7** are able to move the anions inside or outside of the first coordination sphere of the metallacycle, depending on the H bonding and coordination ability of the methanol or pyridine ligands involved.

2.2.1.6 Crystallographic Data of Complexes 1-7

Table 1 *- Crystallographic data for complexes* ***1-4****.*

Complex	**1**	**2**·pyr	**3**	**4**·H_2O
Formula^a	$C_{40}H_{56}N_8O_{20}Cl_2Cu_5$	$C_{51}H_{55}N_{11}O_{16}Cl_2Cu_5$	$C_{66}H_{70}N_{14}O_{16}Cl_2Cu_5$	$C_{66}H_{64}N_{14}O_{17}Cl_2Cu_5$
M_W	1357.53	1466.66	1703.96	1713.91
Crystal Appearance	Green Parallelepiped	Green Parallelepiped	Green Block	Green Parallelepiped
Crystal System	Monoclinic	Triclinic	Triclinic	Triclinic
Space group	*C*2/*c*	*P*-1	*P*-1	*P*-1
a/Å	17.9896(7)	11.283(2)	11.3067(3)	11.3776(7)
b/Å	12.2939(4)	11.482(2)	12.7372(5)	12.6211(9)
c/Å	23.8922(9)	13.688(3)	13.2511(4)	12.6793(8)
α/°	90	72.42(3)	97.753(3)	90.229(6)
β/°	107.805(4)	80.58(3)	104.385(3)	107.558(6)
γ/°	90	61.80(3)	103.130(3)	104.589(6)
V/Å^3	5031.0(3)	1489.4(5)	1762.79(10)	1673.60(19)
Z	4	1	1	1
T/K	150(2)	150(2)	150(2)	150(2)
λ^b/Å	0.7107	0.7107	0.7107	0.7107
D_c/g cm^{-3}	1.792	1.635	1.605	1.701
μ(Mo-Ka)/ mm^{-1}	2.271	1.921	1.637	1.726
Meas./indep., (R_{int}) refl.	4607/3637, (0.0401)	5443/4757, (0.0162)	6450/5592, (0.0185)	6117/4231, (0.0867)
wR2 (all data)	0.0910	0.1152	0.0681	0.2254
$R1^{d,e}$	0.0423	0.0378	0.0267	0.0696
Goodness of fit (GOOF) on F^2	1.074	1.074	1.063	1.023

^{a} Includes guest molecules. ^{b} Mo-Kα radiation, graphite monochromator. ^{c} $wR2= [\sum w(|F_o^2|-|F_c^2|)^2/\sum w|F_o^2|^2]^{1/2}$. ^{d} For observed data. ^{e} $R1= \sum||F_o|- |F_c||/ \sum|F_o|$.

***Table 2** - Crystallographic data for complexes **5**-**7**.*

Complex	**5**	**6**·3MeOH	**7**·H_2O
Formula[a]	$C_{48}H_{56}N_{12}O_{18}Cl_2Cu_5$	$C_{40}H_{47}N_{12}O_{20}Cl_2Cu_5$	$C_{32}H_{40}N_8O_{21}Cl_2Cu_5$
M_W	1477.65	1404.50	1261.32
Crystal Appearance	Green Parallelepiped	Green Parallelepiped	Green Parallelepiped
Crystal System	Monoclinic	Monoclinic	Triclinic
Space group	$P2_1/n$	$P2_1$	P-1
a/Å	12.6809(3)	9.3958(19)	11.0640(3)
b/Å	10.7919(3)	26.777(5)	12.2750(4)
c/Å	20.7122(5)	10.690(2)	17.2399(6)
α/°	90	90.00	110.321(3)
β/°	100.018(2)	100.54(3)	96.075(3)
γ/°	90	90.00	96.316(2)
V/Å^3	2791.27(12)	2644.2(9)	2156.10(12)
Z	2	2	2
T/K	149.8	150.0	150.0
λ^b/Å	0.7107	0.7107	0.7107
D_c/g cm^{-3}	1.758	1.764	1.943
μ(Mo-Ka)/ mm^{-1}	2.054	2.166	2.643
Meas./indep., (R_{int}) refl.	5090/3963, (0.0547)	7736/5930, (0.0694)	7876/6482, (0.0262)
wR2 (all data)	0.0874	0.0758	0.0795
$R1^{d,e}$	0.0379	0.0482	0.0322
Goodness of fit (GOOF) on F^2	1.025	0.963	1.063

[a] Includes guest molecules. [b] Mo-Kα radiation, graphite monochromator. [c] $wR2 = [\sum w(|F_o^2| - |F_c^2|)^2 / \sum w|F_o^2|^2]^{1/2}$. [d] For observed data. [e] $R1 = \sum||F_o| - |F_c|| / \sum|F_o|$.

2.2.2 Solution Studies

Solid state IR spectroscopy on complexes **1**-**7** each gave the characteristic peaks for hydroxamate C-O (~1590 cm^{-1}), C-N (1550 cm^{-1}) and N-O (1100 cm^{-1}) stretching modes.[36, 37] The solution behaviour of $[Cu(II)_5(L_1)_4(MeOH)_4](ClO_4)_2$ (**1**), $[Cu(II)_5(L_1)_4(pyr)_2](ClO_4)_2$·pyr (**2**) and $\{[Cu(II)_5(L_1)_4(4,4'\text{-bipy})_3](ClO_4)_2 \cdot H_2O\}_n$ (**4**) were studied using mass spectrometry and UV-visible spectroscopy. The electrospray time of flight-mass spectra of **1**, **2** and **4** was performed in H_2O-MeCN (50:50) solutions and each spectrum displays two prominent peaks corresponding to $\{Cu_5(L_1)_4\}^{2+}$ (m/z = 515) and $[\{Cu_5(L_1)_4\} + \{ClO_4\}]^+$ (m/z = 1129) (Figure 68). Very small peaks in **1** and **4** with less than 2% abundance may be tentatively attributed to the species [{$Cu_5(L_1)_4(MeCN)_8$} + {ClO_4}]$^+$, where MeCN ligands occupy all remaining Cu(II) coordination sites.

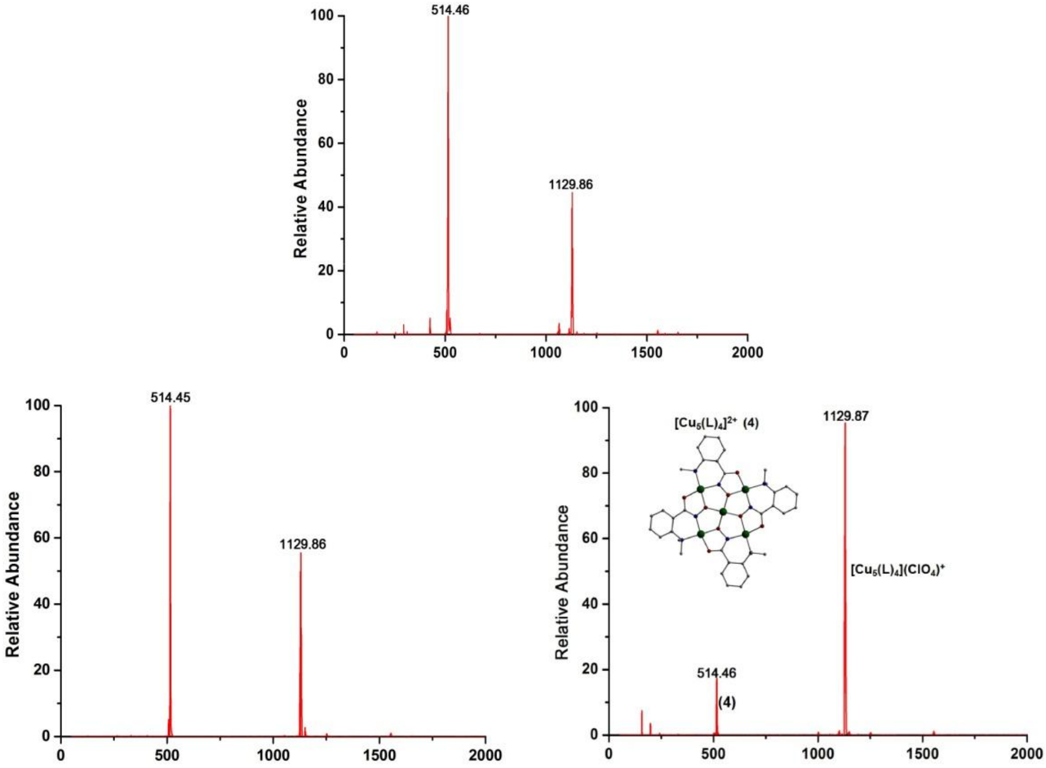

Figure 68 - (Top) Mass spectrum of $[Cu(II)_5(L_1)_4(MeOH)_4](ClO_4)_2$ (***1***)*. (Bottom left) Mass spectrum of* $[Cu(II)_5(L_1)_4(pyr)_2](ClO_4)_2\cdot pyr$ (***2***)*. (Bottom right) Mass spectrum of* $\{[Cu(II)_5(L_1)_4(4,4'\text{-bipy})_3](ClO_4)_2\cdot H_2O\}_n$ (***4***)*. All performed in a 50:50* H_2O*-MeCN solvent mixture.*

UV-vis spectra of L_1H_2, 4,4'-bipyridine, $[Cu(II)_5(L_1)_4(MeOH)_4](ClO_4)_2$ (**1**) and $\{[Cu(II)_5(L_1)_4(4,4'\text{-bipy})_3](ClO_4)_2\cdot H_2O\}_n$ (**4**) were obtained from methanolic solutions. The spectrum in **1** shows absorption peaks at approximately 207 (partially cut off in methanolic solution), 230 and 273 nm which is confirmed by the analysis of L_1H_2 in solution (Figure 69). These transitions can be attributed to π→π* excitations with ε values (10^3 dm^3 mol^{-1} cm^{-1}) of 410.8, 247.2 and 171.2.[36] The spectrum in **4** displays absorption peaks at 206, 234, 267 nm (shoulder) with a broad shoulder at 360 nm. The first three peaks are as a result of π→π* excitations (ε values ranging from 89.8-99.6 x 10^3 dm^3 mol^{-1} cm^{-1}), while the broad shoulder at 360 nm is representative of n→π* excitations (Figure 70). The shoulder at 267 nm may be assigned to metal bound hydroxamate moieties and uncoordinated 4,4'-bipyridine ligands (as a result of disassociation in solution), resulting in the restoration of the $\{Cu_5(L_1)_4(MeOH)_4\}^{2+}$ moiety (i.e. complex **1**). The long and weak $Cu\text{-}N_{4,4'\text{-bipy}}$ bonds between the [Cu_5] units and the 4,4'-bipyridine linker ligands are responsible for the low concentration solubility of the 2D extended architecture in **4**.

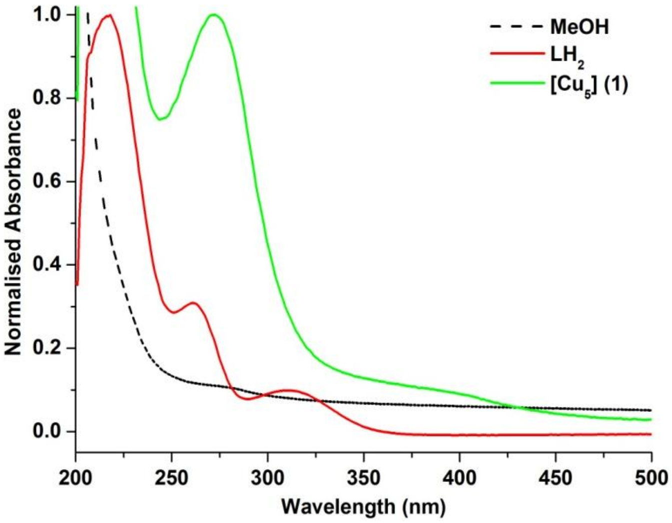

Figure 69 *- Overlay of normalized UV-vis spectra of MeOH (dashed black line), L_1H_2 (red line) and $[Cu(II)_5(L_1)_4(MeOH)_4](ClO_4)_2$ (**1**) (green line).*

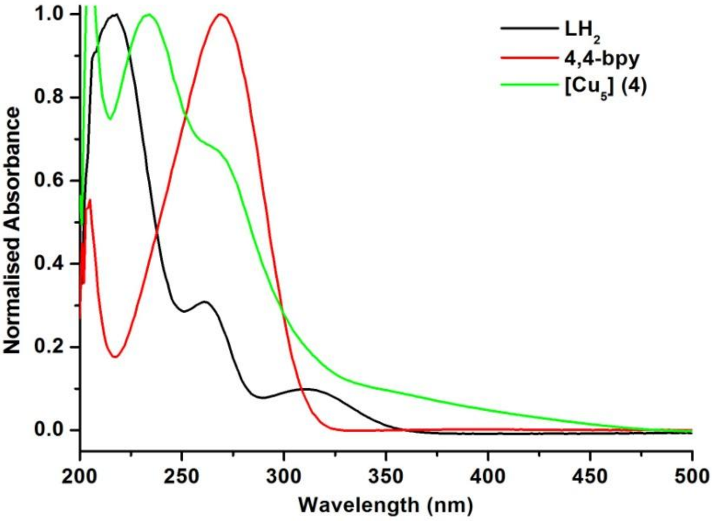

Figure 70 *- Overlay of normalized UV-vis spectra in MeOH of L_1H_2 (black line), 4,4'-bipyridine (red line) and $\{[Cu(II)_5(L_1)_4(4,4'\text{-bipy})_3](ClO_4)_2{\cdot}H_2O\}_n$ (**4**) (green line).*

UV-vis spectra of L_1H_2, 4,4'-bipyridine and **4** were also carried out in MeCN solutions and no significant changes were seen (see Sections 2.4.2.2 and 2.4.2.7). After one week, the same MeOH solutions of **1** and **4** were re-measured to give duplicitous spectra, thus highlighting the solution stability of the $\{Cu_5(L_1)_4\}^{2+}$ cores in these solutions. Previous examples in the literature have observed this solution stability in similar species.[38-40]

UV-vis studies were also carried out on the methanolic solutions of the 1D net $\{[Cu(II)_5(L_2)_4(pz)_2(MeOH)](ClO_4)_2{\cdot}3MeOH\}_n$ (**6**) and the discrete cluster

$[Cu(II)_5(L_2)_4(MeOH)_4](ClO_4)_2 \cdot H_2O$ (**7**) to give similar spectra to those of **1** and **4**. Complex **6** exhibits absorption peaks at approximately 222 and 260 nm with a broad shoulder at 360 nm. The first two peaks are due to π→π* excitations with ε values (x 10^3 dm^3 mol^{-1} cm^{-1}) ranging from 73.1-73.3, while the broad shoulder at 360 nm can be assigned to n→π* transitions (Figure 71). Complex **7** displays absorption peaks at approximately 220 and 265 nm, these can be attributed to π→π* excitations with ε values (x 10^3 dm^3 mol^{-1} cm^{-1}) ranging from 61.3-67.5. In addition, a broad shoulder is observed at 365 nm which is representative of n→π* transitions (Figure 72).

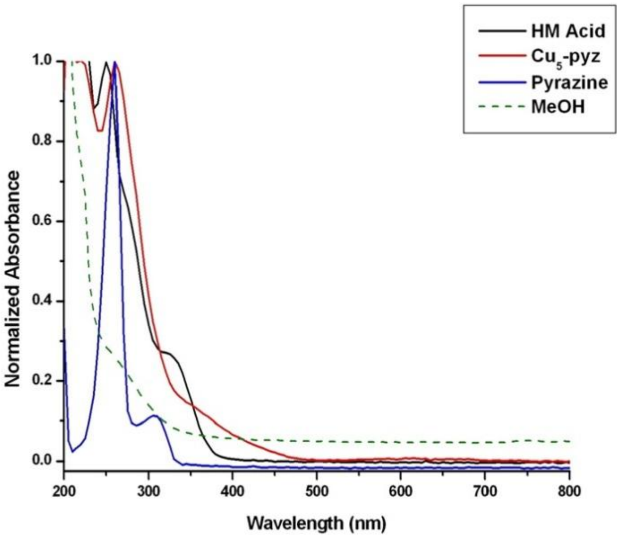

Figure 71 *- Overlay of a normalized UV-vis spectra in MeOH (dashed green line) of L_2H_2 (black line), pyrazine (blue line) and $\{[Cu(II)_5(L_2)_4(pz)_2(MeOH)](ClO_4)_2 \cdot 3MeOH\}_n$ (**6**) (red line).*

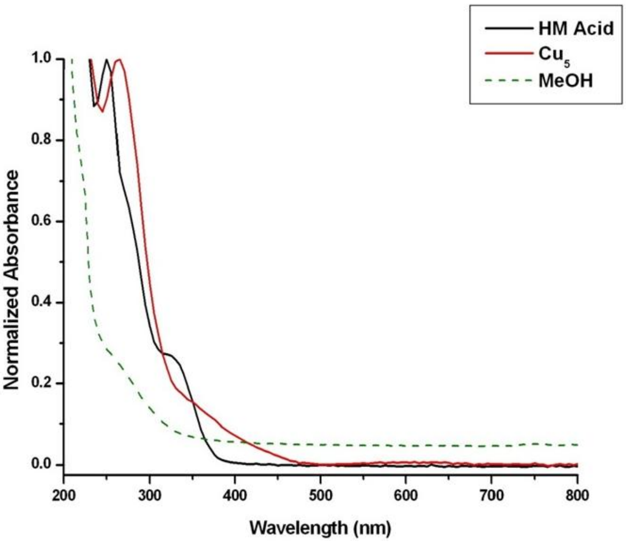

Figure 72 *- Overlay of a normalized UV-vis spectra in MeOH (dashed green line) of L_2H_2 (black line) and $[Cu(II)_5(L_2)_4(MeOH)_4](ClO_4)_2 \cdot H_2O$ (**7**) (red line).*

2.2.3 Magnetic Susceptibility Studies

Dc magnetic susceptibility measurements were performed on powdered microcrystalline samples of $[Cu(II)_5(L_1)_4(MeOH)_4](ClO_4)_2$ (**1**), $\{[Cu(II)_5(L_1)_4(4,4'\text{-}bipy)_3](ClO_4)_2\cdot H_2O\}_n$ (**4**) and $\{[Cu(II)_5(L_2)_4(pz)_2(MeOH)](ClO_4)_2\cdot 3MeOH\}_n$ (**6**) in the 300-5 K temperature range, using an applied field of 0.1 T. The room temperature $\chi_M T$ values of 0.71 (**1**), 1.42 (**4**) and 1.22 (**6**) cm^3 K mol^{-1} obtained are significantly lower than the expected spin-only value of 1.88 cm^3 K mol^{-1} for five non-interacting Cu(II) ions (assuming g = 2.0). As the temperature decreases in **1**, the $\chi_M T$ value drops swiftly before reaching a minimum value of ~0.42 cm^3 K mol^{-1} at 60 K, after which it rises slightly and then plateaus at a value of 0.44 cm^3 K mol^{-1}. The shapes of the curves for **4** and **6** are similar in nature, giving a rapid decrease in the $\chi_M T$ value upon temperature reduction and then a plateau as the temperature lowers further. This indicates the occurrence of strong intra-molecular antiferromagnetic exchange interactions between the Cu(II) ions. In all three complexes, there are two separate magnetic exchange pathways (J_1 and J_2) between the Cu(II) centres, where J_1 represents the $Cu(II)_{outer}$-$Cu(II)_{outer}$ exchange and J_2 represents the $Cu(II)_{outer}$-$Cu(II)_{inner}$ pathway (inset of Figure 73). More specifically, J_1 consists of one Cu-N-O-Cu pathway (angles ranging from 160.46-177.04°) and J_2 is composed of one Cu-N-O-Cu pathway (angles ranging from 17.98-48.16°) and one Cu_{outer}-O-Cu_{inner} bridge (angles ranging from 113.47-121.56°). The above model was used in conjunction with the isotropic spin-Hamiltonian (2.1) for fitting of the data.

$$\begin{aligned}\hat{H} = &-2J_1(\hat{S}_1\bullet\hat{S}_2+\hat{S}_2\bullet\hat{S}_3+\hat{S}_3\bullet\hat{S}_4+\hat{S}_4\bullet\hat{S}_1)\\ &-2J_2(\hat{S}_1\bullet\hat{S}_5+\hat{S}_2\bullet\hat{S}_5+\hat{S}_3\bullet\hat{S}_5+\hat{S}_4\bullet\hat{S}_5)\\ &+\sum_{i=1-5}\left\{\mu_B Bg\hat{S}_i\right\}\end{aligned} \qquad \mathbf{(2.1)}$$

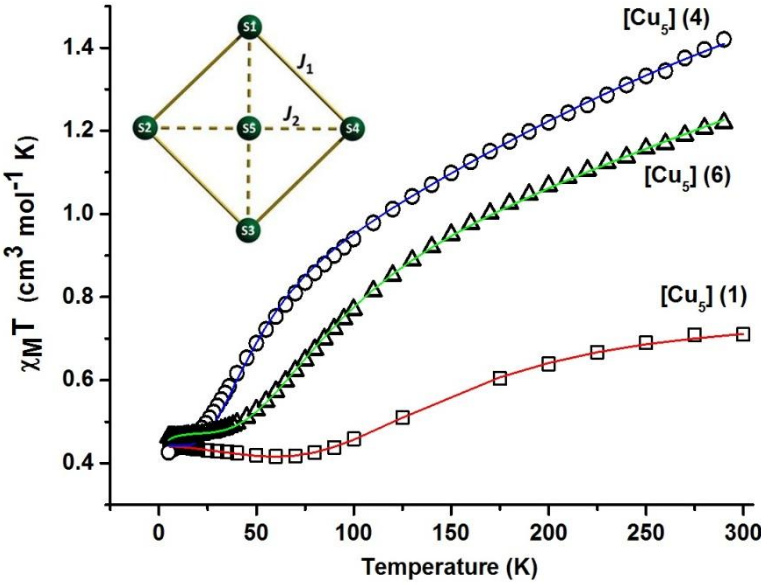

Figure 73 *- Plots of molar magnetic susceptibility ($\chi_M T$) vs. T for* ***1*** *(□),* ***4*** *(○) and* ***6*** *(Δ). The solid lines represent fits of the experimental data with spin-Hamiltonian (2.1) employing the schematic model in the inset.*

The best-fit parameters obtained for **1** and **4** (where g is fixed at 2.15) were J_1 = -139.77 cm^{-1}, J_2 = -295.31 cm^{-1} (**1**) and J_1 = -48.41 cm^{-1}, J_2 = -85.68 cm^{-1} (**4**). In order to fit the data for the 1D net (**6**), the Curie-Weiss parameter (θ) was required to account for inter-molecular exchange through the axial pyrazine linker ligands (via the filled $d_z{}^2$ orbital). This yielded best-fit parameters of J_1 = -86.04 cm^{-1}, J_2 = -145.15 cm^{-1} and θ = -0.23 K (where g = 2.15). The *J* values attained are in line with those previously observed in other similarly bridged Cu(II) cages[25] and generate a ground spin state of S = 1/2 in all complexes. Factors such as structural variation in bond lengths and angles along with electronic effects of the different axial ligands (i.e. MeOH in **1**, 4,4'-bipyridine in **4** and pyrazine in **6**) could potentially influence the diversity in *J* values obtained for **1**, **4** and **6**.

2.3 Conclusions and Observations

We have reported the synthesis of a family of 12-MC$_{Cu(II)}$-4 metallacrowns via the use of the hydroxamic acid ligands 2-(dimethylamino)phenylhydroxamic acid (L_1H_2) and 2-aminophenylhydroxamic acid (L_2H_2). We have shown that N-donor ligands can be progressively added to the vacant axial sites on the Cu(II) ions in the planar [Cu$_5$] core of our prototype metallacrown: [Cu(II)$_5$(L$_1$)$_4$(MeOH)$_4$](ClO$_4$)$_2$ (**1**); thus exploiting both its coordinatively unsaturated nature and the ease of alcohol substitution, resulting in the formation of both the discrete [Cu_5] complexes [$Cu(II)_5(L_1)_4(py)_2](ClO_4)_2\cdot py$ (**2**) and [$Cu(II)_5(L_1)_4(py)_6](ClO_4)_2$ (**3**). Further exploitation of the coordinatively unsaturated Cu(II) cores via the use of N-donor connector ligands produces the 1D and 2D extended architectures $\{[Cu(II)_5(L_1)_4(4,4'\text{-}bipy)_3](ClO_4)_2\cdot H_2O\}_n$ (**4**) and $\{[Cu(II)_5(L_1)_4(4,4'\text{-}azp)_2(MeOH)_2](ClO_4)_2\}_n$ (**5**). In addition, by using a shorter linker ligand (pyrazine) while switching from L_1H_2 to a less bulkier hydroxamic acid ligand L_2H_2, we were able to synthesise the 1D coordination polymer $\{[Cu(II)_5(L_2)_4(pz)_2(MeOH)](ClO_4)_2\cdot 3MeOH\}_n$ (**6**), leading to shorter distances between individual [Cu_5] nodes. Additional investigations into the less bulky ligand L_2H_2 yielded the discrete [Cu_5] metallacrown [$Cu(II)_5(L_2)_4(MeOH)_4](ClO_4)_2\cdot H_2O$ (**7**), which has two unique [Cu_5] units in its asymmetric unit. Electrospray mass spectrometry and UV-vis analysis illustrates the solution stability of the $\{Cu_5(L_x)_4\}^{2+}$ ($x = 1, 2$) cores, which is further highlighted by our ability to manipulate these moieties in solution, resulting in the construction of the 1-2D extended networks **4**-**6**. Magnetic susceptibility studies carried out on **1**, **4** and **6** established strong antiferromagnetic exchange interactions between the Cu(II) ions and isolated S = 1/2 ground spin values in all cases.

2.4 Experimental Section

2.4.1 Instrumentation

Instrumentation utilised in the analysis of complexes **1**-**7** and hydroxamic acids L_xH_2 ($x = 1, 2$) are found below.

2.4.1.1 Carbon, Hydrogen and Nitrogen Microanalysis

Carbon, Hydrogen and Nitrogen Elemental Analyses were performed by Marian Vignoles using a Perkin Elmer Series II CHNS/O Analyzer (2400 Series).

2.4.1.2 Infra-red Spectroscopy

Infra-red spectra were carried out in the 4000-650 cm^{-1} range using a Perkin Elmer FT-IR Spectrum One spectrometer equipped with a Universal Attenuated Total Reflectance (ATR) Sampling accessory.

2.4.1.3 UV-visible Spectroscopy

UV-visible spectra studies were carried out on a Cary 100 Scan (Varian) spectrophotometer. All spectra were normalized (to 1.0) upon completion of ε value calculations.

2.4.1.4 Mass Spectrometry

Electrospray Time of Flight-Mass spectrometry (TOF-MS-ES) were carried out by Dr. Roisin Doohan using a Waters LCT Premier XE system coupled with a Waters E2795 separations module.

2.4.1.5 ^{1}H NMR Spectroscopy

Nuclear Magnetic Resonance (NMR) Spectroscopy analyses were performed by Seamus Collier using a ECX-JEOL 400 MHz ^{1}H NMR spectrometer. NMR spectra were recorded at room temperature in DMSO (d_6).

2.4.1.6 Magnetic Susceptibility Measurements

Variable-temperature, solid-state direct current (dc) magnetic susceptibility data were performed by the Brechin group (University of Edinburgh) on a Quantum Design MPMS-XL SQUID magnetometer equipped with a 7 T dc magnet. Diamagnetic corrections were applied to the observed paramagnetic susceptibilities using Pascal's constants.[41]

2.4.1.7 Single-Crystal X-ray Diffraction

The structures of **1-7** were collected on an Xcalibur S single crystal diffractometer (Oxford Diffraction) using an enhanced Mo source. Each data reduction was performed by the CrysAlisPro software package. The structures were solved by direct methods (SHELXS-97)[42] and refined by full matrix least squares using SHELXL-97.[43] SHELX operations were automated using the OSCAIL software package.[44] All hydrogen atoms were assigned to a calculated position. All non hydrogen atoms were refined anisotropically except for the H_2O (O21) and MeOH (C21 and O20) molecules of crystallisation in **7**. The H_2O molecule was modelled as disordered over three sites (labelled O21A-C). The FLAT command was utilised to restrain the pyridine molecule of crystallisation in **2**.

2.4.2 Syntheses

All reactions were performed under aerobic conditions. All reagents and solvents were used as purchased without further purification. **Caution**: Although no problems were encountered during this work, caution should be exercised when using potentially explosive perchlorate salts.

2.4.2.1 Crystallisation Techniques

Crystallisation can be affected by many factors such as solubility of a sample in a given solvent, the number of nucleation sites, temperature, humidity and time. In addition, it is important to avoid moving the crystal growing vessel as this can lead to poor quality crystals. Two main crystallisation techniques were successfully utilised in this chapter in attempts to obtain X-ray quality crystals.

1) Slow solvent evaporation: this is a very simple technique available for air stable compounds which involves the steady evaporation of solvent from a reaction vessel (can be controlled with a perforated cap), until a saturated solution is achieved from which the product crystallises.

2) Liquid/liquid diffusion: this is a layering technique involving the diffusion of one solvent into another. It is suitable for the use of smaller quantities of air/solvent sensitive reactants. The reactants (excluding the co-ligand in this case) are dissolved into a solution, stirred for the appropriate time and filtered into a reaction vessel. The co-ligand is then dissolved in a small amount of solvent and slowly added to the side of the reaction vessel using a pipette. A discreet layer forms between the solvents and upon slow solvent diffusion crystals form at the boundary of this layer.

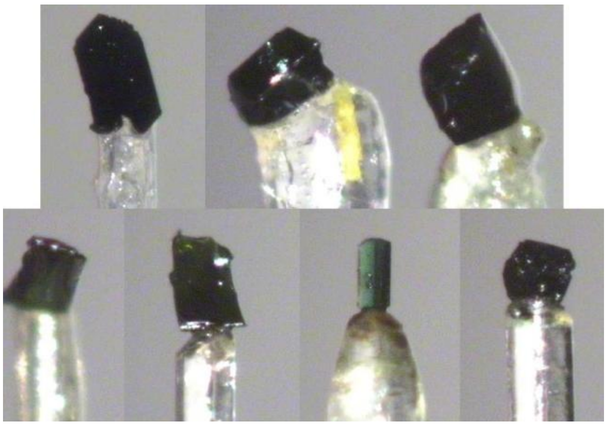

Figure 74 - *Single crystals of complexes* ***1-3*** *(top left to right) and complexes* ***4-7*** *(bottom left to right).*

2.4.2.2 Synthesis of 2-(dimethylamino)phenylhydroxamic acid (L_1H_2)

Synthesis of 2-(dimethylamino)phenylhydroxamic (L_1H_2) by the Gaynor group as per a previously reported procedure.[6]

C, H, N Elemental Analysis

Calculated % for $C_9H_{12}N_2O_2$: C 59.99, H 6.71, N 15.55.

Found %: C 60.34, H 6.46, N 15.91.

FT-IR (cm^{-1}): 3196 (m), 3032 (w), 2953 (w), 2852 (m), 1619 (s), 1587 (s), 1564 (m), 1528 (s), 1495 (s), 1452 (s), 1430 (s), 1335 (m), 1285 (m), 1202 (m), 1162 (m), 1132 (m), 1104 (m), 1061 (m), 1050 (m), 1017 (s), 950 (s), 896 (s), 855 (w), 782 (w), 749 (s).

^1H NMR (400 MHz d_6-DMSO): δ 2.47 ($(CD_3)_2SO$ residual solvent peak), 2.72 (s, 3H, N-CH_3), 3.35 (s, H_2O), 6.92-7.36 (m, 4H, Ar-H), 9.031 (s, 1H, NH) and 10.98 (s, 1H, OH).

UV-vis (MeOH) λ_{max} [nm] (ε_{max} 10^3 dm^3 mol^{-1} cm^{-1}): 218.1 (9.74), 260.9 (3.01), 310 (0.96).

UV-vis (MeCN) λ_{max} [nm] (ε_{max} 10^3 dm^3 mol^{-1} cm^{-1}): 217.9 (18.83), 260 (sh), 320 (sh).

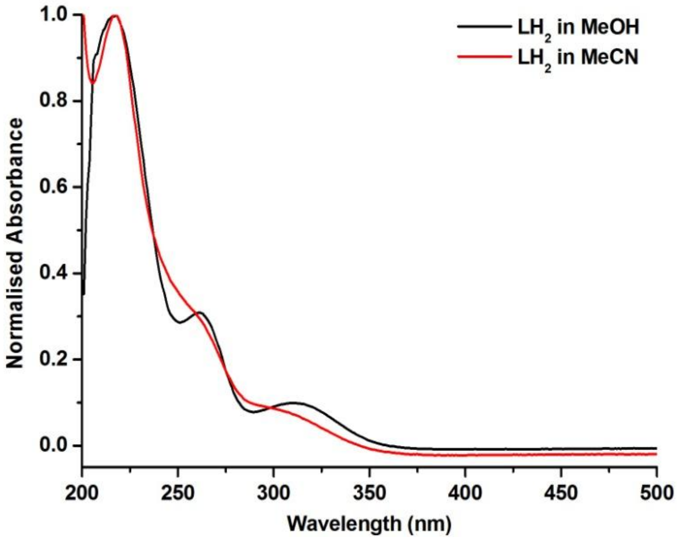

Figure 75 - *Overlay of normalized UV-vis spectra of L_1H_2 in MeOH (black line) and MeCN (red line) solutions.*

2.4.2.3 Synthesis of 2-(amino)phenylhydroxamic acid (L_2H_2)

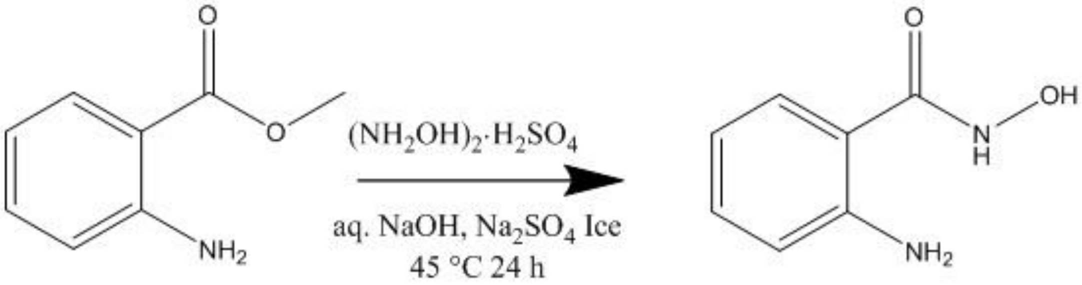

Scheme 1 - *Schematic for the synthesis of 2-(amino)phenylhydroxamic acid (L_2H_2).*

2-(amino)phenylhydroxamic acid was synthesised using a previously reported method.[17] Hydroxylamine sulfate (6.1 g, 37 mmol) and 30 g of ice was added to an aqueous solution of NaOH (7.4 g, 185 mmol, 30 cm^3). Na_2SO_4 (0.58 g, 4.44 mmol) and methyl 2-aminobenzoate (5.6 g, 4.8 cm^3, 37 mmol) were then added to the solution. The mixture was then stirred at 45 °C for 24 h. The solution was then allowed to cool before adjusting the pH to 6 via the addition of 10% H_2SO_4. Some of the light pink hydroxamic acid product precipitated out at this point. This was collected by filtration and re-crystallised from hot H_2O. The filtrate from the previous step was evaporated to dryness under reduced pressure to give a yellow solid. This solid was dissolved in hot MeOH and any remaining solid was filtered. The filtrate was evaporated to dryness under reduced pressure and a second batch of hydroxamic acid was attained. This was then re-crystallised from hot H_2O. The two batches obtained a total yield of (3.94 g) 70%.

C, H, N Elemental Analysis

Calculated % for $C_7H_8N_2O_2$: C 55.26, H 5.3, N 18.41.

Found %: C 54.92, H 4.84, N 18.52.

FT-IR (cm^{-1}): 3500 (w), 3403 (w), 3322 (w), 3155 (w), 2958 (m), 2851 (m), 1613 (m), 1557 (m), 1492 (m), 1448 (m), 1346 (m), 1324 (m), 1297 (m), 1246 (m), 1165 (m), 1111 (w), 1070 (w), 1020 (m), 948 (w), 899 (m), 870 (m), 835 (m), 780 (m), 742 (s), 658 (s).

^1H NMR (400 MHz d_6-DMSO): δ 2.47(($(CD_3)_2SO$ residual solvent peak), 3.38 (s, H_2O) 6.2 (s, 2H, NH_2), 6.43-7.29 (m, 4H, Ar-H), 8.83 (s, 1H, NH) and 10.9 (s, 1H, OH).

UV-vis (MeOH) λ_{max} [nm] (ε_{max} 10^3 dm^3 mol^{-1} cm^{-1}): 212 (26.5), 244.7 (13), 328.5 (3.95).

2.4.2.4 Synthesis of $[Cu(II)_5(L_1)_4(MeOH)_4](ClO_4)_2$ (1)

$Cu(ClO_4)_2{\cdot}6H_2O$ (0.25 g, 0.68 mmol), (L_1H_2) (0.12 g, 0.68 mmol) and NaOH (0.027 g, 0.68 mmol) were dissolved in MeOH (40 cm^3) and stirred for 16 h. The resultant green solution was filtered and dark green X-ray quality crystals of **1** formed upon slow evaporation of the mother liquor. After a few days, the crystals were collected and air dried with a yield of approximately 10%.

C, H, N Elemental Analysis

Calculated % for $C_{40}H_{56}N_8O_{20}Cl_2Cu_5$: C 35.39, H 4.16, N 8.25.

Found %: C 35.52, H 4.22, N 8.03.

FT-IR (cm^{-1}): 3503 (w), 2926 (w), 1627 (w), 1590 (s), 1553 (s), 1468 (m), 1377 (s), 1279 (w), 1247 (w), 1164 (w), 1147 (m), 1068 (s), 1030 (s), 1004 (m), 955 (m), 936 (m), 905 (s), 789 (m), 775 (m), 757 (m), 708 (m), 690 (s), 663 (s).

UV/vis (MeOH): λ_{max} [nm] (ε_{max} 10^3 dm^3 mol^{-1} cm^{-1}): 207 (410.8), 230 (247.2), 271 (171.2).

TOF MS-ES (%) m/z (H_2O/MeCN): 514.5 (100, $[Cu(II)_5(L_1)_4]^{2+}$), 1129.9 (44, $[\{Cu(II)_5(L_1)_4\} + \{ClO_4\}]^+$).

2.4.2.5 Synthesis of $[Cu(II)_5(L_1)_4(pyr)_2](ClO_4){\cdot}pyr$ (2)

$Cu(ClO_4)_2{\cdot}6H_2O$ (0.25 g, 0.68 mmol), L_1H_2 (0.12 g, 0.68 mmol) and NaOH (0.027 g, 0.68 mmol) were dissolved in MeOH (40 cm^3) and stirred. After 5 minutes, 1 cm^3 (12.4 mmol) of pyridine was added and the solution was left to stir for 16 h. Upon filtration the resultant green solution was covered with a perforated cap and left to slowly evaporate in the fume-hood. Dark green X-ray quality crystals of **2** with approximately 15% yield were obtained.

C, H, N Elemental Analysis

Calculated % for $C_{51}H_{55}N_{11}O_{16}Cl_2Cu_5$: C 41.76, H 3.78, N 10.50.

Found %: C 48.01, H 3.95, N 10.68.

FT-IR (cm^{-1}): 3515 (w), 1616 (w), 1587 (m), 1539 (m), 1489 (w), 1469 (m), 1445 (w), 1411 (m), 1381 (m), 1289 (w), 1221 (w), 1150 (w), 1087 (s), 1032 (m), 955 (m), 930 (m), 910 (m), 820 (m), 772 (m), 709 (m), 691 (m), 670 (m).

TOF-MS (%) m/z (H_2O/MeCN): 514.5 (100, $[Cu(II)_5(L_1)_4]^{2+}$), 1129.9 (55, $[\{Cu(II)_5(L_1)_4\} + \{ClO_4\}]^+$).

2.4.2.6 Synthesis of $[Cu(II)_5(L_1)_4(pyr)_6](ClO_4)_2$ (3)

To a solution of $Cu(ClO_4)_2{\cdot}6H_2O$ (0.25 g, 0.68 mmol) in MeOH (40 cm^3) was added L_1H_2 (0.12 g, 0.68 mmol) and NaOH (0.027 g, 0.68 mmol). The solution was stirred for 5 minutes and 5 cm^3 (62 mmol) of pyridine was then added. The solution was left to stir for an additional 16 h and filtered to give a dark green solution. This was covered with a perforated lid and left to stand in the fume-hood. Upon slow evaporation of the mother liquor dark green X-ray quality crystals of **3** were formed in approximately 10% yield.

C, H, N Elemental Analysis

Calculated % for $C_{66}H_{70}N_{14}O_{16}Cl_2Cu_5$: C 46.52, H 4.14, N 11.51.

Found %: C 46.41, H 4.33, N 11.26.

FT-IR (cm^{-1}): 3519 (w), 1612 (w), 1591 (m), 1539 (m), 1492 (w), 1465 (m), 1446 (w), 1408 (m), 1380 (m), 1285 (w), 1220 (w), 1150 (w), 1087 (s), 1031 (m), 957 (m), 934 (m), 912 (m), 815 (m), 775 (m), 705 (m), 692 (m), 669 (m).

2.4.2.7 Synthesis of $\{[Cu(II)_5(L_1)_4(4,4'\text{-bipy})_3](ClO_4)_2{\cdot}H_2O\}_n$ (4)

$Cu(ClO_4)_2{\cdot}6H_2O$ (0.025 g, 0.068 mmol), L_1H_2 (0.012 g, 0.068 mmol) and NaOH (0.003 g, 0.068 mmol) were dissolved in MeOH (10 cm^3) and stirred for 4 h. The green solution obtained was filtered and layered with a MeOH solution (2 cm^3) of 4,4'-bipyridine (0.011 g, 0.068 mmol). The solution was allowed to concentrate upon slow evaporation to give dark green X-ray quality crystals of **4** with a yield of approximately 15%.

C, H, N Elemental Analysis

Calculated % for $C_{66}H_{64}N_{14}O_{17}Cl_2Cu_5$: C 46.25, H 3.76, N 11.44.

Found %: C 46.39, H 3.30, N 11.58.

FT-IR (cm^{-1}): 3514 (w), 1617 (w), 1588 (m), 1537 (m), 1490 (w), 1468 (m), 1447 (w), 1410 (m), 1383 (m), 1288 (w), 1222 (w), 1149 (w), 1085 (s), 1033 (m), 956 (m), 933 (m), 911 (m), 817 (m), 774 (m), 706 (m), 692 (m), 668 (m).

UV/vis (MeOH): λ_{max} [nm] (ε_{max} 10^3 dm^3 mol^{-1} cm^{-1}): 234 (89.8), 267 (sh), 360 (broad sh). (MeCN): λ_{max} [nm] (ε_{max} 10^3 dm^3 mol^{-1} cm^{-1}): 237.1 (75.6), 268.9 (88.8), 365 (broad sh).

TOF MS-ES (%) m/z (H_2O/MeCN) : 514.4 (17, $[Cu(II)_5(L_1)_4]^{2+}$), 1129.9 (100, $[\{Cu(II)_5(L_1)_4\} + \{ClO_4\}]^+$).

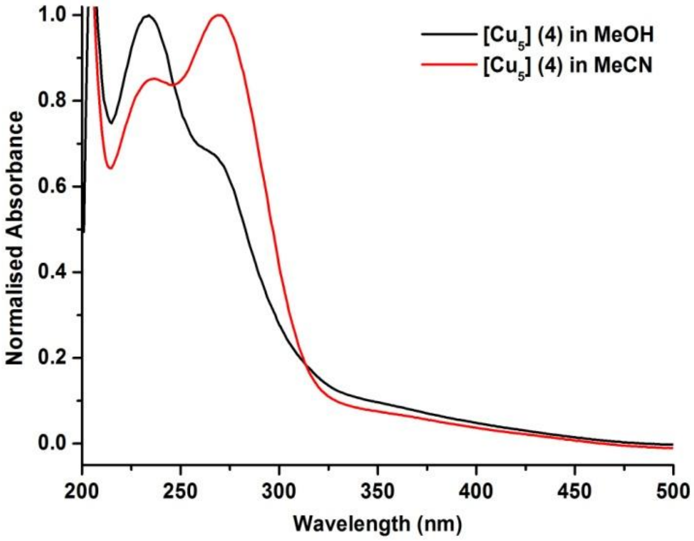

***Figure 76** - Overlay of normalized UV-vis spectra of 2D net (**4**) in MeOH (black line) and MeCN (red line) solutions.*

2.4.2.8 Synthesis of $\{[Cu(II)_5(L_1)_4(4,4'\text{-}azp)_2(MeOH)_2](ClO_4)_2\}_n$ (5)

$Cu(ClO_4)_2 \cdot 6H_2O$ (0.1 g, 0.27 mmol) and L_1H_2 (0.05 g, 0.27 mmol) were dissolved in MeOH (20 cm^3). This was followed by the addition of 4,4'-azopyridine (0.05 g, 0.27 mmol) and NaOH (0.011 g, 0.27 mmol). The solution was allowed to stir for 4 h. Upon filtration and slow evaporation of the mother liquor X-ray quality crystals of **5** formed, which were collected and air dried giving a yield of approximately 12%.

C, H, N Elemental Analysis

Calculated % as $\{[Cu(II)_5(L_1)_4(4,4'\text{-}azp)_2(MeOH)](ClO_4)_2 \cdot 3H_2O\}_n$ ($C_{47}H_{58}N_{12}O_{20}Cl_2Cu_5$): C 37.64, H 3.9, N 11.21.

Found %: C 37.15, H 3.41, N 10.74.

FT-IR (cm^{-1}): 3518 (w), 3028 (w), 2936 (w), 1589 (s), 1552 (s), 1489 (w), 1470 (m), 1412 (m), 1372 (s), 1282 (w), 1254 (w), 1227 (w), 1150 (w), 1087 (s), 1043 (s), 1025 (s), 1014 (s), 959 (m), 938 (m), 909 (s), 876 (m), 844 (m), 775 (s), 761 (m), 712 (m), 692 (m), 658 (m).

2.4.2.9 Synthesis of $\{[Cu(II)_5(L_2)_4(pz)_2(MeOH)](ClO_4)_2{\cdot}3MeOH\}_n$ (6)

$Cu(ClO_4)_2{\cdot}6H_2O$ (0.1 g, 0.27 mmol), L_2H_2 (0.041 g, 0.27 mmol), NaOH (0.011 g, 0.27 mmol) and pyrazine (0.022 g, 0.27 mmol) were dissolved in MeOH (20 cm^3) and stirred for 2 h. The resultant dark green solution was filtered and allowed to stand. Slow evaporation of the mother liquor resulted in the formation of X-ray quality crystals of **6** with a yield of approximately 12%.

C, H, N Elemental Analysis

Calculated % as $\{[Cu(II)_5(L_2)_4(py)_2](ClO_4)_2{\cdot}4H_2O\}_n$ ($C_{36}H_{40}N_{12}O_{20}Cl_2Cu_5$): C 32.04, H 2.99, N 12.46.

Found %: C 31.86, H 2.59, N 12.34.

FT-IR (cm^{-1}): 3209 (w), 1597 (m), 1563 (m), 1542 (s), 1495 (m), 1417 (m), 1381 (s), 1307 (w), 1288 (w), 1088 (s), 1030 (s), 949 (s), 871 (w), 825 (w), 783 (m), 771 (m), 747 (s), 696 (w), 681 (m).

UV/vis (MeOH): λ_{max} [nm] (ε_{max} 10^3 dm^3 mol^{-1} cm^{-1}): 222 (73.3), 260 (73.1), 360 (sh).

2.4.2.10 Synthesis of $[Cu(II)_5(L_2)_4(MeOH)_4](ClO_4)_2{\cdot}H_2O$ (7)

L_2H_2 (0.102 g, 0.68 mmol) and NaOH (0.027 g, 0.68 mmol) were dissolved in a methanolic solution of $Cu(ClO_4)_2{\cdot}6H_2O$ (0.25 g, 0.68 mmol, 30 cm^3). The solution was then left to stir for 3 h at ambient temperature and the resultant dark green solution was filtered. X-ray quality crystals of **7** formed upon slow evaporation of the mother liquor with a yield of approximately 10%.

C, H, N Elemental Analysis

Calculated % as $[Cu(II)_5(L_2)_4(MeOH)](ClO_4)_2{\cdot}H_2O$ ($C_{29}H_{30}N_8O_{18}Cl_2Cu_5$): C 29.84, H 2.59, N 9.60.

Found % C 29.39, H 2.28, N 9.61.

FT-IR (cm^{-1}): 3422 (b), 3299 (w), 3229 (m), 2160 (w), 1980 (w), 1611 (w), 1596 (m), 1566 (s), 1536 (s), 1496 (m), 1445 (w), 1389 (m), 1372 (m), 1314 (w), 1292 (w), 1067 (s), 960 (m), 925 (m), 825 (w), 777 (s), 747 (s), 709 (w), 683 (m).

UV-vis (MeOH): λ_{max} [nm] (ε_{max} 10^3 dm^3 mol^{-1} cm^{-1}): 220 (67.5), 265 (61.3), 375 (sh).

2.5 Bibliography

1. H. Lossen, *Justus Liebigs Ann. Chem.*, 1869, 150, 314-322.
2. D. Griffith, M. Devocelle and C. J. Marmion, in *Hydroxamic Acids: Chemistry, Bioactivity, and Solution and Solid-Phase Synthesis in Amino Acids, Peptides and Proteins in Organic Chemistry*, Wiley-VCH Verlag GmbH & Co. KGaA, A. B. Hughes edn., 2009, vol. 2, pp. 93-144.
3. D. A. Brown, W. K. Glass, R. Mageswaran and B. Girmay, *Magn. Reson. Chem.*, 1988, 26, 970-973.
4. B. Chatterjee, *Coord. Chem. Rev.*, 1978, 26, 281-303.
5. E. Farkas, É. A. Enyedy, G. Micera and E. Garribba, *Polyhedron*, 2000, 19, 1727-1736.
6. D. Gaynor, Z. A. Starikova, S. Ostrovsky, W. Haase and K. B. Nolan, *Chem. Commun.*, 2002, 506-507.
7. P. V. Bernhardt, *Dalton Trans.*, 2007, 3214-3220.
8. Z. Amtul, Atta, R. A. Siddiqui and M. I. Choudhary, *Curr. Med. Chem.*, 2002, 9, 1323-1348.
9. D. T. Puerta and S. M. Cohen, *Curr. Top. Med. Chem.*, 2004, 4, 1551-1573.
10. M. Paris, M. Porcelloni, M. Binaschi and D. Fattori, *J. Med. Chem.*, 2008, 51, 1505-1529.
11. J. Lee, A. J. Chubb, E. Moman, B. M. McLoughlin, C. T. Sharkey, J. G. Kelly, K. B. Nolan, M. Devocelle and D. J. Fitzgerald, *Org. Biomol. Chem.*, 2005, 3, 3678-3685.
12. C. J. Marmion, D. Griffith and K. B. Nolan, *Eur. J. Inorg. Chem.*, 2004, 2004, 3003-3016.
13. E. M. F. Muri, M. J. Nieto, R. D. Sindelar and J. S. Williamson, *Curr. Med. Chem.*, 2002, 9, 1631-1653.
14. R. Codd, *Coord. Chem. Rev.*, 2008, 252, 1387-1408.
15. B. K. Tait, K. E. Mdlalose and I. Taljaard, *Hydrometallurgy*, 1995, 38, 1-6.
16. A. M. Wilson, P. J. Bailey, P. A. Tasker, J. R. Turkington, R. A. Grant and J. B. Love, *Chem. Soc. Rev.*, 2014, 43, 123-134.
17. D. Gaynor, Z. A. Starikova, W. Haase and K. B. Nolan, *J. Chem. Soc., Dalton Trans.*, 2001, 1578-1581.
18. G. Mezei, C. M. Zaleski and V. L. Pecoraro, *Chem. Rev.*, 2007, 107, 4933-5003.
19. M. S. Lah and V. L. Pecoraro, *J. Am. Chem. Soc.*, 1989, 111, 7258-7259.
20. J. Jankolovits, C. M. Andolina, J. W. Kampf, K. N. Raymond and V. L. Pecoraro, *Angew. Chem. Int. Ed.*, 2011, 50, 9660-9664.
21. I. A. Golenya, E. Gumienna-Kontecka, A. N. Boyko, M. Haukka and I. O. Fritsky, *Inorg. Chem.*, 2012, 51, 6221-6227.
22. R. H. Fish, *Coord. Chem. Rev.*, 1999, 185–186, 569-584.
23. G. A. Ardizzoia, S. Cenini, G. La Monica, N. Masciocchi and M. Moret, *Inorg. Chem.*, 1994, 33, 1458-1463.
24. A. Maspero, S. Brenna, S. Galli and A. Penoni, *J. Organomet. Chem.*, 2003, 672, 123-129.
25. A. V. Pavlishchuk, S. V. Kolotilov, M. Zeller, L. K. Thompson, I. O. Fritsky, A. W. Addison and A. D. Hunter, *Eur. J. Inorg. Chem.*, 2010, 2010, 4851-4858.
26. A. V. Pavlishchuk, S. V. Kolotilov, M. Zeller, O. V. Shvets, I. O. Fritsky, S. E. Lofland, A. W. Addison and A. D. Hunter, *Eur. J. Inorg. Chem.*, 2011, 2011, 4826-4836.
27. S. Osa, T. Kido, N. Matsumoto, N. Re, A. Pochaba and J. Mrozinski, *J. Am. Chem. Soc.*, 2003, 126, 420-421.
28. R. W. Saalfrank, A. Scheurer, I. Bernt, F. W. Heinemann, A. V. Postnikov, V. Schunemann, A. X. Trautwein, M. S. Alam, H. Rupp and P. Muller, *Dalton Trans.*, 2006, 2865-2874.

29. T. T. Boron, J. W. Kampf and V. L. Pecoraro, *Inorg. Chem.*, 2010, 49, 9104-9106.
30. A. W. Addison, T. N. Rao, J. Reedijk, J. van Rijn and G. C. Verschoor, *J. Chem. Soc., Dalton Trans.*, 1984, 1349-1356.
31. S. H. Seda, J. Janczak and J. Lisowski, *Inorg. Chim. Acta*, 2006, 359, 1055-1063.
32. J. J. Bodwin and V. L. Pecoraro, *Inorg. Chem.*, 2000, 39, 3434-3435.
33. A. B. Lago, J. Pasan, L. Canadillas-Delgado, O. Fabelo, F. J. M. Casado, M. Julve, F. Lloret and C. Ruiz-Perez, *New J. Chem.*, 2011, 35, 1817-1822.
34. M. Moon, I. Kim and M. S. Lah, *Inorg. Chem.*, 2000, 39, 2710-2711.
35. R. Wang, M. Hong, J. Luo, R. Cao and J. Weng, *Chem. Commun.*, 2003, 1018-1019.
36. D. H. Williams and I. Fleming, *Spectroscopic Methods in Organic Chemistry*, 5th edition edn., 1995.
37. D. A. Brown and A. L. Roche, *Inorg. Chem.*, 1983, 22, 2199-2202.
38. B. R. Gibney, D. P. Kessissoglou, J. W. Kampf and V. L. Pecoraro, *Inorg. Chem.*, 1994, 33, 4840-4849.
39. M. Careri, F. Dallavalle, M. Tegoni and I. Zagnoni, *J. Inorg. Biochem.*, 2003, 93, 174-180.
40. D. Bacco, V. Bertolasi, F. Dallavalle, L. Galliera, N. Marchetti, L. Marchio, M. Remelli and M. Tegoni, *Dalton Trans.*, 2011, 40, 2491-2501.
41. P. Pascal, *Ann. Chim. Phys.* , 1910, 19, 5.
42. G. M. Sheldrick, *Acta Crystallogr. Sect. A: Found. Crystallogr.*, 1990, 46, 467-473.
43. G. M. Sheldrick, *SHELXL-97, A computer program for crystal structure determination*, 1997.
44. P. McArdle, P. Daly and D. Cunningham, *J. Appl. Crystallogr.*, 2002, 35, 378.

Chapter Three

Just Add Water: High Nuclearity Ni(II) Cages Using Hydroxamate Ligands and Their Myriad Bonding Modes

3.1 Introduction

The previous chapter described the synthesis of a family of 12-MC$_{Cu(II)}$-4 metallacrowns[1] via the incorporation of a hydroxamic acid ligand 2-(dimethylamino)phenylhydroxamic acid (L_1H_2) or 2-(amino)phenylhydroxamic acid (L_2H_2). All members of the family maintain the $\{Cu(II)_5(L_x)_4\}^{2+}$ (x = 1, 2) core and through carefully controlled ligand substitution and / or addition the core undergoes the progressive formation of 1-2D extended networks consisting of [Cu_5] nodes.[2] This success inspired us to attempt to utilise the same synthetic approach towards an analogous family of Ni(II) 12-MC$_{Ni(II)}$-4 metallacrowns. Using this procedure we planned to increase the coordination number of Ni(II) ions, sequentially altering their geometries and allowing us to magnetically 'switch on' diamagnetic square planar Ni(II) centres within analogous [Ni_5] metallacrowns.

We herein present the synthesis, structural and magnetic characterisation of the two 12-MC$_{Ni(II)}$-4 metallacrowns: $[Ni(II)_5(L_1)_4(MeOH)_4](ClO_4)_2\cdot 2MeOH$ (**8**) and $[Ni(II)_5(L_1)_4(pyr)_5](ClO_4)_2\cdot 1H_2O$ (**9**) (where L_1^{2-} = 2-(dimethylamino)phenylhydroxamic acid). Even though both complexes share a $\{Ni(II)_5(L_1)_4\}^{2+}$ core, their siblings differ in the number and nature of the ligands located at their Ni(II) axial sites. The addition of pyridine ligands converts previous square planar Ni(II) centres to square-based pyramidal/octahedral geometries, hence introducing more paramagnetic centres and therefore producing variation in terms of their magnetic behaviour. Furthermore, simple alterations in the synthetic schemes (change in solvent, base, metal salt and ligand) for **8** and **9** results in the hepta- and nonanuclear complexes $[Ni(II)_7(L_1H)_8(L_1)_2(H_2O)_6](SO_4)\cdot 15H_2O$ (**10**), $[Ni(II)_9(\mu\text{-}H_2O)_2(L_2)_6(L_2H)_4(H_2O)_2](SO_4)\cdot 29H_2O$ (**11**) and $[Ni(II)_9(\mu\text{-}H_2O)_2(L_2)_6(L_2H)_4(H_2O)_2](ClO_4)_2\cdot 2MeOH\cdot 18H_2O$ (**12**) (where L_2^{2-} = 2-(amino)phenylhydroxamic acid). Complementary dc magnetic susceptibility studies and DFT analysis indicate dominant antiferromagnetic exchange interactions in **8** and **9**. Magnetic susceptibility measurements carried out on **11** and **12** also revealed dominant antiferromagnetic behaviour. However, complex **10** displayed competing ferro- and antiferromagnetic exchange pathways.

3.2 Results and Discussions

3.2.1 Structural Descriptions

3.2.1.1 The Importance of Solvent Ligands Towards Coordination Geometry and Structural Variation in Pentanuclear 12-MC$_{Ni(II)}$-4 Metallacrowns

The 12-MC$_{Ni(II)}$-4 pentanuclear metallacrown $[Ni(II)_5(L_1)_4(MeOH)_4](ClO_4)_2\cdot 2MeOH$ (**8**) was the first complex to be synthesised in this work via the reaction of $Ni(ClO_4)_2\cdot 6H_2O$, 2-(dimethylamino)phenylhydroxamic acid (L_1H_2) (Figure 51 Section 2.1) and NaOH in methanol. Upon slow evaporation of the filtered green mother liquor, green X-ray quality crystals of **8** were formed in approximately 14% yield. Complex **8** crystallises in the triclinic *P*-1 space group with unit cell parameters: a = 11.191(2) Å, b = 12.389(3) Å, c = 12.401(3) Å, α = 70.12(3)°, β = 63.48(3)°, γ = 64.17(3)° (Figure 77). Complete single crystal X-ray diffraction data for **8** is given in Table 3 (Section 3.2.1.3).

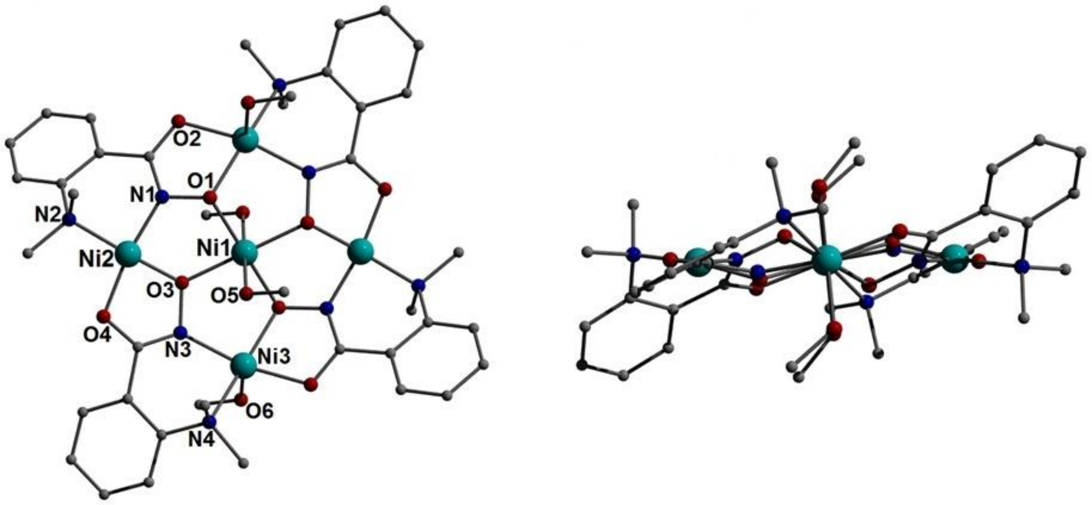

***Figure 77** - Crystal structure of **8** as viewed perpendicular (left) and parallel (right) to the [Ni$_5$] plane. Colour code: light blue (Ni), red (O), dark blue (N), grey (C). The perchlorate counter anions and hydrogen atoms have been omitted for clarity.*

Complex **8** comprises a near planar $\{Ni(II)_5(L_1)_4\}^{2+}$ core, whereby a central Ni(II) ion (labelled Ni1) exhibits distorted octahedral geometry and is surrounded by an outer ring of four other Ni(II) ions (labelled Ni2, Ni3 and their symmetric equivalents (s.e.)). These Ni(II) centres assemble into a 12-MC$_{Ni(II)}$-4 metallacrown topology via the four doubly deprotonated L_1^{2-} ligands each utilising an $\eta^1:\eta^1:\eta^2:\eta^1\text{-}\mu_3$ bonding motif (Figure 78). The central Ni(II) ion is stabilised by four Ni-O bonds, created by the four L_1^{2-} ligands with bond lengths of 1.997(19) Å (Ni1-O1) and 1.964(18) Å (Ni1-O3). The distorted octahedral geometry of Ni1 is completed at the axial positions via two terminal methanol ligands (Ni1-O5 = 2.153(19) Å). Each of the peripheral Ni(II) ions are bridged at their equatorial positions via Ni-O and Ni-N bonds and are established by the L_1^{2-} ligands with bond lengths ranging from 1.826(19) to 2.139(2) Å. Coordination at two of the outer Ni(II) ions (Ni3 and s.e.) are completed at the axial positions via methanol solvent molecules (Ni3-O6 = 2.036(2) Å) and thus display square-based pyramidal geometries (τ = 0.08).[3] The remaining peripheral Ni(II) ions (Ni2 and s.e.) are not axially coordinated and instead exhibit square planar geometry.

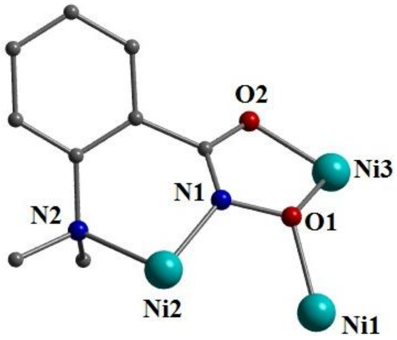

Figure 78 *- The $\eta^1:\eta^1:\eta^2:\eta^1$-$\mu_3$ coordination motif exhibited by L_1^{2-} in relation to the Ni(II) metal centres in* ***8****.*

The $\{Ni(II)_5(L_1)_4(MeOH)_4\}^{2+}$ cations are charge balanced by two perchlorate counter anions, sitting above and below the [Ni_5] plane at a distance of approximately 3.91 Å. The ClO_4^- anions in **8** partake in inter-molecular hydrogen bonding via their oxygen atoms with *1)* aromatic hydroxamate protons (C12(H12)···O8 = 2.506 Å), *2)* aliphatic hydroxamate protons (C18(H18A)···O9 = 2.768 Å) and *3)* terminal MeOH ligands (O5(H5H)···O10 = 2.445 Å). Indeed, hydrogen bonding is also observed between terminal MeOH ligands and MeOH solvents of crystallisation (O6(H6H)···O11 = 2.23 Å). The [Ni_5] units in **8** pack along the *a* cell direction in superimposable columns and these individual stacks then partake in $\pi_{centroid}\cdots\pi_{centroid}$ stacking interactions via adjacent hydroxamate aromatic rings ([C2-C7]···[C2'-C7'] = 3.897 Å) (Figure 79).

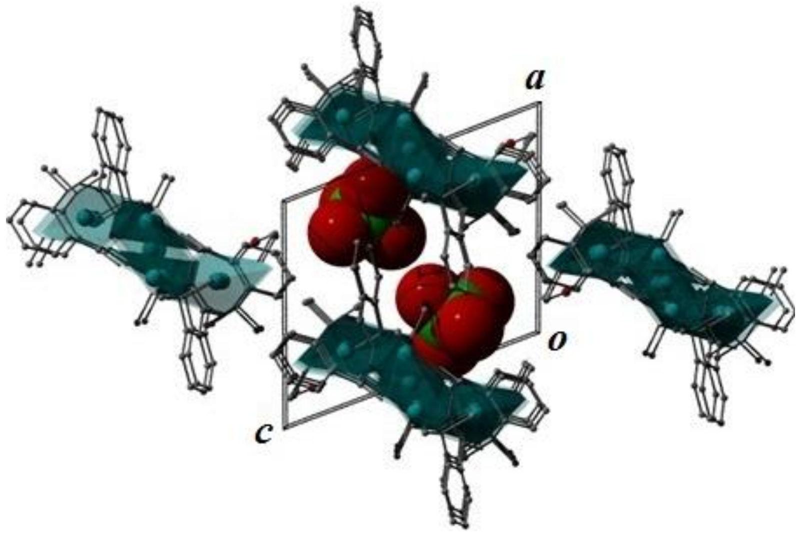

Figure 79 *- Packing arrangement of* ***8*** *as viewed down the b-axis of the unit cell.* ClO_4^- *counter anions are space-fill represented and hydrogen atoms have been removed for clarity. Colour scheme as in Figure 77 and used throughout this chapter.*

The simple addition of pyridine to the synthetic procedure for **8** yielded the analogous 12-$MC_{Ni(II)}$-4 metallacrown $[Ni(II)_5(L_1)_4(pyr)_5](ClO_4)_2 \cdot 1H_2O$ (**9**) (Figure 80). Complex **9** crystallises in the monoclinic $P2_1/n$ space group with unit cell parameters: a = 14.6573(4) Å, b = 15.1811(4) Å, c = 29.7812(11) Å, α = 90°, β = 93.552(3)°, γ = 90°. Complete X-ray crystal diffraction can be seen in Table 3 (Section 3.2.1.3). It must be noted that variation of the amount of pyridine added did not affect the isolated product, or the number of coordinated pyridines ligands found in our complex.

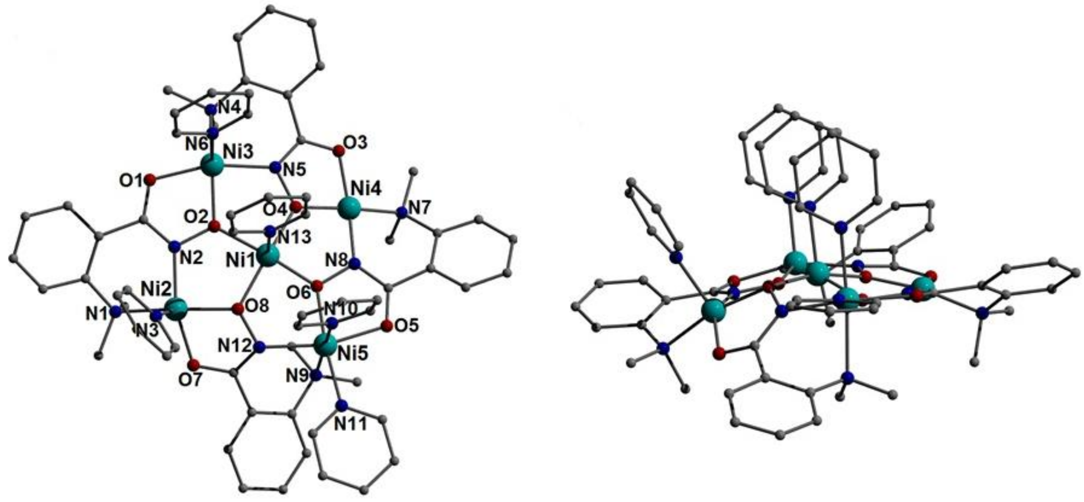

Figure 80 *- Crystal structure of* ***9*** *as viewed perpendicular (left) and parallel (right) to the* $[Ni_5]$ *plane. Hydrogen atoms and* ClO_4^- *counter anions have been omitted for clarity.*

Complex **9** consists of a $\{Ni(II)_5(L_1)_4\}^{2+}$ core as in **8**, where the doubly deprotonated L_1^{2-} ligands exhibit the $\eta^1:\eta^1:\eta^2:\eta^1$-$\mu_3$ coordination mode. As in **8**, the central Ni(II) ion is labelled Ni1; however the peripheral Ni(II) ions are labelled Ni2-Ni5. The addition of pyridine results in many structural differences with respect to the Ni(II) centres in **9**. Firstly, Ni1 now exhibits a distorted square-based pyramidal geometry ($\tau = 0.34$)[3] with a pyridine ligand at the axial position (Ni1-N13 = 2.012(4) Å), replacing the MeOH ligands in **8**. In addition, Ni2 and Ni3 display distorted square-based pyramidal geometries ($\tau = 0.34$ and 0.15 respectively)[3] and their coordination spheres are completed by axially bound pyridine ligands (Ni2-N3 = 2.029(4) Å and Ni3-N6 = 2.036(4) Å). Ni4 is the only peripheral metal centre to remain square planar in configuration, suggesting that it will be the only diamagnetic centre in **9**. The outer Ni5 ion possesses six coordinate geometry, exhibiting bound pyridine ligands at both the axial and equatorial positions (Ni5-N10 = 2.136(4) Å and Ni5-N11 = 2.091(4) Å respectively). As a consequence of the additional pyridine coordinated at the equatorial position, significant distortion of the L_1^{2-} ligand coordinated to Ni5 (via the nitrogen atoms N9 and N12) arises. As it distorts away from the $[Ni_5]$ plane, it is forced to occupy the axial position of the Ni5 metal centres via its $-NMe_2$ group (Ni5-N9 = 2.283(4) Å) (Figure 80). The axial pyridines bound to Ni1, Ni3 and Ni5 are approximately aligned when viewed along the plane of the molecule, promoting $\pi_{centroid}\cdots\pi_{centroid}$ interactions with typical bond distances of 3.674 Å ([C52-N10]···[C50-N13]) and 3.651 Å ([C50-N13]···[C42-N6]) (Figure 80-right). Upon close inspection of **8** and **9**, it becomes clear that the pyridine ligands encourage puckering of the plane in **9** in comparison to the almost planar $[Ni_5]$ core in **8** (Figure 77-right *cf.* Figure 80-right). Unlike complex **8**, the $\{Ni(II)_5(L_1)_4(pyr)_5\}^{2+}$ cationic cores in **9** are charge balanced by two ClO_4^- counter anions located at the periphery of the structure, this contrast is presumably due to the presence of the pyridine ligands, forcing the perchlorate anions towards the edge of the structure. Subsequently, the ClO_4^- counter anions primarily hydrogen bond with the aromatic hydroxamate protons (e.g. C25(H25)···O13 = 2.584 Å, C40(H40)···O16 = 2.590 Å, C43(H43)···O14 = 2.585 Å). The individual pentametallic cages align themselves into 2D brickwork sheets along the *ab* cell diagonal and these sheets then lie in superimposable rows down the *c* axis (Figure 81).

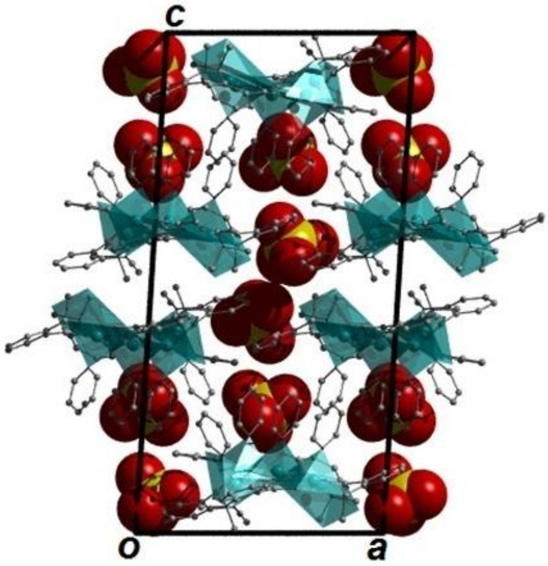

Figure 81 *- Crystal packing in complex* ***9*** *as viewed down the b axis of the unit cell. Perchlorate counter anions are represented in space-fill mode and hydrogen atoms have been removed for clarity.*

It should be noted that despite our numerous attempts we were unable to synthesise analogous 12-$MC_{Ni(II)}$-4 metallacrowns using the ligand 2-(amino)phenylhydroxamic acid (L_2H_2). The production of **8** and **9** adds to the relatively small amount of 12-$MC_{Ni(II)}$-4 metallacrowns known in the literature[4-7] and are the first to be formed utilising 2-(dimethylamino)phenylhydroxamic acid (L_1H_2). In addition, the 12-$MC_{Ni(II)}$-4 general framework is utilised as a building block in the conformation of the elaborate and quite unusually fused metallacrown dimer $Ni(II)_2(mcpa)_2(CH_3OH)_3(H_2O)[12\text{-}MC_{Ni(II)N(shi)2(pko)2}\text{-}4][12\text{-}MC_{Ni(II)N(shi)3(pko)}\text{-}4]$ (where Hmpca = 2-methyl-4-chlorophenoyacetic acid, Hpko = di-(2-pyridyl)ketone oxime and H_3shi = salicylhydroxamic acid).[8]

3.2.1.2 Structural Rearrangements Towards Larger Ni(II) Cage Topologies

As previously reported by our collaborators, the heptanuclear complex $[Ni(II)_7(L_1H)_8(L_1)_2(H_2O)_6](SO_4)\cdot 15H_2O$ (**10**) was synthesised via the reaction of $Ni(SO_4)\cdot 6H_2O$, L_1H_2 and NaOH in a MeOH/H_2O solvent mix.[9] The structural conformation of complex **10** diverts away from the metallacrown formation seen in **8** and **9**, displaying a trigonal bipyramidal (or two face-sharing tetrahedra) arrangement of Ni(II) ions labelled Ni2-Ni6, with two additional Ni(II) metal centres at the axial sites (Figure 82). Complex **10** crystallises in the orthorhombic $P2_12_12_1$ space group with unit cell parameters: a = 16.398(9) Å, b = 23.996(14) Å, c = 30.666(12) Å, α =

90°, β = 90°, γ = 90°. Complete single crystal X-ray diffraction data collected by D. Gaynor et al can be seen in Table 3 (Section 3.2.1.3).[9]

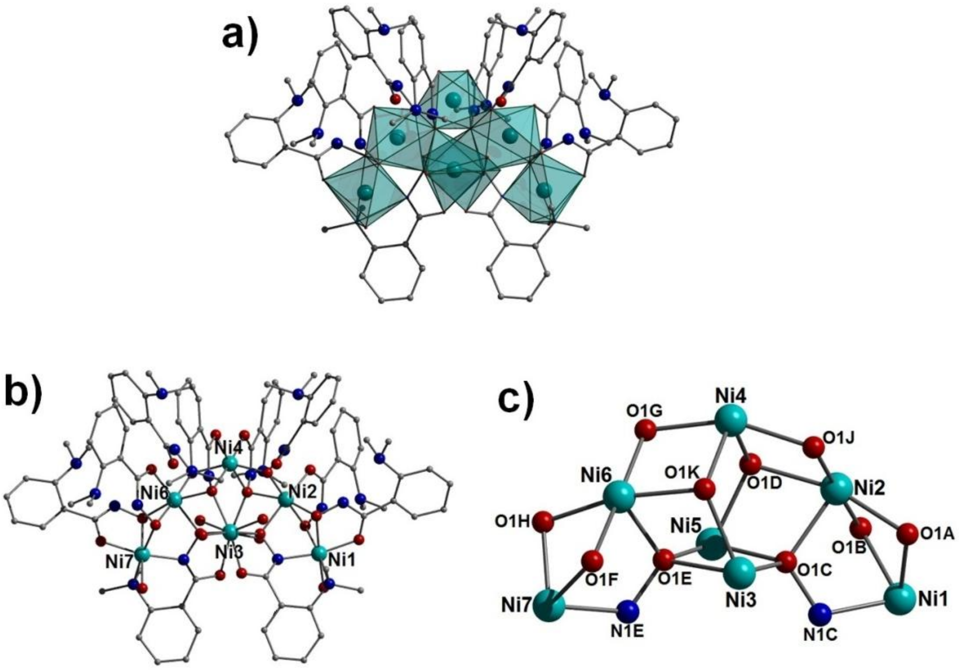

Figure 82 *- (a) Polyhedral and (b) regular representation of the crystal structure of **10**. (c) Schematic of the metallic core in **10**. Sulphate counter anions and hydrogen atoms have been omitted for clarity.*

All Ni(II) centres demonstrate distorted octahedral geometries, linked via hydroxamate (L_1^{2-}) ligands utilising four different types of coordination motifs (η^2-μ, η^1:η^3-μ_3, η^1:η^2-μ and η^1:η^3:η^1:η^1-μ_4) (Figure 83). For further structural description for **10** please refer to reference 9.

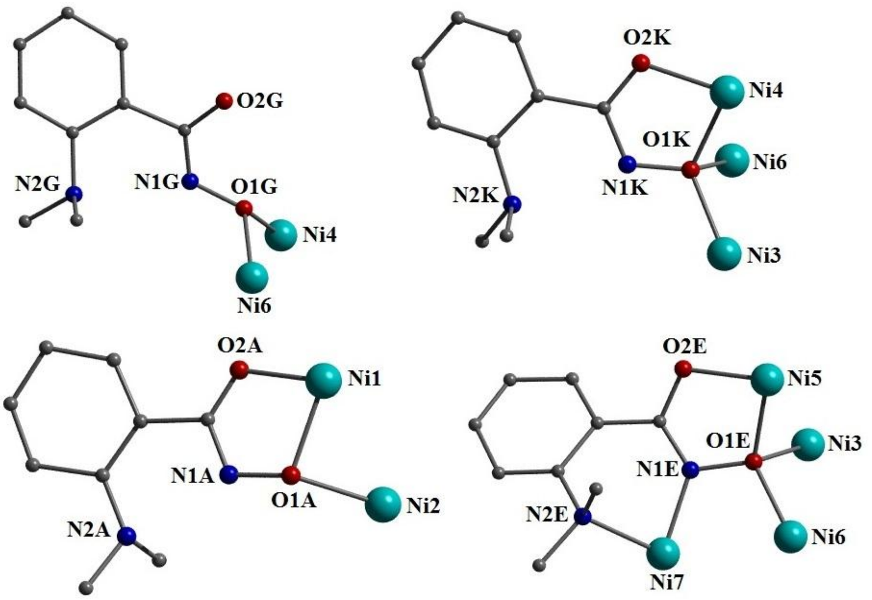

Figure 83 *- Schematic of the various bonding modes displayed by the hydroxamate ligands in complex **10**. (Top right) η^2-μ, (top left) η^1:η^3-μ_3, (bottom right) η^1:η^2-μ and (bottom left) η^1:η^3:η^1:η^1-μ_4.*

The deviation in the topology of complex **10** away from the metallacrown conformation piqued our interest and we decided to further investigate the systematic variation of reaction conditions (i.e. solvent system, metal salts, ligand type etc.). For instance, the reaction of $NiSO_4{\cdot}6H_2O$, L_2H_2 and $NEt_4(OH)$ in a MeOH/H_2O solution yielded the nonanuclear Ni(II) cage $[Ni(II)_9(\mu\text{-}H_2O)_2(L_2)_6(L_2H)_4(H_2O)_2](SO_4){\cdot}29H_2O$ (**11**). Furthermore, the perchlorate analogue $[Ni(II)_9(\mu\text{-}H_2O)_2(L_2)_6(L_2H)_4(H_2O)_2](ClO_4)_2{\cdot}2MeOH{\cdot}18H_2O$ (**12**) was readily formed using $Ni(ClO_4)_2{\cdot}6H_2O$ as the metal ion source. Complex **11** crystallises in the orthorhombic *Ima*2 space group with unit cell parameters: a = 29.1847(11) Å, b = 21.2385(7) Å, c = 19.7536(6) Å, α = 90°, β = 90°, γ = 90°. Complex **12** crystallises in the monoclinic *Cc* space group with unit cell parameters: a = 20.0036(7) Å, b = 25.0628(9) Å, c = 21.2234(5) Å, α = 90°, β = 90.320(2)°, γ = 90°. Complete X-ray crystal diffraction data for **11** and **12** are given in Table 4 (Section 3.2.1.3). The cores of both complexes can be described as comprising two tetrahedral arrays of distorted octahedral Ni(II) metal ions connected via a single, central, six coordinate Ni(II) centre (labelled Ni5 in both complexes) (Figures 84 and 85). The Ni(II) ions are bridged via a combination of four singly (L_2H^-) and six doubly (L_2^{2-}) deprotonated hydroxamate ligands, displaying η^1:η^2-μ and η^1:η^3:η^1:η^1-μ_4 coordination modes respectively (as seen previously in complex **10**) (Figure 83). In both circumstances the Ni5 centres connect to the two tetrahedral moieties via two μ-bridging H_2O ligands (Ni5-O12 = 2.150(6)

Å in **11** and Ni5-O10 = 2.204(8) Å, Ni5-O23 = 2.204(8) Å in **12**). In addition, terminal water solvents complete the coordination at two of the peripheral Ni(II) centres with bond lengths of 2.023(6) Å (Ni3-O11) in **11**; 2.041(8) Å (Ni9-O17) and 2.052(8) Å (Ni1-O3) in **12**. The $\{Ni(II)_9(\mu\text{-}H_2O)_2(L_2)_6(L_2H)_4(H_2O)_2\}^{2+}$ cationic moieties are charge balanced by one SO_4^{2-} in **11** and two ClO_4^{-} counter anions in **12**. Furthermore, twenty nine H_2O solvents of crystallisations were calculated to be present within the porous channels in **11** (see section 3.4.1.1 for details), while eighteen H_2O and two MeOH solvents of crystallisation are present in **12**.

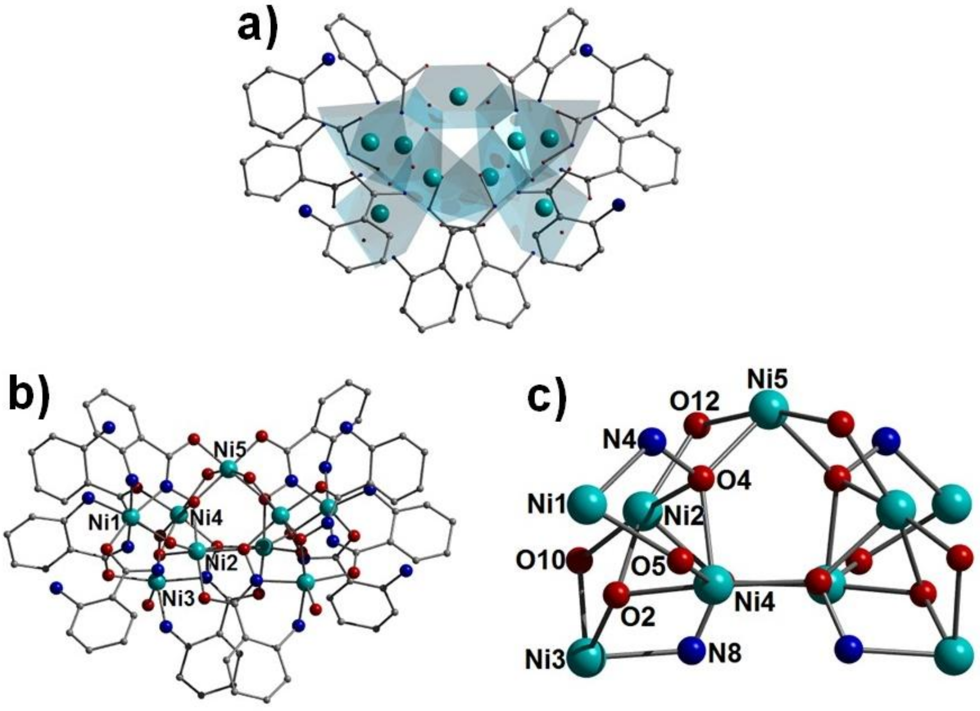

Figure 84 - *(a) Polyhedral and (b) regular representation of the crystal structure of* ***11****. (c) Schematic of the metallic core in* ***11****. Sulphate counter anions and hydrogen atoms have been omitted for clarity.*

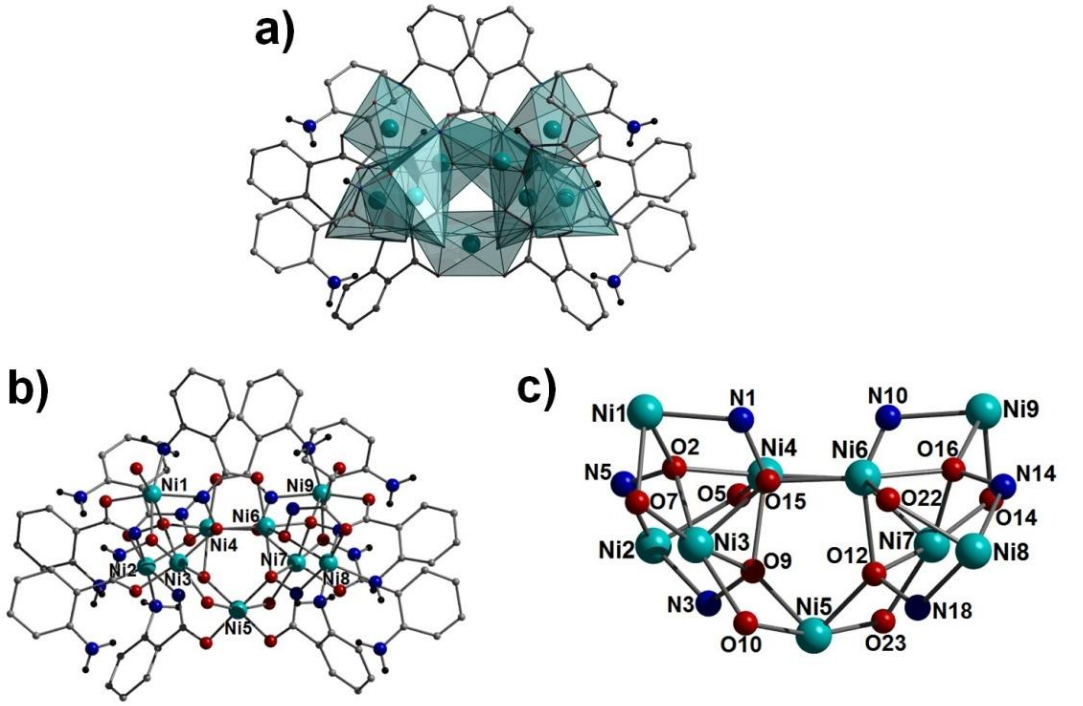

***Figure 85** - (a) Polyhedral and (b) regular representation of the crystal structure of **12**. (c) Schematic of the metallic core in **12**. The majority of hydrogen atoms have been removed for clarity except for the -NH_2 protons which have been represented by black spheres. The ClO_4^- counter anions have been omitted for clarity.*

The individual [Ni_9] units in **11** organize into a common brickwork conformation as viewed down the *a* axis, and are linked together via $\pi_{centroid}\cdots\pi_{centroid}$ interactions of neighbouring [Ni_9] hydroxamate aromatic rings ([C8-C13]$\cdots$[C15-C20] = 3.605 Å). In addition, linkage is further enhanced by hydrogen bonding interactions via sulphate counter anions and aliphatic hydroxamate protons (e.g. N10(H10A)$\cdots$O13 = 2.104 Å). Sequentially, these sheet-like motifs form superimposable rows along the *a* cell direction completing the 3D connectivity of the crystal in **11** (Figure 86). Complex **12** exhibits hydrogen bonding interactions between H_2O solvents of crystallisation and *1)* aliphatic hydroxamate protons (e.g. -NH_2 group N17(H17B)$\cdots$O28 = 2.386 Å) and =NH groups N12(H12A)$\cdots$O37 = 2.005 Å), *2)* μ-bridging H_2O ligands (e.g. O23(H23A)$\cdots$O34 = 1.725 Å), *3)* MeOH solvents of crystallisation (e.g. O61(H61A)$\cdots$O42 = 2.202 Å), *4)* aromatic hydroxamate protons (e.g. C66(H66)$\cdots$O36 = 2.446 Å) and *5)* perchlorate counter anions (e.g. Cl2(O56)$\cdots$O43 = 2.425 Å). As in **11** the [Ni_9] cages in **12** also align themselves into a brickwork topology along the *ac* plane of the unit cell, partaking in $\pi_{centroid}\cdots\pi_{centroid}$ stacking interactions between adjacent hydroxamate aromatic rings of neighbouring [Ni_9] units (e.g. [C9-C14]$\cdots$[C58-C63] = 3.538 Å and [C37-C42]$\cdots$[C65-C70] = 3.575 Å). These sheet-like conformations stack into staggered arrangements as opposed to the superimposable rows observed in **11** (Figure 87).

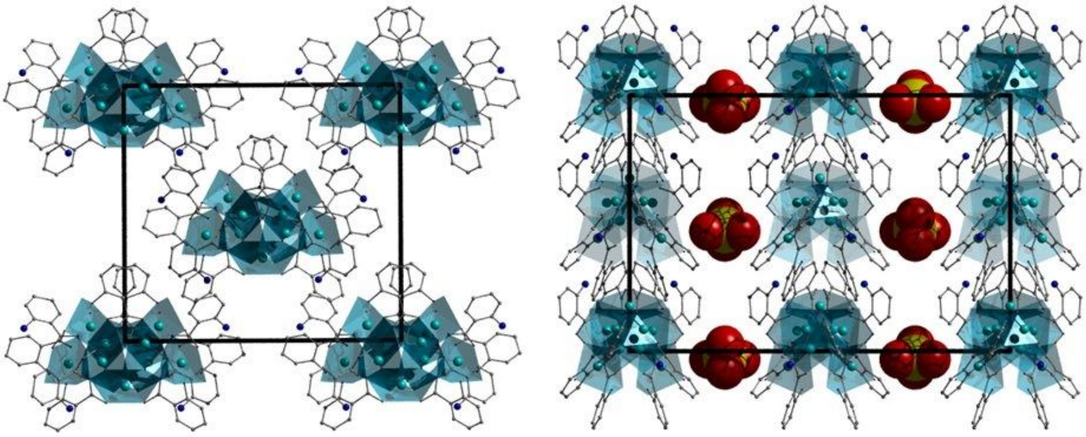

Figure 86 *- Crystal packing arrangement observed in* ***11*** *as viewed along the a cell direction (left) and b cell direction (right). Hydrogen atoms and solvents of crystallisation have been removed for clarity. The* SO_4^{2} *counter anions are in space-fill mode in the figure on the right and omitted for clarity on the left.*

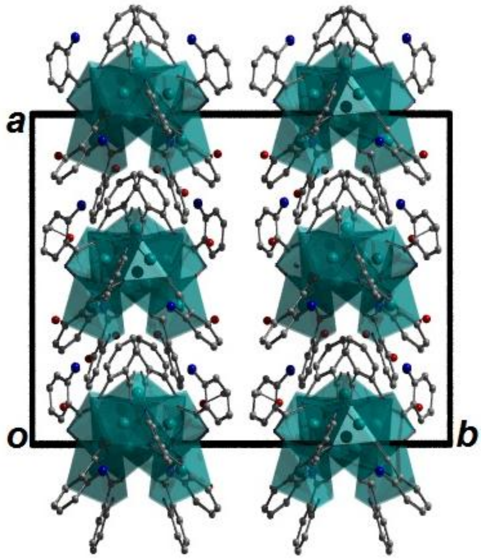

Figure 87 *- Packing orientation observed in* ***12*** *as viewed down the c axis of the unit cell. Hydrogen atoms, perchlorate counter anions and waters of crystallisation have been removed for clarity.*

It is somewhat difficult to rationalise the change in structure from **8** and **9** (Ni_5) to **10** (Ni_7), since the reactions involve the use of a different metal salt (perchlorate versus sulphate) and a different solvent system (MeOH versus MeOH/H_2O). The difference in reaction schemes between [Ni_5] and [Ni_9] involve a change in ligand (L_1H_2 to L_2H_2), base (NaOH to NEt_4OH) and solvent (MeOH to MeOH/H_2O), while the difference in the reaction that produces [Ni_7] versus [Ni_9] is a change in ligand (L_1H_2

to L_2H_2) and base (NaOH to NEt_4OH). Elucidating the roles of each reaction variable would therefore require a larger library of complexes to be isolated, and we are currently working to that end. However, we can say that the role of ligand selection (i.e. L_1^{2-} in **10** versus L_2^{2-} in **11**) and more specifically the steric effects of functional groups (Me groups in L_1^{2-} versus H groups in L_2^{2-}) appears to be significant in terms of structure-directing influences, leading to the production of complex **11** over **10**.

3.2.1.3 Crystallographic Data of Complexes 8-12

Table 3 *- Crystallographic data for complexes* ***8-10****.*

Complex	**8**·2MeOH	**9**·1H_2O	**10**·15H_2O*
Formula[a]	$C_{42}H_{64}N_8O_{22}Cl_2Ni_5$	$C_{61}H_{67}N_{13}O_{17}Cl_2Ni_5$	$C_{90}H_{150}N_{20}O_{45}SNi_7$
M_W	1397.46	1618.71	2675.33
Crystal Appearance	Green Parallelepiped	Green Parallelepiped	Green Prism
Crystal System	Triclinic	Monoclinic	Orthorhombic
Space group	*P*-1	$P2_1/n$	$P2_12_12_1$
a/Å	11.191(2)	14.6573(4)	16.398(9)
b/Å	12.389(3)	15.1811(4)	23.996(14)
c/Å	12.401(3)	29.7812(11)	30.666(12)
α/°	70.12(3)	90.00	90.00
β/°	63.48(3)	93.552(3)	90.00
γ/°	64.17(3)	90.00	90.00
V/Å^3	1362.0(7)	6614.0(4)	12067(10)
Z	1	4	4
T/K	150.1(1)	150(2)	110(2)
λ^b/Å	0.71073	0.7107	0.71073
D_c/g cm^{-3}	1.704	1.624	1.473
μ(Mo-Ka)/ mm^{-1}	1.880	1.558	1.177
Collected/Unique, (R_{int}) refl.	8896/4974, (0.0158)	52717/12096, (0.0785)	41850/20598, (0.1354)
wR2 (all data)	0.0758	0.1139	0.1158
$R1^{d,e}$	0.0308	0.0482	0.0601
Goodness of fit (GOOF) on F^2	1.024	1.023	0.644
Flack parameter	n/a	n/a	0.059(15)

[a] Includes guest molecules. [b] Mo-Kα radiation, graphite monochromator. [c] $wR2 = [\sum w(|F_o^2| - |F_c^2|)^2 / \sum w|F_o^2|^2]^{1/2}$. [d] For observed data. [e] $R1 = \sum||F_o| - |F_c|| / \sum|F_o|$. * Synthesised and collected by D. Gaynor et al.[9]

***Table 4** - Crystallographic data for complexes **11** and **12**.*

Complex	**11**$\cdot 29H_2O$	**12**$\cdot 2MeOH\cdot 18H_2O$
Formula[a]	$C_{70}H_{130}N_{20}O_{57}S_1Ni_9$	$C_{74}H_{116}N_{20}O_{52}Cl_2Ni_9$
M_W	2724.18	2716.96
Crystal Appearance	Turquoise Parallelepiped	Turquoise Parallelepiped
Crystal System	Orthorhombic	Monoclinic
Space group	*Ima*2	*Cc*
a/Å	29.1847(11)	20.0036(7)
b/Å	21.2385(7)	25.0628(9)
c/Å	19.7536(6)	21.2234(5)
α/°	90.00	90.00
β/°	90.00	90.320(2)
γ/°	90.00	90.00
V/Å^3	12244.1(7)	10640.1(6)
Z	4	4
T/K	150(2)	150(2)
λ^b/Å	0.7107	0.7107
D_c/g cm^{-3}	1.192	1.656
μ(Mo-Ka)/ mm^{-1}	1.431	1.708
Collected/Unique, (R_{int}) refl.	52181/11376, (0.1403)	40644/16130, (0.0946)
wR2 (all data)	0.1531	0.1769
$R1^{d,\,e}$	0.0598	0.0693
Goodness of fit (GOOF) on F^2	0.964	1.027
Flack parameter	0.009(18)	0.026(18)

[a] Includes guest molecules. [b] Mo-Kα radiation, graphite monochromator. [c] $wR2 = [\sum w(|F_o^2| - |F_c^2|)^2 / \sum w|F_o^2|^2]^{1/2}$. [d] For observed data. [e] $R1 = \sum||F_o| - |F_c|| / \sum|F_o|$.

3.2.2 Theoretical Determination of Paramagnetic Centres in Complexes 8 and 9

As mentioned previously, complexes $[Ni(II)_5(L_1)_4(MeOH)_4](ClO_4)_2\cdot 2MeOH$ (**8**) and $[Ni(II)_5(L_1)_4(pyr)_5](ClO_4)_2\cdot 1H_2O$ (**9**) both contain pentametallic Ni(II) centres, whereby three unique distorted geometries are utilised (square planar, square-based pyramidal and octahedral). In general, square planar Ni(II) centres tend to be diamagnetic in nature, while the magnetic properties of square-based pyramidal Ni(II) centres are influenced by the ligand strength at the axial positions and can be either diamagnetic[10-14] or paramagnetic.[15, 16] However, octahedral Ni(II) centres will always be paramagnetic in nature. In order to determine the number of paramagnetic centres in complexes **8** and **9**, DFT calculations were carried out utilising a range of spin state combinations (s = 0 versus s = 1) for each individual Ni(II) centre in both complexes (Figure 88).

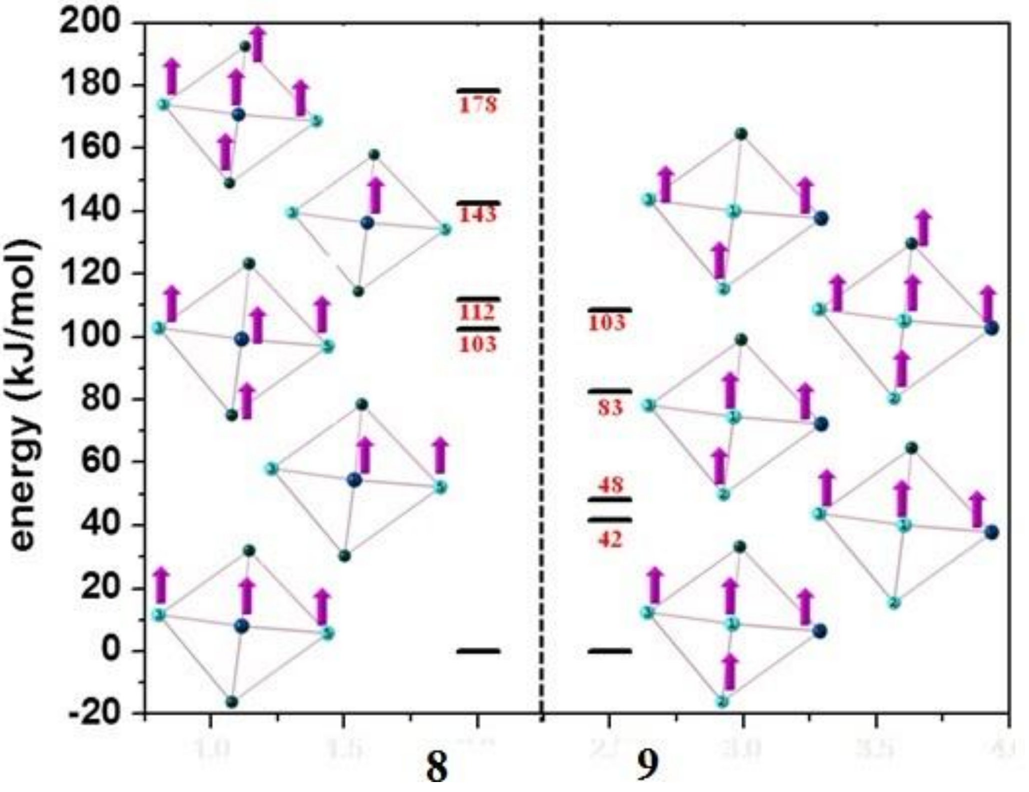

Figure 88 *- Depiction of all possible total spin (S_T) configurations of individual Ni(II) ions in **8** (left) and **9** (right) with respective energies (kJ/mol) on the y axis.*

Firstly, we assumed that all Ni(II) ions in **8** were paramagnetic (i.e. s = 1), then we began to gradually decrease the number of paramagnetic centres, while simultaneously increasing the number of diamagnetic metal centres (i.e. s = 0). This yielded five different spin states for **8**, resulting in triple ground states for metal centres Ni1 (octahedral), Ni3 and its symmetric equivalent Ni3A (square pyramidal). As can be seen in Figure 88, all other configurations are much higher in energy in comparison to the calculated triple ground state and therefore are relatively unlikely to be accessible at ambient conditions. Therefore, the square planar Ni2 centre and its symmetric equivalent have isolated diamagnetic (s = 0) ground states and so we can conclude that all experimental magnetic properties in **8** are uniquely due to paramagnetic (s = 1) ground state configurations at Ni1, Ni3 and its symmetric equivalent Ni3A. In the same way, we were able to compute five different spin states for complex **9**, where it was discovered that in the ground state Ni(II) centres Ni1, Ni2, Ni3 and Ni5 display paramagnetic behaviour (s = 1), while the square planar Ni4 exhibits diamagnetic behaviour (s = 0). All other possible configurations are higher in energy; however unlike complex **8** these excited energy states lie closer together, with the first excited state lying approximately 42 kJ/mol above the ground state (Figure 88).

3.2.3 Magnetic Susceptibility Measurements

Dc magnetic susceptibility studies were carried out on powdered microcrystalline samples of $[Ni(II)_5(L_1)_4(MeOH)_4](ClO_4)_2 \cdot 2MeOH$ (**8**), $[Ni(II)_5(L_1)_4(pyr)_5](ClO_4)_2 \cdot 1H_2O$ (**9**), $[Ni(II)_7(L_1H)_8(L_1)_2(H_2O)_6](SO_4) \cdot 15H_2O$ (**10**), $[Ni(II)_9(\mu\text{-}H_2O)_2(L_2)_6(L_2H)_4(H_2O)_2](ClO_4)_2 \cdot 2MeOH \cdot 18H_2O$ (**12**) in the 300-5 K temperature range with an external magnetic field of 0.1 T and were plotted as their $\chi_M T$ products (Figure 89). The room temperature $\chi_M T$ values of 3.55 (**8**) and 3.43 (**9**) $cm^3\ mol^{-1}$ K are lower than the expected values for three (3.63 $cm^3\ mol^{-1}$ K) and four (4.84 $cm^3\ mol^{-1}$ K) non interacting, paramagnetic Ni(II) centres (assuming g = 2.2). Upon decreasing temperature, a steady drop of the $\chi_M T$ value is seen in both complexes, eventually reaching values of 1.28 and 1.10 $cm^3\ mol^{-1}$ K respectively at 5 K. These resultant curvatures present evidence for dominant intra-molecular antiferromagnetic interactions in both complexes, where the exchange in **9** is stronger than in **8** (Figure 89).

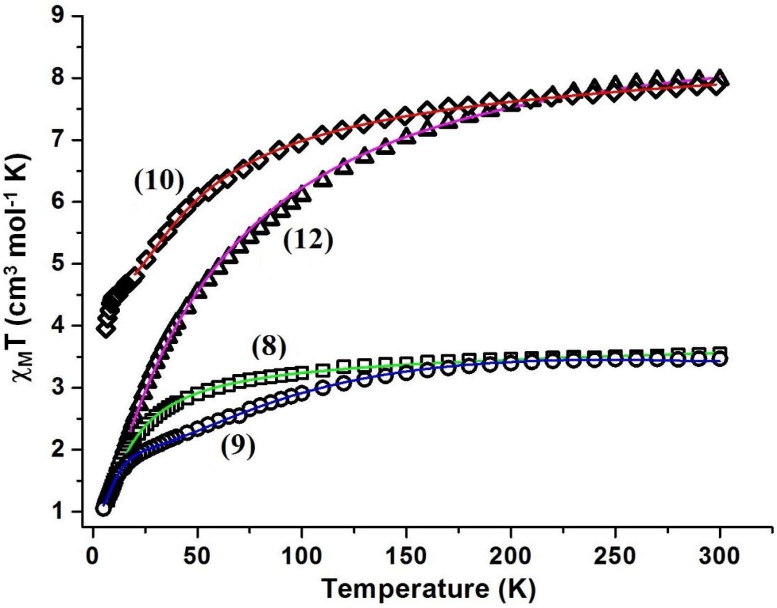

Figure 89 - *Plots of molar magnetic susceptibility $\chi_M T$ vs. T for **8** (□), **9** (○), **10** (◊) and **12** (Δ), where the solid lines represent best-fits of experimental data.*

The isotropic spin-Hamiltonians 3.1 and 3.2 (where $\hat{S}$ is the spin-operator) were employed in conjunction with the models given in Figure 90 towards magnetic data interpretation for complexes **8** and **9** respectively. J_1 represents the isotropic exchange parameter between the central Ni(II) ion and the surrounding paramagnetic Ni(II) ions, which consist of one Ni-O-Ni and one Ni-O-N-Ni pathway. J_2 describes the Ni(II)$_{outer}$-Ni(II)$_{outer}$ exchange parameter between peripheral paramagnetic Ni(II) ions comprising a single Ni-O-N-Ni pathway.[17] The best fit parameters obtained were S = 1, J_1 = -3.51 cm^{-1} (**8**) and S = 1, J_1 = -16.87 cm^{-1} and J_2 = -7.83 cm^{-1} (**9**). Moreover, an S = 0 state lies only 1.43 cm^{-1} above the S = 1 state in **9** (Figure 91). The individual Ni-O-Ni magnetic pathways in **8** (Ni1-O1-Ni3 = 103.98°) and **9** (Ni1-O8-Ni2 = 113.85°, Ni1-O2-Ni3 = 120.54° and Ni1-O6-Ni5 = 115.18°) all lie in the expected range, favouring antiferromagnetic exchange, where stronger interactions are exhibited by the larger angles in **9** as seen experimentally.[18-23]

$$\hat{H}_{ex} = -2J_1(\hat{S}_{Ni1} \bullet \hat{S}_{Ni3} + \hat{S}_{Ni1} \bullet \hat{S}_{Ni3A}) \quad \textbf{(3.1)}$$

$$\hat{H}_{ex} = -2J_1(\hat{S}_{Ni1} \bullet \hat{S}_{Ni2} + \hat{S}_{Ni1} \bullet \hat{S}_{Ni3} + \hat{S}_{Ni1} \bullet \hat{S}_{Ni5}) - 2J_2(\hat{S}_{Ni2} \bullet \hat{S}_{Ni5} + \hat{S}_{Ni2} \bullet \hat{S}_{Ni3}) \quad \textbf{(3.2)}$$

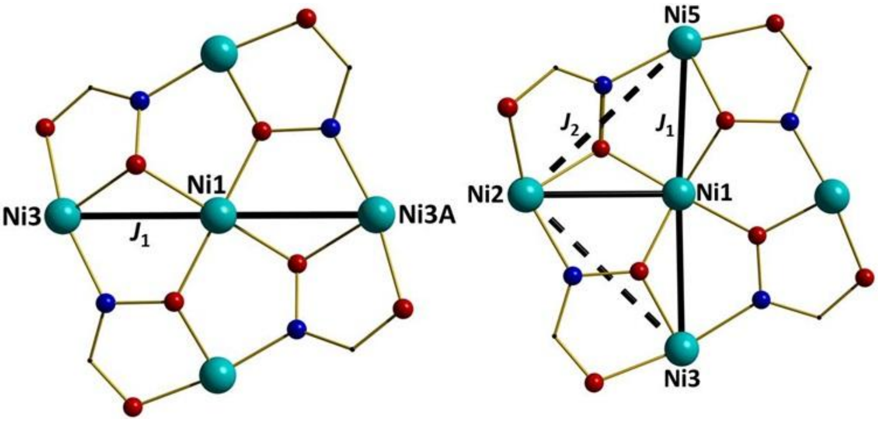

Figure 90 *- Schematic of the models utilised in the fitting of magnetic data for* ***8*** *and* ***9****. See main text for details.*

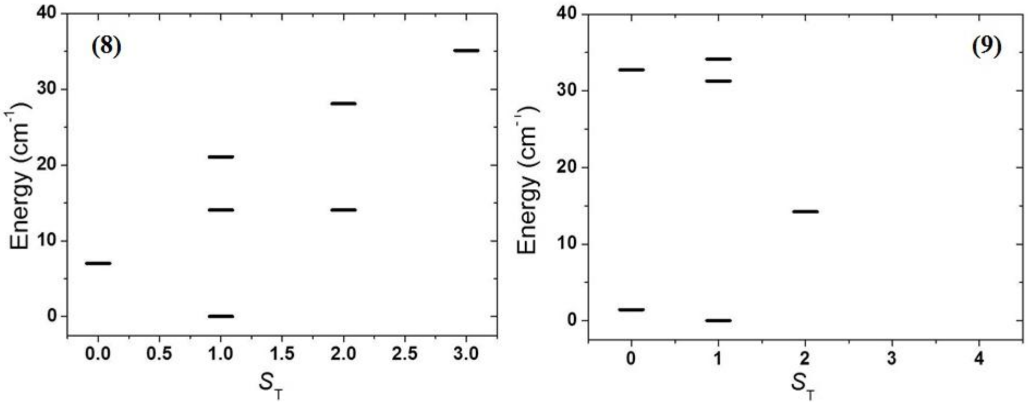

Figure 91 - *Energy vs. S_T (total spin state) plots of the lowest lying energy states in* ***8*** *and* ***9****, as determined from the isotropic fit of the susceptibility data.*

Magnetic susceptibility studies performed on complex **12** highlights the presence of dominant antiferromagnetic exchange pathways between Ni(II) centres, while the data for complex **10** indicates the presence of competing ferro- and anti-ferromagnetic exchange interactions (Figure 89). The χ_MT room temperature values of 7.87 (**10**) and 7.98 (**12**) cm^3 mol^{-1} K are lower than the expected values for seven and nine non-interacting, paramagnetic Ni(II) centres (8.47 (**10**) and 10.89 (**12**) cm^3 mol^{-1} K where g = 2.2). A uniform decrease in the χ_MT value in **12** is observed upon decreasing temperature, before reaching a minimum value of 1.14 cm^3 mol^{-1} K at 5 K. For complex **10**, a more complicated curvature is seen where the decrease in temperature exhibits a much slower drop in the χ_MT value, reaching a brief plateau at approximately 4.5 cm^3 mol^{-1} K at 25 K, before lowering further to give a minimum value of 3.95 cm^3 mol^{-1} K at 5 K. The structural complexity of **10** and **12** prevents detailed quantitative analyses of the susceptibility data due to the numerous different exchange interactions. However, it was possible to estimate the magnitude of the exchange through the utilisation of simple models (Figure 92 and 93). For both complexes we attempted to fit the data where all Ni···Ni interactions were assumed to be of similar magnitude and therefore only one *J* value would be required. Magnetic data was successfully fitted using this model along with the isotropic spin-Hamiltonian 3.3 (below) for complex **12** (Figure 92). This yielded best fit parameters S = 1 and J_1 = -5.27 cm^{-1} where g = 2.2. J_1 represents the Ni-O-Ni magnetic pathway and ranges from 77.26 to 139.44°, which gives rise to an overall weak antiferromagnetic *J* value for complex **12**.

$$\hat{H}_{ex} = -2J_1(\hat{S}_1 \bullet \hat{S}_2 + \hat{S}_1 \bullet \hat{S}_3 + \hat{S}_1 \bullet \hat{S}_4 + \hat{S}_2 \bullet \hat{S}_3 + \hat{S}_2 \bullet \hat{S}_4 + \hat{S}_3 \bullet \hat{S}_4 + \hat{S}_3 \bullet \hat{S}_5 + \hat{S}_3 \bullet \hat{S}_6 + \hat{S}_4 \bullet \hat{S}_5 + \\ \hat{S}_4 \bullet \hat{S}_6 + \hat{S}_4 \bullet \hat{S}_7 + \hat{S}_5 \bullet \hat{S}_6 + \hat{S}_5 \bullet \hat{S}_7 + \hat{S}_6 \bullet \hat{S}_7 + \hat{S}_6 \bullet \hat{S}_8 + \hat{S}_6 \bullet \hat{S}_9 + \hat{S}_7 \bullet \hat{S}_8 + \hat{S}_7 \bullet \hat{S}_9 + \hat{S}_8 \bullet \hat{S}_9) \\ + \sum_{i=1-9} \mu_B B g \hat{S}_i \; \} \tag{3.3}$$

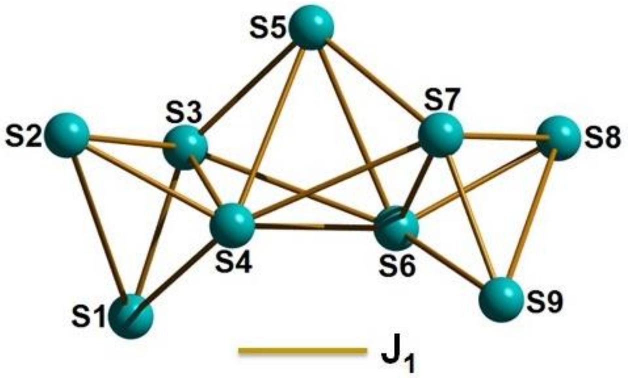

Figure 92 *- Schematic of the model employed for the fitting of the magnetic data for* ***12****. See main text for details.*

The above method was unsuitable for complex **10**, as two J values were required to fit the susceptibility data, where J_1 represents the Ni(II) ions connected by a one atom bridge (Ni-O-Ni) and J_2 portrays the Ni-O-N-Ni pathway (Figure 93). This yielded the best fit parameters S = 3, $J_1 = +0.64$ and $J_2 = -8.94$ cm^3 mol^{-1} K where g = 2.2. Please note these numbers are a guide only, but are similar to structurally related Ni(II) cages in the literature.[18-23]

$$\hat{H}_{ex} = -2J_1(\hat{S}_{Ni1} \bullet \hat{S}_{Ni2} + \hat{S}_{Ni2} \bullet \hat{S}_{Ni3} + \hat{S}_{Ni2} \bullet \hat{S}_{Ni4} + \hat{S}_{Ni2} \bullet \hat{S}_{Ni5} + \hat{S}_{Ni3} \bullet \hat{S}_{Ni4} + \hat{S}_{Ni3} \bullet \hat{S}_{Ni5} + \\ \hat{S}_{Ni3} \bullet \hat{S}_{Ni6} + \hat{S}_{Ni4} \bullet \hat{S}_{Ni5} + \hat{S}_{Ni4} \bullet \hat{S}_{Ni6} + \hat{S}_{Ni5} \bullet \hat{S}_{Ni6} + \hat{S}_{Ni6} \bullet \hat{S}_{Ni7}) \\ - 2J_2(\hat{S}_{Ni1} \bullet \hat{S}_{Ni3} + \hat{S}_{Ni1} \bullet \hat{S}_{Ni5} + \hat{S}_{Ni3} \bullet \hat{S}_{Ni7} + \hat{S}_{Ni5} \bullet \hat{S}_{Ni7}) \tag{3.4}$$

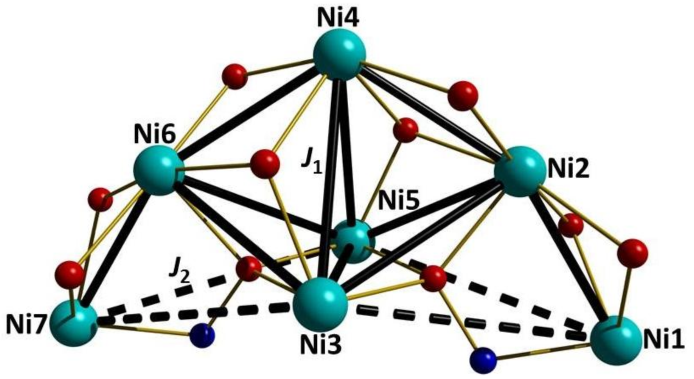

Figure 93 *- Representation of the model utilised to fit the experimental data for* ***10****. Refer to main text for details.*

3.2.4 Magnetisation versus Field Studies

Magnetisation (M) vs. field (H) measurements were performed on samples $[Ni(II)_5(L_1)_4(MeOH)_4](ClO_4)_2 \cdot 2MeOH$ (**8**), $[Ni(II)_5(L_1)_4(pyr)_5](ClO_4)_2 \cdot 1H_2O$ (**9**) and $[Ni(II)_9(\mu\text{-}H_2O)_2(L_2)_6(L_2H)_4(H_2O)_2](ClO_4)_2 \cdot 2MeOH \cdot 18H_2O$ (**12**) at 2 K in the 0.5 to 7 T magnetic field range (Figure 94). Data from complexes **8** and **9** exhibit linearly shaped curves with larger magnetisation values in all fields for **9**, indicating the presence and occupation of low lying excited spin states. The M vs. H data for **12** displays an entirely different shape with the introduction of a plateau in the magnetisation product at approximately 2.13 and 7 T, corroborating the S = 1 ground spin state. In addition, M vs. H data in the 2-7 K temperature range along with reduced magnetisation ($M/N\mu_B$ vs. H/T) data for **12** are shown (Figure 95).

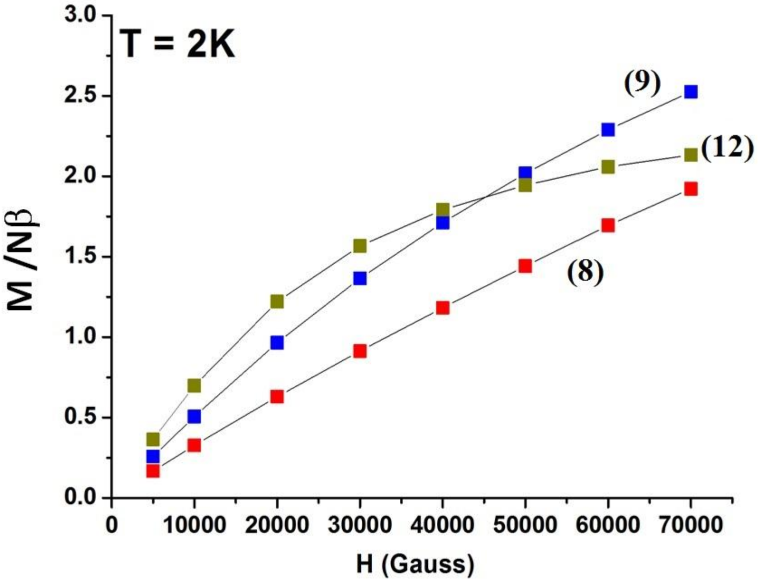

Figure 94 *- Plots of Magnetisation (M) vs. Field (H) data for* ***8*** *(red),* ***9*** *(blue) and* ***12*** *(green) at 2 K in 0.5-7 T applied magnetic fields (solid line acts as a guide for the eye).*

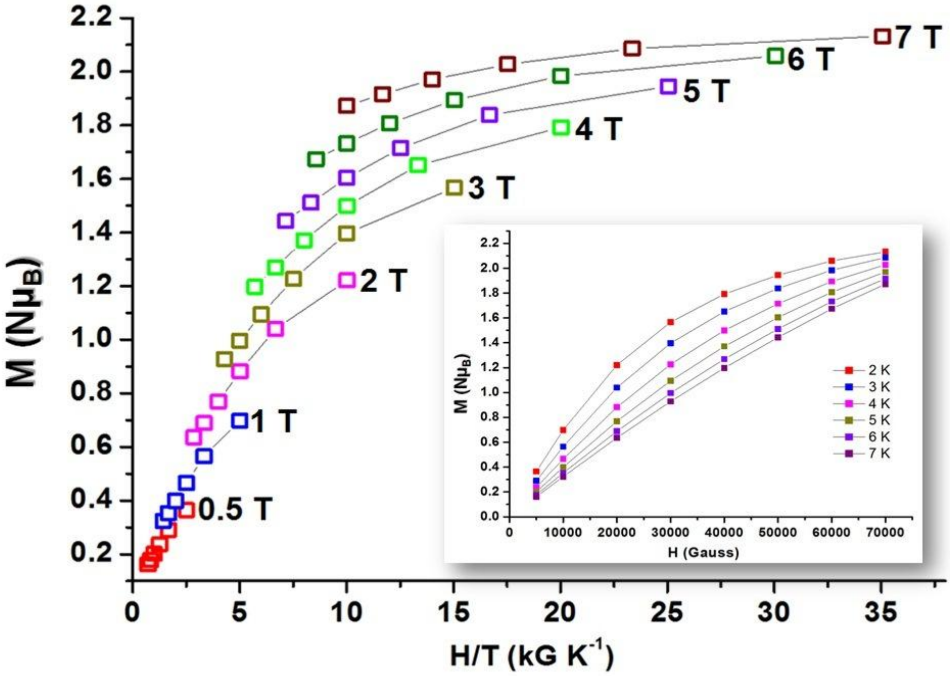

Figure 95 *- Reduced magnetisation (M/Nμ_B) vs. Field (H/T) data for complex* ***12*** *in the applied magnetic field range 0.5-7 T. The solid lines represent a best fit to the experimental data. (Inset) Magnetisation (M) vs. Field (H) in the 2-7 K temperature range and 0.5-7 T field range.*

3.2.5 Theoretical Studies of Magnetic Exchange in Complexes 8 and 9

DFT analysis were performed on $[Ni(II)_5(L_1)_4(MeOH)_4](ClO_4)_2\cdot 2MeOH$ (**8**) and $[Ni(II)_5(L_1)_4(pyr)_5](ClO_4)_2\cdot 1H_2O$ (**9**) in order to understand their intra-molecular magnetic exchange coupling interactions. We computed the energies of four different spin configurations, resulting in two exchange coupling constants (*J*) for the ground state in **8** (Table 5). Since complex **9** is asymmetric, five independent *J* values were computed using seven different spin configurations (Table 6). The corresponding Hamiltonians for **8** and **9** are given in Section 3.4.1.2 and all computed magnetic coupling constants calculated for **8** and **9** are shown in Figure 96.

Table 5 **-** *Illustrations of all accessible spin projections of* ***8****. Colour code: orange sphere (s = 0), red arrow (s = -1) and black arrow (s = +1).*

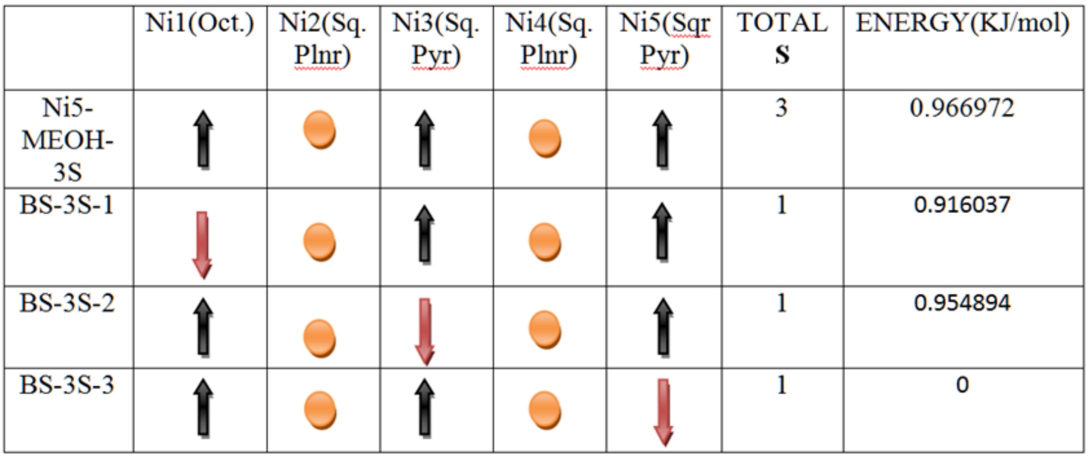

	Ni1(Oct.)	Ni2(Sq. Plnr)	Ni3(Sq. Pyr)	Ni4(Sq. Plnr)	Ni5(Sqr Pyr)	TOTAL S	ENERGY(KJ/mol)
Ni5-MEOH-3S	↑	●	↑	●	↑	3	0.966972
BS-3S-1	↓	●	↑	●	↑	1	0.916037
BS-3S-2	↑	●	↓	●	↑	1	0.954894
BS-3S-3	↑	●	↑	●	↓	1	0

Table 6 **-** *Depiction of all accessible spin projections of* ***9****. Colour scheme as in Table 5.*

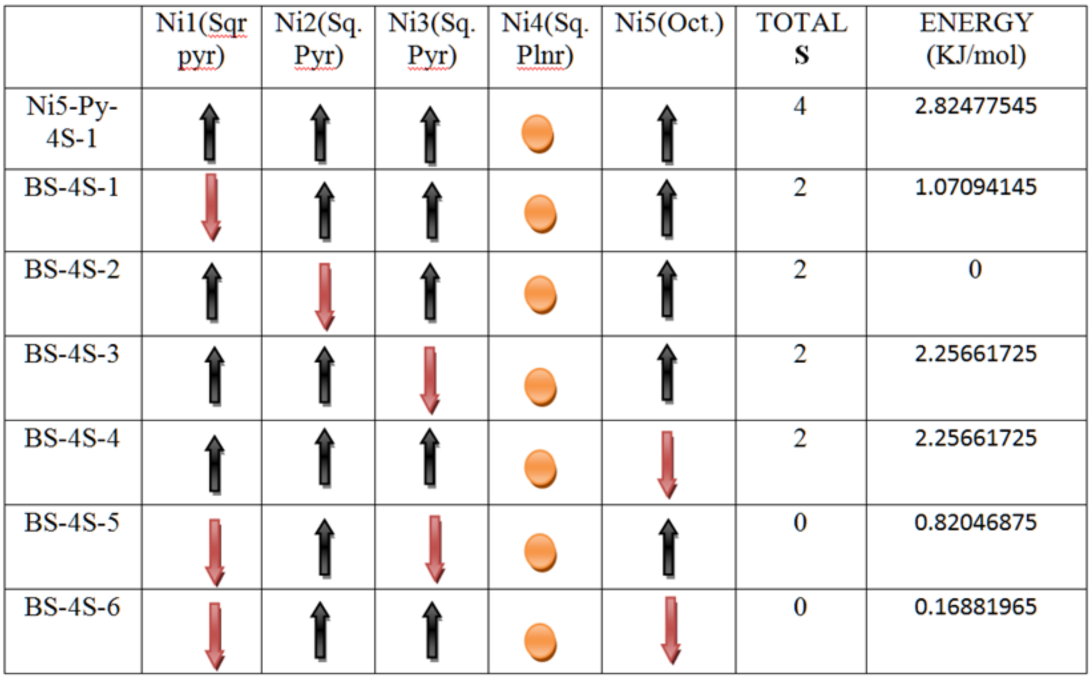

	Ni1(Sqr pyr)	Ni2(Sq. Pyr)	Ni3(Sq. Pyr)	Ni4(Sq. Plnr)	Ni5(Oct.)	TOTAL S	ENERGY (KJ/mol)
Ni5-Py-4S-1	↑	↑	↑	●	↑	4	2.82477545
BS-4S-1	↓	↑	↑	●	↑	2	1.07094145
BS-4S-2	↑	↓	↑	●	↑	2	0
BS-4S-3	↑	↑	↓	●	↑	2	2.25661725
BS-4S-4	↑	↑	↑	●	↓	2	2.25661725
BS-4S-5	↓	↑	↓	●	↑	0	0.82046875
BS-4S-6	↓	↑	↑	●	↓	0	0.16881965

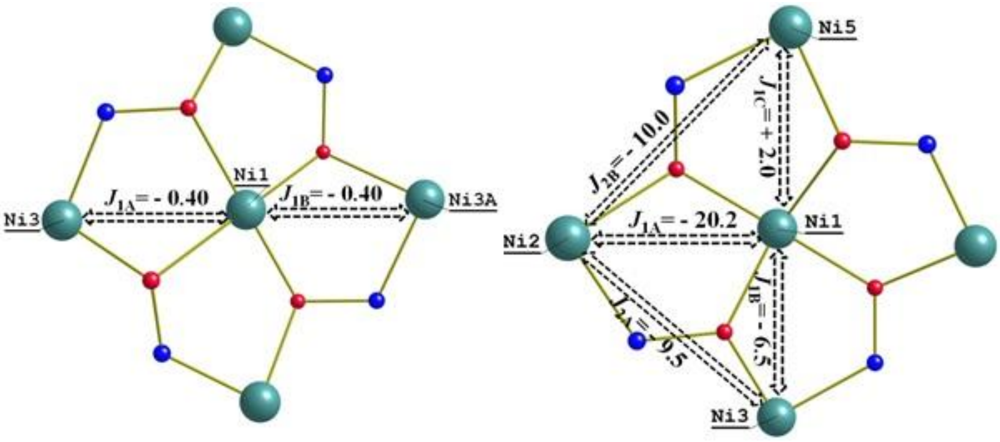

***Figure 96** - Schematic representations of the calculated magnetic exchange coupling constants (cm^{-1}) in **8** (left) and **9** (right).*

Compared to the experimentally derived J values (J_1 = -3.5 cm^{-1}) in section 3.2.4, DFT calculations for complex **8** produced slightly weaker antiferromagnetic J values (J_{1A} = J_{1B} = -0.4 cm^{-1}). The computed spin density plot for the high spin configuration (S = 3) for complex **8** shows dominant spin delocalisation leading to antiferromagnetic coupling (Figure 97). This is further supported by computed overlap integrals, where significant overlap between $d_{x^2-y^2}$ orbitals are seen (Table 7).

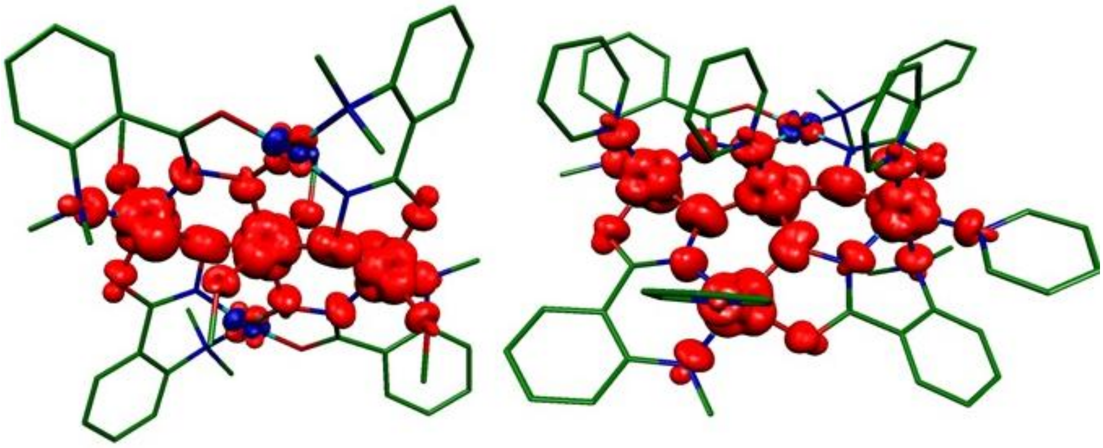

***Figure 97** - DFT computed spin density plots for complex **8** (left) and **9** (right). Colour code: red = positive spin density and blue = negative spin density.*

***Table 7** - Calculated overlap integrals for complex **8**.*

Alpha/Beta	Ni3-$d_{x^2-y^2}$	Ni3-d_{z^2}	Ni5-$d_{x^2-y^2}$	Ni5-d_{z^2}
Ni1-$d_{x^2-y^2}$	0.11	0.10	0.11	0.10
Ni1-d_{z^2}	0.04	0.06	0.04	0.06

Calculations carried out on complex **9** reveal that the assumption that $J_2 = J_{2A} = J_{2B}$ is valid and that the experimental values (J_2 = -7.83 cm^{-1}) are comparable with computed values (J_{2A} = -9.5 cm^{-1} and J_{2B} = -10.0 cm^{-1}). The theoretical J_1 values ($J_{1A\text{-}C}$) display a range of exchange types, from weakly ferromagnetic (J_{1C} = +2.0 cm^{-1}) to strongly antiferromagnetic (J_{1A} = -20.2 cm^{-1}). This is in contrast to the experimental value (J_1 = -16.37 cm^{-1}) and therefore the assumption that $J_1 = J_{1A} = J_{1B} = J_{1C}$ is not true. The $J_{1A\text{-}C}$ exchange interactions in **9** are established via a combination of Ni-$O_{oximato}$-Ni and Ni-N-O-Ni pathways, while J_{2A} and J_{2B} are exclusively achieved via NO bridges. The exchange interaction J_{1C} was the only calculated J value for **9** which was shown to be ferromagnetic in nature. This results from the inherent orthogonality of the $d_{x^2-y^2}$ orbitals belonging to centres Ni1 and Ni5. The orthogonality arises from the relatively acute Ni1-O6-Ni5 angle (115.18°) and the large Ni1-O8-N12-Ni5 dihedral twist (31.58°) observed along the Ni1···Ni5 pathway in **9** (Figure 98 and Table 8).

Table 8 *- Selected structural parameters corresponding to the computed J values for* ***9****.*

Calculated *J* constants	**Ni-O-Ni Angle (˚)**	**Ni-N-O-Ni Dihedral**	**Ni-Ni Distance (Å)**
J_{1A}	114	14	3.3
J_{1B}	121	16	3.4
J_{1C}	115	32	3.3
J_{2A}	-----	176	4.7
J_{2B}	-----	165	4.8

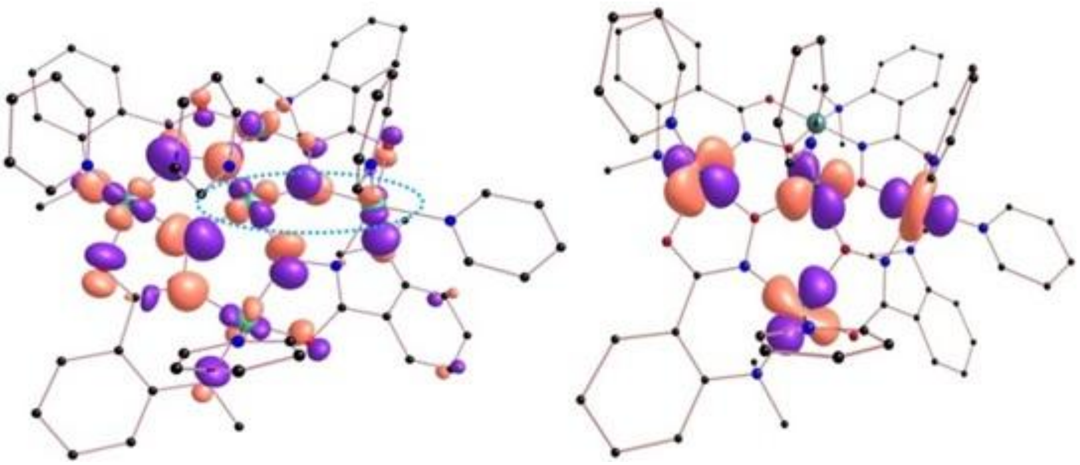

***Figure 98** - (Left) Illustration of the orthogonality between the $d_{x^2-y^2}$ magnetic orbitals of Ni1 and Ni5 centres (highlighted by a blue dotted line) in complex **9**. (Right) Natural hybrid orbitals[24] representing the dominant orbital interaction in the molecular plane of **9** (see Table 9 for computed overlap integral values).*

***Table 9** - Calculated overlap integrals for complex **9**.*

Alpha/Beta	**Ni3-d_{z^2}**	**Ni3-$d_{x^2-y^2}$**	**Ni2-d_{z^2}**	**Ni2-$d_{x^2-y^2}$**	**Ni5-d_{z^2}**	**Ni5-$d_{x^2-y^2}$**
Ni1-d_{z^2}	0.04	0.02	0.07	0.17	0.02	0.02
Ni1-$d_{x^2-y^2}$	0.06	0.22	0.06	0.24	0.10	0.01
Ni3-d_{z^2}			0.09	0.06		
Ni3-$d_{x^2-y^2}$			0.03	0.22		
Ni5-d_{z^2}			0.05	0.23		
Ni5-$d_{x^2-y^2}$			0.04	0.10		

The dominant magnetic interaction in both complexes occurs in the [Ni_5] plane and the relatively small differences in the exchange interactions between complexes **8** and **9** can be explained and illustrated through the orientations of their molecular orbitals. All the paramagnetic Ni(II) ions in **8** have their $d_{x^2-y^2}$ orbitals in the [Ni_5] plane, while the Ni5 centre in complex **9** does not; here the d_{z^2} orbitals lie in the plane (Figure 98-right). Significant overlap between the $d_{x^2-y^2}$ and the $d_{x^2-y^2}/d_{z^2}$ magnetic orbitals gives rise to antiferromagnetic exchange pathways in **9** (Figure 98-right). In addition, a significant $d_{x^2-y^2}|p|d_{x^2-y^2}$ overlap along the Ni1$\cdots$Ni2 vector was observed, further supporting the strong antiferromagnetic J_{1A} value (Table 9). Furthermore, a dominant spin delocalization mechanism with larger spin densities occupying the oxygen atoms is observed in the spin density plot for **9** (Figure 97).

3.3 Conclusions and Observations

We successfully utilised the hydroxamic acid ligands 2-(dimethylamino)phenylhydroxamic acid (L_1H_2) and 2-(amino)phenylhydroxamic acid (L_2H_2) as bridging ligands in the synthesis of a family of Ni(II) cages with nuclearities ranging from penta- to nonametallic. The simple addition of pyridine to the synthetic procedure for the founding member $[Ni(II)_5(L_1)_4(MeOH)_4](ClO_4)_2 \cdot 2MeOH$ (**8**) yielded the 12-$MC_{Ni(II)}$-4 metallacrown analogue $[Ni(II)_5(L_1)_4(pyr)_5](ClO_4)_2 \cdot 1H_2O$ (**9**), where pyridine ligands occupy the axial positions at selected Ni(II) centres. This resulted in the conversion of square planar sites to square-based pyramidal/octahedral sites and hence 'switching on' of additional magnetic superexchange pathways. DFT analysis calculated triplet S = 1 ground states for both complexes **8** and **9**. By simple modification of reaction conditions (e.g. change of solvent, base and ligand) it was possible to structurally rearrange to a non-metallacrown conformation, yielding hepta- and nonanuclear cages $[Ni(II)_7(L_1H)_8(L_1)_2(H_2O)_6](SO_4) \cdot 15H_2O$ (**10**), $[Ni(II)_9(\mu\text{-}H_2O)_2(L_2)_6(L_2H)_4(H_2O)_2](SO_4) \cdot 29H_2O$ (**11**) and $[Ni(II)_9(\mu\text{-}H_2O)_2(L_2)_6(L_2H)_4(H_2O)_2](ClO_4)_2 \cdot 2MeOH \cdot 18H_2O$ (**12**). These complexes present metallic skeletons consisting of two bicapped, face sharing tetrahedra in **10** and two annexed tetrahedra in **11** and **12**. Magnetic susceptibility measurements performed on three linear antiferromagnetically exchanged Ni(II) centres in **8** yield an S = 1 ground spin state. Additionally, antiferromagnetic exchange dominates in complexes **9** and **12**, while complex **10** displays competing ferro- and antiferromagnetic exchange between the seven Ni(II) centres, yielding an intermediate S = 3 ground spin state. DFT calculations were carried out on **8** and **9** to clarify the ground spin configurations (s = 0 vs. s = 1) of all Ni(II) centres, yielding three and four paramagnetic (s = 1) Ni(II) centres in **8** and **9** respectively. DFT computed magnetic exchange interactions nicely reflect our experimental data. In addition, overlap between the magnetic orbitals observed in DFT computed calculations can be employed to rationalise the nature and magnitude of the interactions.

3.4 Experimental Section

3.4.1 Instrumentation

For details on instrumentation utilised in the analyses of complexes **8**-**12** see Chapter Two (Section 2.4.1).

3.4.1.1 Single Crystal X-ray Diffraction

The structures of **8**-**12** were collected on an Xcalibur S single crystal diffractometer (Oxford Diffraction) using an enhanced Mo source. Complex **10** was previously collected and published elsewhere (CCDC No: 175223).[9] All hydrogen atoms were assigned to calculated positions. All non-hydrogen atoms were refined anisotropically except for the sulphate and perchlorate anions in **11** and **12** respectively, which remained isotropic. The DFIX command was used to restrain one of the two ClO_4^- counter anions in **12** (labelled Cl1-O50-O53). In addition, DFIX restraints were utilised on the S1-O15 bond of the SO_4^{2-} anion in **11**. Residual electron density in solvent accessible voids and channels were observed in **11** and therefore were modelled using the SQUEEZE program.[25, 26] The two large channels (total voids volume ~1143 Å^3) in **11** contained extremely diffuse electron density and were assumed to contain numerous waters of crystallisation. These observations were supported by CHN analysis on **11**. The PLATON program suggests the orthorhombic *Aba*2 space group for the structure in **12**; however despite our best efforts, no plausible structural solution was obtained.

3.4.1.2 Density Functional Theory (DFT) Computational Details

DFT studies were carried out on complexes **8** and **9** to predict the ground spin state of each individual Ni(II) ion and to determine the exchange coupling constants between ions. All calculations were performed using the Gaussian 09 suite of programmes,[27] along with the hybrid B3LYP function[28-31] and the TZV[32-34] basis set for Ni(II) and all other elements. Density Functional Theory along with broken symmetry[35-38] has proven to be a dependable tool when computing exchange coupling. In a system with two paramagnetic centres the magnetic coupling constant (*J*) corresponds to the energy difference between the high and low spin configurations. However, as our systems are pentametallic there is a greater number of possible configurations ($2^n/2$; where n = number of paramagnetic centres). In complexes **8** and **9** we have used the spin-Hamiltonians in equations 3.5 and 3.6 respectively. Here the *Ji* values (1A-B in **8**; 1A-C and 2A-B in **9**) correspond to the isotropic exchange coupling constants and the S_i values represents the spin moment on the Ni(II) centres. The eigenvalue spectra and magnetic susceptibility are reconstructed from the computed *J* values using the MAGPACK code.[39]

$$\hat{H} = -2J_{1A}(\hat{S}_1 \bullet \hat{S}_3) - 2J_{1B}(\hat{S}_1 \bullet \hat{S}_{3A}) \quad \textbf{(3.5)}$$

$$\hat{H} = -2J_{1A}(\hat{S}_1 \bullet \hat{S}_2) - 2J_{1B}(\hat{S}_1 \bullet \hat{S}_3) - 2J_{2A}(\hat{S}_2 \bullet \hat{S}_3) - 2J_{2B}(\hat{S}_2 \bullet \hat{S}_5) - 2J_{1C}(\hat{S}_1 \bullet \hat{S}_5) \quad \textbf{(3.6)}$$

3.4.2 Syntheses

Reagents and solvents were used as purchased without further purification. All reactions were performed under aerobic conditions. **Caution**: Although no difficulties were encountered during this work, great care should be exercised when using the potentially explosive perchlorate salts.

For the synthesis of 2-(dimethylamino)phenylhydroxamic acid (L_1H_2) and 2-(amino)phenylhydroxamic acid (L_2H_2) see Chapter Two (Section 2.4.2.2 - 2.4.2.3).

3.4.2.1 Crystallisation Techniques

In addition to the slow solvent evaporation technique mentioned in Chapter Two (Section 2.4.2.1), a diethyl ether diffusion technique was utilised in this chapter in an attempt to achieve X-ray quality crystals. A small vial is half filled with the mother liquor solution using a pipette and is then placed in a larger vial with roughly 2 cm^3 of Et_2O. This is then capped, sealed with parafilm and left to stand to allow the more volatile solvent (Et_2O) to slowly diffuse into the mother liquor. Et_2O concentration increases in the small sample vial allowing the formation of crystals as they are less soluble in the ether solution.

Figure 99 *- Single crystals of complexes **8**, **9**, **11**, **12** (left to right) used in X-ray data collection.*

3.4.2.2 Synthesis of [Ni(II)$_5$(L$_1$)$_4$(MeOH)$_4$](ClO$_4$)$_2$·2MeOH (8)

$Ni(ClO_4)_2 \cdot 6H_2O$ (0.2 g, 0.55 mmol), L_1H_2 (0.1 g, 0.55 mmol) and NaOH (0.022 g, 0.55 mmol) were dissolved in 30 cm^3 of MeOH and stirred for 2 h. The green solution obtained was filtered, allowed to concentrate upon slow evaporation, resulting in the formation of X-ray quality crystals of **8**. In addition, crystals were also obtained from Et_2O diffusion of aliquots of mother liquor. The crystals of **8** were collected and air dried with a yield of approximately 14%.

C, H, N Elemental Analysis

Calculated % as [Ni(II)$_5$(L$_1$)$_4$(MeOH)$_2$](ClO$_4$)$_2$·5H$_2$O ($C_{38}H_{58}N_8O_{23}Cl_2Ni_5$): C 33.58, H 4.30, N 8.24.

Found %: C 33.36, H 4.20, N 8.22.

FT-IR (cm^{-1}): 3511 (w), 1591 (s), 1559 (m), 1465 (w), 1373 (m), 1279 (w), 1084 (s), 1014 (m), 936 (m), 910 (m), 777 (m), 704 (m), 688 (m), 676 (m), 663 (s).

3.4.2.3 Synthesis of [Ni(II)$_5$(L$_1$)$_4$(pyr)$_5$](ClO$_4$)$_2$·H$_2$O (9)

$Ni(ClO_4)_2 \cdot 6H_2O$ (0.25 g, 0.68 mmol), L_1H_2 (0.12 g, 0.68 mmol) and NaOH (0.027 g, 0.68 mmol) were dissolved in 35 cm^3 of MeOH. After 5 minutes 1 cm^3 (12.4 mmol) of pyridine was added and the solution was stirred for a further 2 h. The resultant green solution was filtered and X-ray quality crystals of **9** were obtained upon slow evaporation of the mother liquor. Crystals of **9** were also obtained using the Et_2O diffusion method. Both batches of **9** were collected and air dried with a yield of ~10%.

C, H, N Elemental Analysis

Calculated % as [Ni(II)$_5$(L$_1$)$_4$(pyr)$_5$](ClO$_4$)$_2$·3H$_2$O ($C_{61}H_{69}N_{13}O_{19}Cl_2Ni_5$): C 44.33, H 4.21, N 11.02.

Found %: C 44.01, H 4.22, N 10.99.

FT-IR (cm^{-1}): 2990 (w), 1590 (m), 1566 (w), 1541 (m), 1486 (w), 1467 (w), 1447 (m), 1375 (m), 1284 (w), 1218 (w), 1147 (w), 1082 (s), 1028 (m), 1014 (m), 946 (m), 918 (m), 784 (w), 765 (m), 751 (m), 704 (m), 689 (s), 673 (m), 662 (m).

3.4.2.4 Synthesis of $[Ni_7(L_1H)_8(L_1)_2(H_2O)_6](SO_4)\cdot15H_2O$ (10)

Synthesis of $[Ni_7(L_1H)_8(L_1)_2(H_2O)_6](SO_4)\cdot15H_2O$ (**10**) by the Gaynor group as per a previously reported procedure.[9]

C, H, N Elemental Analysis

Calculated % for ($C_{90}H_{150}N_{20}O_{45}SNi_7$): C 40.41, H 5.65, N 10.47.

Found %: C 39.98, H 5.32, N 10.19.

FT-IR (cm^{-1}): 2987 (s), 2795 (s) 1608 (s) 1562 (s), 1289 (m).

3.4.2.5 Synthesis of $[Ni_9(\mu\text{-}H_2O)_2(L_2)_6(L_2H)_4(H_2O)_2](SO_4)\cdot29H_2O$ (11)

$Ni(SO_4)\cdot6H_2O$ (0.25 g, 0.95 mmol), L_2H_2 (0.145 g, 0.95 mmol) and $NEt_4(OH)$ (0.7 cm^3, 0.72 g, 4.89 mmol) were dissolved in 40 cm^3 of a 1:1 MeOH:H_2O solution. The solution was stirred for 4 h, resulting in a green solution, which was then filtered and allowed to stand. Upon slow evaporation, green X-ray quality crystals of **11** formed after a few days. The crystals were collected and air dried with a yield of ~11%.

C, H, N Elemental Analysis

Calculated % as $[Ni_9(\mu\text{-}H_2O)_2(L_2)_6(L_2H)_4(H_2O)_2](SO_4)\cdot12H_2O$ ($C_{70}H_{96}N_{20}O_{40}S_1Ni_9$): C 34.77, H 4.00, N 11.59.

Found %: C 35.14, H 3.61, N 11.40.

FT-IR (cm^{-1}): 3200 (w), 1583 (m), 1547 (s), 1492 (m), 1450 (w), 1373 (m), 1152 (w), 1080 (m), 1017 (m), 935 (w), 903 (m), 819 (w), 747 (s), 692 (m), 670 (s).

3.4.2.6 Synthesis of $[Ni_9(\mu\text{-}H_2O)_2(L_2)_6(L_2H)_4(H_2O)_2](ClO_4)_2\cdot2MeOH\cdot18H_2O$ (12)

$Ni(ClO_4)_2\cdot6H_2O$ (0.25 g, 0.68 mmol), L_2H_2 (0.104 g, 0.68 mmol) and $NEt_4(OH)$ (0.7 cm^3, 0.72 g, 4.89 mmol); were dissolved in 40 cm^3 of a 1:1 MeOH:CH_3CN solution. The solution was stirred for 4 h, resulting in a green solution, which was filtered and evaporated to dryness. The green solid was subsequently re-dissolved in 20 cm^3 of a 1:1 MeOH:H_2O solution and stirred for a further 2 h. The resultant green solution was filtered and X-ray quality crystals of **12** were obtained upon slow evaporation of the reaction mixture in 10% yield.

C, H, N Elemental Analysis

Calculated % as $[Ni_9(\mu\text{-}H_2O)_2(L_2)_6(L_2H)_4(H_2O)_2](ClO_4)_2\cdot 20H_2O$ ($C_{70}H_{112}N_{20}O_{52}Ni_9$): C 31.55, H 4.24, N 10.51.

Found %: C 31.82, H 3.92, N 10.25.

FT-IR (cm^{-1}): 3203 (m), 1611 (m), 1583 (m), 1547 (s), 1494 (m), 1450 (w), 1374 (m), 1153 (m), 1091 (m), 1014 (m), 936 (m), 903 (s), 869 (w), 819 (w), 749 (s), 694 (m), 671 (s).

3.5 Bibliography

1. G. Mezei, C. M. Zaleski and V. L. Pecoraro, *Chem. Rev.*, 2007, 107, 4933-5003.
2. C. McDonald, T. Whyte, S. M. Taylor, S. Sanz, E. K. Brechin, D. Gaynor and L. F. Jones, *CrystEngComm*, 2013, 15, 6672-6681.
3. A. W. Addison, T. N. Rao, J. Reedijk, J. van Rijn and G. C. Verschoor, *J. Chem. Soc., Dalton Trans.*, 1984, 1349-1356.
4. G. Psomas, A. J. Stemmler, C. Dendrinou-Samara, J. J. Bodwin, M. Schneider, M. Alexiou, J. W. Kampf, D. P. Kessissoglou and V. L. Pecoraro, *Inorg. Chem.*, 2001, 40, 1562-1570.
5. M. Alexiou, I. Tsivikas, C. Dendrinou-Samara, A. A. Pantazaki, P. Trikalitis, N. Lalioti, D. A. Kyriakidis and D. P. Kessissoglou, *J. Inorg. Biochem.*, 2003, 93, 256-264.
6. Z. Chen, M. Jia, Z. Zhang and F. Liang, *Cryst. Growth Des.*, 2010, 10, 4806-4814.
7. D. Bacco, V. Bertolasi, F. Dallavalle, L. Galliera, N. Marchetti, L. Marchio, M. Remelli and M. Tegoni, *Dalton Trans.*, 2011, 40, 2491-2501.
8. G. Psomas, C. Dendrinou-Samara, M. Alexiou, A. Tsohos, C. P. Raptopoulou, A. Terzis and D. P. Kessissoglou, *Inorg. Chem.*, 1998, 37, 6556-6557.
9. D. Gaynor, Z. A. Starikova, S. Ostrovsky, W. Haase and K. B. Nolan, *Chem. Commun.*, 2002, 506-507.
10. A. F. Kolodziej, in *Prog. Inorg. Chem.*, John Wiley & Sons, Inc., 2007, pp. 493-597.
11. M. A. Halcrow and G. Christou, *Chem. Rev.*, 1994, 94, 2421-2481.
12. J. J. Wilker, A. Gelasco, M. A. Pressler, R. O. Day and M. J. Maroney, *J. Am. Chem. Soc.*, 1991, 113, 6342-6343.
13. M. Cha, C. L. Gatlin, S. C. Critchlow and J. A. Kovacs, *Inorg. Chem.*, 1993, 32, 5868-5877.
14. D. C. Goodman, P. J. Farmer, M. Y. Darensbourg and J. H. Reibenspies, *Inorg. Chem.*, 1996, 35, 4989-4994.
15. S. Brooker and P. D. Croucher, *Chem. Commun.*, 1997, 459-460.
16. U. Lehmann, J. Lach, C. Loose, T. Hahn, B. Kersting and J. Kortus, *Dalton Trans.*, 2013, 42, 987-996.
17. W. H. Press, S. A. Teukolsky, W. T. Vetterling and B. P. Flannery, Cambridge Univ. Press, New York, 1992.
18. K. K. Nanda, R. Das, L. K. Thompson, K. Venkatsubramanian and K. Nag, *Inorg. Chem.*, 1994, 33, 5934-5939.
19. K. K. Nanda, R. Das, L. K. Thompson, K. Venkatsubramanian, P. Paul and K. Nag, *Inorg. Chem.*, 1994, 33, 1188-1193.
20. K. K. Nanda, L. K. Thompson, J. N. Bridson and K. Nag, *J. Chem. Soc., Chem. Commun.*, 1994, 1337-1338.
21. A. J. Stemmler, J. W. Kampf, M. L. Kirk and V. L. Pecoraro, *J. Am. Chem. Soc.*, 1995, 117, 6368-6369.
22. M. Arnold, D. A. Brown, O. Deeg, W. Errington, W. Haase, K. Herlihy, T. J. Kemp, H. Nimir and R. Werner, *Inorg. Chem.*, 1998, 37, 2920-2925.
23. B. Biswas, U. Pieper, T. Weyhermüller and P. Chaudhuri, *Inorg. Chem.*, 2009, 48, 6781-6793.
24. A. Upadhyay, J. Rajpurohit, M. Kumar Singh, R. Dubey, A. Kumar Srivastava, A. Kumar, G. Rajaraman and M. Shanmugam, *Chem. Euro. J.*, 2014, 20, 6061-6070.
25. A. Spek, *J. Appl. Crystallogr.*, 2003, 36, 7-13.
26. P. van der Sluis and A. L. Spek, *Acta Crystallogr. Sect. A: Found. Crystallogr.*, 1990, 46, 194-201.
27. M. J. Frisch, G. W. Trucks, H. B. Schlegel, G. E. Scuseria, M. A. Robb, J. R. Cheeseman, G. Scalmani, V. Barone, B. Mennucci, G. A. Petersson, H. Nakatsuji, M. Caricato, X. Li, H. P. Hratchian, A. F. Izmaylov, J. Bloino, G. Zheng, J. L.

Sonnenberg, M. Hada, M. Ehara, K. Toyota, R. Fukuda, J. Hasegawa, M. Ishida, T. Nakajima, Y. Honda, O. Kitao, H. Nakai, T. Vreven, J. A. Montgomery, Jr., J. E. Peralta, F. Ogliaro, M. Bearpark, J. J. Heyd, E. Brothers, K. N. Kudin, V. N. Staroverov, R. Kobayashi, J. Normand, K. Raghavachari, A. Rendell, J. C. Burant, S. S. Iyengar, J. Tomasi, M. Cossi, N. Rega, N. J. Millam, M. Klene, J. E. Knox, J. B. Cross, V. Bakken, C. Adamo, J. Jaramillo, R. Gomperts, R. E. Stratmann, O. Yazyev, A. J. Austin, R. Cammi, C. Pomelli, J. W. Ochterski, R. L. Martin, K. Morokuma, V. G. Zakrzewski, G. A. Voth, P. Salvador, J. J. Dannenberg, S. Dapprich, A. D. Daniels, Ö. Farkas, J. B. Foresman, J. V. Ortiz, J. Cioslowski and D. J. Fox, Gaussian Inc., Wallingford CT, GAUSSIAN 09 edn., 2009.

28. C. Lee, W. Yang and R. G. Parr, *Phys. Rev. B: Condens. Matter.*, 1988, 37, 785-789.
29. A. D. Becke, *J. Chem. Phys.*, 1993, 98, 5648-5652.
30. A. D. Becke, *J. Chem. Phys.*, 1993, 98, 1372-1377.
31. P. J. Stephens, F. J. Devlin, C. F. Chabalowski and M. J. Frisch, *J. Phys. Chem.*, 1994, 98, 11623-11627.
32. G. E. Scuseria and H. F. Schaefer, *J. Chem. Phys.*, 1989, 90, 3700-3703.
33. A. Schäfer, H. Horn and R. Ahlrichs, *J. Chem. Phys.*, 1992, 97, 2571-2577.
34. A. Schäfer, C. Huber and R. Ahlrichs, *J. Chem. Phys.*, 1994, 100, 5829-5835.
35. L. Noodleman and J. G. Norman, *J. Chem. Phys.*, 1979, 70, 4903-4906.
36. L. Noodleman, *J. Chem. Phys.*, 1981, 74, 5737-5743.
37. L. Noodleman and E. R. Davidson, *Chem. Phys.*, 1986, 109, 131-143.
38. L. Noodleman and D. A. Case, *Adv. Inorg. Chem*, 1992, 38, 423-470.
39. J. J. Borrás-Almenar, J. M. Clemente-Juan, E. Coronado and B. S. Tsukerblat, *J. Comput. Chem.*, 2001, 22, 985-991.

Chapter Four

Layered Cu(II) Cages Using Polydentate Ligands with Premeditated High Binding Site Concentrations

4.1 Introduction

The strategic formation of predesigned ligands from their 'simpler' organic precursors closely followed by their metal complexation offers an important synthetic tool towards otherwise unattainable metal-ligand architectures of varying complexities. This procedure is commonly referred to as *subcomponent self assembly*[1] and represents a subtle extension upon the field of *template-directed synthesis*.[2] Other examples of subcomponent self assembly exist in the literature;[3-6] however the Nitschke group in particular have demonstrated that the Schiff base condensation of various aldehyde and amine moieties, driven by reversible C=N and M-N bond formation,[1] are versatile and ideal precursors towards the construction of numerous host-guest metal container complexes of varying topologies (Figure 100).[7, 8]

Figure 100 has been removed due to copyright restrictions and can be viewed in reference 7.

Indeed the '*in-situ*' formation of a ligand in the presence of a metal ion source has also prospered in the field of molecular magnetism. A number of polymetallic transition metal cages have been synthesised via more serendipitous pathways including a $[Mn_{14}]$ complex,[9] a $[Fe_{10}]$ complex[10] and a $[Dy_8]$ complex[11] reported by Anwar et al and Batten et al respectively. Similarly, in this chapter we investigate the in-situ ligand formation and subsequent Cu(II) ligation of the polydentate ligands *o*-[(*E*)-(2-Hydroxy-3-methoxyphenyl)methylideneamino]benzohydroxamic acid (L_3H_3), [[2-[(E)-(2-hydroxy-3-methoxy-phenyl)methyleneamino]benzoyl]amino]ethanimidate (L_4H_2) and *o*-[(*E*)-(*o*-Hydroxyphenyl)methylideneamino]benzohydroxamic acid (L_5H_3). These ligands are formed via an in-situ Schiff base condensation reaction of 2-(amino)phenylhydroxamic acid (L_2H_2) and either 2-hydroxy-3-methoxybenzaldehyde (for L_3H_3 and L_4H_2) or 2-hydroxybenzaldehyde (for L_5H_3) (Scheme 2 for L_3H_3 and L_5H_3 formation and Figure 106 for structure representation of L_4H_2). This research involves the combination of two of the most recently utilised ligand types in the Jones group (i.e. hydroxamic acids[12, 13] and phenolic imines[14-17]), towards the formation of ligands comprising several potential metal binding sites and subsequently the construction of polynuclear cages. It should also be noted that to the best of our knowledge the ligands L_3H_3, L_4H_2 and L_5H_3 are unknown in the literature in terms of their synthesis and their metal coordination complexes.

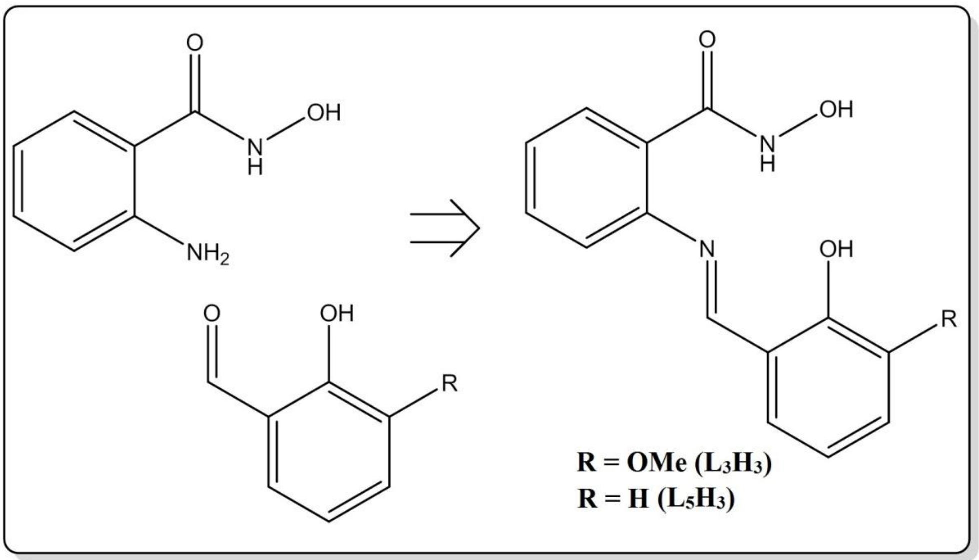

***Scheme 2** - Illustration of precursors (left) and Schiff base ligands L_3H_3 and L_5H_3 (right) utilised in this chapter.*

We herein present the premeditated in-situ formation of the polydentate ligands *o*-[(*E*)-(2-Hydroxy-3-methoxyphenyl)methylideneamino]benzohydroxamic acid (L_3H_3) and *o*-[(*E*)-(*o*-Hydroxyphenyl)methylideneamino]benzohydroxamic acid (L_5H_3) and the subsequent Cu(II) ligation towards the self-assembly of polynuclear cages. This chapter describes the synthesis and structure of a family of discrete Cu(II) cage complexes of formulae: $[Cu(II)_{10}(L_3)_4(L_2)_2(H_2O)_2](ClO_4)_4\cdot5MeOH\cdot H_2O$ (**13**), $[Cu(II)_{14}(L_3)_8(MeOH)_3(H_2O)_5](NO_3)_4\cdot2MeOH\cdot3H_2O$ (**15**), $[Cu(II)_{14}(L_5)_8(MeOH)_6(NO_3)_4(H_2O)_2]\cdot6MeOH\cdot10H_2O$ (**16**) and $[Cu(II)_{30}(O)_1(OH)_4(OMe)_2(L_3)_{16}(MeOH)_4(H_2O)_2](ClO_4)_4\cdot2MeOH\cdot27H_2O$ (**17**). Furthermore, slight alterations to the reaction scheme for **13** (the addition of CH_3CN) resulted in the unexpected formation of the Cu(II) 1D coordination polymer $\{[Cu(II)(L_4)]\cdot H_2O\}_n$ (**14**) (where L_4^{2-} = [[2-[(E)-(2-hydroxy-3-methoxy-phenyl)methyleneamino]benzoyl]amino]ethanimidate) (Figure 106).

4.2 Results and Discussion

4.2.1 Structural Descriptions

4.2.1.1 Formation of a Decanuclear Cu(II) Complex

The first complex to be synthesised in this work was the decametallic complex $[Cu(II)_{10}(L_3)_4(L_2)_2(H_2O)_2](ClO_4)_4\cdot5MeOH\cdot H_2O$ (**13**) (Figure 101) and was synthesised via the stirring reaction of a methanolic solution of $Cu(ClO_4)_2{\cdot}6H_2O$, a 1:1 equimolar mixture of L_3H_3 precursors 2-(amino)phenylhydroxamic acid and 2-hydroxy-3-methoxybenzaldehyde, in the presence of NaOH (see Scheme 2 for L_3H_3 formation). Upon slow evaporation of the dark green solution, X-ray quality crystals of **13** were formed in 5% yield. Complex **13** crystallises in the monoclinic $C2/c$ space group with unit cell parameters: a = 23.6341(10) Å, b = 25.5162(8) Å, c = 16.5739(9) Å, α = 90°, β = 104.244(5)°, γ = 90°. Complete single crystal X-ray diffraction data for complex **13** are given in Table 10 (Section 4.2.1.5). The formation of **13** adds to a relatively small number of discrete decametallic Cu(II) assemblies,[18-22] although there are a small number of wheel-like decanuclear Cu(II) architectures residing in the literature.[23, 24]

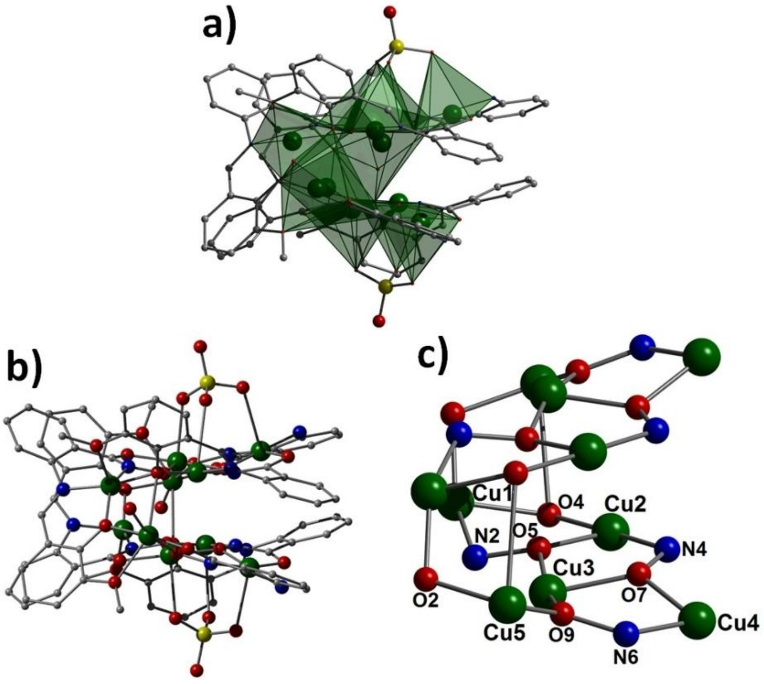

***Figure 101** - (a) Polyhedral and (b) regular representation of the crystal structure in **13**. (c) Crystal structure of the metallic core in **13**. All hydrogen atoms and solvents of crystallisation have been omitted for clarity. The ClO_4^- counter anions have been removed from figure c. Colour code: green (Cu), red (O), blue (N), grey (C) and yellow (Cl).*

The core of **13** comprises two near planar $\{Cu_5\}$ sheets which arrange in an offset manner and are linked via long Cu-O contacts (e.g. Cu5-O4 = 2.776 Å) and bridging phenoxy oxygen atoms (e.g. Cu1-O2 = 1.936(6) Å), resulting in the formation of an unusual taco-shaped topology (Figure 101 and 102).

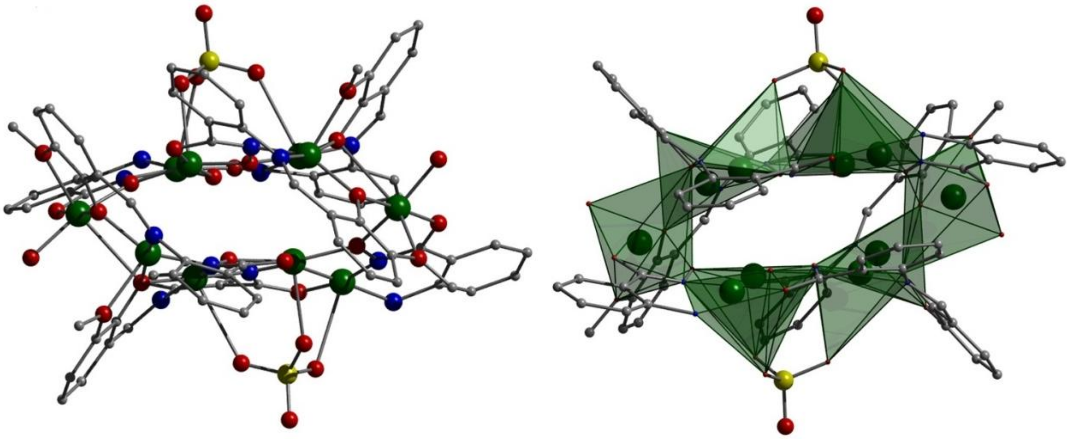

Figure 102 *- Alternative views of complex **13** as viewed along its tubular topology. Hydrogen atoms have been omitted for clarity. Colour code as in Figure 101 and used throughout this chapter.*

The Cu(II) ions of each {Cu_5} layer form three distorted edge sharing triangles, whereby the edges are occupied by 2 x L_3^{3-} ligands and a single 2-(amino)phenylhydroxamic acid (L_2^{2-}) moiety (precursor ligand to the formation of L_3H_3). Interestingly, complex **13** possesses two ligand units in the form of the L_3^{3-} and L_2^{2-} bridging anions, which are consistently present even with variation of the synthetic reaction. On the other hand, their later siblings (complexes **15-17**) contain only the premeditated Schiff base ligands L_3^{3-} (in **15** and **17**) or L_5^{3-} (in **16**). The four L_3^{3-} ligands in **13** utilise a $\eta^1:\eta^2:\eta^1:\eta^1:\eta^2:\eta^1-\mu_4$ bonding motif as highlighted in Figure 103.

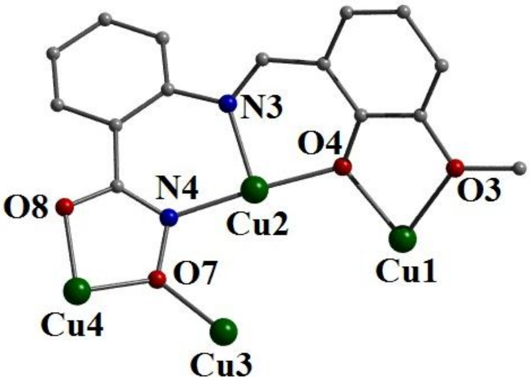

Figure 103 *- The $\eta^1:\eta^2:\eta^1:\eta^1:\eta^2:\eta^1$-$\mu_4$ coordination mode utilised via L_3^{3-} in complex **13**. All hydrogen atoms have been removed for clarity.*

The metal centres Cu1, Cu3 and Cu4 (and their s.e.) all display distorted square based pyramidal geometries with τ values of 0.36, 0.11, 0.14 respectively.[25] The Cu(II) metal centre labelled Cu1 (and its s.e.) are coordinated at three equatorial positions via a chelating L_3^{3-} ligand with Cu1-N2 (1.906(8) Å), Cu1-O2 (1.936(6) Å) and Cu1-N1

(1.955(8) Å) bonds. The remaining equatorial position is occupied by a second L_3^{3-} moiety via its phenolic oxygen atom (O4) resulting in a Cu1-O4 bond length of 2.026(6) Å. Coordination at Cu1 is completed at the axial position via a methoxy group of a second L_3^{3-} ligand moiety with a Cu1-O3 bond length of 2.258(7) Å. Two of the equatorial positions at Cu4 (and its s.e.) are occupied by oxygen atoms (O7 and O8) of a chelating L_3^{3-} moiety, while a chelating L_2^{2-} ligand coordinates via its nitrogen atoms (N5 and N6) at the other two equatorial sites, resulting in bond lengths in the range of 1.872(7)-1.939(7) Å. The Cu3 metal centre (and its s.e.) coordinate to three separate ligand moieties at its equatorial sites. Firstly, to a chelating L_3^{3-} ligand via its oxygen atoms Cu3-O5 (1.898(6) Å) and Cu3-O6 (1.937(7) Å). Secondly, to a second L_3^{3-} moiety via Cu3-O7 (1.904(7) Å), further enhancing the linkage between Cu3 and Cu4 (and their s.e.) metal centres. Finally, the remaining equatorial position is occupied via an oxygen atom (O9) of a L_2^{2-} ligand group with a resultant Cu3-O9 bond length of 1.956(6) Å. Both Cu(II) ions exhibit long axial close contacts via oxygen atoms of a nearby ClO_4^- counter anion with bond lengths of 2.436(8) (Cu3-O17) and 2.787 Å (Cu4-O18). The Cu2 metal centre (and its s.e.) possesses a distorted square planar geometry, whereby three of the equatorial positions are occupied via a chelating L_3^{3-} ligand and the final equatorial position is filled by a O-donor (O5) atom of a second L_3^{3-} moiety. However, it should be noted that at the axial site of Cu2 a very long Cu-O contact via the aforementioned perchlorate counter anion exists with a bond length of 2.876 Å (Cu2-O19). The Cu5 metal centre (and its s.e.) display a Jahn-Teller distorted octahedral geometry via two axially elongated Cu-O bonds (Cu5-O1 = 2.225(8) Å and Cu5-O4 = 2.776 Å). An L_2^{2-} moiety coordinates to Cu5 at two of the equatorial positions (Cu5-O10 = 1.879(7) Å and Cu5-O9 = 1.955(6) Å), while a phenolic oxygen atom of a L_3^{3-} ligand binds at the third equatorial site (Cu5-O2 = 1.958(6) Å). Finally, the distorted octahedral geometry at Cu5 is completed at its remaining equatorial position via a terminal H_2O ligand (Cu5-O11 = 1.975(7) Å). Despite the close proximity of the $\{Cu_5\}$ units in **13**, no formal intra-molecular π-π interactions are observed between their respective L_3^{3-} and L_2^{2-} aromatic rings. The $\{Cu(II)_{10}(L_3)_4(L_2)_2(H_2O)_2\}^{4+}$ cations are charge balanced via two sets of symmetry equivalent ClO_4^- counter anions, whereby one set directly binds to the $\{Cu_{10}\}$ cage through long Cu-O contacts (Cu3-O17 = 2.436(8) Å and Cu4-O18 = 2.787 Å), while the second set of ClO_4^- counter anions are located more towards the periphery of the structure. The first set of ClO_4^- counter anions are held in place via hydrogen bonding interactions with aromatic protons (e.g. Cl1(O16)···(H27)C27 = 2.533 Å, Cl1(O19)···(H18)C18 = 2.443 Å and Cl1(O19)···(H32)C32 = 2.444 Å), while the second set of ClO_4^- counter anions are hydrogen bonded in place via aromatic and aliphatic protons (e.g. Cl2(O14)···(H5)C5 = 2.677 Å, Cl2(O13)···(H10)C10 = 2.574 Å, Cl2(O14)···(H8)C8 = 2.684 Å). In addition, hydrogen bonding interactions are also observed between ClO_4^- counter anions and MeOH (e.g. Cl1(O17)···(H40A)C40 = 2.609 Å) or H_2O solvents of crystallisation (e.g. Cl2(O12)···O25 = 2.788 Å). These MeOH and H_2O solvent molecules, along with the perchlorate counter anions, connect the individual $\{Cu_{10}\}$ units and therefore act as molecular mortar within the unit cell in **13** (e.g. C90(H90C)···C26 = 2.797 Å, C40(O22)···(H27)C27 = 2.653 Å and O11···O25 = 2.646 Å). The individual $[Cu_{10}]$ moieties in **13** arrange themselves into a space efficient brickwork motif along the *ab* plane of the unit cell and these sheets then stack in parallel off-set rows along the *c* cell direction (Figure 104).

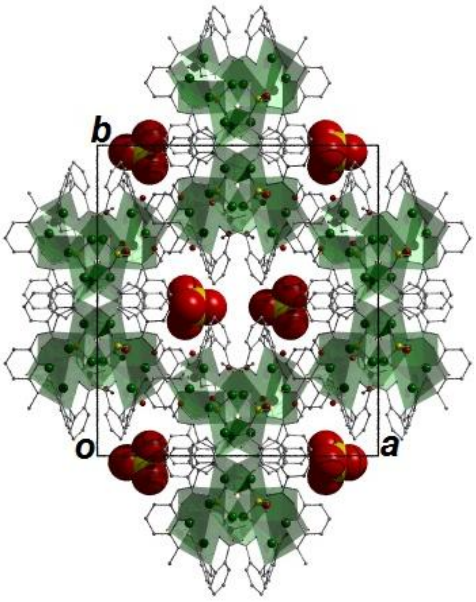

Figure 104 *- Crystal packing of* ***13*** *as viewed down the c axis of the unit cell. Note that only the non-coordinated perchlorate counter anions are represented in space-fill mode. Hydrogen atoms have been omitted for clarity.*

4.2.1.2 Further Attempts Towards Decanuclear Cu(II) Complexes

In Chapters 2 and 3 we successfully exchanged terminally bound solvent ligands (MeOH) with pyridine moieties in a controlled manner towards an increase in the coordination number at the M(II) centres (where M(II) = Cu(II) and Ni(II)). Here, we wished to investigate whether or not the $[Cu_{10}]$ topology in **13** would be maintained upon addition of pyridine. By simply adding pyridine to the synthetic procedure for complex **13**, we were able to produce its pyridine analogue with an approximate formula of $[Cu(II)_{10}(L_3)_6(MeOH)_2(H_2O)_2](ClO_4)_2 \cdot pyr \cdot MeOH$ (**13′**) (Figure 105). Interestingly the incorporated pyridine solvent molecule does not actually directly coordinate to the $[Cu_{10}]$ core and is only present as a solvent of crystallisation. As a consequence of the addition of pyridine, a number of alterations are observed to the $[Cu_{10}]$ core. For example, the decametallic units only possess one organic building block unit in the form of L_3^{3-} and two types of coordination motifs are utilised to bridge the Cu(II) metal centres ($\eta^1:\eta^1:\eta^1:\eta^1:\eta^2-\mu_3$ and $\eta^1:\eta^2:\eta^1:\eta^1:\eta^1:\eta^2-\mu_4$). In addition, the perchlorate counter anions have been relocated to the periphery of the $[Cu_{10}]$ and thus no longer act as close contacts to any Cu(II) metal centres. Single crystal X-ray diffraction data for complex **13'** can be seen in Table 10 (Section 4.2.1.5). However, it should be noted that despite many attempts, we were only able to obtain crystals with relatively poor diffraction data and therefore the crystallographic data and figures produced for complex **13'** are only used for the purposes of showing connectivity.

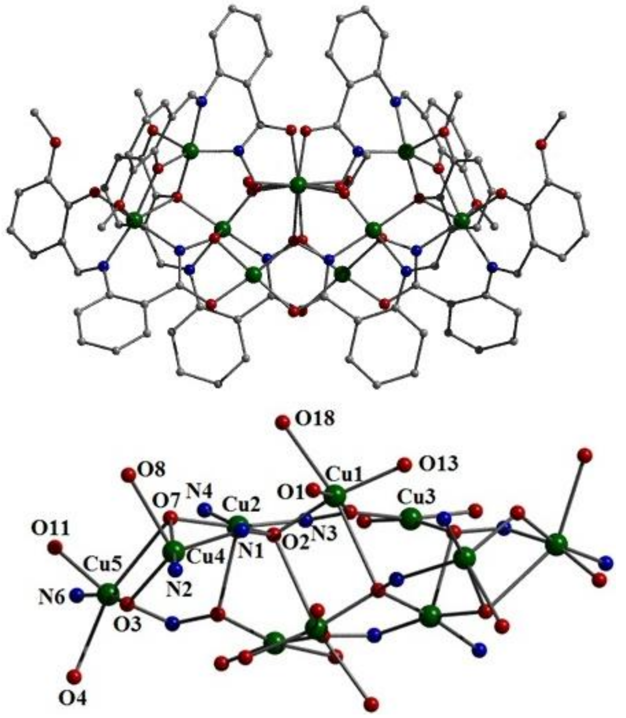

Figure 105 *- (Top) Crystal structure of the $[Cu_{10}]$ pyridine complex* ***13′****. (Bottom) Metallic core of* ***13′****. All hydrogen atoms, pyridine solvents of crystallisation and ClO_4^- counter anions have been removed for clarity.*

We decided to alter the reaction scheme slightly in the hopes of obtaining better quality X-ray crystals of **13′**. The addition of pyridine to a methanolic reaction mixture comprising $Cu(ClO_4)_2 \cdot 6H_2O$, 2-(amino)phenylhydroxamic acid, 2-hydroxy-3-

methoxybenzaldehyde and NaOMe was evaporated to dryness under reduced pressure (to aid Schiff base condensation) and the resultant powder re-crystallised using acetonitrile. The result was the rather unexpected 1D coordination polymer: $\{[\mathrm{Cu(II)}(\mathrm{L}_4)]\cdot\mathrm{H}_2\mathrm{O}\}_n$ (**14**) (where L_4^{2-} = [[2-[(E)-(2-hydroxy-3-methoxy-phenyl)methyleneamino]benzoyl]amino]ethanimidate) (Figure 106). Interestingly and rather unexpectedly, the addition of MeCN as the solvent in the reaction mixture for **14** results in the addition of a MeCN group at the hydroxyl position of the hydroxamate moiety, thus introducing an ethanimidate functionality resulting in a pseudo macrocycle that is stabilised by Cu(II) ligation (Figure 106). Indeed, Tolman et al report the attachment of MeCN to a pyrazolyl ring via a Cu-mediated cycloaddition reaction, resulting in a novel heterocyclic ring system.[26] Complex **14** crystallises in the monoclinic *C*2/*c* space group with unit cell parameters: a = 36.1459(12) Å, b = 5.2200(2) Å, c = 18.0068(7) Å, α = 90.0°, β = 101.697(3)°, γ = 90.0°. Complete single crystal X-ray diffraction data for complex **14** are given in Table 10 (Section 4.2.1.5).

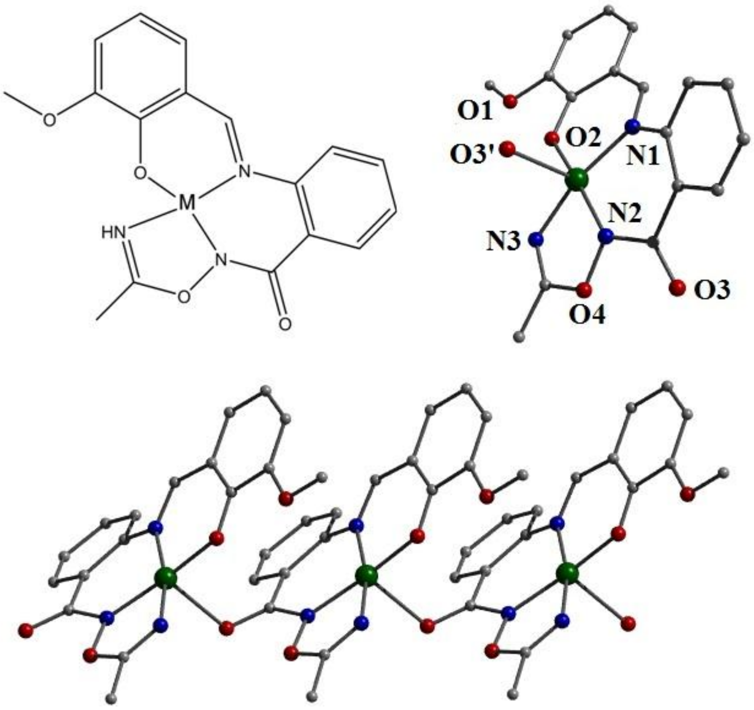

Figure 106 *- (Top left) Structure representation of the metal ligated L_4^{2-} moiety. (Top right) Crystal structure of one [Cu(II)(L_4)] unit in **14** including the next bridging oxygen O3 atom. (Bottom) Representation of the repeating 1D structure in **14** (comprising three [Cu(II)(L_4)] units). Hydrogen atoms and H_2O solvents of crystallisation have been omitted for clarity.*

L_4^{2-} utilises a $\eta^1:\eta^1:\eta^1:\eta^1$-μ coordination motif towards the formation of **14**. The Cu(II) centres display an almost perfect square based pyramidal geometry with a τ value of 0.016.[25] The equatorial positions at the Cu1 metal centre (and its s.e.) are occupied by a single chelating L_4^{2-} ligand moiety via the phenolic oxygen atom (O2), the imine nitrogen atom (N1), the nitrogen atom of the hydroxamate functional group (N2) and the nitrogen atom of the ethanimidate group (N3), resulting in bond lengths ranging between 1.921(16) and 1.970(19) Å. The coordination is completed at the axial position of the Cu1 centre via the carbonyl oxygen atom (O3) of a second L_4^{2-} ligand with a Cu1-O3' bond length of 2.338(17) Å, resulting in the formation of a 1D coordination polymer, with an intra-chain Cu1···Cu1 distance of 5.220 Å. Hydrogen bonding interactions occur between the H_2O solvent of crystallisation and aliphatic protons of nearby L_4^{2-} ligand moieties (e.g. O5···N3(H3H) = 2.142 Å and O5···(H1B)C1 = 2.716 Å), as well as oxygen atoms of the L_4^{2-} ligand (e.g. O5(H5A)···O2 = 2.303 Å and O5(H5A)···O1 = 2.206 Å). Furthermore, the H_2O solvents of crystallisation take part in inter-molecular hydrogen bonding interactions with each other (i.e. O5···(H5B')O5' = 2.151 Å). Inter-molecular hydrogen bonding is also observed between aliphatic protons of the ethanimidate group of one L_4^{2-} ligand and oxygen atoms of a second L_4^{2-} ligand (e.g. C17(H17B)···O4' = 2.684 Å and C17(H17A)···O3' = 2.647 Å). The individual 1D rows in **14** propagate along the *b* axis of the unit cell in a superimposable manner and these rows then pack into a common brickwork motif (Figure 107).

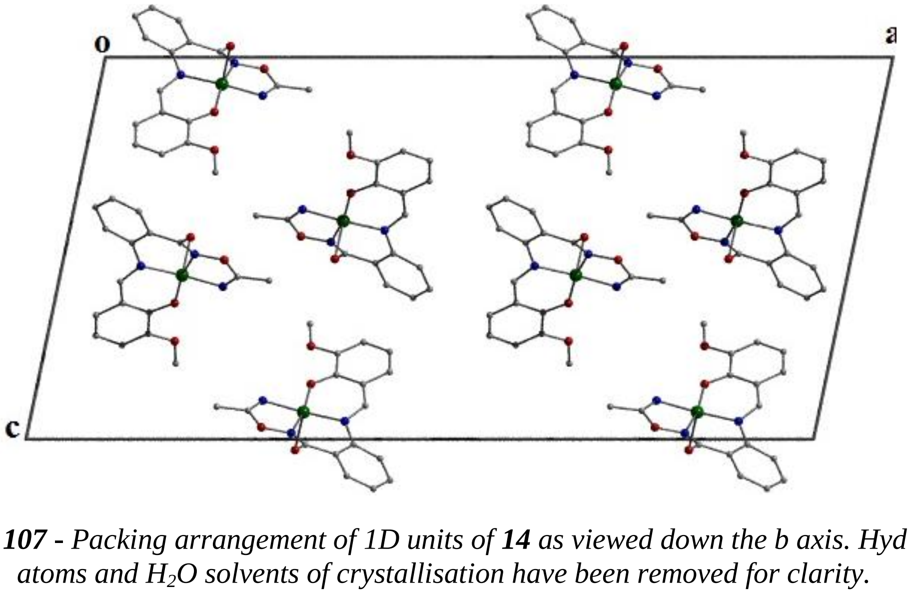

Figure 107 *- Packing arrangement of 1D units of* ***14*** *as viewed down the b axis. Hydrogen atoms and H_2O solvents of crystallisation have been removed for clarity.*

4.2.1.3 From Decanuclear to Tetradecanuclear Cu(II) Complexes

The methanolic reaction of $Cu(NO_3)_2 \cdot 3H_2O$ and precursors for L_xH_3 ($x = 3$ (**15**), $x = 5$ (**16**)) in the presence of NaOH resulted in the formation of the analogous complexes $[Cu(II)_{14}(L_3)_8(MeOH)_3(H_2O)_5](NO_3)_4 \cdot 2MeOH \cdot 3H_2O$ (**15**) and $[Cu(II)_{14}(L_5)_8(MeOH)_6(NO_3)_4(H_2O)_2] \cdot 6MeOH \cdot 10H_2O$ (**16**) (Figures 108 and 109). The formation of the homovalent $[Cu(II)_{14}]$ complexes adds to a relatively small group of tetradecametallic copper clusters. One of these members is a homovalent $[Cu(I)_{14}(\mu_6\text{-}S)(\mu_3\text{-}SPhMe\text{-}4)_{12}(PPh_3)_6]$ cage reported by Zhang et al,[27] while the remaining members are mixed valent $[Cu(I/II)_{14}]$ cages.[28-32] Complex **15** crystallises in the triclinic $P\text{-}1$ space group with unit cell parameters: a = 15.4185(6) Å, b = 22.8429(7) Å, c = 25.1092(9) Å, α = 71.435(3)°, β = 77.204(3)°, γ = 80.405(3)°. Complex **16** crystallises in the monoclinic $P2_1/c$ space group with unit cell parameters: a = 18.989(4) Å, b = 13.838(3) Å, c = 26.748(5) Å, α = 90.00°, β = 91.05(3)°, γ = 90.00°. Complete single crystal X-ray diffraction data for complexes **15** and **16** are given in Table 10 and 11 (Section 4.2.1.5) respectively.

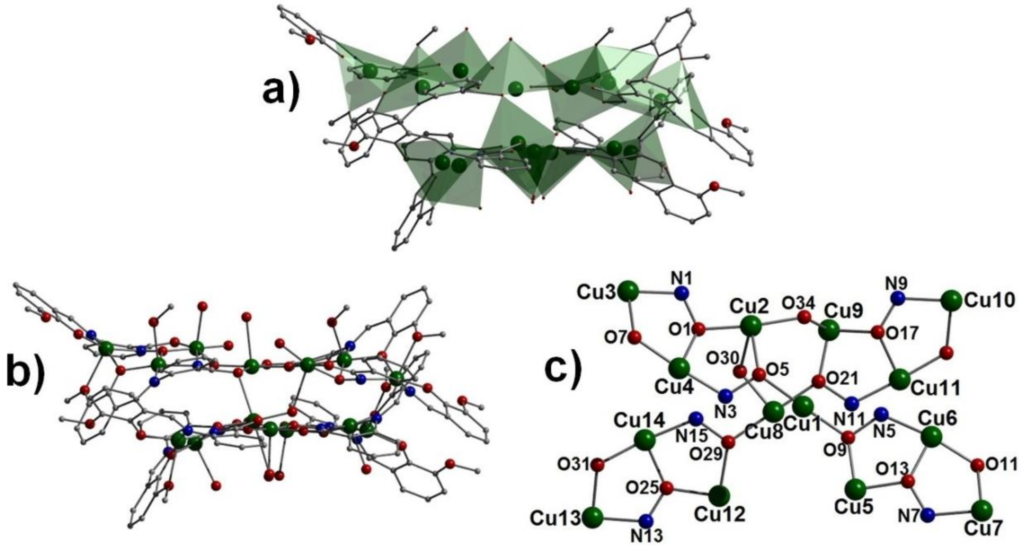

***Figure 108** - (a) Polyhedral and (b) regular representation of the crystal structure in **15**. (c) The metallic core in **15**. All hydrogen atoms, solvents of crystallisation and nitrate counter anions have been omitted for clarity.*

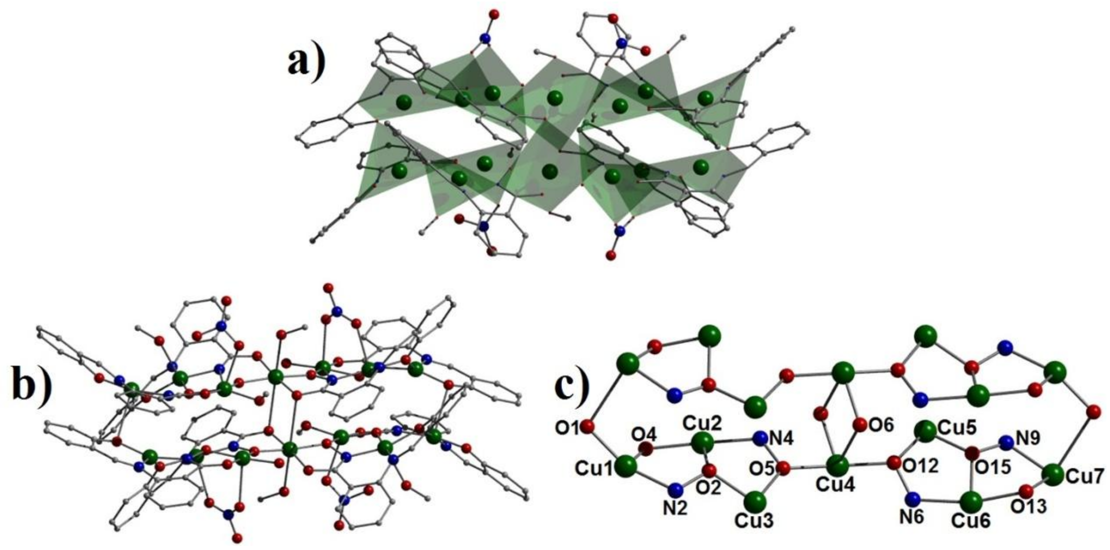

***Figure 109** - (a) Polyhedral and (b) regular representation of the crystal structure in **16**. (c) The inorganic core in **16**. All hydrogen atoms and solvents of crystallisation have been removed for clarity.*

Akin to the structure in **13**, complexes **15** and **16** display layered structures, which comprise two $\{Cu_7\}$ units as opposed to the $\{Cu_5\}$ units in **13** (Figures 108 and 109). The contrast in symmetries of **15** and **16** is highlighted by the stacking arrangements of the $\{Cu_7\}$ units in relation to one another. For instance, the two heptanuclear $\{Cu_7\}$ units in **16** stack directly on top of one another in a pseudo superimposable fashion, while the two $\{Cu_7\}$ units in **15** sit at approximate right angles to one another (Figure 110). Furthermore the L_3^{3-} ligands in **15** utilise two coordination modes in the form of $\eta^1:\eta^2:\eta^1:\eta^1:\eta^2:\eta^1\text{-}\mu_4$ and $\eta^1:\eta^2:\eta^1:\eta^1:\eta^1\text{-}\mu_3$ towards the construction of their $\{Cu_7\}$ units, while the L_5^{3-} moieties in **16** employ the $\eta^1:\eta^2:\eta^1:\eta^1:\eta^2\text{-}\mu_4$ and $\eta^1:\eta^2:\eta^1:\eta^1:\eta^1\text{-}\mu_3$ bonding motifs in their construction (Figure 111). That being said, complexes **15** and **16** also share many similarities. For example, the Cu(II) centres within each $\{Cu_7\}$ unit in **15** and **16** comprise two triangular arrays joined by a central cupric ion (Cu1 and Cu8 in each $\{Cu_7\}$ unit respectively in **15** and Cu4 in **16**). The $\{Cu_7\}$ planes in **15** and **16** are then linked via long axial Cu-O contacts (i.e. Cu2-O30 = 2.697 Å and Cu9-O34 = 2.480 Å in **15**; Cu4-O6' = 2.856 Å and Cu7-O1 = 2.721 Å in **16**), resulting in their final tetradecametallic topologies (Figure 108 and 109). The majority of Cu(II) metal centres in **15** exhibit square based pyramidal geometries (τ value range: 0.002-0.231),[25] while Cu2 and Cu9 display distorted octahedral geometries via long contacts with H_2O, carbonyl oxygen atoms and methanol ligands respectively (i.e. Cu2-O50A = 2.767 Å, Cu2-O30 = 2.697 Å and Cu9-O40 = 2.763 Å). Nitrate counter anions act as close contacts to the Cu1 and Cu8 metal centres, completing their square based pyramidal geometries at the axial positions (Cu1-O60A = 2.537 Å, Cu8-O49A = 2.752 Å). Terminal H_2O ligands complete coordination spheres in Cu4, Cu5, Cu9 and Cu12 metal centres (e.g. Cu4-O35 = 2.378(6) Å, Cu5-O36 = 2.314(7) Å and Cu5-O37 = 1.958(5) Å). Furthermore, terminally bound methanol ligands are observed at the axial positions of Cu6 and Cu14 metal centres (Cu6-O60B = 2.379(12) Å and Cu14-O43 = 2.311(5) Å). In complex **16**, the Cu1 metal centre (and its s.e.) exhibits a distorted square planar geometry, while the remaining Cu(II) metal centres display distorted square based pyramidal geometries with τ values of 0.047 (Cu2), 0.049 (Cu3), 0.0503 (Cu4), 0.262 (Cu5), 0.161 (Cu6) and 0.16 (Cu7).[25] Coordination is completed at metal centres Cu4 and Cu6 (and s.e.) via terminal methanol solvent ligands (Cu4-O43 = 2.521(12) Å and Cu6-O21 = 2.309(9) Å), while the nitrate counter anions form long contacts with metal centres Cu2, Cu3 and Cu5 (Cu2-O7 = 2.362(9) Å, Cu3-O9 = 2.466 Å and Cu5-O17 = 2.348(10) Å).

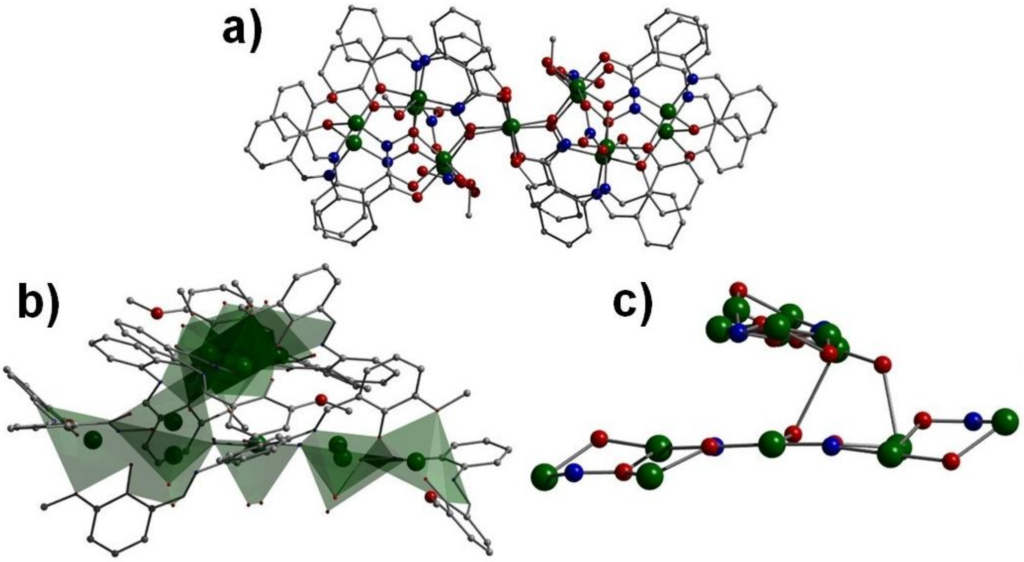

Figure 110 *- Crystal structures of a) the pseudo superimposable stacking arrangement of {*Cu_7*} units in* ***16*** *as opposed to b) and c) the criss-cross orientation of the {*Cu_7*} planes in* ***15****. Hydrogen atoms and solvents of crystallisation have been omitted for clarity.*

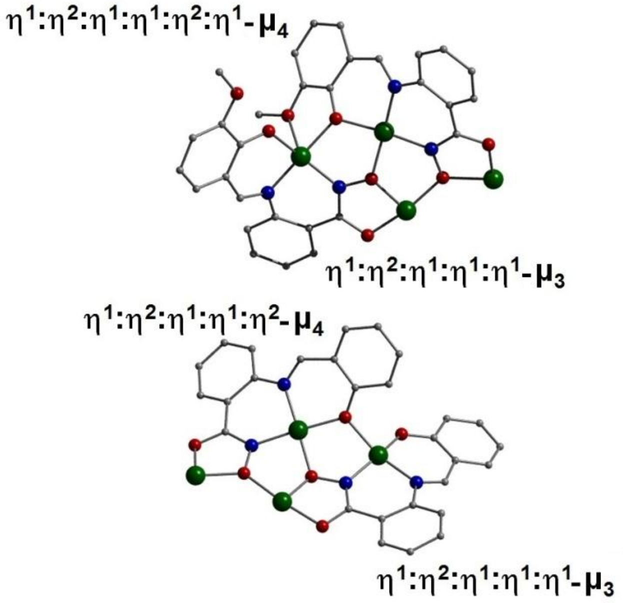

***Figure 111** - Crystal structures highlighting the two coordination modes utilised by L_3^{3-} in **15** (top) and L_5^{3-} in **16** (bottom). Hydrogen atoms have been removed for clarity.*

In complex **15**, inter-molecular interactions are observed between ligated H_2O molecules and unbound NO_3^- counter anions (O50A···O53A = 2.538 Å). Similarly, MeOH solvents of crystallisation interact with unbound NO_3^- counter anions (O45(H45)···O53A = 1.845 Å and O46(H46)···O50 = 2.050 Å). Furthermore, a network of MeOH and H_2O solvents of crystallisation along with unbound NO_3^- counter anions interact with adjacent {Cu_{14}} units in **15**, thus acting as molecular mortar within the unit cell (e.g. O45···O34 = 2.654 Å, O102···O35 = 2.555 Å and O52···(H25)C25 = 2.578 Å). Intra-molecular interactions are also observed between terminal H_2O ligands and juxtaposed carbonyl oxygen atoms (e.g. O41···O22 = 2.591 Å). The individual {Cu_{14}} units in **15** arrange in superimposable rows along the *a* direction of the unit cell and pack along the *bc* plane in the familiar brickwork pattern, while partaking in weak inter-chain $\pi_{centroid}\cdots\pi_{centroid}$ interactions (i.e. [C99-C104]···[C99′-C104′] = 4.361 Å) (Figure 112-left).

Complex **16** exhibits intra-molecular interactions between metal bound NO_3^- counter anions and metal bound methanol ligands (e.g. O21(H21A)···O18 = 2.042 Å), as well as with methanol solvents of crystallisation (e.g. O8···O42 = 2.777 Å). Furthermore, H_2O solvents of crystallisation are positioned in-between the {Cu_{14}} moieties and effectively connect the individual tetradecametallic units to one another via hydrogen bonding interactions in conjunction with: *1)* Cu(II) bound methanol ligands (e.g. O43(H43)···O47 = 2.200 Å); *2)* H_2O ligands (e.g. O10···O40 = 2.544 Å) and *3)* NO_3^-

ligands (e.g. O8···O45 = 2.790 Å). In addition, a close intra-molecular contact is displayed between the carbonyl O atoms (O11) of the L_5^{3-} ligands and adjacent terminal water ligands (O11···O10 = 2.584 Å). The $\{Cu_{14}\}$ moieties in **16** arrange in superimposable rows along the *c* direction of the unit cell and exhibit weak inter-chain $\pi_{centroid}\cdots\pi_{centroid}$ interactions (i.e. [C43-C48]···[C50-C55] = 4.508 Å). These individual rows pack in a space efficient brickwork motif along the *ab* plane (Figure 112-right).

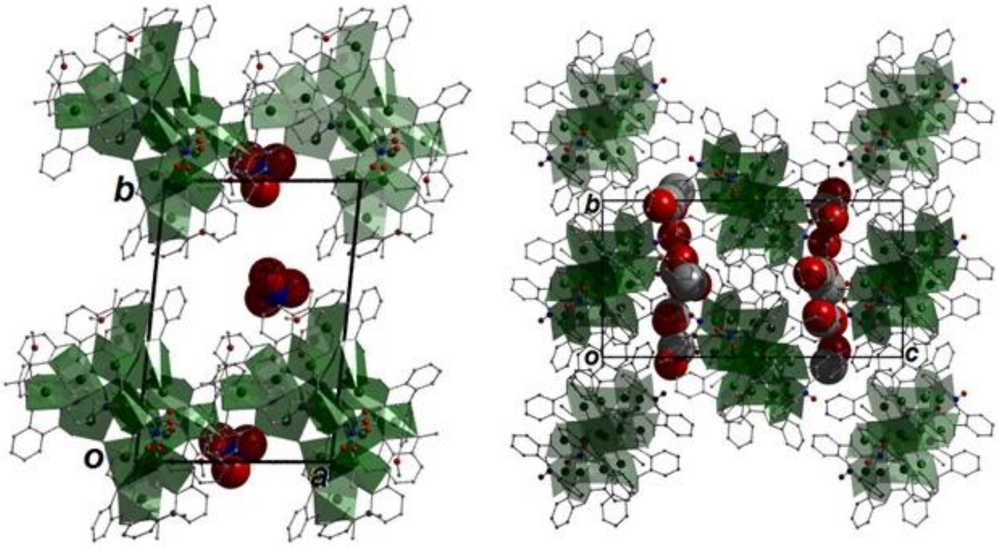

Figure 112 *- (Left) Crystal packing diagram of* ***15*** *as viewed along the c axis of the unit cell. Non-coordinated* NO_3^- *counter anions are represented in space-fill mode. (Right) Packing arrangement in* ***16*** *as viewed along the a axis of the unit cell. Methanol solvents of crystallisation are exhibited in space-fill mode. Hydrogen atoms have been omitted for clarity.*

4.2.1.4 Formation of a Cu(II) Super Cage Topology

In order to determine the influence of different reaction conditions on the formation and topology of our Cu(II) cages, we decided to attempt to repeat the synthetic reaction for complex **13** under solvothermal conditions. The solvothermal heating of the reactants used previously in the formation of complex **13** resulted in the formation of the triacontametallic complex $[Cu_{30}(O)_1(OH)_4(OMe)_2(L_3)_{16}(MeOH)_4(H_2O)_2](ClO_4)_4\cdot 2MeOH\cdot 27H_2O$ (**17**) (Figure 113). There are a number of extremely large copper-chalcogenide nanocluster structures known in the literature,[33-37] for example the incredible $[Cu_{136}S_{56}(SCH_2C_4H_3O)_{24}(dpppt)_{10}]$ cage (where dpppt = 1,5-bis(diphenylphosphino)pentane).[38] However, excluding these compound types, our $[Cu_{30}]$ complex (**17**) is one of the largest O-donor Cu(II) cages known in the literature. It is only defeated by the impressive $[Cu(II)_{36}]$ and $[Cu(II)_{44}]$ cages of formulae

$[K_4(\mu\text{-MeOH})_4[Cu(II)_{36}(\mu_3\text{-OH})_{32}(\mu\text{-OR})_8Cl_6(ndpa)_8(H_2O)_5\{KCl_6\}]$ (where R is H or Me and H_3ndpa = (nitrilodipropionic)acetic acid)[39] and $[Cu(II)_{44}(\mu_8\text{-Br})_2(\mu_3\text{-OH})_{36}(\mu\text{-OH})_4(ntp)_{12}Br_8(H_2O)_{28}]Br_2\cdot 81H_2O$ (where H_3ntp = aminopolycarboxylate nitrilotripropionic acid),[40] synthesised by Powell and co-workers. Complex **17** crystallises in the triclinic *P*-1 space group with unit cell parameters: a = 18.6255(5) Å, b = 20.6535(7) Å, c = 38.2976(12) Å, α = 92.913(3)°, β = 99.064(3)°, γ = 103.632(3)°. Complete single crystal X-ray diffraction data for complex **17** are given in Table 11 (Section 4.2.1.5).

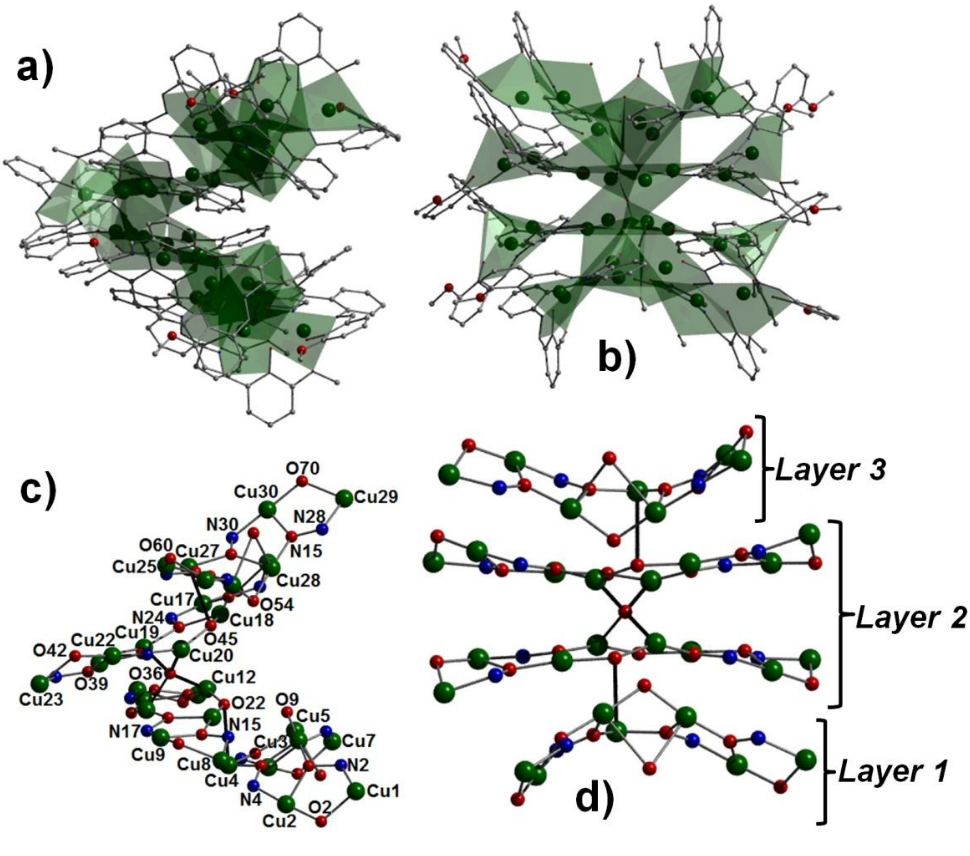

Figure 113* - (*a* and *b*) *Two polyhedral perspectives of the* $[Cu_{30}]$ *cluster in* ***17*. All hydrogen atoms,* ClO_4^- *counter anions and solvents of crystallisation have been removed for clarity. (****c*** *and* ***d****) Crystal structure of the inorganic core in* ***17*** *from two viewpoints. Figure* ***d*** *exhibits the three distinct near planar layers which comprise the core of* ***17****. The long Cu-O contacts are represented by thick black lines.*

Similarly to siblings (**13**, **15** and **16**), the core of **17** consists of a layered structure. More specifically, a central $\{Cu_{16}(O)(OH)_4(L_3)_8\}^{2+}$ unit (layer 2 in Figure 113d) forms a platform which is sandwiched between two offset $\{Cu_7(OMe)(L_3)_4(MeOH)_2(H_2O)_x\}^+$ layers (x = 0 in layer 1; x = 2 in layer 3; Figure 113d), resulting in a Pac-Man shaped $[Cu_{30}]$ superstructure in **17** (Figure 113a and 113b). Furthermore, the central $\{Cu_{16}\}$ moiety can also be described as comprising two near planar {Cu_8} sub-moieties, connected via a centrally located and tetrahedrally distorted μ_4- bridging O^{2-} anion (O36; Figure 113c). The metal centres within each {Cu_8} moiety are connected together via two μ-bridging OH^- ions (labelled O22, O31, O45 and O57) in conjunction with four L_3^{3-} organic ligands displaying 1:1 distribution of the coordination modes η^1:η^2:η^1:η^1:η^2:η^1-μ_4 and η^1:η^2:η^1:η^1:η^1-μ_3 (Figure 114). In addition, these coordination motifs are also utilised by the four L_3^{3-} ligands that bridge the metal centres within each of the {Cu_7} moieties in **17**. Moreover, these heptanuclear inorganic core units can be described as puckered versions of the {Cu_7} units observed in siblings **15** and **16** (Figure 108 and 109 *cf.* Figure 113d). Within each heptanuclear fragment, a single μ-OMe^- ion reinforces cage formation via O9 (i.e. O9-Cu5 = 1.902(9) Å and O9-Cu3 = 1.919(9) Å) and O73 (i.e. O73-Cu26 = 2.480 Å and O73-Cu28 = 2.545 Å), respectively. Two terminal H_2O ligands via O75 and O76 complete the coordination spheres at metal centres Cu3, Cu5 and Cu6 (Cu3-O76 = 2.574 Å, Cu5-O76 = 2.514 Å, Cu6-O75 = 2.481 Å). In the same way, terminal MeOH ligands complete coordination at metal centres labelled Cu2 (Cu2-O74 = 2.541 Å), Cu4 (Cu4-O85 = 2.630 Å), Cu25 (Cu25-O61 = 2.328(10) Å), Cu26 (Cu26-O73 = 2.480 Å) and Cu28 (Cu28-O73 = 2.545 Å). The two {Cu_7} moieties in **17** are connected to the {Cu_{16}} mainframe via characteristically long Cu-O contacts via μ-bridging OMe^- groups (e.g. Cu4-O22 = 2.673 Å and Cu27-O45 = 2.689 Å) and oxygen atoms of L_3^{3-} ligands (e.g. Cu28-O46 = 2.691 Å and Cu3-O21 = 2.752 Å). Three of the Cu(II) centres in **17** display distorted octahedral geometry (Cu3, Cu4, Cu28), while the remaining 27 metal centres exhibit distorted square planar or square based pyramidal geometries. More specifically, the majority of Cu(II) metal centres within the central {Cu_{16}} belt exhibit distorted square planar geometries, while a distorted square based pyramidal geometry dominates within the two {Cu_7} moieties in **17** (τ values ranging from 0.017 (Cu26) to 0.298 (Cu1)).

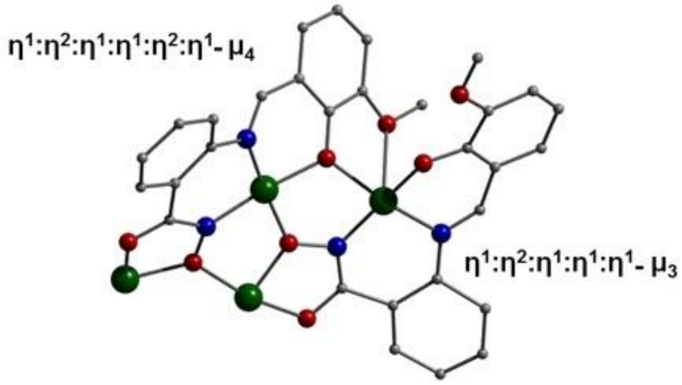

Figure 114 *- Illustration of the two types of coordination motifs utilised by* L_3^{3-} *in complex* ***17****. All hydrogen atoms have been omitted for clarity.*

The $\{Cu(II)_{30}(O)_1(OH)_4(OMe)_2(L_3)_{16}(MeOH)_4(H_2O)_2\}^{4+}$ cations in **17** are charged balanced by four crystallographically unique ClO_4^- counter anions located at the periphery of the $\{Cu_{30}\}$ structure. Here, they are held in place by hydrogen bonding interactions via adjacent L_3^{3-} ligand protons (e.g. Cl1(O90)···(H338)C338 = 2.414 Å, Cl4(O80)···(H271)C271 = 2.498 Å and Cl3(O66)···(H40)C40 = 2.654 Å). No obvious intra-molecular interactions are observed within the $[Cu_{30}]$ cage in **17**; however this is compensated by inter-molecular exchange interactions. For instance, the methanol and water solvents of crystallisation located at the periphery of the structure partake in inter-molecular interactions with one another (e.g. O96(H96)···O72 = 1.778 Å). Furthermore, inter-molecular hydrogen bonding interactions occur between ClO_4^- counter anions and methanol solvents of crystallisation (e.g. O95(H95A)···O133 = 2.639 Å) and H_2O solvents of crystallisation (e.g. Cl4(O81)···O72 = 2.893 Å). Individual $\{Cu_{30}\}$ units form rows along the *b* cell direction (Figure 115). Within these rows individual $\{Cu_{30}\}$ moieties form in a superimposable manner to one another.

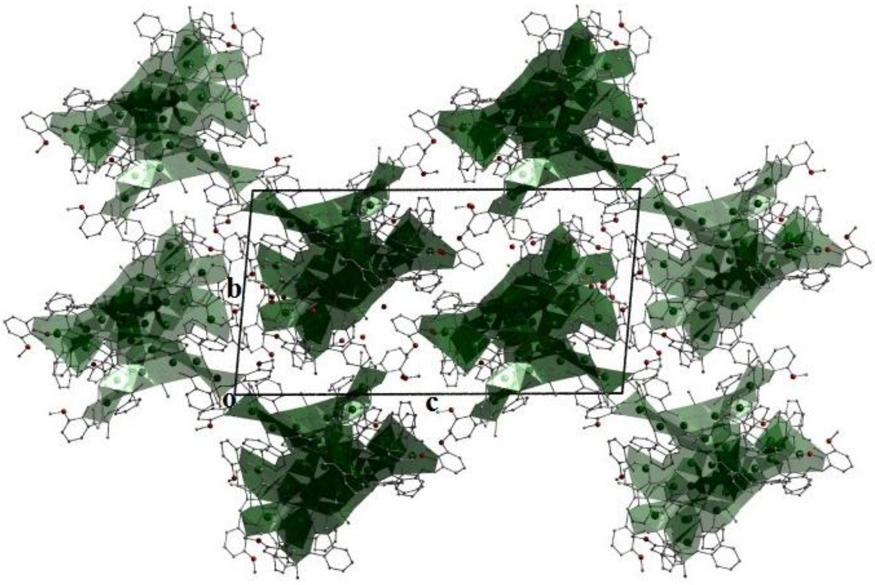

Figure 115 *- Crystal packing arrangement of individual {Cu*$_{30}$*} moieties in complex* ***17*** *as viewed along the a axis. All hydrogen atoms and perchlorate counter anions have been removed for clarity.*

The planar units observed in complexes **13** and **15**-**17** can also be described as fragments of metallacrown structures, which were first discovered and significantly developed by Pecoraro et al.[41] This is not surprising as the organic ligands L_3H_3 and L_5H_3 have similar features to known metallacrown-directing ligands such as hydroxamic acids.[42] Furthermore, the subsequent linking of our planar units into larger architectures also has precedence in metallacrown coordination chemistry.[43]

4.2.1.5 Crystallographic Data for Complexes 13-17

***Table 10** - Crystallographic data for complexes **13-14**.*

Complex	**13**·5MeOH·H_2O	**13'**·pyr·MeOH	**14**·H_2O
Formula[a]	$C_{79}H_{71}N_{12}O_{44}Cl_4Cu_{10}$	$C_{98}H_{87}N_{13}O_{37}Cl_2Cu_{10}$	$C_{17}H_{17}N_3O_5Cu$
M_W	2669.68	2745.17	406.88
Crystal Appearance	Green Parallelepiped	Green Parallelepiped	Green Parallelepiped
Crystal System	Monoclinic	Tetragonal	Monoclinic
Space group	*C*2/*c*	*P*4/*n*cc	*C*2/*c*
a/Å	23.6341(10)	26.5654(7)	36.1459(12)
b/Å	25.5162(8)	26.5654(7)	5.2200(2)
c/Å	16.5739(9)	37.7320(17)	18.0068(7)
α/°	90.00	90	90.00
β/°	104.244(5)	90	101.697(3)
γ/°	90.00	90	90.00
V/Å^3	9687.7(7)	26628.2(18)	3327.0(2)
Z	4	8	8
T/K	150(2)	150(2)	150(2)
λ^b/Å	0.7107	0.71073	0.7107
D_c/g cm^{-3}	1.830	1.327	1.625
μ(Mo-Ka)/ mm^{-1}	2.359	1.674	1.348
Meas./indep., (R_{int}) refl.	8858/5206, (0.1077)	17830/4533, (0.4856)	3047/2627, (0.0249)
wR2 (all data)	0.2481	0.5093	0.0842
$R1^{d,e}$	0.0808	0.1704	0.0315
Goodness of fit (GOOF) on F^2	1.065	1.146	1.066

[a] Includes guest molecules. [b] Mo-Kα radiation, graphite monochromator. [c] $wR2= [\sum w(|F_o^2|-|F_c^2|)^2/ \sum w|F_o^2|^2]^{1/2}$. [d] For observed data. [e] $R1= \sum||F_o|- |F_c||/ \sum|F_o|$.

Table 11 *- Crystallographic data for complexes* ***15-17****.*

Complex	**15**·2MeOH·3H_2O	**16**·6MeOH·10H_2O	**17**·2MeOH·27H_2O
Formula[a]	$C_{112}H_{112}N_{20}O_{54}Cu_{14}$	$C_{124}H_{144}N_{20}O_{60}Cu_{14}$	$C_{248}H_{268}N_{32}O_{122}Cl_4Cu_{30}$
M_W	3491.84	3764.22	7697.13
Crystal	Green Parallelepiped	Green Parallelepiped	Green Block
Crystal System	Triclinic	Monoclinic	Triclinic
Space group	P-1	$P2_1/c$	P-1
a/Å	15.4185(6)	18.989(4)	18.6255(5)
b/Å	22.8429(7)	13.838(3)	20.6535(7)
c/Å	25.1092(9)	26.748(5)	38.2976(12)
$\alpha/^o$	71.435(3)	90.00	92.913(3)
$\beta/^o$	77.204(3)	91.05(3)	99.064(3)
$\gamma/^o$	80.405(3)	90.00	103.632(3)
V/Å^3	8130.8(5)	7028(2)	14079.1(8)
Z	1	2	2
T/K	150(2)	150(2)	150(3)
λ^b/Å	0.7107	0.7107	0.7107
D_c/g cm^{-3}	1.533	1.767	1.726
μ(Mo-Ka)/ $^{-1}$	1.879	2.173	2.344
Meas./indep., (R_{int}) refl.	37057/14191, (0.1112)	12859/8172, (0.1128)	51469/25283, (0.1037)
wR2 (all data)	0.2602	0.2481	0.3650
$R1^{d,e}$	0.0909	0.0984	0.1313
Goodness of fit (GOOF) on F^2	0.963	1.056	1.085

[a] Includes guest molecules. [b] Mo-Kα radiation, graphite monochromator. [c] $wR2= [\sum w(|F_o^2|-|F_c^2|)^2/ \sum w|F_o^2|^2]^{1/2}$. [d] For observed data. [e] $R1= \sum||F_o|- |F_c||/ \sum|F_o|$.

4.3 Conclusions and Observations

The Schiff base condensation reactions of precursors 2-(amino)phenylhydroxamic acid (L_2H_2) and either 2-hydroxy-3-methoxybenzaldehyde or 2-hydroxybenzaldehyde in the presence of Cu(II) ions results in the in-situ formation and subsequent metal ligation of the polydentate ligands *o*-[(*E*)-(2-Hydroxy-3-methoxyphenyl)methylideneamino]benzohydroxamic acid (L_3H_3) and *o*-[(*E*)-(*o*-Hydroxyphenyl)methylideneamino]benzohydroxamic acid (L_5H_3) respectively. By varying reaction conditions and methodologies employed a family of Cu(II) cages were synthesised with the following formulae: $[Cu_{10}(L_3)_4(L_2)_2(H_2O)_2](ClO_4)_4\cdot5MeOH\cdot H_2O$ (**13**), $[Cu_{14}(L_3)_8(MeOH)_3(H_2O)_5](NO_3)_4\cdot2MeOH\cdot3H_2O$ (**15**), $[Cu_{14}(L_5)_8(MeOH)_6(NO_3)_4(H_2O)_2]\cdot6MeOH\cdot10H_2O$ (**16**) and $[Cu_{30}(O)_1(OH)_4(OMe)_2(L_3)_{16}(MeOH)_4(H_2O)_2](ClO_4)_4\cdot2MeOH\cdot27H_2O$ (**17**). Simple alterations to the reaction scheme for **13** (including the addition of MeCN), resulted in the formation of a new ligand [[2-[(E)-(2-hydroxy-3-methoxy-phenyl)methyleneamino]benzoyl]amino]ethanimidate (L_4H_2), which led to the unexpected formation of the 1D Cu(II) coordination polymer $\{[Cu(II)(L_4)]\cdot H_2O\}_n$ (**14**). Magnetic susceptibility studies of complexes **13** and **15-17** will be carried out in the near future at the School of Chemistry, University of Edinburgh. All of these findings will be disseminated in a peer reviewed journal paper at a later date.

4.4 Experimental Section

4.4.1 Instrumentation

For details on instrumentation utilised in the analyses of complexes **13-17** see Chapter Two (Section 2.4.1).

4.4.1.1 Single Crystal X-ray Diffraction

The structures of **13-17** were collected on an Xcalibur S single crystal diffractometer (Oxford Diffraction) using an enhanced Mo source. All hydrogen atoms in **13-17** were assigned to calculated positions. All non-hydrogen atoms were refined anisotropic with the exception of one NO_3^- anion in **16** (N10-O17-O19). In addition, a DFIX restraint was also required for this anion. All solvent molecules of crystallisation located in the lattice also remained isotropic. The DFIX command was used to restrain one of the two ClO_4^- counter anions in **17** (labelled Cl1-O88-O91). DFIX restraints were used for MeOH solvents of crystallisation in complexes **13** (C91-O26) and **16** (C71-O42, C72-O41 and C73-O44). Residual electron density in solvent accessible voids and channels were observed in **17** and therefore were modelled using the SQUEEZE program.[44, 45] The three channels in **17** (with a total voids volume ~1323 Å^3) contained extremely diffuse electron density and were assumed to contain numerous waters of crystallisation. CHN analysis performed on **17** support these observations.

4.4.2 Syntheses

All reagents and solvents were used as purchased without further purification. The microwave synthesis of **15** was performed in a CEM Discover® microwave reactor. The solvothermal synthesis of **17** was carried out in a Hereaus (UT6420-Thermo Scientific) oven using spring loaded stainless steel digestion vessels (23 cm^3 capacity) produced by the Parr Instrument Company. **Caution**: Although no problems were encountered in this work, great care should be taken when manipulating the potentially explosive perchlorate and nitrate salts. See Chapter 2 (Section 2.4.2.3) for the synthesis of 2-(amino)phenylhydroxamic acid (L_2H_2).

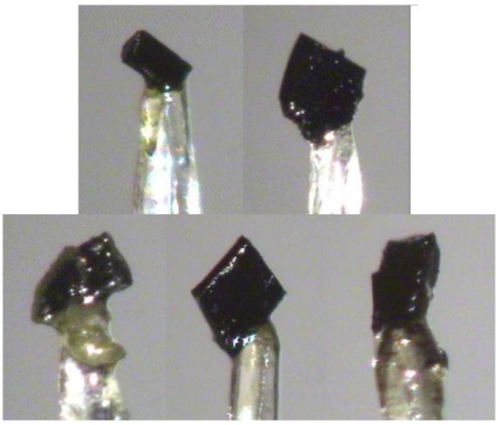

Figure 116 *- Single crystals of complexes* ***13*** *and* ***14*** *(top left to right) and complexes* ***15-17*** *(bottom left to right).*

4.4.2.1 Synthesis of $[Cu(II)_{10}(L_3)_4(L_2)_2(H_2O)_2](ClO_4)_4 \cdot 5MeOH \cdot H_2O$ (13)

$Cu(ClO_4)_2 \cdot 6H_2O$ (0.25 g, 0.68 mmol), 2-(amino)phenylhydroxamic acid (L_2H_2; 0.052 g, 0.34 mmol), 2-hydroxy-3-methoxybenzaldehyde (0.052 g, 0.34 mmol) and NaOH (0.027 g, 0.68 mmol) were dissolved in 30 cm^3 of MeOH and stirred for 4 h. The resultant dark green solution was then filtered and aliquots of the mother liquor were then diffused with diethyl ether. After two days, dark green X-ray quality crystals of **13** began to form. The crystals of **13** were collected and air dried to give a yield of approximately 5%.

C, H, N Elemental Analysis

Calculated % as $[Cu(II)_{10}(L_3)_4(L_2)_2(H_2O)_2](ClO_4)_4 \cdot 5MeOH \cdot H_2O$ ($C_{79}H_{71}N_{12}O_{44}Cl_4Cu_{10}$): C 35.54, H 2.68, N 6.30.

Found %: C 35.27, H 2.89, N 6.59.

FT-IR (cm^{-1}): 2937 (w), 1605 (m), 1580 (m), 1543 (m), 1490 (w), 1433 (m), 1373 (m), 1298 (w), 1234 (m), 1183 (m), 1160 (w), 1078 (s), 977 (w), 932 (m), 871 (w), 853 (w), 771 (m), 740 (m), 687 (m), 651 (w), 621 (s), 579 (m), 556 (m), 536 (m), 524 (m), 519 (s).

4.4.2.2 Synthesis of $\{[Cu(II)(L_4)]\cdot H_2O\}_n$ (14)

$Cu(ClO_4)_2\cdot 6H_2O$ (0.25 g, 0.68 mmol), L_2H_2 (0.104 g, 0.68 mmol) and 2-hydroxy-3-methoxybenzaldehyde (0.104 g, 0.68 mmol) were dissolved in 30 cm^3 of MeOH and stirred for 5 min. NaOMe (0.073 g, 1.36 mmol) was added to the solution along with 1 cm^3 of pyridine. The dark green solution was stirred overnight for 16 h. The solution was then evaporated to dryness under reduced pressure, re-dissolved in 20 cm^3 of MeCN and stirred for a further 1 h. This solution was then filtered and left to slowly evaporate for a few days, resulting in the formation of dark green X-ray quality crystals of **14**. The crystals were collected and air dried to give a yield of 20%.

C, H, N Elemental Analysis

Calculated % as $[Cu(II)(L_4)]$ ($C_{17}H_{15}N_3O_4Cu$): C 52.51, H 3.89, N 10.81.

Found %: C 52.16, H 3.88, N 10.41.

FT-IR (cm^{-1}): 3428 (w), 3347 (w), 3061 (w), 1673 (w), 1583 (s), 1559 (m), 1530 (m), 1447 (s), 1391 (m), 1349 (m), 1234 (s), 1183 (s), 1143 (m), 1108 (m), 1078 (m), 1025 (w), 1009 (m), 985 (m), 940 (m), 899 (w), 877 (m), 860 (m), 836 (m), 771 (m), 735 (s), 700 (s).

4.4.2.3 Synthesis of $[Cu(II)_{14}(L_3)_8(MeOH)_3(H_2O)_5](NO_3)_4\cdot 2MeOH\cdot 3H_2O$ (15)

Method A: $Cu(NO_3)_2\cdot 3H_2O$ (0.25 g, 1.04 mmol) was added to a 30 cm^3 methanolic solution of L_2H_2 (0.08 g, 0.53 mmol) and 2-hydroxy-3-methoxybenzaldehyde (0.08 g, 0.53 mmol) and stirred for 2 min. NaOH (0.042 g, 1.04 mmol) was added to the methanolic solution and it was left to stir for 4 h. The resultant dark green solution was then filtered and X-ray quality crystals of **15** began to form after two days. The crystals were collected and air dried with a yield of 10%.

Method B: $Cu(NO_3)_2\cdot 3H_2O$ (0.25 g, 1.04 mmol), L_2H_2 (0.08 g, 0.53 mmol), 2-hydroxy-3-methoxybenzaldehyde (0.08 g, 0.53 mmol) and NaOH (0.042 g, 1.04 mmol) were dissolved in 15 cm^3 of MeOH in a microwave reactor vial which was stirred for 2 min. The glass vial was then sealed and inserted into a microwave oven reactor. The reaction was maintained at T = 110 °C, pressure = 110 psi and power = 200 W for a total of 5 min. The resultant green solution was left to cool before filtration and slow evaporation of the mother liquor gave X-ray quality crystals of **15** after two days. The crystals were collected and air dried with a yield of 10%.

C, H, N Elemental Analysis

Calculated % for $[Cu(II)_{14}(L_3)_8(MeOH)_3(H_2O)_5](NO_3)_4 \cdot 2MeOH \cdot 8H_2O$ ($C_{122}H_{122}N_{20}O_{59}Cu_{14}$): C 39.58, H 3.32, N 7.57.

Found %: C 39.18, H 2.96, N 7.30.

FT-IR (cm^{-1}): 3065 (w), 1607 (w), 1581 (m), 1541 (m), 1490 (w), 1457 (w), 1432 (m), 1372 (m), 1328 (m), 1233 (m), 1183 (m), 1100 (m), 1080 (w), 1027 (w), 979 (m), 932 (m), 871 (w), 854 (m), 827 (w), 786 (m), 772 (m), 740 (s), 689 (m), 652 (m), 625 (m), 586 (m), 555 (m), 535 (m), 524 (s).

4.4.2.4 Synthesis of $[Cu(II)_{14}(L_5)_8(MeOH)_6(NO_3)_4(H_2O)_2] \cdot 6MeOH \cdot 10H_2O$ (16)

$Cu(NO_3)_2 \cdot 3H_2O$ (0.25 g, 1.04 mmol) and L_2H_2 (0.08 g, 0.53 mmol) were dissolved in 30 cm^3 of MeOH and stirred. 2-hydroxybenzaldehyde (0.065 g, 0.058 cm^3, 0.53 mmol) and NaOH (0.042 g, 1.04 mmol) were subsequently added and the reaction mixture stirred for 4 h. The resultant dark green solution was filtered and was allowed to concentrate upon slow evaporation. Additionally, aliquots of the mother liquor were diffused with diethyl ether. Both reactions produced dark green X-ray quality crystals of **16** which were collected and air dried to give a total yield of ~10%.

C, H, N Elemental Analysis

Calculated % as $[Cu(II)_{14}(L_5)_8(MeOH)_6(NO_3)_4(H_2O)_2] \cdot 6MeOH \cdot 6H_2O$ ($C_{124}H_{136}N_{20}O_{56}Cu_{14}$): C 40.34, H 3.71, N 7.59.

Found %: C 40.09, H 3.83, N 7.30.

FT-IR (cm^{-1}): 3404 (w), 3075 (w), 1607 (m), 1578 (m), 1543 (m), 1486 (m), 1463 (m), 1434 (m), 1373 (m), 1328 (m), 1284 (s), 1228 (m), 1184 (m), 1152 (m), 1099 (s), 1029 (w), 987 (m), 930 (m), 863 (m), 806 (m), 753 (s), 740 (s), 679 (s).

4.4.2.5 Synthesis of $[Cu(II)_{30}(O)_1(OH)_4(OMe)_2(L_3)_{16}(MeOH)_4(H_2O)_2](ClO_4)_4 \cdot 2MeOH \cdot 27H_2O$ (17)

$Cu(ClO_4)_2 \cdot 6H_2O$ (0.1 g, 0.27 mmol), 2-(amino)phenylhydroxamic acid (0.021 g, 0.14 mmol), 2-hydroxy-3-methoxybenzaldehyde (0.021 g, 0.14 mmol) and $NEt_4(OH)$ (0.7 cm^3, 0.72 g, 4.89 mmol) were dissolved in 10 cm^3 of MeOH and stirred for 1 h. The resultant dark green solution was then placed in a teflon lined stainless steel autoclave and heated at 100 °C for 24 h followed by slow cooling over a further 24 h period. Dark green X-ray quality crystals of **17** were air dried and collected to give a yield of 5%.

C, H, N Elemental Analysis

Calculated % as $[Cu(II)_{30}(O)_1(OH)_4(OMe)_2(L_3)_{16}(MeOH)_4(H_2O)_2](ClO_4)_4 \cdot 11H_2O$ ($C_{246}H_{228}O_{104}Cl_4Cu_{30}$): C 40.23, H 3.13, N 6.10.

Found %: C 39.74, H 2.85, N 6.59.

FT-IR (cm^{-1}): 3387 (w), 1605 (m), 1579 (m), 1540 (m), 1488 (w), 1432 (m), 1374 (m), 1297 (w), 1233 (m), 1184 (m), 1093 (s), 978 (m), 947 (m), 853 (w), 771 (m), 737 (s), 687 (m), 651 (m), 623 (s), 557 (m), 531 (m), 524 (m).

4.5 Bibliography

1. T. K. Ronson, S. Zarra, S. P. Black and J. R. Nitschke, *Chem. Commun.*, 2013, 49, 2476-2490.
2. C. D. Meyer, C. S. Joiner and J. F. Stoddart, *Chem. Soc. Rev.*, 2007, 36, 1705-1723.
3. X.-P. Zhou, J. Liu, S.-Z. Zhan, J.-R. Yang, D. Li, K.-M. Ng, R. W.-Y. Sun and C.-M. Che, *J. Am. Chem. Soc.*, 2012, 134, 8042-8045.
4. X.-P. Zhou, Y. Wu and D. Li, *J. Am. Chem. Soc.*, 2013, 135, 16062-16065.
5. S. Yi, V. Brega, B. Captain and A. E. Kaifer, *Chem. Commun.*, 2012, 48, 10295-10297.
6. H. Bunzen, Nonappa, E. Kalenius, S. Hietala and E. Kolehmainen, *Chem. Euro. J.*, 2013, 19, 12978-12981.
7. P. P. Neelakandan, A. Jimenez and J. R. Nitschke, *Chem. Sci.*, 2014, 5, 908-915.
8. J. Mosquera, S. Zarra and J. R. Nitschke, *Angew. Chem. Int. Ed.*, 2014, 53, 1556-1559.
9. M. U. Anwar, Y. Lan, L. M. C. Beltran, R. Clérac, S. Pfirrmann, C. E. Anson and A. K. Powell, *Inorg. Chem.*, 2009, 48, 5177-5186.
10. D. R. Turner, S. N. Pek, J. D. Cashion, B. Moubaraki, K. S. Murray and S. R. Batten, *Dalton Trans.*, 2008, 6877-6879.
11. A. S. R. Chesman, D. R. Turner, B. Moubaraki, K. S. Murray, G. B. Deacon and S. R. Batten, *Dalton Trans.*, 2012, 41, 3751-3757.
12. C. McDonald, T. Whyte, S. M. Taylor, S. Sanz, E. K. Brechin, D. Gaynor and L. F. Jones, *CrystEngComm*, 2013, 15, 6672-6681.
13. C. McDonald, S. Sanz, E. K. Brechin, M. K. Singh, G. Rajaraman, D. Gaynor and L. F. Jones, *RSC Adv.*, 2014, 4, 38182-38191.
14. S. T. Meally, G. Karotsis, E. K. Brechin, G. S. Papaefstathiou, P. W. Dunne, P. McArdle and L. F. Jones, *CrystEngComm*, 2010, 12, 59-63.
15. S. T. Meally, C. McDonald, G. Karotsis, G. S. Papaefstathiou, E. K. Brechin, P. W. Dunne, P. McArdle, N. P. Power and L. F. Jones, *Dalton Trans.*, 2010, 39, 4809-4816.
16. S. T. Meally, C. McDonald, P. Kealy, S. M. Taylor, E. K. Brechin and L. F. Jones, *Dalton Trans.*, 2012, 41, 5610-5616.
17. S. T. Meally, S. M. Taylor, E. K. Brechin, S. Piligkos and L. F. Jones, *Dalton Trans.*, 2013, 42, 10315-10325.
18. G. L. Abbati, A. Caneschi, A. Cornia, A. C. Fabretti, Y. A. Pozdniakova and O. I. Shchegolikhina, *Angew. Chem. Int. Ed.*, 2002, 41, 4517-4520.
19. T. Kajiwara, N. Kon, S. Yokozawa, T. Ito, N. Iki and S. Miyano, *J. Am. Chem. Soc.*, 2002, 124, 11274-11275.
20. V. Chandrasekhar, L. Nagarajan, K. Gopal, V. Baskar and P. Kogerler, *Dalton Trans.*, 2005, 3143-3145.
21. F. Pan, J. Wu, H. Hou and Y. Fan, *Crys. Growth Des.*, 2010, 10, 3835-3837.
22. V. Chandrasekhar, L. Nagarajan, S. Hossain, K. Gopal, S. Ghosh and S. Verma, *Inorg. Chem.*, 2012, 51, 5605-5616.
23. C.-H. Chang, K. C. Hwang, C.-S. Liu, Y. Chi, A. J. Carty, L. Scoles, S.-M. Peng, G.-H. Lee and J. Reedijk, *Angew. Chem. Int. Ed.*, 2001, 40, 4651-4653.
24. G. C. Vlahopoulou, T. C. Stamatatos, V. Psycharis, S. P. Perlepes and G. Christou, *Dalton Trans.*, 2009, 3646-3649.
25. A. W. Addison, T. N. Rao, J. Reedijk, J. van Rijn and G. C. Verschoor, *J. Chem. Soc., Dalton Trans.*, 1984, 1349-1356.
26. J. L. Schneider, V. G. Young and W. B. Tolman, *Inorg. Chem.*, 2000, 40, 165-168.
27. C. Xu, X.-Y. Yi, T.-K. Duan, Q. Chen and Q.-F. Zhang, *Polyhedron*, 2011, 30, 2637-2643.
28. P. J. M. W. L. Birker and H. C. Freeman, *J. Am. Chem. Soc.*, 1977, 99, 6890-6899.

29. P. J. M. W. L. Birker, *Inorg. Chem.*, 1979, 18, 3502-3506.
30. H. J. Schugar, C.-C. Ou, J. A. Thich, J. A. Potenza, T. R. Felthouse, M. S. Haddad, D. N. Hendrickson, W. Furey and R. A. Lalancette, *Inorg. Chem.*, 1980, 19, 543-552.
31. A. Mukherjee, M. Nethaji and A. R. Chakravarty, *Angew. Chem. Int. Ed.*, 2004, 43, 87-90.
32. M. B. Duriska, S. M. Neville, J. Lu, S. S. Iremonger, J. F. Boas, C. J. Kepert and S. R. Batten, *Angew. Chem. Int. Ed.*, 2009, 48, 8919-8922.
33. S. Dehnen and D. Fenske, *Chem. Euro. J.*, 1996, 2, 1407-1416.
34. N. Zhu and D. Fenske, *J. Chem. Soc., Dalton Trans.*, 1999, 1067-1076.
35. M. W. DeGroot, M. W. Cockburn, M. S. Workentin and J. F. Corrigan, *Inorg. Chem.*, 2001, 40, 4678-4685.
36. O. Fuhr, L. Fernandez-Recio and D. Fenske, *Eur. J. Inorg. Chem.*, 2005, 2005, 2306-2314.
37. E. A. Turner, Y. Huang and J. F. Corrigan, *Z. Anorg. Allg. Chem.*, 2007, 633, 2135-2137.
38. M.-L. Fu, I. Issac, D. Fenske and O. Fuhr, *Angew. Chem. Int. Ed.*, 2010, 49, 6899-6903.
39. M. Murugesu, R. Clerac, C. E. Anson and A. K. Powell, *Chem. Commun.*, 2004, 1598-1599.
40. M. Murugesu, R. Clérac, C. E. Anson and A. K. Powell, *Inorg. Chem.*, 2004, 43, 7269-7271.
41. M. S. Lah and V. L. Pecoraro, *J. Am. Chem. Soc.*, 1989, 111, 7258-7259.
42. G. Mezei, C. M. Zaleski and V. L. Pecoraro, *Chem. Rev.*, 2007, 107, 4933-5003.
43. G. Psomas, C. Dendrinou-Samara, M. Alexiou, A. Tsohos, C. P. Raptopoulou, A. Terzis and D. P. Kessissoglou, *Inorg. Chem.*, 1998, 37, 6556-6557.
44. A. Spek, *J. Appl. Crystallogr.*, 2003, 36, 7-13.
45. P. van der Sluis and A. L. Spek, *Acta Crystallogr. Sect. A: Found. Crystallogr.*, 1990, 46, 194-201.

Chapter Five

Microwave-Assisted Synthesis of a Family of Dinuclear $[Ln(III)_2(L_6)_2(ROH)_x(H_2O)_y(NO_3)_4]$ Complexes (Ln = La, Ce, Gd, Tb and Dy; R = Me, Et)

5.1 Introduction

5.1.1 Microwave Synthesis

Microwaves are a type of electromagnetic radiation located in between infrared and radio waves on the electromagnetic spectrum (Figure 117). They have wavelengths ranging from 1.0 mm to 1 m, corresponding to frequencies of between 0.3 and 300 GHz.[1] Microwave kitchen ovens and the majority of microwave reactors run at a frequency of 2.45 GHz to avoid interference from wireless networks, telecommunication devices and cellular phones. As they are members of the electromagnetic radiation series, microwave radiation can be divided into two components, the electric field and the magnetic field. Microwave chemistry is based on the ability of a material with electric charge (i.e. a polar solvent/reagent) to absorb microwave energy and to convert it into heat, leading to the efficient heating of materials.[2] The electric field utilises a dielectric heating method, which consists of a dipolar polarization interaction in conjunction with a conduction mechanism (Figure 118).

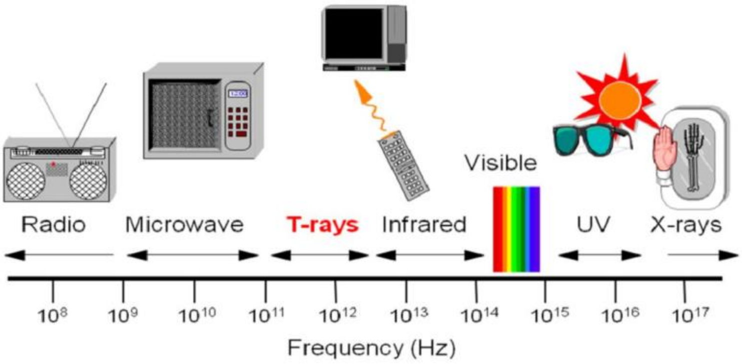

Figure 117 *- Illustration of the electromagnetic spectrum from "Electromagnetic Waves and Their Application to Charged Particle Acceleration" by Hitendra K. Malik.*[3]

1) Dipolar polarization**:** In order for a substance to be heated via microwave irradiation it must have a dipole moment. Upon application of the electric field, the dipole will attempt to realign itself with the oscillating electric field and the energy supplied from the electric field allows for this. The ability of molecules in a liquid to align with the electric field is determined by the frequency of the electric field and the viscosity of the liquid. Under the microwave radiation region, the frequency of the electric field (2.45 GHz) is low enough to allow the dipoles to rotate; however the frequency is not high enough to allow the dipole to fully realign with the oscillating electric field. Hence, a phase difference is generated between the direction of the field and the dipole. Dielectric heating arises from the loss of energy of the dipole via molecular collisions and frictions.[1]

2) Conduction**:** Upon application of an electric field the ions in a solution move through the solution, creating kinetic energy and converting it into heat. This mechanism has a much higher heat generating capability than the dipolar polarization interaction.[1]

Figure 118 has been removed due to copyright restrictions and can be seen in references 4 and 5.

There are two parameters that define the dielectric properties of a material. *1) the dielectric constant* ε': expresses the ability of a substance to be polarized by the electric field and *2) the dielectric loss* ε'': depicts the efficiency at which electromagnetic radiation is converted to heat. The ratio of these two parameters describes the term known as the loss factor $\tan \delta = \varepsilon''/\varepsilon'$, which is a measure of the ability of a particular substance to convert electromagnetic radiation into heat at a given frequency and temperature.[2, 4] This means that a solvent medium with a high $\tan \delta$ value will have efficient absorption resulting in a rapid heating process. For the most part, a solvent with a $\tan \delta > 0.5$ is classified as a high microwave absorbing solvent, while a $\tan \delta$ of 0.1-0.5 and a $\tan \delta < 0.1$ are labelled medium and low absorbing solvents respectively.[2] In relation to our studies, our solvents of choice MeOH and EtOH are both representatives of high microwave absorbing solvents with $\tan \delta$ values of 0.659 and 0.941 respectively.[6]

Microwaves have been used in everyday life for the rapid heating of food for many years, but their use in research fields such as inorganic and organic chemistry is still relatively new. The delay in the operation of microwave technology towards synthetic chemistry is thought to be due to a number of factors including safety issues, a poor understanding of the microwave dielectric heating mechanism, along with a lack of controllability and reproducibility. The mid 1990's saw a significant growth in the role of microwave technology in chemical synthesis, especially in the field of organic chemistry.[2, 7, 8] The greater availability of microwave equipment along with the development of solvent free techniques has led to an increased interest in microwave-assisted synthesis. In addition, microwave technology allows for shorter reaction times, along with a wider range of reaction conditions which may have previously been impractical or inaccessible. Although, the use of microwave-assisted synthesis in inorganic chemistry is still a relatively new technique, it has been utilised in the synthesis of a wide variety of materials such as zeolites,[9, 10] metallic nanoparticles,[11-13] discrete polynuclear complexes,[14-16] metal directed self-assembled cyclic arrays[17] and 1-3D coordination polymers.[18-21]

5.1.2 Magnetic Properties of the Lanthanoid Series

The elements La-Lu are regularly denoted by the generic symbol Ln. For the most part, ionization beyond the Ln(III) ion is not energetically favoured, resulting in the characteristic +3 oxidation state. The unpaired electrons of all Ln(III) elements lie in the 4f-orbitals with the exception of La(III) and Lu(III) (no unpaired electrons). There are seven f-orbitals which are commonly represented in a cubic set comprising: f_{x^3}, f_{y^3}, f_{z^3}, f_{xyz}, $f_{z(x^2-y^2)}$, $f_{y(z^2-x^2)}$ and $f_{x(z^2-y^2)}$ (Figure 119). Generally, the 4f-atomic orbitals do not partake in covalent bonding as they are well shielded by the filled 5s and 5p orbitals. Their energies are therefore unaffected by coordinated ligands, giving rise to small crystal field splitting of the degenerate f-orbitals. Ln(III) ions are hard, preferring to coordinate to hard F- and O- donor atoms. Due to the size of lanthanoid metals, Ln(III) complexes are able to accommodate more ligands and therefore tend to have high coordination numbers, whereby 8, 9 and 10 coordinate complexes are common. Spin-orbit coupling plays a more important role here than crystal field splitting, as orbital angular momentum remains unquenched (unlike d block metal ions), allowing for large spin-orbit coupling.

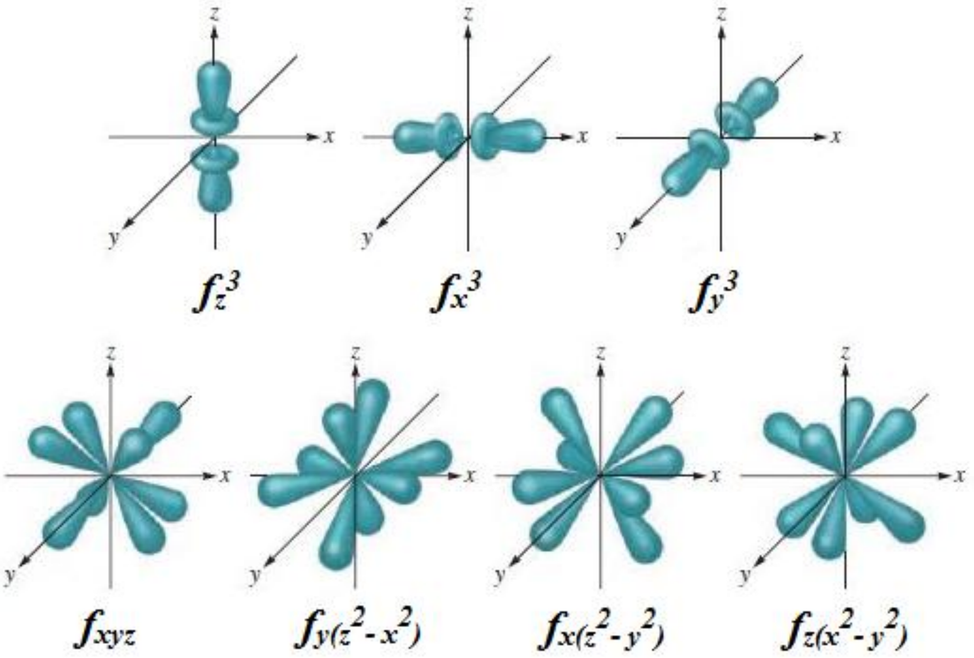

Figure 119 *- Illustration of the seven f-orbitals using the cubic set representation.*[22]

The f-orbitals can hold up to fourteen electrons, whereby the orbital quantum number (l) = 3 and the magnetic orbital quantum number (m_l) ranges from -3 to +3. As a result, Ln(III) complexes tend to exhibit interesting magnetic properties such as large ground spin states, significant single ion anisotropy, weak exchange and slow relaxation of magnetisation. Furthermore, as a result of these properties, Ln(III) clusters have immense potential applications as Single-Molecule Magnets (SMMs). In particular, various dimeric [$Dy(III)_2$] complexes exist in the literature which display SMM behaviour.[23-30] Additionally, SMMs offer promising contenders for use in molecular spintronic devices.[31] On the other hand, Gd(III) complexes are ideal candidates for molecular coolant devices as they can exhibit large ground spin states coupled with negligible anisotropy (D = 0).[32-35] This is brought about by the isotropic nature of Gd(III) ions (S = 7/2, L = 0). In particular, dimeric Gd(III) complexes have shown great potential as molecular coolants. For example, the dimeric gadolinium acetate ($[Gd(III)_2(O_2CCH_3)_6(H_2O)_4]\cdot4H_2O$) complex possesses exceptionally large magneto-caloric effects in the low temperature regime.[36]

5.1.3 2,6-dimethoxyphenol as our Choice of Ligand

Previous research in our group involved the synthesis of a family of heptanuclear [M_7] (M = Co(II/III), Ni(II), Zn(II)) pseudo metallocalix[6]arene complexes via the incorporation of the Schiff base ligand 2-imino-6-methoxyphenol (Figure 120). These disc-like structural units were shown to act as solid state hosts for a variety of organic guest molecules and counter anions.[37-39]

The work described in this chapter details the investigation of the coordination chemistry of the ligand 2,6-dimethoxyphenol (L_6H) - an analogue to the ligand 2-imino-6-methoxyphenol (Figure 120). In addition, 2,6-dimethoxyphenol would appear to be a good choice of building block for the construction of [Ln(III)$_2$] dimers, given that it is pre-designed to direct the formation of two oxophilic compartments. Prior to the work described in this chapter, very little research into the construction of metal coordination compounds had been carried out with L_6H. Rare examples include its use in alkene polymerization catalyst studies,[40] as well as in the synthesis of poly(aryl)silane and heterometallic aluminium-lithium compounds.[41, 42]

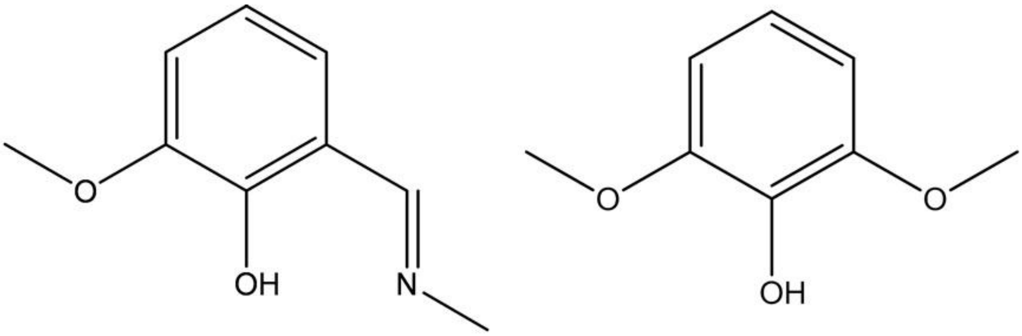

Figure 120 *- (Left) Structure of the Schiff base ligand 2-imino-6-methoxyphenol previously used in the synthesis of [M_7] pseudo metallocalix[6]arene complexes. (Right) Structure of the 2,6-dimethoxyphenol (L_6H) ligand used in this work.*

This chapter details the synthesis, structural and magnetic properties of a family of alkoxide bridged dinuclear [Ln(III)$_2$] complexes of general formula $[Ln(III)_2(L_6)_2(ROH)_x(H_2O)_y(NO_3)_4]\cdot z EtOH$; where Ln = La, R = Et, $x = 4$, $y = 0$, $z = 0$ (**18**); Ln = Ce, R = Et, $x = 4$, $y = 0$, $z = 0$ (**19**); Ln = Gd, $x = 0$, $y = 2$, $z = 2$ (**20**); Ln = Gd, R = Me, $x = 2$, $y = 0$, $z = 0$ (**21**); Ln = Tb, R = Et, $x = 2$, $y = 0$, $z = 1$ (**22**); Ln = Tb, R = Me, $x = 2$, $y = 0$, $z = 0$ (**23**); Ln = Dy, $x = 0$, $y = 2$, $z = 2$ (**24**). A microwave-assisted technique was utilised in the synthesis of all members of the series, due to the miniscule yields obtained under both reflux and ambient bench top conditions, illustrating the importance of exploring alternative reaction conditions for polynuclear cage formation. We also show here that the number of {Ln(III)$_2$} units observed in the asymmetric unit (1 versus 2) can be controlled through solvent selection. Complementary dc magnetic susceptibility measurements and DFT analysis reveal the presence of weak antiferromagnetic exchange in all family members. DFT calculations are also employed to investigate the mechanisms responsible for the exchange interactions in our complexes (vide infra).

5.2 Results and Discussion

5.2.1 Structural Descriptions of our Dinuclear [Ln(III)$_2$] Family

The first member of our [Ln(III)$_2$] series to be synthesised was [Gd(III)$_2$(L$_6$)$_2$(MeOH)$_2$(NO$_3$)$_4$] (**21**) via the methanolic reaction of Gd(III)(NO$_3$)$_3$·6H$_2$O, L$_6$H and NaOH (Figure 121). Complex **21** crystallises in the monoclinic *P*2$_1$/*c* space group with unit cell parameters: *a* = 8.8472(18) Å, *b* = 10.817(2) Å, *c* = 15.665(3) Å, *α* = 90°, *β* = 102.81(3)°, *γ* = 90°. Complete crystallographic X-ray data can be seen in Table 13 (Section 5.2.1.1).

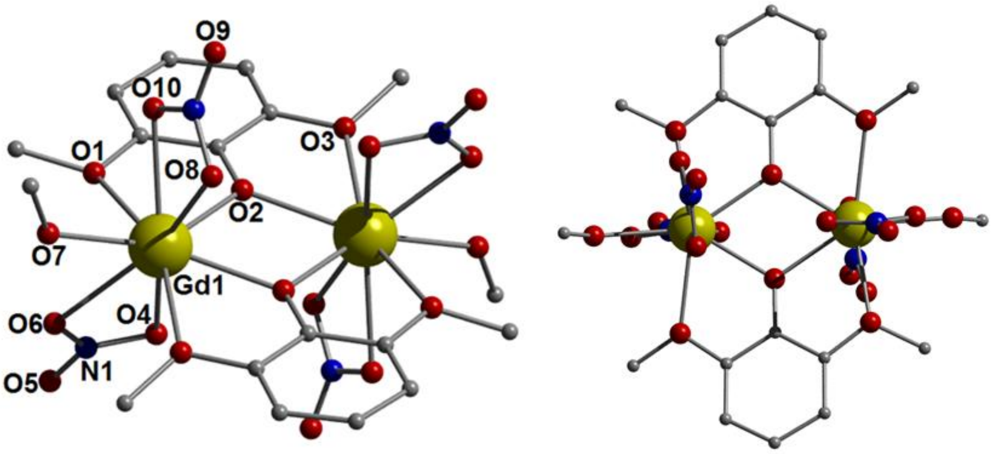

***Figure 121** - Crystal structure representations of [Gd(III)$_2$(L$_6$)$_2$(MeOH)$_2$(NO$_3$)$_4$] (**21**). Colour code: yellow (Gd), red (O), blue (N) and grey (C). Hydrogen atoms have been omitted for clarity.*

Despite many repeated attempts and the variation of synthetic parameters, complex **21** was only ever obtained in poor yields under ambient bench conditions. Reflux conditions were also utilised in an attempt to increase yields, but to no avail. In addition, both synthetic paths required up to 2 months for crystal formation! However, we established an improved synthetic procedure for the synthesis of **21** via a microwave-assisted technique. The above mixture was first stirred at room temperature for 20 minutes and then heated in a microwave reactor for a further 20 minutes at 110 °C, 200 W and 110 psi. The methanolic solution was allowed to cool, filtered and aliquots of the mother liquid were diffused with Et$_2$O. This resulted in the formation of X-ray quality crystals of **21** with an increased yield (see Section 5.4.2.4

for details). Through the utilisation of a microwave reactor, we went on to synthesise another six members (**18-20** and **22-24**) which are listed in Table 12 along with relevant structural data. As complexes **18-24** differ structurally only in their ligated solvent (and crystallisation habit), a full structural description of complex **21** will be given here. The core of **21** is composed of two symmetrically equivalent Gd(III) ions, which are nine coordinate and are related via an inversion centre. The two centres are linked by two singly deprotonated 2,6-dimethoxyphenol (L_6^-) ligands via their bridging phenoxy oxygen atoms (O2 and its s.e.) with bond lengths of 2.311(17) Å (Gd1-O2) and 2.312(16) Å (Gd1-O2'). The linkage between the two centres is further enhanced by the methoxy moieties of L_6^- (via O1 and O3), which bond to one Gd(III) metal centre each, resulting in bond lengths of 2.533(16) Å (Gd1-O1) and 2.512(17) Å (Gd1-O3) respectively. This completes the η^1:η^2:η^1-μ coordination motif displayed by both L_6^- ligands (Figure 122). Both of the Gd(III) centres are coordinated to chelating nitrate groups via their oxygen atoms (O4, O5 and O8, O10) exhibiting bond lengths in the range of 2.434(18)-2.504(17) Å. Coordination is completed via a terminal methanol ligand with a bond length of 2.422(16) Å (Gd1-O7). A Gd(III)···Gd(III) distance of 3.886 Å and Gd(III)-O2-Gd(III) angle of 114.42° is observed here. Ln(III)···Ln(III) distances and Ln(III)-O2-Ln(III) angles observed for the remaining complexes can be seen in Table 12.

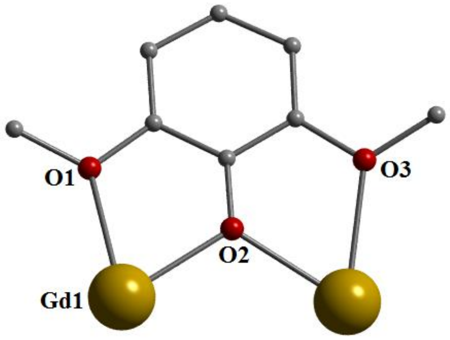

Figure 122 *- Schematic of the η^1:η^2:η^1-μ_3 coordination mode of L_6H in relation to the Gd(III) metal ions in* ***21****.*

The next two siblings synthesised were [La(III)$_2$(L$_6$)$_2$(EtOH)$_4$(NO$_3$)$_4$ (**18**) and [Ce(III)$_2$(L$_6$)$_2$(EtOH)$_4$(NO$_3$)$_4$] (**19**) (Figure 123). Both complexes crystallise in the triclinic *P*-1 space group and have identical unit cell parameters of: a = 9.0125(18) Å, b = 10.285(2) Å, c = 10.712(2) Å, α = 102.05(3)°, β = 102.57(3)°, γ = 101.48(3)°. Complete crystallographic X-ray data can be seen in Table 13 (Section 5.2.1.1).

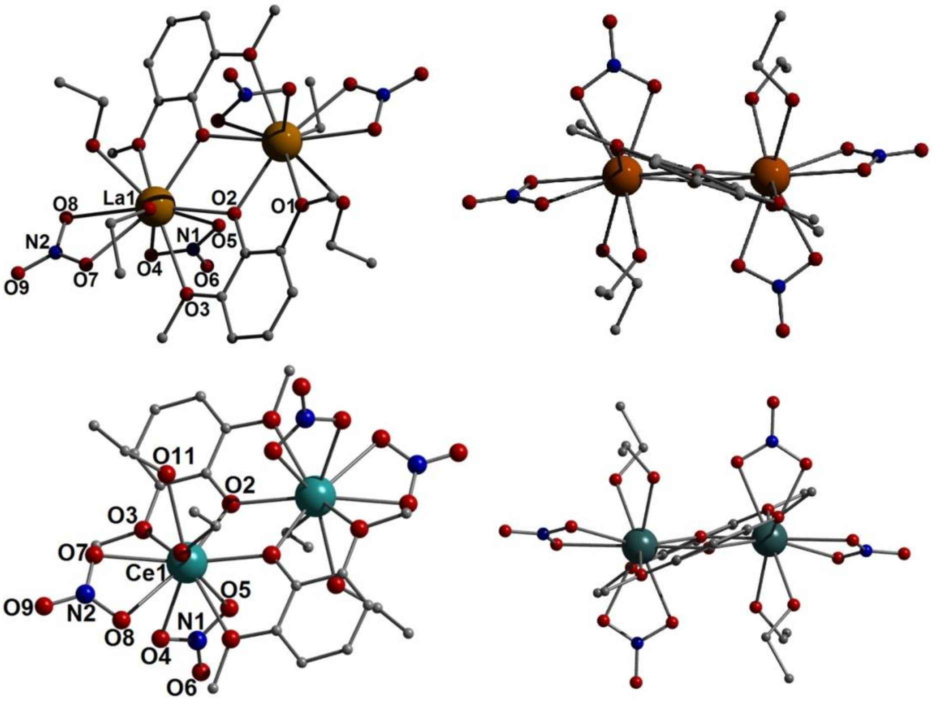

Figure 123 *- Crystal structures of dinuclear [Ln(III)$_2$] complexes* ***18*** *(top) and* ***19*** *(bottom) as viewed from two perspectives. Colour code: light brown (La) and aqua (Ce). Hydrogen atoms have been removed for clarity.*

These two complexes were synthesised in EtOH and therefore these solvent ligands successfully replace the terminal MeOH ligand molecules observed in complex **21**, with bond lengths ranging between 2.559(15) (Ce1-O10) and 2.587(16) Å (La1-O11). An additional EtOH molecule is ligated to each metal centre, producing ten coordinate Ln(III) (La(III) (**18**) and Ce(III) (**19**)) centres which display distorted bi-capped square anti-prismatic geometries in both siblings (Figure 127). Furthermore, the additional coordinated solvent molecule at each Ln(III) ion forces one of the bound nitrates to shift position. Indeed, an increase in the Ln-O$_{\text{nitrate}}$ bond lengths is observed with values ranging from 2.588(18) Å (Ce1-O7) to 2.723(16) Å (La1-O8).

The reaction synthesis for [Gd(III)$_2$(L$_6$)$_2$(H$_2$O)$_2$(NO$_3$)$_4$]·2EtOH (**20**), [Tb(III)$_2$(L$_6$)$_2$(EtOH)$_2$(NO$_3$)$_4$]·EtOH (**22**) and [Dy(III)$_2$(L$_6$)$_2$(H$_2$O)$_2$(NO$_3$)$_4$]·2EtOH (**24**) were all carried out in EtOH. Complexes **20** and **24** crystallise in the triclinic P-1 space group with unit cell parameters: a = 10.1121(3) Å, b = 10.9974(3) Å, c = 15.4570(4) Å, α = 73.058(2)°, β = 88.261(2)°, γ = 82.024(2)° for **20** and a = 10.0418(9) Å, b = 10.9358(10) Å, c = 15.3718(11) Å, α = 73.217(7)°, β = 88.489(7)°, γ = 81.882(8)° for **24**. Complex **22** crystallises in the monoclinic $P2_1/c$ space group with unit cell parameters: a = 18.8178(4) Å, b = 10.9671(3) Å, c = 16.5010(3) Å, α = 90°, β = 95.085(2)°, γ = 90°. Complete crystallographic X-ray data for these complexes are given in Tables 13 and 14 (Section 5.2.1.1). All three complexes possess two {Ln(III)$_2$} units in their asymmetric unit (see Figure 124 for the two {Dy(III)$_2$} units in **24**). The ligated methanol solvents in complex **21** are replaced by H_2O ligand molecules in complexes **20** and **24** with Ln(III)-O_{H_2O} bond lengths lying in the 2.358(9)-2.417(3) Å range (where Ln(III) = Gd(III) in **20** and Dy(III) in **24**). Coordinated EtOH ligands are observed in the structure of [Tb(III)$_2$(L$_6$)$_2$(EtOH)$_2$(NO$_3$)$_4$]·EtOH (**22**), giving rise to Ln(III)-O_{EtOH} bond lengths ranging between 2.399(3) (Tb2-O20) and 2.408(3) Å (Tb1-O10). All three complexes contain one (**22**) or two (**20** and **24**) EtOH solvents of crystallisation at the structures periphery and these are held in position by hydrogen bonding interactions with: *1)* bound H_2O molecules (i.e. O22(H22)$\cdots$O10 = 2.986 Å in **20** and O29(H29)$\cdots$O10 = 1.878 Å in **24**) and nitrate groups and coordinated EtOH ligands (i.e. O21(H21)$\cdots$O6$_{\text{nitrate}}$ = 2.099 Å and O10(H10)$\cdots$O21$_{\text{(EtOH)}}$ = 1.853 Å in **22**) (Figure 125).

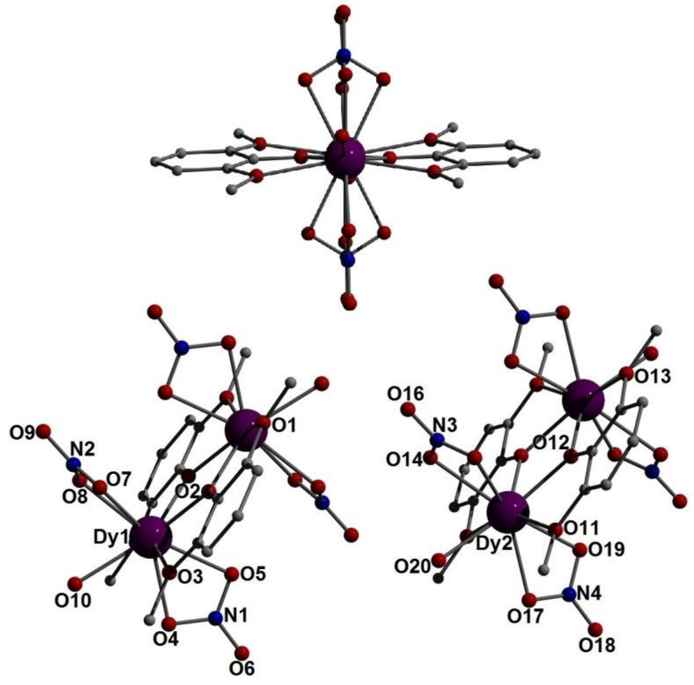

Figure 124 *- (Top) Crystal structure of **24** as viewed along the Dy(III)$\cdots$Dy(III) plane. (Bottom) Representation of the two {Dy(III)$_2$} units in the asymmetric unit of **24**. Colour code: purple (Dy). Hydrogen atoms and EtOH solvents of crystallisation have been omitted for clarity.*

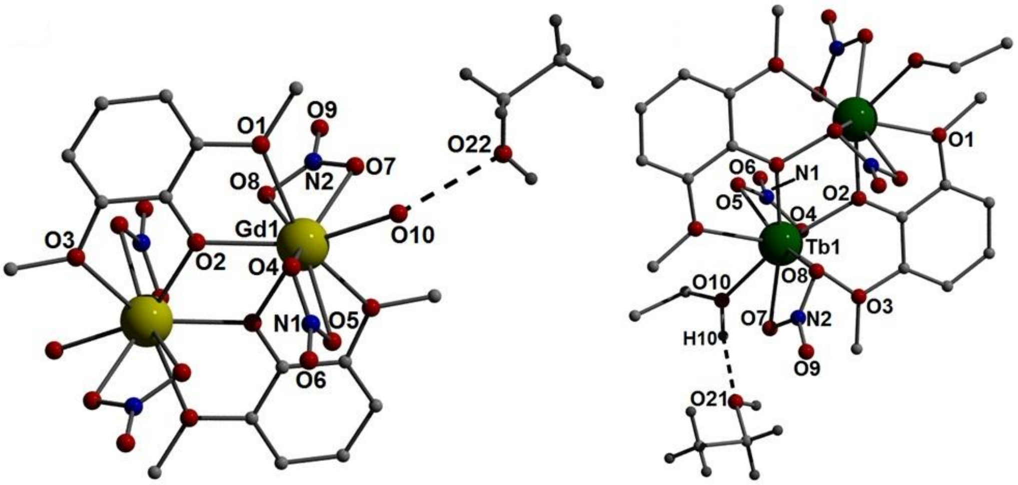

***Figure 125** - Crystal structures of **20** (left) and **22** (right), illustrating the hydrogen bonding interactions of the EtOH solvents of crystallisation (dashed lines). Only one {Ln(III)$_2$} unit from the asymmetric unit is shown and the majority of hydrogen atoms in each have been removed for clarity. Hydrogen bond distances (Å): O22(H22)···O10 = 2.986 in **20**; O10(H10)···O21 = 1.853 in **22**.*

As previously mentioned, complexes **20**, **22** and **24** possess two {Ln(III)$_2$} moieties in their asymmetric units. In such scenarios, and if the dimers are structurally different, any magnetic data analysis is rendered impossible. However, we have overcome this hurdle using a simple solvent substitution to the synthetic procedure. That is, by replacing EtOH with MeOH ligands at the Ln(III) centres, it was possible to synthesise the analogues [Gd(III)$_2$(L$_6$)$_2$(MeOH)$_2$(NO$_3$)$_4$] (**21**) and [Tb(III)$_2$(L$_6$)$_2$(MeOH)$_2$(NO$_3$)$_4$] (**23**) (Figure 126), both of which display just one {Ln(III)$_2$} unit in their asymmetric units (Scheme 4, Section 5.4.2). Complex **23** crystallises in the monoclinic $P2_1/c$ space group with unit cell parameters: a = 8.8442(2) Å, b = 10.7861(3) Å, c = 15.5930(4) Å, α = 90°, β = 102.63(2)°, γ = 90°. Complete crystallographic X-ray data can be seen in Table 14 (Section 5.2.1.1).

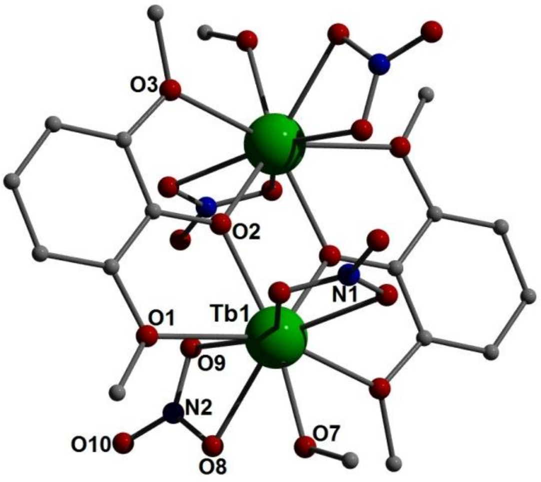

Figure 126 *- Crystal structure of complex* ***23****. Hydrogen atoms have been omitted for clarity.*

As stated previously, complexes **18** and **19** are ten coordinate (exhibiting distorted bi-capped square anti-prismatic geometries), while complexes **20**-**24** are all nine coordinate and display distorted mono-capped dodecahedral geometries (Figure 127). Individual {Ln(III)$_2$} units in complexes **18-24** pack in a space efficient brickwork pattern along the *bc* plane of the unit cell, forming 2D sheets which then align in parallel arrangements along the *b* direction of their unit cells (Figure 128-130).

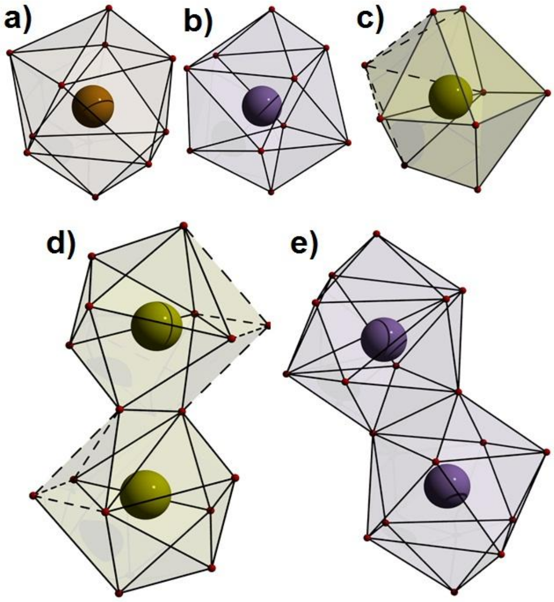

Figure 127 *- (a and b) Polyhedral representations of the distorted bi-capped square anti-prismatic geometries in* ***18*** *and* ***19*** *respectively. (c) Schematic of the distorted mono-capped dodecahedral geometries in* ***20*** *(and* ***21-24****). (d and e) Illustrations of the edge sharing polyhedra in* ***20*** *and* ***19*** *respectively, where oxygen donor atoms are represented by red spheres. The mono-cap observed in* ***20*** *(and* ***21-24****) is depicted by dashed lines.*

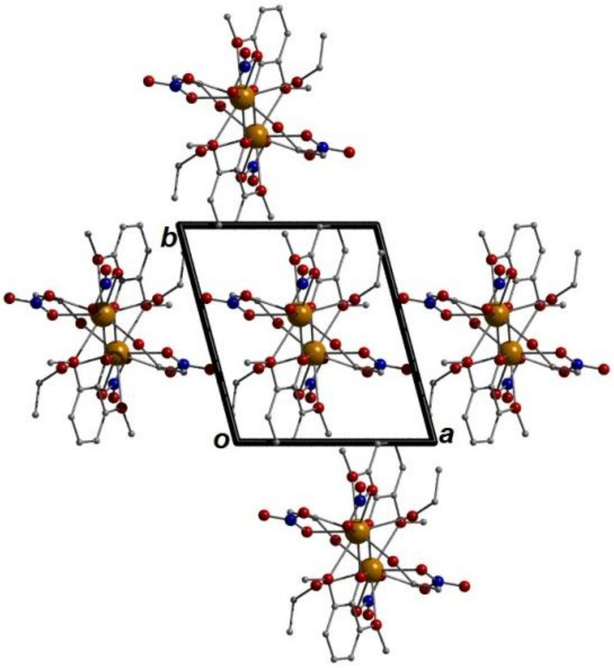

***Figure 128** - Crystal packing representation of [La(III)$_2$(L$_6$)$_2$(EtOH)$_4$(NO$_3$)$_4$] (**18**) as viewed down the c axis of the unit cell. Hydrogen atoms have been omitted for clarity.*

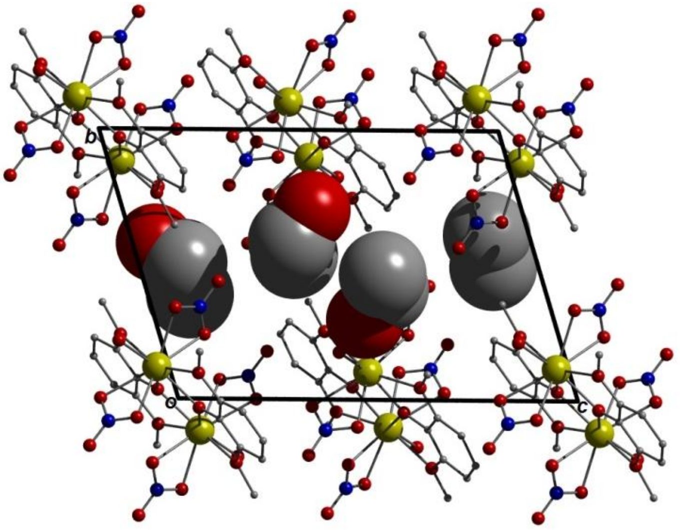

***Figure 129** - Crystal packing diagram of [Gd(III)$_2$(L$_6$)$_2$(H$_2$O)$_2$(NO$_3$)$_4$]·2EtOH (**20**) as viewed down the a axis of the unit cell. Hydrogen atoms have been removed for clarity and EtOH solvents of crystallisation are represented in space-fill mode.*

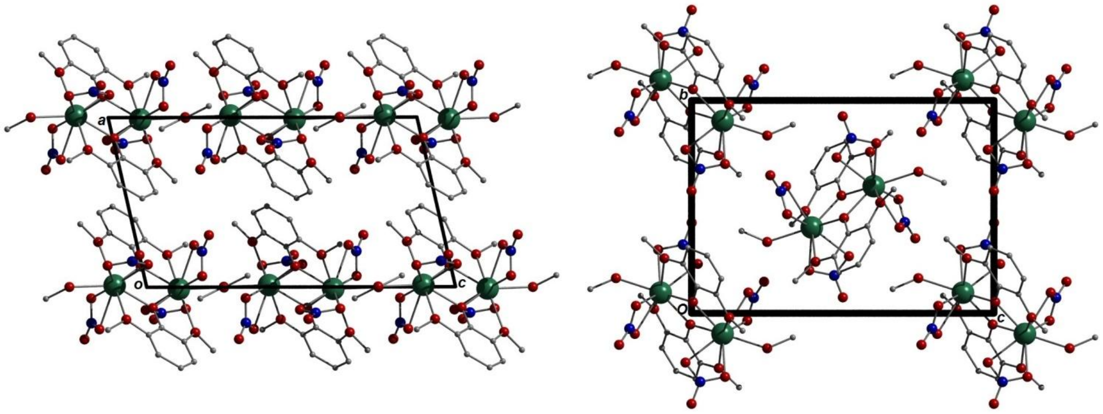

Figure 130 *- Packing diagram of [Tb(III)$_2$(L$_6$)$_2$(MeOH)$_2$(NO$_3$)$_4$]* ***(23)*** *as viewed down the b (left) and the a axis (right) respectively. All hydrogen atoms have been removed for clarity.*

Table 12 *- Summary of complexes* ***18-24*** *along with relevant structural data. Note: * symbol denotes the presence of two {Ln(III)$_2$} units in the asymmetric unit. In these instances the distances and the angles in the table represent Ln1···Ln1', Ln2···Ln2' and Ln1-O$_{phen}$-Ln1', Ln2-O$_{phen}$-Ln2' respectively.*

Complex	***M···M distance (Å)***	***M-O$_{phen}$-M angle (°)***	***Ln(III) C.N***
[La(III)$_2$(L$_6$)$_2$(EtOH)$_4$(NO$_3$)$_4$] (**18**)	4.100	114.79	10
[Ce(III)$_2$(L$_6$)$_2$(EtOH)$_4$(NO$_3$)$_4$] (**19**)	4.081	115.02	10
[Gd(III)$_2$(L$_6$)$_2$(H$_2$O)$_2$(NO$_3$)$_4$]·2EtOH (**20**)*	3.844, 3.857	113.49, 114.16	9, 9
[Gd(III)$_2$(L$_6$)$_2$(MeOH)$_2$(NO$_3$)$_4$] (**21**)	3.886	114.42	9
[Tb(III)$_2$(L$_6$)$_2$(EtOH)$_2$(NO$_3$)$_4$]·EtOH (**22**)*	3.827, 3.849	113.49, 114.48	9, 9
[Tb(III)$_2$(L$_6$)$_2$(MeOH)$_2$(NO$_3$)$_4$] (**23**)	3.861	114.71	9
[Dy(III)$_2$(L$_6$)$_2$(H$_2$O)$_2$(NO$_3$)$_4$]·2EtOH (**24**)*	3.797, 3.812	113.80, 115.03	9, 9

5.2.1.1 Crystallographic Data of Complexes 18-24

Table 13 *- Crystallographic data for complexes* ***18-21****.*

Complex	**18**	**19**	**20**·2EtOH	**21**
Formula[a]	$C_{24}H_{42}N_4O_{22}La_2$	$C_{24}H_{42}N_4O_{22}Ce_2$	$C_{20}H_{34}N_4O_{22}Gd_2$	$C_{18}H_{26}N_4O_{20}Gd_2$
M_W	1016.44	1018.86	997.003	932.93
Crystal Appearance	Colourless Parallelepiped	Pink Parallelepiped	Pink Parallelepiped	Pink Parallelepiped
Crystal System	Triclinic	Triclinic	Triclinic	Monoclinic
Space group	P-1	P-1	P-1	$P2_1/c$
a/Å	9.0215(18)	9.0215(18)	10.1121(3)	8.8472(18)
b/Å	10.285(2)	10.285(2)	10.9974(3)	10.817(2)
c/Å	10.712(2)	10.712(2)	15.4570(4)	15.665(3)
$\alpha/^o$	102.05(3)	102.05(3)	73.058(2)	90.00
$\beta/^o$	102.57(3)	102.57(3)	88.261(2)	102.81(3)
$\gamma/^o$	101.48(3)	101.48(3)	82.024(2)	90.00
V/Å^3	917.1(3)	917.1(3)	1628.32(8)	1461.8(5)
Z	1	1	2	2
T/K	149.9	150(2)	150(2)	150
λ^b/Å	0.7107	0.7107	0.7107	0.7107
D_c/g cm^{-3}	1.840	1.845	2.025	2.119
μ(Mo-Ka)/ mm^{-1}	2.388	2.540	4.132	4.590
Meas./indep.(R_{int}) refl.	3341/3169 (0.0142)	3341/3202 (0.0114)	5953/5101 (0.0215)	2669/2406 (0.0158)
Restraints, Parameters	0, 239	0, 239	0, 394	0, 202
wR2 (all data)	0.0380	0.0344	0.0595	0.0322
$R1^{d,e}$	0.0158	0.0137	0.0253	0.0149
Goodness of fit (GOOF) on F^2	1.058	1.112	1.085	1.039

[a] Includes guest molecules. [b] Mo-Kα radiation, graphite monochromator. [c] $wR2 = [\sum w(|F_o^2| - |F_c^2|)^2 / \sum w|F_o^2|^2]^{1/2}$. [d] For observed data. [e] $R1 = \sum||F_o| - |F_c|| / \sum|F_o|$.

***Table 14** - Crystallographic data for complexes **22-24**.*

Complex	**22**·EtOH	**23**	**24**·2EtOH
Formula[a]	$C_{22}H_{36}N_4O_{21}Tb_2$	$C_{18}H_{26}N_4O_{20}Tb_2$	$C_{20}H_{34}N_4O_{22}Dy_2$
M_W	1010.39	936.27	1007.5
Crystal Appearance	Light Pink Parallelepiped	Purple Block	Light Pink Parallelepiped
Crystal System	Monoclinic	Monoclinic	Triclinic
Space group	$P2_1/c$	$P2_1/c$	P-1
a/Å	18.8178(4)	8.8442(2)	10.0418(9)
b/Å	10.9671(3)	10.7861(3)	10.9358(10)
c/Å	16.5010(3)	15.5930(4)	15.3718(11)
$\alpha/^o$	90	90	73.217(7)
$\beta/^o$	95.085(2)	102.630(2)	88.489(7)
$\gamma/^o$	90	90	81.882(8)
V/Å^3	3392.02(13)	1451.49(6)	1599.8(2)
Z	4	2	2
T/K	150(2)	150(2)	150(2)
λ[b]/Å	0.7107	0.7107	0.7107
D_c/g cm^{-3}	1.979	2.142	2.083
μ(Mo-Ka)/ mm^{-1}	4.226	4.926	4.731
Meas./indep.(R_{int}) refl.	6193/5436 (0.0268)	2649/2400 (0.0199)	5853/4337 (0.0678)
Restraints, Parameters	0, 435	0, 202	0, 395
wR2 (all data)	0.0793	0.0404	0.2285
$R1$[d,e]	0.0269	0.0178	0.0812
Goodness of fit (GOOF) on F^2	1.199	1.092	1.060

[a] Includes guest molecules. [b] Mo-Kα radiation, graphite monochromator. [c] $wR2 = [\sum w(|F_o^2| - |F_c^2|)^2 / \sum w|F_o^2|^2]^{1/2}$. [d] For observed data. [e] $R1 = \sum||F_o| - |F_c|| / \sum|F_o|$.

5.2.2 NMR Studies of [La(III)$_2$(L$_6$)$_2$(EtOH)$_4$(NO$_3$)$_4$] (18)

The dissolution of [La(III)$_2$(L$_6$)$_2$(EtOH)$_4$(NO$_3$)$_4$] (**18**) in $(CD_3)_2SO$ gives rise to a deep purple solution and its subsequent ^{1}H and ^{13}C NMR spectra indicate that core structural integrity is retained as well as highlighting the lowering of symmetry upon La(III) ligation and solubilisation (Figure 131). Enhanced H_2O and weak EtOH signals in both spectra of **18** corroborate EtOH ligand loss and subsequent hygroscopic behaviour in **18** (and **19-24**), as indicated upon microanalysis on all siblings (see Experimental Section 5.4).

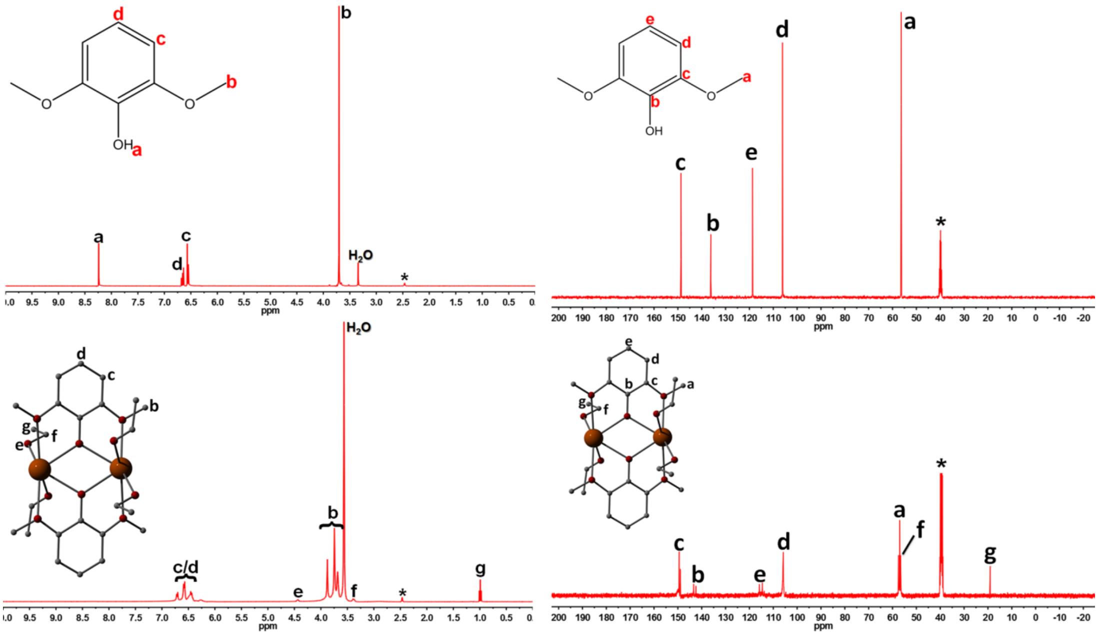

***Figure 131** - (Left) ^{1}H NMR spectra and labelled assignment of L_6H (top) and complex **18** (bottom). (Right) ^{13}C NMR spectra and labelled assignment of L_6H (top) and complex **18** (bottom). The * symbol represents the residual $(CD_3)_2SO$ solvent peak.*

5.2.3 Differential Scanning Calorimetry and Thermo-Gravimetric Analyses of $[Dy(III)_2(L_6)_2(H_2O)_2(NO_3)_4]\cdot 2EtOH$ (24)

DSC and TG analyses were simultaneously performed on a freshly produced and 14 month old sample of **24** (Figure 132 and 133). Analysis of the plots show that both samples exhibit similar curvatures with three distinct weight loss regions. The initial weight loss (of 11.0% and 9.7% respectively) corresponds to the loss of the 2 x EtOH solvents of crystallisation and 2 x H_2O terminal ligands in **24** (calculated as 12.7%) across the 25-300 °C temperature range. The second weight loss step (of 25.1% and 22.3% respectively) between 300 °C and 400 °C is consistent with the loss of all four metal bound nitrates (calculated as 24.6%). The final weight loss step (of 26.2% and 35.3% respectively) begins at 400 °C and can be attributed to the loss of the two metal bound L_6^- ligands (calculated as 30.4%). Further heating results in the decomposition of the remaining combustible materials.

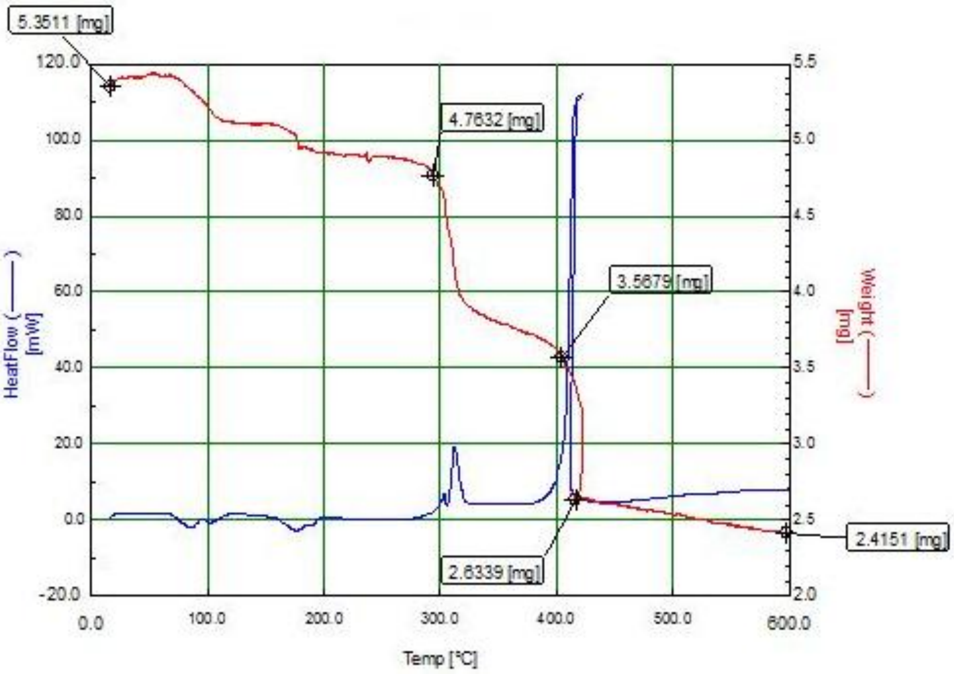

***Figure 132** - Schematic of DSC-TG analysis on a fresh crystalline sample of **24** analysed in the 25-600 °C temperature range in a N_2 atmosphere.*

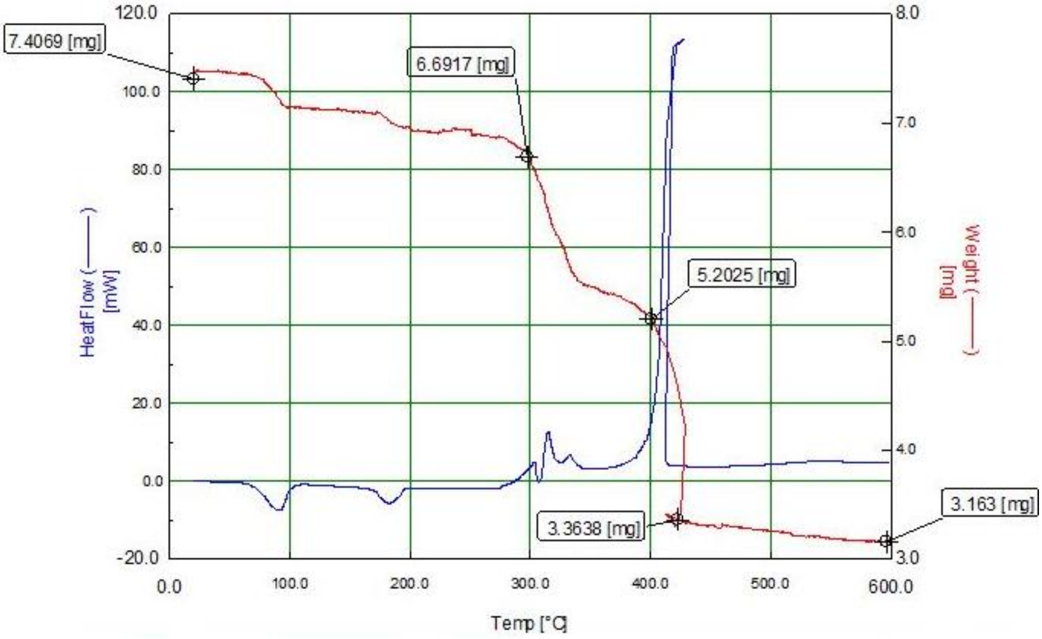

***Figure 133** - Plot of DSC-TG analysis for a 14 month old crystalline sample of **24** analysed in the 25-600 °C temperature range in an N_2 atmosphere.*

5.2.4 Magnetic Susceptibility Studies of [Ln(III)$_2$] Family

Dc magnetic susceptibility measurements were performed on powdered microcrystalline samples of $[Ce(III)_2(L_6)_2(EtOH)_4(NO_3)_4]$ (**19**), $[Gd(III)_2(L_6)_2(MeOH)_2(NO_3)_4]$ (**21**), $[Tb(III)_2(L_6)_2(MeOH)_2(NO_3)_4]$ (**23**) and

$[Dy(III)_2(L_6)_2(H_2O)_2(NO_3)_4]\cdot 2EtOH$ (**24**) in the 300-5 K temperature range with an applied field of 0.1 T and plotted as $\chi_M T$ versus T in Figure 134. The room temperature $\chi_M T$ value of 1.18 cm^3 mol^{-1} K for **19** is below that expected for a spin-only [Ce(III)$_2$] (1.62 cm^3 mol^{-1} K) moiety (Ce(III): $^2F_{5/2}$, S = 1/2, L = 3, J = 5/2 g = 6/7), while the room temperature $\chi_M T$ value of 33.01 cm^3 mol^{-1} K for **24** is slightly larger than that expected for two non-interacting Dy(III) ions (28.35 cm^3 mol^{-1} K) (Dy(III): $^6H_{15/2}$, S = 5/2, L = 5, J = 15/2, g = 4/3). The room temperature $\chi_M T$ values of 15.57 (**21**) and 23.82 (**23**) cm^3 mol^{-1} K are comparable with those expected for [Gd(III)$_2$] (15.75 cm^3 mol^{-1} K) and [Tb(III)$_2$] (23.63 cm^3 mol^{-1} K) (Gd(III): $^8S_{7/2}$, S = 7/2, L = 0, J = 7/2, g = 2; Tb(III): $^7F_6$, S = 3, L = 3, J = 6, g = 3/2) complexes. Complexes **19** and **21** share a similar curvature where the $\chi_M T$ product is almost constant with decreasing temperature. The $\chi_M T$ value for complex **19** is almost maintained with a minimum value of 0.95 cm^3 mol^{-1} K at low temperatures of approximately 5 K. A slightly larger gradual decrease is observed in complex **21**, reaching a minimum $\chi_M T$ product of 13.48 cm^3 mol^{-1} K at low temperatures. Upon decreasing temperature, a slightly steeper decline in the $\chi_M T$ products is noted for **23** and **24**, which begins to reduce in a more abrupt fashion at approximately 100 K in both cases, reaching minimum values of 14.46 and 19.90 cm^3 mol^{-1} K, respectively (Figure 134). This behaviour (i.e. the decline in the $\chi_M T$ values with decreasing temperature) is suggestive of very weak antiferromagnetic intra-molecular exchange interactions between Ln(III) ions in all cases. The direct relationship of $\chi_M T$ with decreasing temperature in complexes **21**, **23** and **24** can also be assigned to the thermal depopulation of their Stark-sublevels and / or the presence of significant anisotropy (only in **23** and **24**).

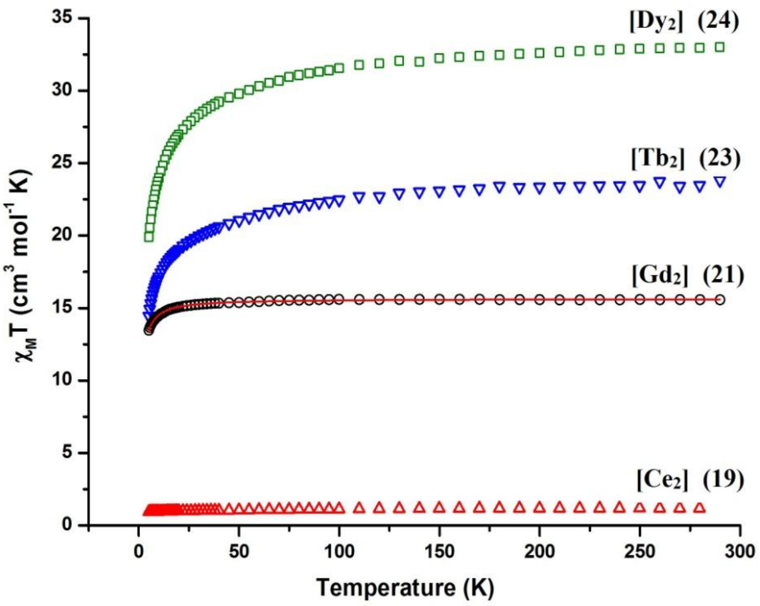

Figure 134 *- Magnetic susceptibility ($\chi_M T$) vs. T plots for **19** (Δ), **21** (○), **23** (∇) and **24** (□) where the solid red line in **21** represents the best fit to the experimental data.*

The χ_MT product of **21** was numerically fitted via the use of the simplex algorithm,[43] to spin-Hamiltonian 5.1 (see below) by numerical diagonalisation of the spin-Hamiltonian matrix. $\hat{S}_1$ and $\hat{S}_2$ describe the spin-operators for Gd1 and Gd2, μ_B is the Bohr magneton, and B represents the applied magnetic field. This yielded the best fit parameter J = -0.05 cm^{-1} (g = 2.0) with an S = 7/2 ground state (single ion spin of each Gd(III) ion), where J represents the Gd(III)-Gd(III) isotropic exchange parameter. The magnetic exchange parameter (J) obtained is consistent with those previously reported in the literature for similar Gd complexes.[44-47]

$$\hat{H} = -2J\hat{S}_1 \bullet \hat{S}_2 + \mu_B B g \sum_{1,2} \hat{S}_i \quad (\mathbf{5.1})$$

5.2.5 Magnetisation versus Field Studies

Variable temperature and variable dc field magnetisation experiments were performed on samples of $[Ce(III)_2(L_6)_2(EtOH)_4(NO_3)_4]$ (**19**), $[Gd(III)_2(L_6)_2(MeOH)_2(NO_3)_4]$ (**21**), $[Tb(III)_2(L_6)_2(MeOH)_2(NO_3)_4]$ (**23**) and $[Dy(III)_2(L_6)_2(H_2O)_2(NO_3)_4]\cdot 2EtOH$ (**24**) in the 2-7 K temperature range with a magnetic field range of 0.5-7 T. This experimental data is presented as magnetisation vs. field (M vs. H) and reduced magnetisation ($M/N\mu_B$ vs. H/T) plots in Figures 135-138. Once again the numerical data for **21** was fitted to the spin-Hamiltonian 5.1 (see above) and J was kept fitted to the previously determined value of -0.05 cm^3 to corroborate the S = 7/2 ground spin state and a (as expected) negligible D value. In complexes **19**, **21**, **23** and **24** magnetic saturation is observed at 7 T with values of 2.08 (**19**), 13.87 (**21**), 9.64 (**23**) and 13.24 (**24**). This confirms very weak exchange and can therefore be readily overcome by an applied magnetic field in all four complexes. Ac magnetisation studies indicated no frequency dependence signals for all members, dismissing slow relaxation of magnetisation (i.e. no SMM properties) at temperatures above 2 K.

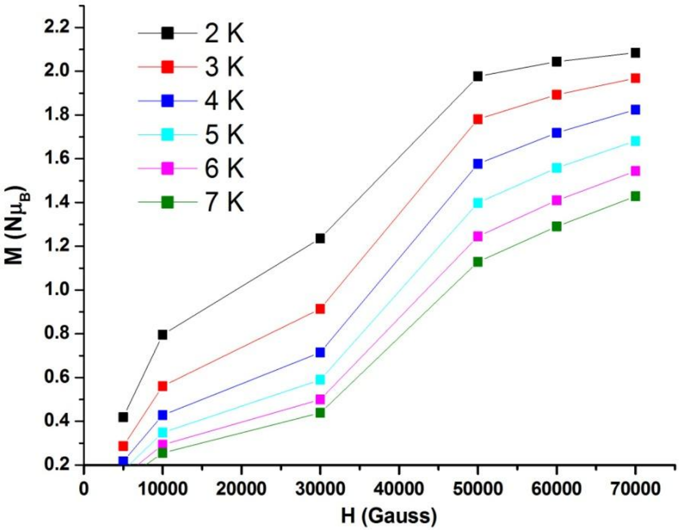

Figure 135 *- Plot of magnetisation (M) vs. field (H) for* ***19*** *in the temperature range 2-7 K with a magnetic field range of 0.5-7 T. The solid lines are a guide for the eye only.*

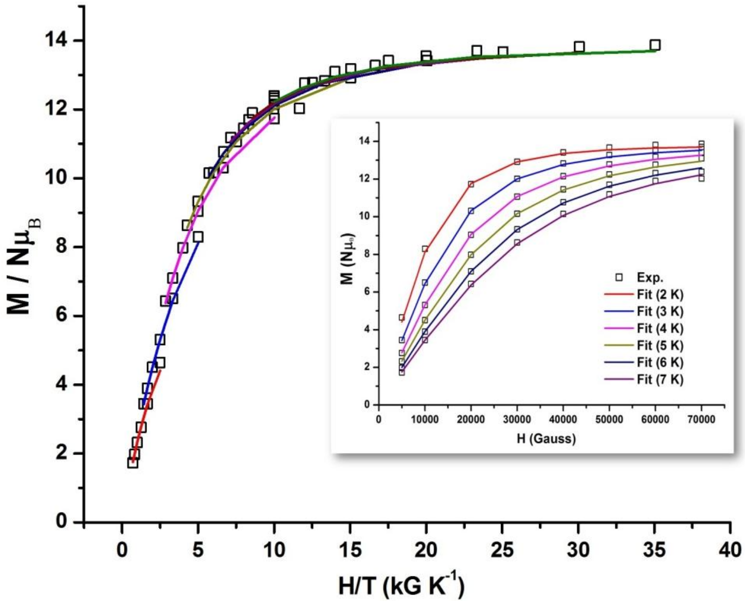

Figure 136 *- Reduced magnetisation ($M/N\mu_B$) vs. field (H/T) data for* ***21*** *performed in the 2-7 K temperature range and 0.5-7 T applied magnetic field. The coloured solid lines are best fit representations of the experimental data (red = 0.5 T, green = 7 T). (Inset) Plot of magnetisation (M) vs. field (H) for* ***21*** *performed in the 2-7 K temperature range and 0.5-7 T field range.*

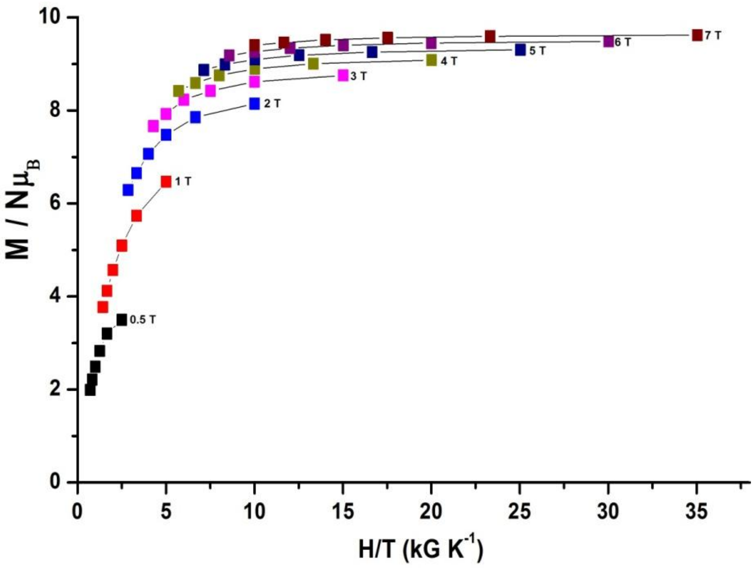

Figure 137 *- Plot of reduced magnetisation (M/Nμ_B) vs. field (H/T) data for complex* ***23*** *carried out in the 2-7 K temperature range and the 0.5-7 T magnetic field range. The solid lines act as a guide for the eye only.*

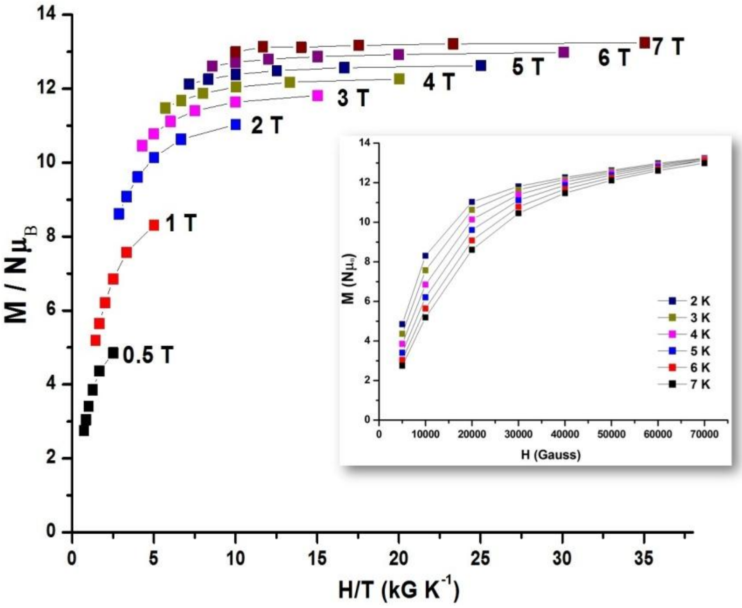

Figure 138 *- Plot of reduced magnetisation(M/Nμ_B) vs. field (H/T) data for complex* ***24*** *performed in the 2-7 K temperature range and 0.5-7 T applied magnetic field. The solid lines act as a guide for the eye. (Inset) Plot of magnetisation (M) vs. field (H) for* ***24*** *carried out in the 2-7 K temperature range and 0.5-7 T field range.*

5.2.6 Density Functional Theory (DFT) Studies

DFT and *ab initio* calculations were performed on [Ce(III)$_2$(L$_6$)$_2$(EtOH)$_4$(NO$_3$)$_4$] (**19**), [Gd(III)$_2$(L$_6$)$_2$(MeOH)$_2$(NO$_3$)$_4$] (**21**), [Tb(III)$_2$(L$_6$)$_2$(MeOH)$_2$(NO$_3$)$_4$] (**23**) and [Dy(III)$_2$(L$_6$)$_2$(H$_2$O)$_2$(NO$_3$)$_4$]·2EtOH (**24**) in order to gain further understanding of the magnetic properties of our {Ln(III)$_2$} family. In order to reduce computational cost and time, one of the Ln(III) centres of each dimeric complex was substituted with a diamagnetic La(III) centre, keeping the other Ln(III) ion intact for the resultant calculation. Another calculation was then performed by substituting another Ln(III) with La(III) while keeping the other Ln(III) intact. All DFT calculations were carried out by Gopalan Rajaraman and Tulika Gupta at the Indian Institute of Technology in Mumbai.

5.2.6.1 DFT Calculations on [$Gd(III)_2(L_6)_2(MeOH)_2(NO_3)_4$] (21)

DFT calculations were carried out on complex **21** to estimate the magnetic exchange interaction value (see DFT details in experimental section 5.4.1.6). This yielded a *J* value of -0.03 cm^{-1} for **21**, which is in good agreement with our experimental *J* value of -0.05 cm^{-1}. Earlier DFT studies carried out on dinuclear gadolinium acetate moieties by Rajaraman et al. suggested that the Gd-O-Gd angle plays an important role in determining the strength of magnetic coupling.[48]

The Gd1-O2-Gd1' angles in **21** are found to be rather acute (114.42°) and the Gd1-O2 distances of 2.31(17) and 2.312(16) Å are also rather short (cf. to Gd-O-Gd = 115.3° and Gd-O = 2.558 and 2.393 Å in reference 48), thus leading to antiferromagnetic coupling for this pair. To investigate the mechanism for this antiferromagnetic exchange interaction we employed molecular orbital (MO) analysis on complex **21**. We utilised the Kahn-Brait model,[49, 50] which relates the overlap of non-orthogonal orbitals to the nature of exchange interactions, allowing us to further understand the individual contribution to the net exchange interaction parameter *J*. The *J* value is composed of both J_F (ferromagnetic) and J_{AF} (antiferromagnetic) components and the dominating constituent determines the sign of the *J* value. Spin density plots were utilised to examine the electronic origin of exchange. In complex **21**, the spin densities of the two Gd(III) ions were calculated to be 7.022 (Table 15); a larger than expected value which suggests a spin polarisation mechanism is operational. The combined spin density plot and negative spin density values of the coordinated atoms suggest that spin delocalisation is poor, due to the contracted nature of the 4f-orbitals in the Gd(III) ions (Figure 139a and Table 15). Consequently, the spin polarization mechanism is more prominent than spin delocalisation, resulting in opposing spin densities on the ligand atoms surrounding the Gd(III) ions. The bridging oxygen atoms of L_6^- (O2 in Figure 139) have noticeably greater spin densities than the other oxygen atoms within the structure, due to a polarization effect brought about by the two Gd(III) ions. Overlap integrals between the singly occupied magnetic orbitals were computed to probe the contribution of the J_{AF} component towards total exchange. In contrast to earlier cases where many of the 4f-orbitals are orthogonal, a schematic mechanism was derived for {Gd(III)-Gd(III)} coupling where all the 49 f-f interactions are found to be significant (Figure 139b and Table 16).[51] The presence of these non-orthogonal 4f-orbitals results in the occurrence of moderate antiferromagnetic coupling interactions between the two Gd(III) centres in **21**. Additionally, the ligands enforce a low symmetry coordination environment upon the {Gd(III)$_2$} system, resulting in mixing of the 4f-orbitals and consequently the existence of antiferromagnetic coupling.

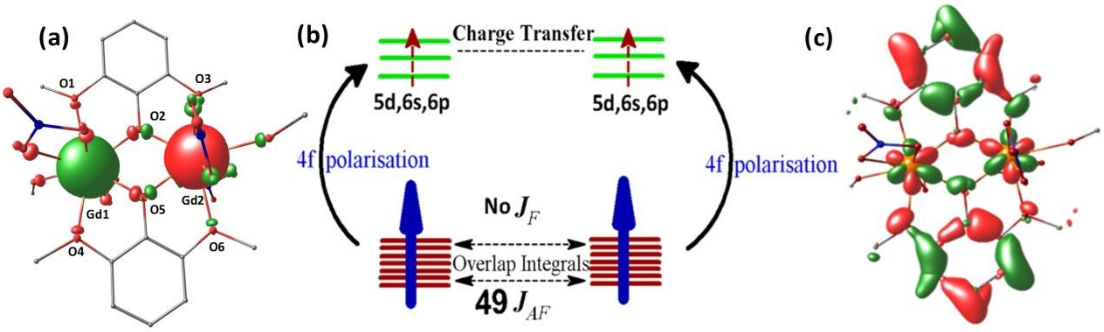

Figure 139 *- (a) Spin density plot of the S = 0 state of complex **21**. (b) Schematic of the spin polarisation mechanism for the Gd(III)-Gd(III) coupling interaction. (c) Illustration depicting the superimposed 4f-* f_{xyz} *orbitals of the Gd(III) centres where the computed overlap integral* (S_{ab} *= 0.22) value is utilised.*

Table 15 *- DFT computed spin density values for atoms in complex **21**.*

Atom specification	*HS (High Spin)*	*BS (Broken Symmetry)*
Gd1	7.02	-7.02
Gd2	7.02	7.02
O1	-0.0013	0.0013
O2	-0.0043	0.0004
O3	-0.0007	-0.0007
O4	-0.0007	0.0006
O5	-0.0043	-0.0004
O6	-0.0013	0.0014

Table 16 *- Overlap integral analysis between the seven 4f-orbitals of complex* ***21****.*

Alpha	***Beta***						
	83	*84*	*85*	*86*	*87*	*88*	*89*
	Overlap integrals						
83	0.22	0.04	0.07	-0.05	-0.07	0.04	-0.15
84	0.04	0.01	-0.06	0.21	0.20	0.06	0.01
85	0.07	-0.06	-0.01	-0.02	0.01	-0.03	0.04
86	-0.05	0.21	-0.02	0.05	-0.02	0.04	0.01
87	-0.07	0.2	0	-0.02	-0.08	0.02	-0.01
88	0.04	0.06	-0.03	0.04	0.02	0.01	0.04
89	-0.15	0.01	0.05	0.01	-0.01	0.04	-0.12

5.2.6.2 DFT Calculations on $[Dy(III)_2(L_6)_2(H_2O)_2(NO_3)_4]\cdot 2EtOH$ (24)

DFT analysis on $\{Dy(III)_2\}$ dimers are widely studied via computational methods in the literature and so were employed to analyse $[Dy(III)_2(L_6)_2(H_2O)_2(NO_3)_4]\cdot 2EtOH$ (**24**).[27, 28, 52-54] We applied the complete active space self-consistent field (CASSCF) coupled with the restricted active space state interaction (RASSI-SO)[55] procedure to estimate the ground state anisotropy and other parameters which dictate the magnetic properties of the complex. All calculations were performed with twenty one sextets, as it has been shown to produce good numerical estimates of the energy spectrum and g-anisotropy.[56-58] The computed energy spectrum of the eight lowest lying Kramer's doublets along with their g-anisotropies are presented in Table 17. Employing the crystal field parameters obtained from the calculations, the experimental data points were fitted and plotted using the Lines model via the PHI software site[59] (see section 5.4.1.6 for more details) (Figure 140). The fit produced an antiferromagnetic *J* value of -2.72 cm^{-1} which is line with other $\{Dy(III)_2\}$ dimers in the literature.[26, 60]

Table 17 *- Calculated energy spectrum, g-tensors,* $L_{z,}$ *product of g-tensors and the Φ and θ angles computed for the eight lowest lying Kramer's doublets for complex* ***24****. Dy(1a) and Dy(1b) represent the two different Dy(III) ions in complex* ***24****. See scheme 3 below for explanation of the angles Φ and θ.*

Dy ions	***Kramer's doublet***	***Energy (cm^{-1})***	g_x	g_y	g_z	***ϕ (°)***	***θ (°)***
Dy(1a) Dy(1b)	1 1	0.0 0.0	0.0 0.0	0.0 0.0	19.85 19.32	- -	8.4 175.9
Dy(1a) Dy(1b)	2 2	180.4 52.7	0.39 0.01	0.55 0.21	18.01 17.54	30.6 26.4	25.4 151.0
Dy(1a) Dy(1b)	3 3	217.9 117.6	1.02 1.53	2.32 1.87	13.95 13.97	19.0 22.8	12.4 153.1
Dy(1a) Dy(1b)	4 4	263.2 166.4	2.51 3.86	5.47 5.63	9.77 9.99	30.8 31.9	25.3 152.2
Dy(1a) Dy(1b)	5 5	342.1 222.8	8.27 10.92	4.76 6.24	0.004 1.26	131.0 10.7	122.7 165.3
Dy(1a) Dy(1b)	6 6	366.5 275.2	1.97 2.22	3.57 4.62	15.40 8.46	124.5 99.4	116.2 80.6
Dy(1a) Dy(1b)	7 7	437.2 312.7	1.15 2.78	1.99 6.32	12.57 10.99	93.7 96.7	85.4 79.2
Dy(1a) Dy(1b)	8 8	504.8 377.5	0.58 0.34	2.55 0.99	16.40 17.31	91.8 111.8	83.5 65.6

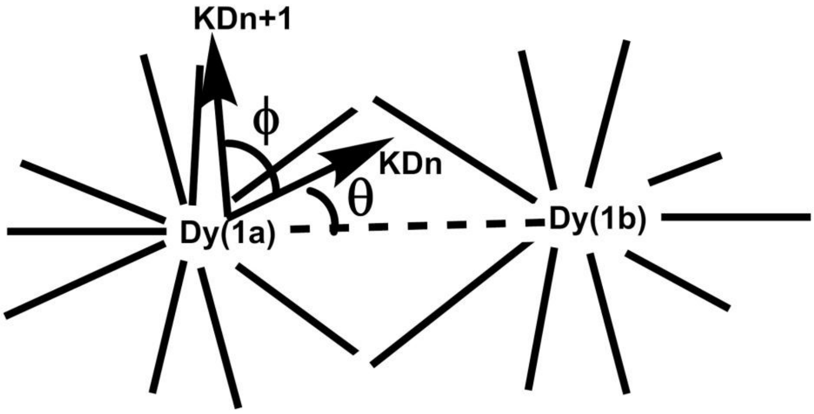

Scheme 3 *- Depiction of Φ which represents the angle between the anisotropy axis of the ground state and the first excited state doublet (for the Kramer's ions Ce(III) and Dy(III)) and pseudo doublets (in the case of the non-Kramer's ion Tb(III)). The symbol θ represents the angle between the ground state anisotropy axis and the Ln-Ln bond vector.*

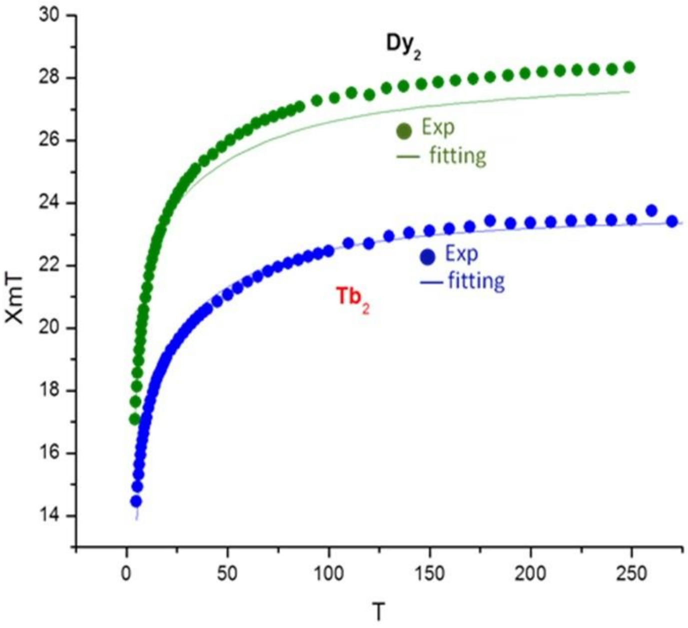

Figure 140 - *Plot of $\chi_M T$ vs. T of experimental data points (fitted using the PHI software) for the exchange interaction between two Dy(III) ions in complex* ***24****(green circles) and two Tb(III) ions in complex* ***23*** *(blue circles).*

The orientation of the ground state g-tensors along with the relative orientation of the g_z tensor of the first excited Kramer's doublet is displayed in Figure 141. At the ground state a strong axial anisotropy parameter was calculated for both Dy(III) centres with ($g_x = 0.0$, $g_y = 0.0$, $g_z = 19.85$) for Dy(1a) and ($g_x = 0.0$, $g_y = 0.0$, $g_z = 19.32$) for Dy(1b). The close proximity of the g_z value to 20 indicates that $m_J = \pm 15/2$ is the ground state for both Dy(III) ions. In addition, this suggests that the ground state has a zero magnetic moment in the XY plane, leaving the entire magnetic moment in the z-axis; therefore forming an ideal Ising state ($g_z = 20$). The first excited Kramer's doublet also displays an Ising state with $m_J = \pm 13/2$; however unlike the ground state some transverse anisotropy occurs here. In particular, the Dy(1a) centre exhibits larger g_x and g_y values than the Dy(1b) centre ($g_x = 0.39$ and $g_y = 0.55$ vs. $g_x = 0.01$ and $g_y = 0.21$), which suggests that these two sites are asymmetric in nature. The second Kramer's doublet presents an even more significant transverse anisotropy ($g_z \approx 14$, $g_{x,y} < 4$), as a result of scrambling of the m_J functions. The energy gap for the ground state-first excited state were calculated as 180.4 cm^{-1} and 52.7 cm^{-1} for Dy(1a) and Dy(1b) respectively. These supposedly represent the effective barrier to magnetisation reorientation (U_{eff}) for the individual Dy(III) sites; however as no *ac* signals are witnessed for complex **24** multiple relaxation channels are possible for magnetisation relaxation. The Dy(1a) and Dy(1b) ions are relatively strongly coupled, assuming a pseudo doublet ground state, strong coupling between the m_J levels would produce a diamagnetic ground state with an excited state at ~3.7 K, i.e. no relaxation is expected for temperatures below 3.7 K. Above this temperature, single-ion behaviour is expected to emerge and the relaxation is therefore controlled by the magnetic properties of the individual Dy(III) ions. Even though the ground state is axial in nature, the angle (Φ) between the ground state and the first excited Kramer's doublet varies from 30.6° to 26.4° for the Dy(1a) and Dy(1b) ions respectively. As there is an appreciable non-coincidence for both these sites, a significant relaxation due to the Orbach process is expected.[61, 62] The Orbach process is a thermal mechanism via an excited state, which was first described by Orbach et al when studying a Cerium Magnesium Nitrate complex.[63] In addition, Quantum Tunnelling of Magnetisation (QTM) and/or Raman relaxation is also expected to be present and the dominance of these relaxation processes results in the suppression of SMM behaviour in complex **24**.

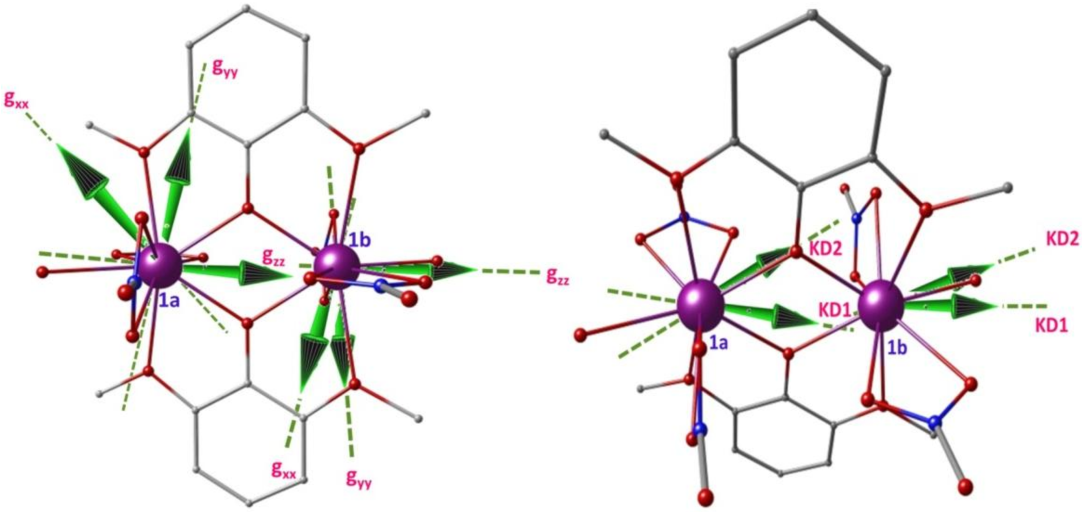

Figure 141 *- Representation of the CASSCF computed orientation of (left) the g_x, g_y and g_z axis of the ground state Kramer's doublet and (right) the simultaneous direction of the g_z anisotropic axis of the ground (KD1) and first excited state (KD2) Kramer's doublet of the Dy(1a) and Dy(1b) atoms in complex* ***24****. Hydrogen atoms have been omitted for clarity. Colour code: Deep purple (Dy), blue (N), red (O) and grey (C).*

In order to establish a greater understanding of the relaxation dynamics occurring, magnetisation relaxation analysis was performed on Dy(1a) and Dy(1b) (Figure 142). For both Dy(III) atoms the QTM found between the ground state Kramer's doublet was found to be small; however for Dy(1b) it is found to be larger than Dy(1a). Furthermore, the Orbach and Raman relaxation processes are also found to be smaller for Dy(1a) than Dy(1b). As expected Orbach followed by thermally assisted QTM is found to be the major relaxation mechanism by which the magnetization relaxes. It must also be noted that molecular relaxation mechanisms originating from weak inter-molecular exchange cannot be ruled out here.

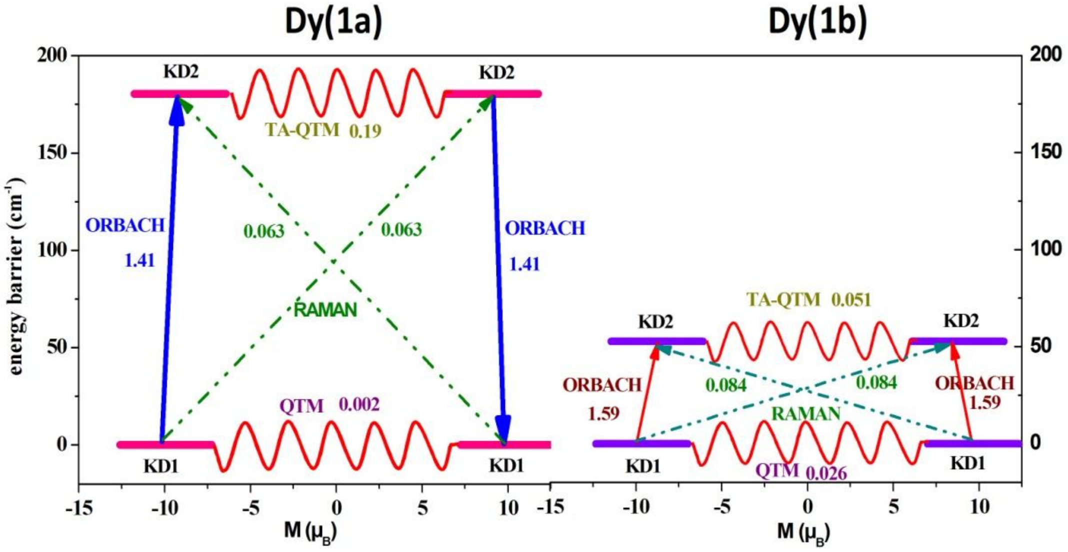

***Figure 142** - Magnetic relaxation study performed using results from ab initio calculations for Dy(1a) and Dy(1b) in complex **24**. Once again KD1 and KD2 represents the ground state and the first excited state Kramer's doublets respectively.*

In addition, we have also utilised a recently developed electrostatic model[64] to predict the orientation of the electrostatic anisotropy axis of complex **24** (Figure 143). Furthermore, this axis is predicted to be close to the *ab initio* anisotropic axis (deviation of about 21.45° for Dy(1a) and 11.08° for Dy(1b) sites), suggesting that the orientation of the anisotropy is dominated by the electrostatic charges of the ligands. In complex **24** the Dy(III) ions are surrounded by four nitrate oxygen atoms and four L_6^- oxygen atoms. All of which have a formal negative charge of -1. Therefore, if the anisotropic axis is perpendicular to the molecular plane, the oblate electron density of the Dy(III) sites would interact strongly with the four negatively charged nitrate oxygen atoms and result in a relatively high energy configuration. Thus the anisotropy axis would point in the general direction of the neutral H_2O ligands and hence minimise the repulsive force.

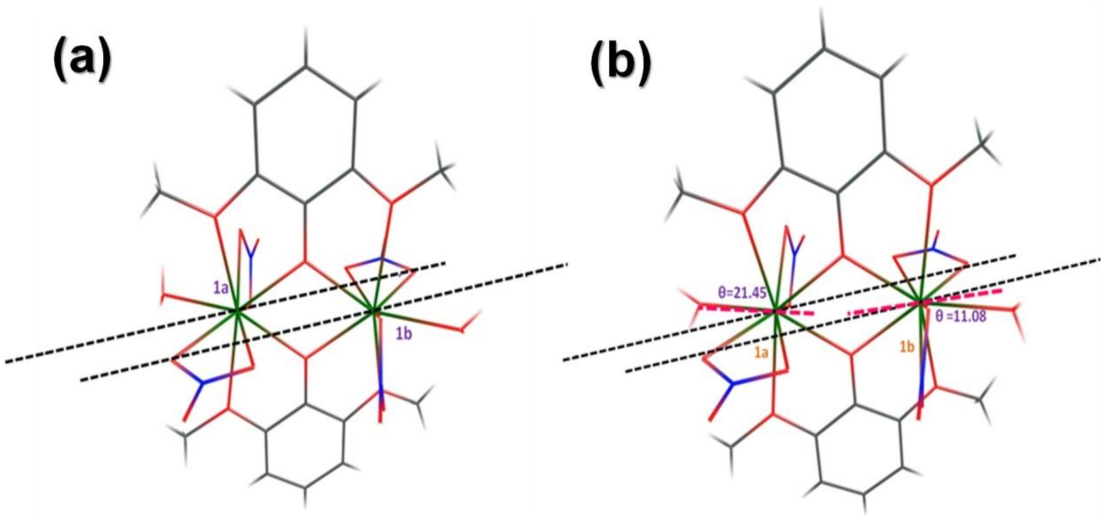

Figure 143 - *(a) Orientation of the electrostatic anisotropic axis (black dotted line) of the ground state Kramer's doublet in complex* ***24****. (b) Orientation of the ab initio anisotropic axis (red dotted line) with respect to the electrostatic anisotropic axis in* ***24****. The angle between the ab initio anisotropic axis and the electrostatic anisotropic axis (i.e. the electrostatic deviation angle) is represented by θ.*

We have also calculated the electrostatic energy surface for Dy(1a) by variation of the two polar angles α and β, which denotes the orientation of the quantization axis of the ground state wave function m_J = ±15/2 with respect to the crystal field of the ligands (Figure 144). The potential energy surface plot obtained from these calculations and given in Figure 144 shows two minima and two maxima values (labelled **a-d**). Two minima are noted when the α angle is at ~90° degrees while β lies at ~120° (point **b**) or 300° (point **a**). These two minima denote the orientation of the g_z tensor, where point **a** denotes a direction similar to that shown in Figure 141 and point **b** symbolises that another minima can be obtained if the g_z tensor points along the Dy-OH_2 axis of Dy(1a). The maxima points **c** and **d** are observed when the g_z axis is perpendicular to the molecular plane (along the coordinated nitrates).

4f-orbitals for Dy(1a) and Dy(1b) were also generated using the CASSCF method (Figures 145 and 146). Even though both the Dy(III) centres are symmetric with respect to their L_6^- ligand environments, the orientation of the H_2O ligands coordinated to the Dy(III) centres are different. One H_2O is located above, while the other is situated below the $\{Dy_2O_2\}$ plane and this appears to create a slight difference in the interaction of the H_2O orbitals with some of the 4f-orbitals. In addition, this is probably the reason for the difference in the behaviour observed between Dy(1a) and Dy(1b). Small topical deviations like these are known to significantly affect the anisotropy of Dy(III) ions.[65, 66]

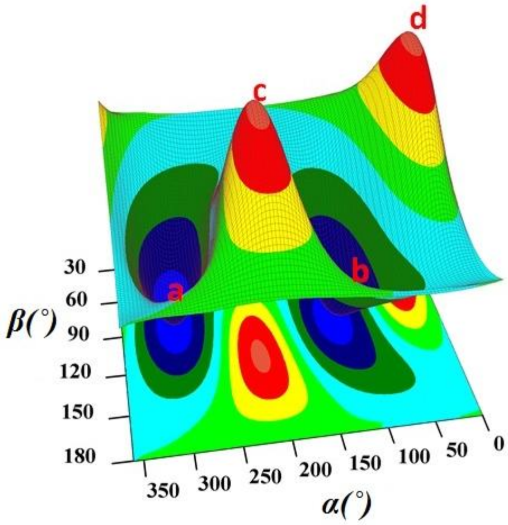

Figure 144 *- Illustration of the electrostatic energy surface of complex* ***24****. This is calculated by considering all the possible orientations (α and β) of the anisotropy axis generated by the charged ligands in complex* ***24****.*

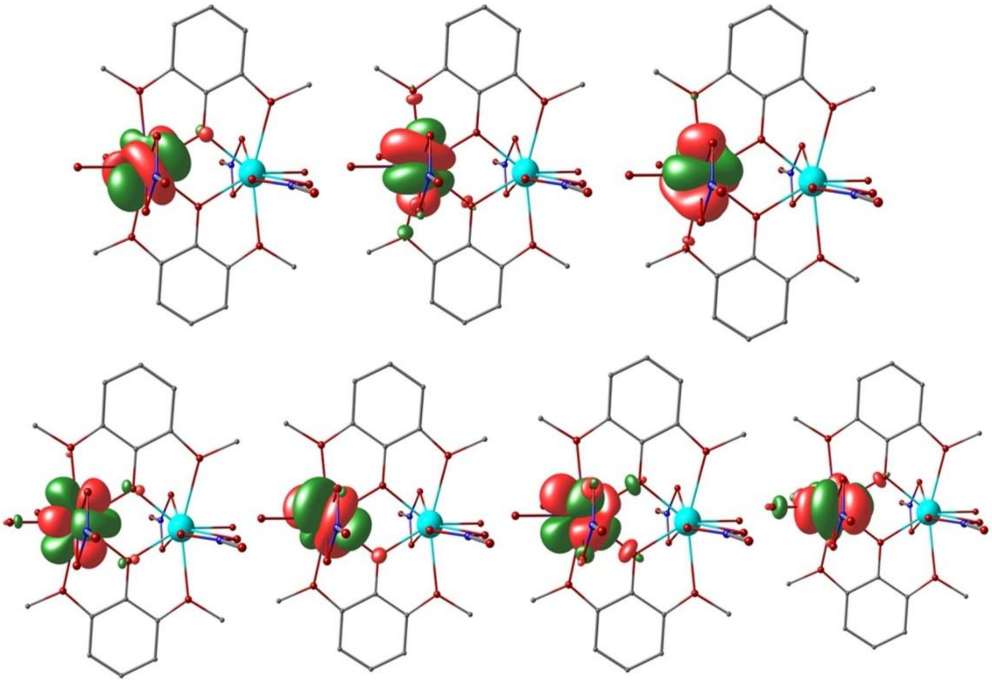

Figure 145 *- Illustration of the CASSCF computed 4f-orbitals for Dy(1a) in complex* ***24****. Turquoise colour represents Dy(1b) centre.*

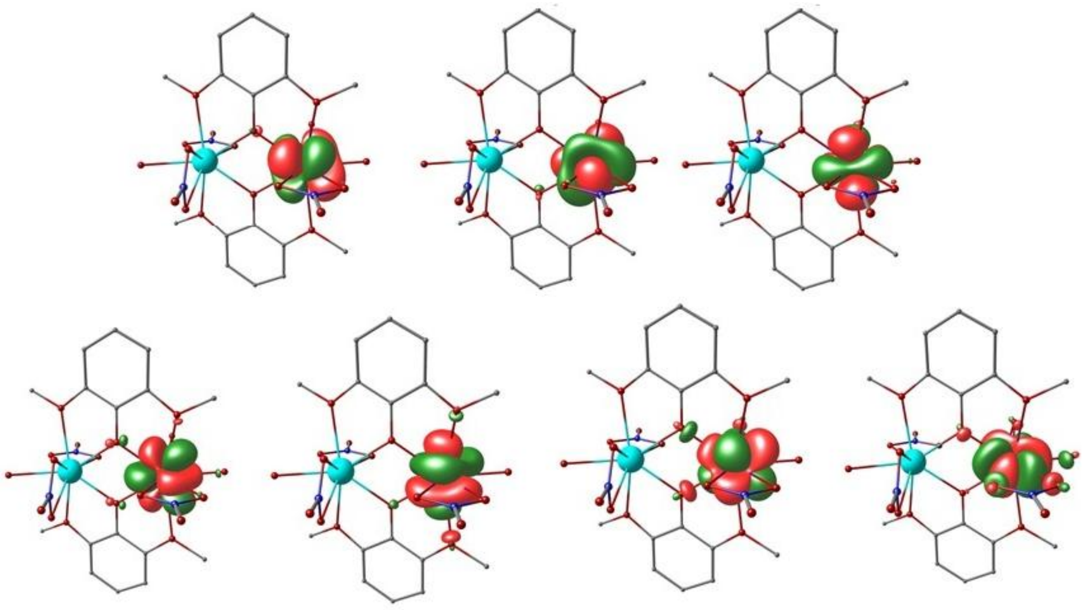

***Figure 146** - Representation of the CASSCF generated 4f-orbitals for Dy(1b) in complex **24**. Turquoise sphere denotes Dy(1a).*

5.2.6.3 DFT Calculations on [Tb(III)$_2$(L$_6$)$_2$(MeOH)$_2$(NO$_3$)$_4$] (23)

Here, we employed the same procedure as that for complex **24** with the exception of the number of roots computed (7 septets, 140 quintets and 195 triplet roots). The RASSI module allowed all the energy states within approximately 40,000 cm^{-1} (7 septets, 105 quintets and 112 triplets) to interact via spin-orbit coupling. Computed anisotropy for the six pseudo doublets and the singlet state for each Tb(III) ion in complex **23** are presented in Table 18. Other excited states are found to lie beyond 2190 cm^{-1}. The computed crystal field parameter lines model yields a J value of -0.076 cm^{-1} for complex **23** (Figure 140). This is indicative of an antiferromagnetic exchange interaction, where the value is much weaker than that obtained for the {Dy(III)$_2$} dimer, but similar in magnitude to that observed for the {Gd(III)$_2$} dimer. The ground pseudo doublet state has g_z values of 17.89 and 17.87 for Tb(1a) and Tb(1b) respectively and $g_{x,y}$ values of 0 for both ions. This is suggestive of a pure $m_J = \pm6$ ground state and the g_z values of ~18 are characteristic of an Ising ideal state. Indeed, the $g_{x,y}$ values are zero for all six pseudo doublets, with values above zero along the z direction; therefore an ideal Ising state is maintained throughout the six pseudo doublets. Up until the fourth pseudo doublet a decrease in the g_z tensor value is observed, reaching a minimum value of g_z ~10. After the fourth pseudo doublet the g_z value begins to rise, reaching a value of 17.71 for Tb(1b) in the highest energy pseudo doublet. This is almost as large as the ground state pseudo doublet and highlights the low symmetry nature of the crystal field.[67] The calculated effective energy gaps for Tb(1a) and Tb(1b) in the ±2 state are approximately 113 cm^{-1}. As we go from the ground state to the highest energy pseudo doublet state, larger ϕ values (the angle between the anisotropy axis of the ground state and the higher energy pseudo doublet state) are observed. The ϕ value for the highest energy pseudo doublet ranges from 85.15° for Tb(1a) to 87.47° for Tb(1b) (i.e. it is almost orthogonal to the ground state).

Table 18 *- Calculated energy spectrum, g-tensors, L_z, product of g-tensors and the Φ and θ angles computed for six pseudo doublets and one singlet state (note the * symbol represents the singlet state) in complex **24**. Tb(1a) and Tb(1b) denote the two different Tb(III) centres in complex **24**. See scheme 3 for description of the angles Φ and θ.*

Tb ions	***Pseudo Doublet/Singlet State***	***Energy (cm^{-1})***	***g_z***	***ϕ (°)***	***θ (°)***
Tb(1a)	1	0.00	17.89	-	11.98
	2	0.1			167.91
Tb(1b)	1	0.00	17.87	-	
	2	0.1			
Tb(1a)	3	112.8	14.94	11.63	1.69
	4	113.4			178.4
Tb(1b)	3	113.0	14.94	11.77	
	4	113.5			
Tb(1a)	5	207.1	11.45	12.03	5.25
	6	212.3			174.9
Tb(1b)	5	207.6	11.45	12.10	
	6	212.7			
Tb(1a)	7*	268.4	-		
Tb(1b)	7*	269.2	-		
Tb(1a)	8	305.6	9.99	82.41	91.27
	9	316.3			88.73
Tb(1b)	8	306.4	10.02	82.29	
	9	317.1			
Tb(1a)	10	354.1	13.07	82.99	94.66
	11	361.7			85.20
Tb(1b)	10	354.4	13.11	83.00	
	11	362.0			
Tb(1a)	12	556.6	17.6	85.15	97.12
	13	556.9			80.49
Tb(1b)	12	556.4	17.71	87.47	
	13	556.7			

The orientation of the computed ground state g axes along with the g_z axis for the first excited state pseudo doublet are shown in Figure 147. The g_z axes point in the direction of the Tb-MeOH bond, as MeOH is a neutral ligand this suggests that the anisotropic direction is controlled by electrostatic charges brought about by Tb(III) oblate electron density. As seen previously in complex **24**, QTM and thermally assisted QTM are not expected to be dominant mechanisms. Raman and / or Orbach processes may lead to relaxation of the magnetization in **23**. The quantitative relaxation mechanism calculations were not performed as they require several roots and are beyond our computational resources.

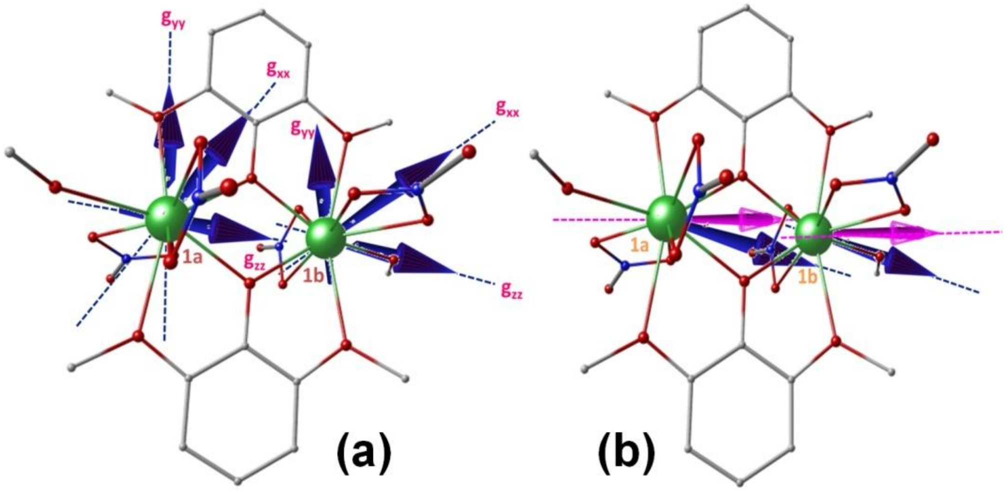

Figure 147 *- CASSCF computed orientation of the (a) g_x, g_y and g_z axis for the ground state pseudo doublet and (b) the simultaneous direction of the g_z anisotropic axis of the ground (deep blue arrow) and first excited state (pink arrow) pseudo doublet of the Tb(1a) and Tb(1b) atoms in* ***23****. Colour code: Green (Tb), blue (N), red (O) and grey (C).*

5.2.6.4 DFT Calculations on [Ce(III)$_2$(L$_6$)$_2$(EtOH)$_4$(NO$_3$)$_4$] (19)

The RASSI model was utilised for the configuration interaction (CI) procedure for complex **19** and consists of 7 doublets. Computed anisotropy parameters, energy spectrum and g-tensors for the Kramer's doublets of the ground $^2F_{5/2}$ multiplet of the Ce(III) ions can be seen in Table 19.

Table 19 *- Calculated energy spectrum, g-tensors, L_z, product of g-tensors and the Φ and θ angles computed for complex* ***19****. Ce(1a) and Ce(1b) represent the two different Ce(III) sites present in complex* ***19****. See scheme 3 for description of the angles Φ and θ.*

Ce ion	***Kramer's doublet***	***Energy (cm^{-1})***	***g_x***	***g_y***	***g_z***	***ϕ (°)***	***θ (°)***
Ce(1a)	1	0.0	0.56	0.92	3.51	-	73.19
Ce(1b)	1	0.0	0.55	0.93	3.51	-	106.96
Ce(1a)	2	253.9	2.36	1.49	0.55	67.22	60.87
Ce(1b)	2	253.3	2.35	1.48	0.56	67.03	119.22
Ce(1a)	3	574.6	0.50	0.76	3.71	77.19	10.15
Ce(1b)	3	573.5	0.49	0.76	3.71	77.01	169.81

The ground state Kramer's doublets for Ce(1a) and Ce(1b) are strongly rhombic in nature with large transverse components along the *x,y* directions and a small *z* component, while the x,y components for the first excited state are larger than the z component. The first excited state possesses an anisotropy direction that is very different from the ground state with an increase in ϕ of approximately 67°. Since uniaxial magnetic anisotropy is absent, no SMM behaviour is expected as corroborated from the experimental study. The large g_x and g_y values of the lowest state ensures the presence of significant components of low angular momentum eigenstates, as these are more stable compared to high angular momentum eigenstates in such a crystal field. Significant local fluctuating transverse magnetic fields enhance the relaxation via thermally assisted QTM (through 2-, 2+). The magnetic moment lies entirely along the *z* axis. The calculated effective energy gap to the ±2 states in **19** are found to be 254 cm^{-1} for both Ce(III) ions. Similarly to the Tb(III) ions in complex **23**, both the Ce(III) ions are found to be symmetric in nature. The computed orientation of the g-anisotropy for the ground state of complex **19** is shown in Figure 148(a). Drastic structural changes are observed in **19** in comparison to the structures for [Tb(III)$_2$] (**23**) and [Dy(III)$_2$] (**24**), resulting in a significant alteration to the g_z direction. The nitrate groups coordinate along the {Ce_2O_2} plane and as Ce(III) possesses oblate electron density it is highly unlikely that the g_z component will lie along this plane. Since the two neutral EtOH ligands located on each Ce(III) are perpendicular to the molecular plane, the g_z axis is expected to be pointed along this direction. This is in agreement with previous electrostatic investigations and as our calculations correspond with this expectation (see Ce(1a) site) it would indicate that the direction of the anisotropy can easily be determined by the ligand charges. In order to preserve the co-linearity between the two Ce(III) ions, the g_z for the Ce(1b) site points along the nitrate group. Since g_y is also significant here, its orientation in the {Ce_2O_2} plane is also found to deviate from the coordinated nitrate ions to yield a less repulsive ground state electronic structure. Magnetisation relaxation analysis calculations are summarized in Figure 148(b). In contrast to the Dy(III) ions in complex **24**, QTM mechanisms between the ground state Kramer's doublet are relatively large, while Orbach and Raman processes between the ground state and excited state Kramer's doublets are also significant. Thermally assisted (TA)-QTM appears to be likely to dominate over Raman processes.

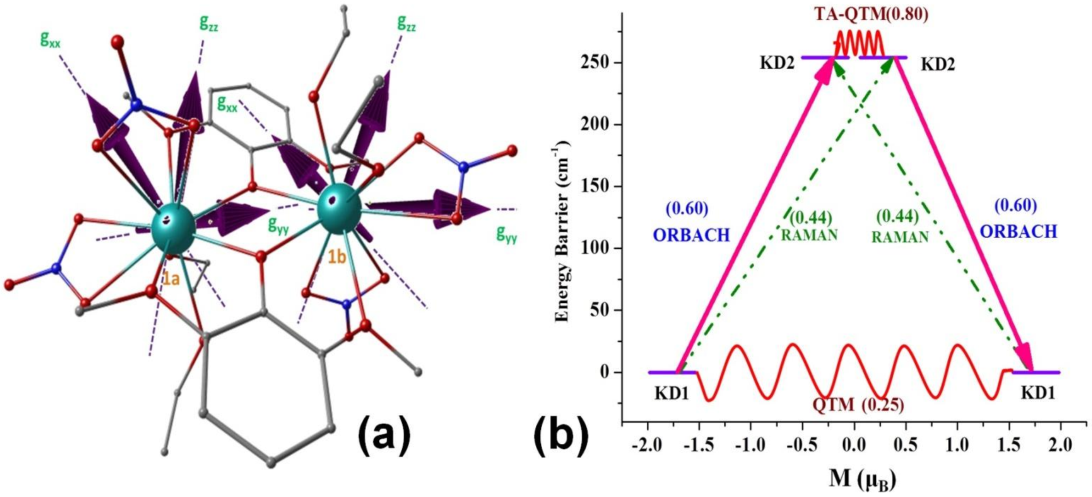

***Figure 148** - (a) CASSCF computed orientation of the g_x, g_y, g_z axis for the ground state Kramer's doublet for Ce(1a) and Ce(1b) in complex **19**. (b) Depiction of the magnetic relaxation study performed using results from the ab initio calculations for Ce(1a) and Ce(1b). The ground state and excited state are denoted by KD1 and KD2 respectively. Colour code: Aqua marine (Ce), blue (N), red (O) and grey (C).*

5.3 Conclusions and Observations

Through the utilisation of microwave technology we were able to synthesise a family of seven dinuclear [Ln(III)$_2$] complexes. These products were either unattainable or exhibited extremely poor yields via ambient bench and reflux conditions. This highlights the importance of exploring a range of reaction pathways when attempting to form paramagnetic cages. In particular, this illustrates the usefulness of microwave heating towards obtaining shorter reaction times, a wider range of reaction conditions and frequently larger yields. Furthermore, we have shown that by a simple solvent selection it is possible to control the number of {Ln(III)$_2$} moieties in the asymmetric units of our siblings. Dc magnetic susceptibility and magnetisation measurements revealed weak antiferromagnetic exchange in complexes [Ce(III)$_2$(L$_6$)$_2$(EtOH)$_4$(NO$_3$)$_4$] (**19**), [Gd(III)$_2$(L$_6$)$_2$(MeOH)$_2$(NO$_3$)$_4$] (**21**), [Tb(III)$_2$(L$_6$)$_2$(MeOH)$_2$(NO$_3$)$_4$] (**23**) and [Dy(III)$_2$(L$_6$)$_2$(H$_2$O)$_2$(NO$_3$)$_4$]·2EtOH (**24**). Fitting of the data for complex **21** yielded a *J* value of -0.05 cm^{-1} with S = 7/2. In complexes **19**, **21** and **23** magnetic saturation was observed at 7 T, confirming very weak exchange which can be easily overcome by an applied magnetic field. Ac magnetisation studies indicated no frequency dependence signals for all members; therefore SMM properties at temperatures above 2 K can be ruled out. DFT and *ab initio* calculations were successfully performed on complexes **19**, **21**, **23** and **24**. The

DFT computed magnetic exchange interactions are in agreement with those obtained experimentally. In addition, investigations into the mechanisms associated with these magnetic exchange interactions were explored. Larger spin density values than expected were calculated for complex **21**, suggesting that a spin polarisation mechanism is in operation. DFT calculations were performed on the g-tensors for complexes **19**, **23** and **24**. Complex **19** does not display uniaxial magnetic anisotropy; therefore it is not expected to exhibit SMM behaviour and this is in agreement with our experimental studies. In addition, the two Ce(III) ions appeared to behave in a symmetric manner. In complex **23** the six pseudo doublets demonstrated ideal Ising states and the Tb(III) ions were shown to be symmetric in nature. For complex **24**, these calculations indicated that the ground state and first excited Kramer's doublet were ideal Ising states and that Dy(1a) and Dy(1b) ions were asymmetric in nature. Computational analysis of magnetisation relaxation were carried out to gain a better understanding of the expected relaxation pathways for complex **19** and **24**. These calculations revealed that Orbach followed closely by thermally assisted (TA)-QTM processes were the dominant relaxation mechanisms likely to occur in complex **24**. Unlike complex **24**, the QTM mechanisms between the ground state Kramer's doublet in complex **19** were shown to be relatively large, while the Orbach and Raman between the ground state and excited state Kramer's doublets were also observed to be of significance. Thermally assisted (TA)-QTM was expected to dominate over Raman pathways. Orientation of the g-anisotropy were computed for complexes **19**, **23** and **24**. In addition to this, an electrostatic model was employed in an attempt to predict the electrostatic anisotropy orientation for complex **24**. This study suggested that the orientation of the anisotropy is greatly influenced by the electrostatic charges of the ligands, thus the anisotropy axis would be more likely to point along the lower energy configuration direction (i.e. along the bound H_2O ligands pathway) and as these H_2O ligands are neutral they exhibited minimal repulsive force. Likewise, from these studies electrostatic charges were expected to have an important role in complexes **19** and **23**. In complex **19**, the g_z axis is anticipated to align along the direction of the neutral EtOH ligands in Ce(1a) and the nitrate group in Ce(1b) in order to maintain co-linearity between the two Ce(III) sites. The anisotropy axis is anticipated to form along the direction of the neutral MeOH ligands in complex **23**. In terms of our future work, we would like to utilise the general synthetic procedure described herein in an attempt to produce heterometallic 3d-4f dimeric complexes.[68] As well as extending our family, this would allow us to further probe the magnitude and nature of the resultant exchange interactions towards developing a more detailed magneto-structural correlation.

5.4 Experimental Section

5.4.1 Instrumentation

For further details on instrumentation utilised in the analyses of complexes **18**-**24** see Chapter Two (Section 2.4.1).

5.4.1.1 Carbon, Hydrogen and Nitrogen Microanalysis

It should be noted that all elemental analysis carried out on [Ln(III)$_2$] analogues indicated a rapid loss of solvents of crystallisation (MeOH, EtOH) and hygroscopic behaviour. This was further supported by the swift decline in their crystallinity (lustre) upon exposure to air.

5.4.1.2 ^{1}H and ^{13}C NMR Spectroscopy

The hygroscopic behaviour of the [Ln(III)$_2$] analogues was once again observed with the appearance of enhanced H_2O signals in the NMR of **18**.

5.4.1.3 Thermal Gravimetric Analysis (TGA) and Differential Scanning Calorimetry (DSC)

TGA and DSC analysis were simultaneously carried out on samples of [Dy(III)$_2$(L$_6$)$_2$(NO$_3$)$_4$(H$_2$O)$_2$]·2EtOH (**24**) by Dermot McGrath using an Rheometric Scientific STA 625.

5.4.1.4 Powder X-ray Diffraction

Powder diffraction analysis were carried out on samples of **24** by Katarzyna Gniado using an Inel Equinox 6000 Powder X-ray Diffractometer.

5.4.1.5 Single Crystal X-ray Diffraction

The structures of **18**-**24** were collected on an Xcalibur S single crystal diffractometer (Oxford Diffraction) using an enhanced Mo source. All hydrogen atoms were placed in calculated positions. The non-hydrogen atoms were refined anisotropic except for the EtOH solvents of crystallisation in **20**, **22** and **24** which were left isotropic.

5.4.1.6 Density Functional Theory (DFT) Computational Details

All calculations for $[Gd_2(L_6)_2(NO_3)_4(MeOH)_2]$ (**21**) were performed using the Gaussian 09 suite of programmes,[69] in conjunction with the hybrid B3LYP function,[70-81] Noodleman's BS approach,[82] ECP-CSDZ[83] and TZV[84] for Gd(III) and the remaining elements. The absence of orbital contribution for Gd(III) allows for the determination of the exchange coupling constant via an isotropic HDVV spin-Hamiltonian. The spin-Hamiltonian 5.2 denotes the magnetic exchange interaction between the two Gd(III) ions.

$$\hat{H} = -J\hat{S}_{Gd} \bullet \hat{S}_{Gd} \quad \mathbf{(5.2)}$$

Post-Hartree-Fock *ab initio* calculations were carried out with the MOLCAS 7.8 program package.[85] The Douglas-Kroll Hamiltonian[86] approach was used to treat the relativistic effects in two steps. The complete active space self-consistent field (CASSCF) method was utilised to determine spin-free wave functions and energies of basis sets. Spin-orbit free states were obtained by employing the RASSCF method, whereas spin-orbit coupling has been taken into account using the RASSI-SO method.[55] The RASSI-SO method utilises CASSCF wave functions as the basis sets and multi-configurational wave functions as input states. The input of the resultant wave functions and energies of the molecular multiplets into a specially designed model called SINGLE-ANISO[87] allowed for the calculation of the anisotropic magnetic properties and g-tensors of the lowest state. The magnetic properties of a single magnetic ion are calculated by a fully *ab initio* approach, in which the spin-orbit coupling is considered non-perturbatively. The ANO-RCC-VDZ basis sets for all the atoms used in the calculations were taken from the ANO-RCC basis library in the MOLCAS 7.8 program package. The g-tensors for the Kramer doublets of the Dy(III) and Ce(III) ions and those for the pseudo-doublets of the Tb(III) centres were calculated based on the pseudo-spin $\tilde{S}$ = 1/2 formalism in the RASSI and SINGLE-ANISO modules. Note that for non-Kramer ions, the values of g_x and g_y are equal to zero in the pseudo-spin $\tilde{S}$ = 1/2 formalism, due to vanishing off-diagonal matrix elements between the conjugate states.[88]

In order to reduce computational cost and time, we substituted one of the Ln(III) of each dimeric complex with a diamagnetic La(III) centre, keeping the other Ln(III) ion intact for the resultant calculation. Another calculation was then performed by substituting another Ln(III) with La(III) while keeping the other Ln(III) intact.

Ligand exchange interactions between two Ln(III) centres are weak as a result of their associated deep seated 4f-orbitals. *Ab initio* calculations have been developed for lanthanides; however these tend to be more suitable for mononuclear species. Unfortunately, phenomenological Hamiltonians utilise empirical fits in order to measure exchange interactions in polynuclear systems. The introduction of the software package PHI[59] has solved this problem and we have used this program to calculate the exchange parameter J.

5.4.2 Syntheses

All reagents and solvents were used as purchased without further purification. All reactions were performed in a CEM Discover® microwave reactor (Figure 149). **Caution**: It should be noted that although no difficulties were encountered during this work, nitrate salts are potentially explosive and great care should be exercised when using them.

Figure 149 *- Image of the CEM Discover microwave oven used in this research.*

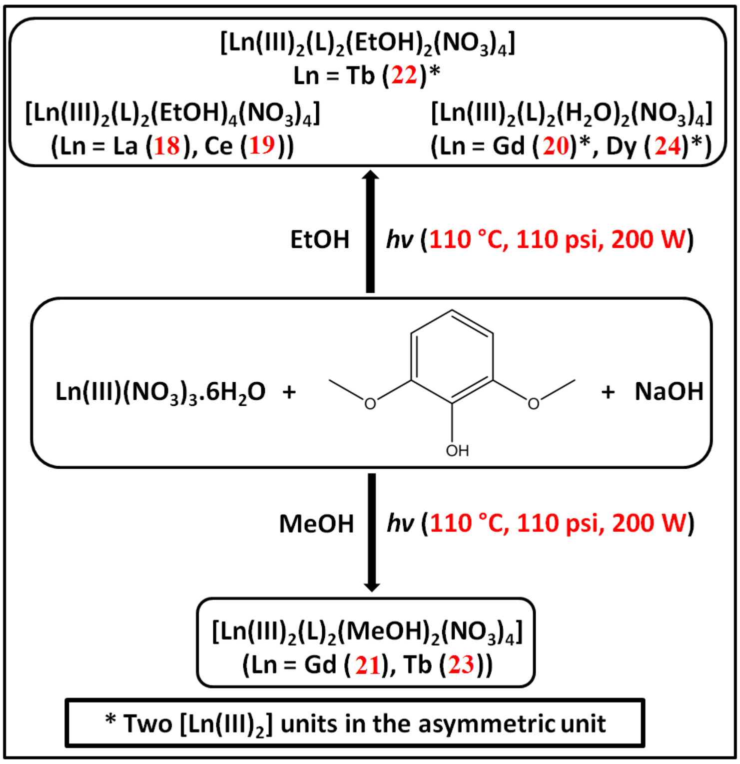

Scheme 4 *- Depiction of the synthetic routes for complexes* ***18-24****. Solvents of crystallisation have been omitted.*

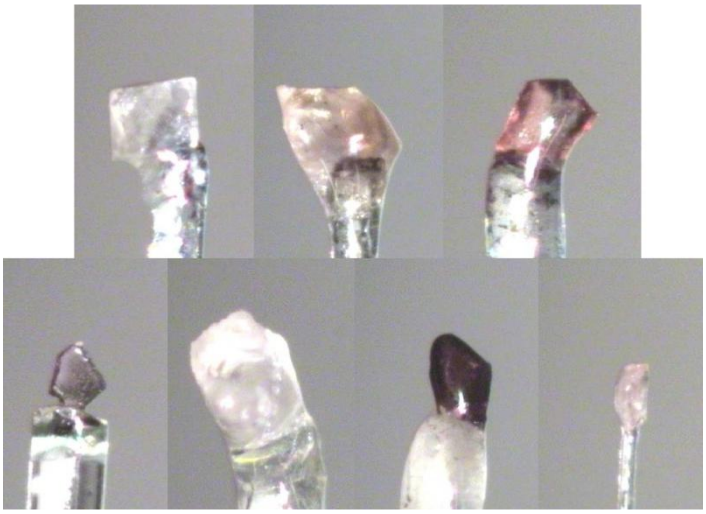

Figure 150 *- (Left to right) Single crystals of complexes* ***18-20*** *(top) and* ***21-24*** *(bottom).*

5.4.2.1 Synthesis of $[La(III)_2(L_6)_2(EtOH)_4(NO_3)_4]$ (18)

$La(NO_3)_3 \cdot 6H_2O$ (0.25 g, 0.58 mmol), 2,6-dimethoxyphenol (L_6H) (0.089 g, 0.58 mmol) and NaOH (0.023 g, 0.58 mmol) were dissolved in a sealed microwavable glass vial containing 20 cm^3 of EtOH and stirred for 20 min. The sealed glass vial was inserted into a microwave reactor and stirred at the following settings (T = 110 °C, pressure = 110 psi and power = 200 W) for 20 min. Upon cooling the solution was filtered to give an almost clear solution which was allowed to concentrate via slow evaporation. After a few days, the mother liquor developed a pink colour and colourless X-ray quality crystals of **18** formed. The crystals were collected and air dried with a yield of 20%.

C, H, N Elemental Analysis

Calculated % as $[La(III)_2(L_6)_2(H_2O)_4(NO_3)_4]$ ($C_{16}H_{26}N_4O_{22}La_2$): C 21.25, H 2.90, N 6.20.

Found %: C 20.93, H 2.46, N 6.43.

FT-IR (cm^{-1}): 3460 (w), 1648 (w), 1592 (w), 1491 (m), 1476 (m), 1435 (s), 1293 (s), 1245 (m), 1227 (m), 1192 (w), 1169 (w), 1084 (s), 1040 (m), 1015 (m), 840 (m), 816 (w), 765 (m), 740 (w), 727 (m), 713 (m).

^{1}H NMR (400 MHz, d$_6$-DMSO, 25 °C): δ = 1.15 (t, 3H, CH_3: EtOH (g)), 2.46 ($(CD_3)_2SO$ residual peak), 3.39 (q, 2H, CH_2: EtOH (f)), 3.56 (s, H_2O), 3.68-3.87 (m; multiple environs of O-CH_3 (b)), 4.43 (s, OH, EtOH (e)), 6.27-6.70 (m, Ar-H (c/d)).

^{13}C NMR: (400 MHz, d$_6$-DMSO, 25 °C): δ = 19.02 (CH_3: EtOH (g)), 39.50 ($(CD_3)_2SO$ residual peaks), 56.63 (CH_2: EtOH (f)), 56.96 and 57.49 (two environs for C1 (a)), 105.79 and 105.97 (two environs for C3 (d)), 114.59 and 115.81 (two environs for C4 (e)), 142.43 and 143.37 (two environs for C5 (b)), 148.97 and 149.44 (two environs for C2 (c)).

UV/vis Analyses

UV-vis studies of **18** were carried out in MeOH and MeCN solutions displaying characteristic $\pi \rightarrow \pi^*$ absorption peaks at 203.1, 203 and 246 nm (ε values ranging from 26.7-207.4 x 10^3 dm^3 mol^{-1} cm^{-1}). The peaks at 271 and 272.8 nm are due to $n \rightarrow \pi^*$ excitations (ε values ranging from 16.6-22.8 x 10^3 dm^3 mol^{-1} cm^{-1}).

(MeOH): λ_{max} [nm] (ε_{max} 10^3 dm^3 mol^{-1} cm^{-1}): 203.1 (207.4), 272.8 (16.6).

(MeCN): λ_{max} [nm] (ε_{max} 10^3 dm^3 mol^{-1} cm^{-1}): 203 (145.3), 246 (26.7), 271 (22.8).

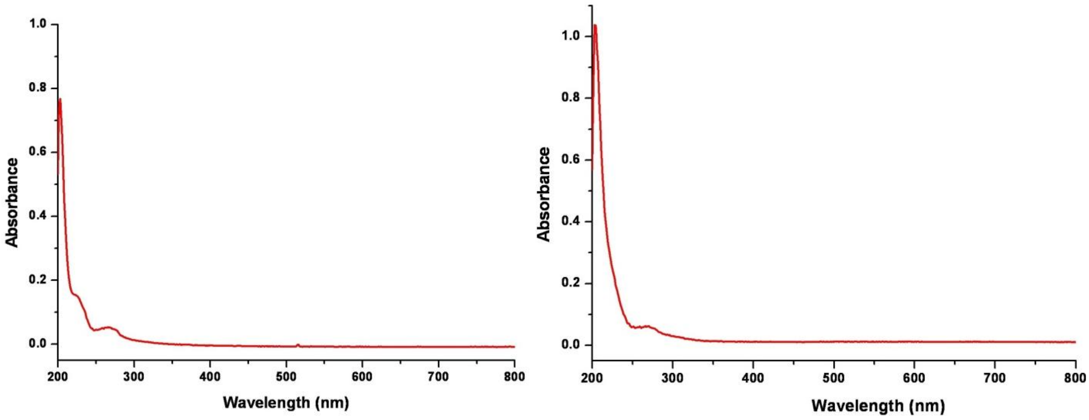

Figure 151 *- UV-visible spectra of 2,6-dimethoxyphenol (L_6H) (left) and* ***18*** *in MeOH.*

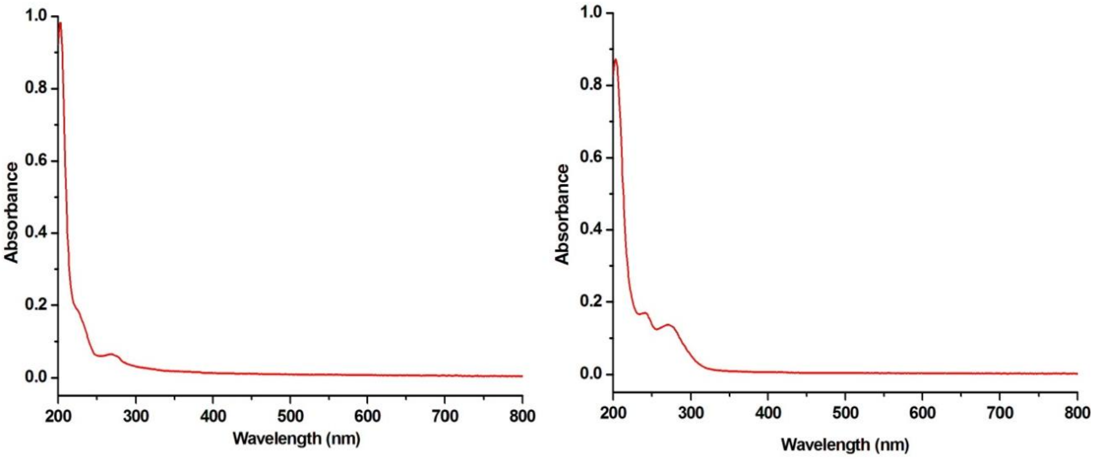

Figure 152 *- UV-visible spectra of (L_6H) (left) and* ***18*** *in MeCN.*

5.4.2.2 Synthesis of $[Ce(III)_2(L_6)_2(EtOH)_4(NO_3)_4]$ (19)

To a 20 cm^3 ethanolic solution of $Ce(NO_3)_3{\cdot}6H_2O$ (0.25 g, 0.58 mmol) in a glass lined microwavable reaction vessel was added L_6H (0.089 g, 0.58 mmol) and NaOH (0.023 g, 0.58 mmol). The reaction vial was inserted into a microwave reactor and heated at the following settings (T = 110 °C, pressure = 110 psi and power = 200 W) for 20 min. Upon cooling the light brown solution was filtered and allowed to stand. Slow evaporation of the mother liquor produced light pink X-ray quality crystals of **19** within 24 h. The crystals were collected and air dried with a yield of 19%.

C, H, N Elemental Analysis

Calculated % as $[Ce(III)_2(L_6)_2(H_2O)_4(NO_3)_4]$ ($C_{16}H_{26}N_4O_{22}Ce_2$): C 21.20, H 2.89, N 6.18.

Found %: C 21.08, H 2.73, N 6.01.

FT-IR (cm^{-1}): 3463 (w), 1648 (w), 1593 (w), 1492 (m), 1476 (m), 1435 (s), 1310 (s), 1293 (s), 1246 (m), 1228 (m), 1192 (w), 1169 (w), 1085 (s), 1042 (m), 1016 (m), 841 (m), 816 (w), 765 (m), 741 (w), 727 (m), 714 (m).

UV/vis Analyses

UV-vis studies of **19** were performed in solutions of MeOH and MeCN. Absorption peaks at 202.1 and 203 nm are representative of $\pi\rightarrow\pi^*$ transitions (ε values ranging from 85.3 to 193.2 x 10^3 dm^3 mol^{-1} cm^{-1}), while absorption at wavelengths 268.3 and 272.8 nm are indicative of $n\rightarrow\pi^*$ excitations (ε values ranging from 7.2 to 16.6 x 10^3 dm^3 mol^{-1} cm^{-1}).

(MeOH): λ_{max} [nm] (ε_{max} 10^3 dm^3 mol^{-1} cm^{-1}): 203 (85.3), 268.3 (7.2).

(MeCN): λ_{max} [nm] (ε_{max} 10^3 dm^3 mol^{-1} cm^{-1}): 202.1 (193.2), 272.8 (16.6).

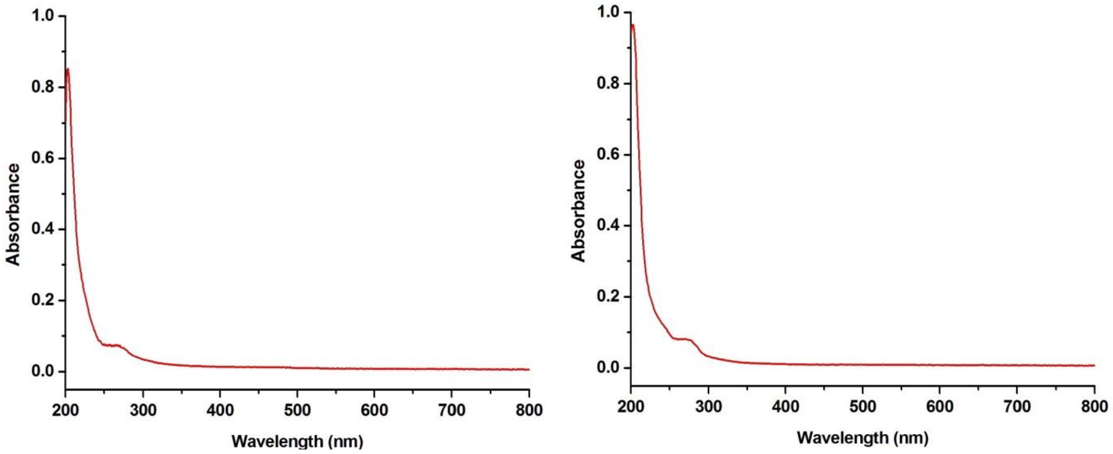

***Figure 153** - UV-visible spectra of **19** in MeOH (left) and MeCN (right).*

5.4.2.3 Synthesis of [Gd(III)$_2$(L$_6$)$_2$(H$_2$O)$_2$(NO$_3$)$_4$]·2EtOH (20)

$Gd(NO_3)_3\cdot6H_2O$ (0.25 g, 0.55 mmol), L_6H (0.085 g, 0.55 mmol) and NaOH (0.022 g, 0.55 mmol) were stirred in a microwavable glass vial containing 20 cm^3 of EtOH for 20 min to allow complete dissolution of the reactants. The solution was then stirred under microwave settings: T = 110 °C, pressure = 110 psi and power = 200 W for 20 min to afford a light pink solution. Upon cooling, the solution was filtered and allowed to slowly evaporate off, resulting in the formation of pink X-ray quality crystals after a few days with a yield of 16%.

C, H, N Elemental Analysis

Calculated % as $[Gd(III)_2(L_6)_2(H_2O)_2(NO_3)_4]\cdot 4H_2O$ ($C_{16}H_{30}N_4O_{24}Gd_2$): C 19.67, H 3.10 , N 5.74.

Found %: C 19.96, H 2.76, N 5.29.

FT-IR (cm^{-1}): 3421 (w), 2976 (w), 1599 (w), 1477 (s), 1281 (s), 1250 (m), 1227 (w), 1190 (w), 1169 (w), 1083 (s), 1040 (m), 1025 (m), 1009 (m), 875 (w), 847 (m), 812 (m), 767 (m), 743 (m), 712 (s), 679 (m).

UV/vis Analyses

UV-vis analysis of **20** were carried out in MeOH and MeCN solutions. Characteristic $\pi\rightarrow\pi^*$ absorption peaks are observed at 201, 203, 271 nm (ε values ranging from 35-230 x 10^3 dm^3 mol^{-1} cm^{-1}). In addition, in MeOH an absorption peak occurs at 270 nm which is as a result of an $n\rightarrow\pi^*$ excitation (ε values of 21.2 x 10^3 dm^3 mol^{-1} cm^{-1}).

(MeOH): λ_{max} [nm] (ε_{max} 10^3 dm^3 mol^{-1} cm^{-1}): 203 (182.8), 270 (21.2).

(MeCN): λ_{max} [nm] (ε_{max} 10^3 dm^3 mol^{-1} cm^{-1}): 201 (230), 271 (35).

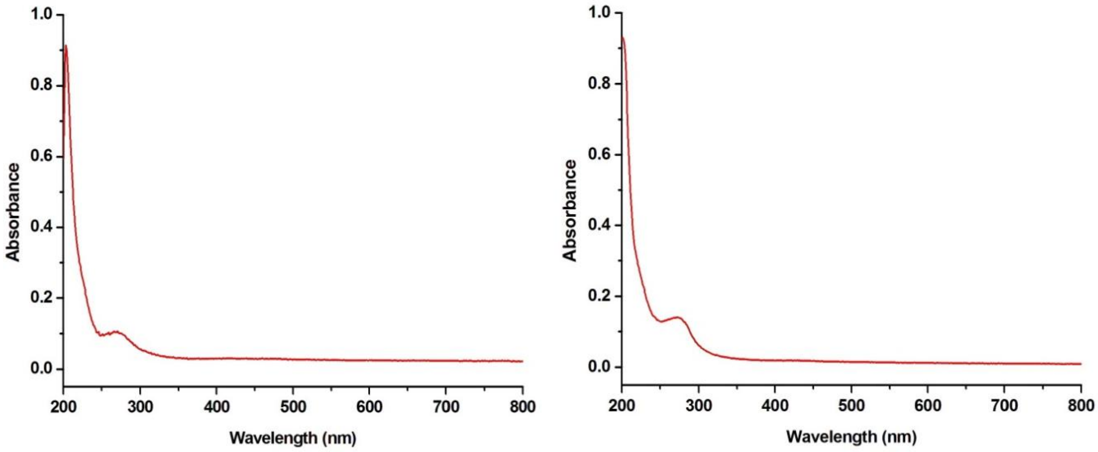

***Figure 154** - UV-visible spectra of **20** in MeOH (left) and MeCN (right).*

5.4.2.4 Synthesis of $[Gd(III)_2(L_6)_2(NO_3)_4(MeOH)_2]$ (21)

L_6H (0.085 g, 0.55 mmol) and NaOH (0.22 g, 0.55 mmol) were added to a 20 cm^3 methanolic solution of $Gd(NO_3)_3\cdot 6H_2O$ (0.25 g, 0.55 mmol) in a microwavable glass reaction vessel. The solution was stirred for 20 min to ensure dissolution and was then stirred in a microwave reactor for 20 min at the following settings: T = 110 °C, pressure = 110 psi and power = 200 W. The solution was allowed to cool and then aliquots of the mother liquor were slowly diffused with diethyl ether. It was noted that the solution colour changed from an almost clear solution to a pink solution within a few hours. Light pink X-ray quality crystals of **21** formed within 2 days with a yield of approximately 12%.

C, H, N Elemental Analysis

Calculated % as $[Gd(III)_2(L_6)_2(H_2O)_2(NO_3)_4]\cdot 5H_2O$ **(**$C_{16}H_{32}N_4O_{25}Gd_2$): C 19.31, H 3.24, N 5.63.

Found %: C 19.65, H 2.80, N 5.17.

FT-IR (cm^{-1}): 3430 (w), 2847 (w), 1629 (w), 1599 (w), 1478 (s), 1297 (s), 1247 (m), 1226 (w), 1187 (w), 1170 (w), 1081 (s), 1036 (m), 1027 (m), 1006 (m), 846 (m), 811 (m), 762 (m), 746 (m), 712 (s), 676 (m).

UV/vis Analyses

UV-vis studies of **21** were performed in methanol and acetonitrile with absorption peaks at 202 nm and 203, 239 and 271.9 nm respectively. The absorptions at 202 and 203 nm are representative of $\pi \rightarrow \pi^*$ excitations (ε values ranging from 87.8 to 89.4 x 10^3 dm^3 mol^{-1} cm^{-1}). The absorption peaks observed in MeCN solutions of **21** at 239 and 271.9 are indicative of $n \rightarrow \pi^*$ excitations (ε values ranging from 21.9 to 24.7 x 10^3 dm^3 mol^{-1} cm^{-1}).

(MeOH): λ_{max} [nm] (ε_{max} 10^3 dm^3 mol^{-1} cm^{-1}): 202 (89.4).

(MeCN): λ_{max} [nm] (ε_{max} 10^3 dm^3 mol^{-1} cm^{-1}): 203 (87.8), 239 (21.9), 271.9 (24.7).

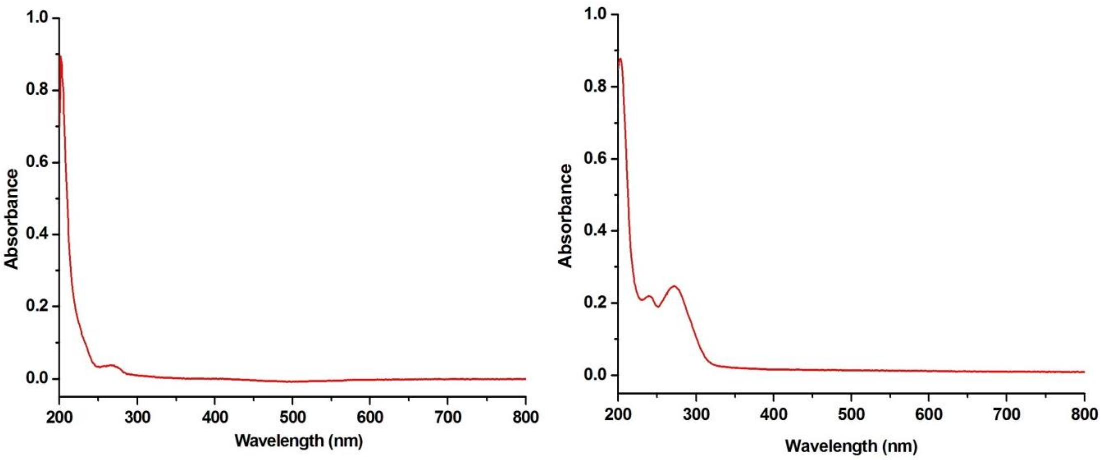

Figure 155 *- UV-visible spectra of* ***21*** *in MeOH (left) and MeCN (right).*

5.4.2.5 Synthesis of [Tb(III)$_2$(L$_6$)$_2$(NO$_3$)$_4$(EtOH)$_2$]EtOH (22)

$Tb(NO_3)_3{\cdot}5H_2O$ (0.25 g, 0.55 mmol), L_6H (0.085 g, 0.55 mmol) and NaOH (0.022 g, 0.55 mmol) were placed in a sealed glass vial containing 20 cm^3 of EtOH. The glass vial was then inserted into a microwave reactor and heated at the following settings: T = 110 °C, pressure = 110 psi and power = 200 W for 20 min. Upon cooling the light pink solution was filtered and left to concentrate via slow solvent evaporation, resulting in the formation of pink X-ray quality crystals of **22** after a few days. It was once again noted that the pink solution colour intensified after a day. The crystals were collected and air dried with a yield of approximately 14%.

C, H, N Elemental Analysis

Calculated % as $[Tb(III)_2(L_6)_2(H_2O)_2(NO_3)_4]{\cdot}5H_2O$ ($C_{16}H_{32}N_4O_{25}Tb_2$): C 19.25, H 3.23, N 5.61.

Found %: C 18.72, H 2.89, N 5.67.

FT-IR (cm^{-1}): 3430 (w), 1636 (w), 1599 (w), 1478 (s), 1297 (s), 1247 (m), 1187 (w), 1170 (w), 1085 (s), 1037 (m), 1007 (m), 846 (m), 811 (m), 762 (m), 747 (m), 712 (s).

UV/vis Analyses

UV-vis studies of **22** were carried out in MeOH and MeCN solutions, displaying characteristic $\pi \rightarrow \pi^*$ absorption peaks at 204 and 270.1 nm (ε values ranging from 32.2-204 x 10^3 dm^3 mol^{-1} cm^{-1}).

(MeOH): λ_{max} [nm] (ε_{max} 10^3 dm^3 mol^{-1} cm^{-1}): 204 (172.4), 270.1 (32.2).

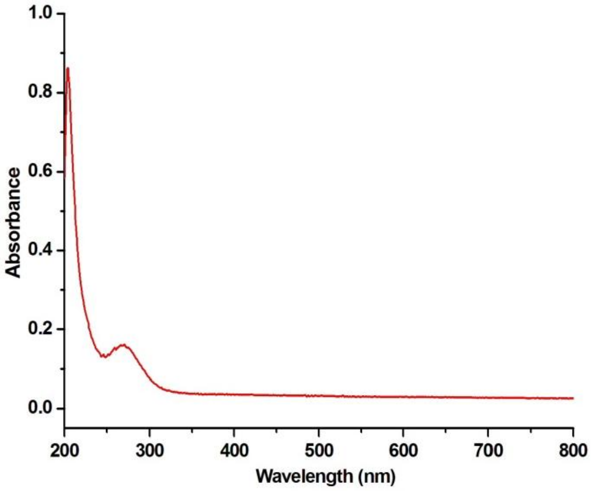

Figure 156 *- UV-Visible spectra of* ***22*** *in a methanolic solution.*

5.4.2.6 Synthesis of $[Tb(III)_2(L_6)_2(NO_3)_4(MeOH)_2]$ (23)

$Tb(NO_3)_3·6H_2O$ (0.25 g, 0.55 mmol), L_6H (0.085 g, 0.55 mmol) and NaOH (0.022 g, 0.55 mmol) were stirred for 20 min in a microwavable glass lined reaction vessel containing 20 cm^3 of MeOH. The solution was then inserted into a microwave reactor and heated using the following microwave settings: T = 110 °C, pressure = 110 psi and power = 200 W for 20 min. The solution was left to cool and then filtered to give a very light pink solution. Ether diffusion of aliquots of the mother liquor led to the formation of X-ray quality crystals of **23**, which was collected within a few days with a yield of 15%.

C, H, N Elemental Analysis

Calculated % as $[Tb(III)_2(L_6)_2(H_2O)_2(NO_3)_4]·H_2O$ **(**$C_{16}H_{24}N_4O_{21}Tb_2$): C 20.75, H 2.61, N 6.05.

Found %: C 20.87, H 2.52, N 5.73.

FT-IR (cm^{-1}): 3425 (w), 2958 (w), 1625 (w), 1600 (w), 1497 (m), 1477 (s), 1387 (w), 1277 (s), 1247 (m), 1192 (w), 1168 (m), 1080 (s), 1028 (m), 1006 (m), 989 (m), 890 (w), 847 (m), 810 (m), 770 (m), 743 (m), 726 (m), 712 (m).

5.4.2.7 Synthesis of $[Dy(III)_2(L_6)_2(NO_3)_4(H_2O)_2]·2EtOH$ (24)

$Dy(NO_3)_3·6H_2O$ (0.25 g, 0.55 mmol), L_6H (0.084 g, 0.55 mmol) and NaOH (0.022 g, 0.55 mmol) were placed in a sealed glass vial containing 20 cm^3 of EtOH. The glass vial was then inserted into a microwave reactor at the following settings (T = 110 °C, pressure = 110 psi and power = 200 W) for 20 min. Upon cooling the light pink solution was filtered and allowed to slowly evaporate off, resulting in the formation of pink X-ray quality crystals of **24** after a few days. It was noted that the solution colour became a more intense pink after a day. The crystals were collected and air dried with a yield of 13%.

C, H, N Elemental Analysis

Calculated % as $[Dy(III)_2(L_6)_2(H_2O)_2(NO_3)_4]\cdot 5H_2O$ **(**$C_{16}H_{32}N_4O_{25}Dy_2$): C 19.11, H 3.21, N 5.57.

Found %: C 18.85, H 2.83, N 5.56.

FT-IR (cm^{-1}): 3531 (w), 3427 (w), 2848 (w), 1790 (w), 1637 (w), 1600 (w), 1492 (m), 1478 (s), 1312 (s), 1298 (s), 1248 (m), 1227 (w), 1188 (w), 1170 (w), 1081 (s), 1038 (m), 1007 (m), 847 (m), 811 (m), 761 (m), 748 (m), 713 (m), 684 (m).

UV/vis Analyses

UV-vis studies of **24** were performed in both MeOH and MeCN solutions. Characteristic $\pi \rightarrow \pi^*$ absorption peaks were observed at 203 nm in both samples (ε values ranging from 96.5 to 173.2 x 10^3 dm^3 mol^{-1} cm^{-1}). The remaining transitions at 269 and 271 nm are representative of $n \rightarrow \pi^*$ excitations (ε values ranging from 9.2 to 15.8 x 10^3 dm^3 mol^{-1} cm^{-1}).

(MeOH): λ_{max} [nm] (ε_{max} 10^3 dm^3 mol^{-1} cm^{-1}): 203 (173.2), 271 (9.2).

(MeCN): λ_{max} [nm] (ε_{max} 10^3 dm^3 mol^{-1} cm^{-1}): 203 (96.5), 269 (15.8).

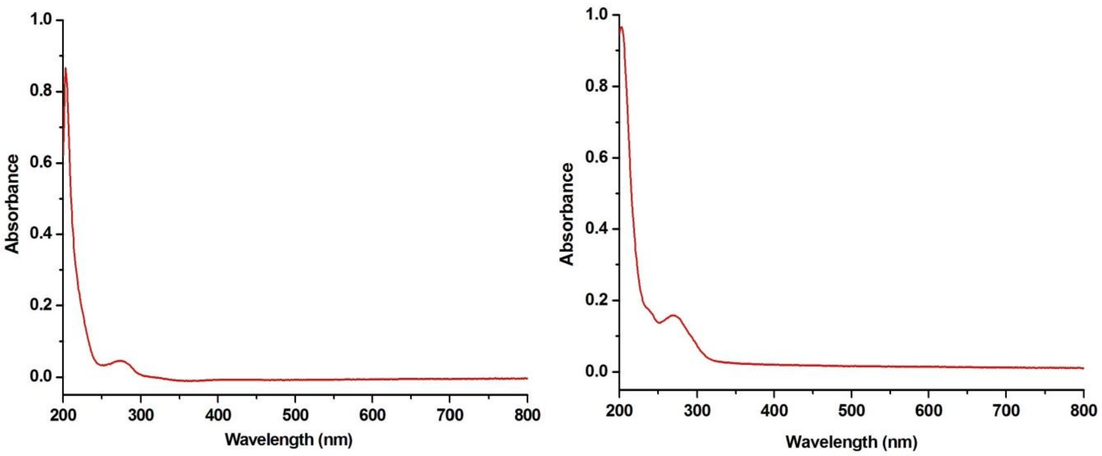

Figure 157 - *UV-visible spectra of* ***24*** *in MeOH (left) and MeCN (right).*

Powder X-ray Diffraction

Powder X-ray diffraction analysis was performed on a fresh sample (green line) and 14 month old sample (blue line) of **24** (Figure 158). The powder X-ray diffraction peaks for both samples are comparable with each other and are also in agreement with DSC analysis (Section 5.2.3).

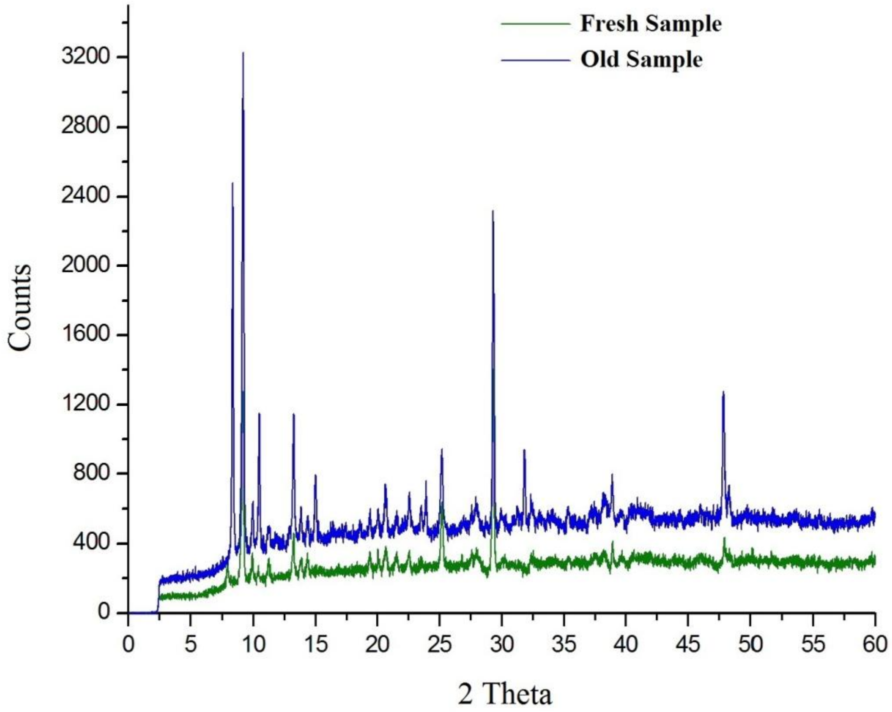

Figure 158 - *Overlay of powder diffraction analysis for a fresh sample of complex* ***24*** *(green line) and for a 14 month old sample of complex* ***24*** *(blue line).*

5.5 Bibliography

1. P. Lidström, J. Tierney, B. Wathey and J. Westman, *Tetrahedron*, 2001, 57, 9225-9283.
2. C. O. Kappe, *Angew. Chem. Int. Ed.*, 2004, 43, 6250-6284.
3. H. K. Malik, *Electromagnetic Waves and Their Application to Charged Particle Acceleration*, 2013.
4. I. Bilecka and M. Niederberger, *Nanoscale*, 2010, 2, 1358-1374.
5. C. O. Kappe, D. Dallinger and S. S. Murphree, *Practical microwave synthesis for organic chemists*, John Wiley & Sons, 2008.
6. B. L. Hayes, *Microwave synthesis: chemistry at the speed of light*, Cem Corp, 2002.
7. D. M. P. Mingos, *Res. Chem. Intermed.*, 1994, 20, 85-91.
8. C. O. Kappe, B. Pieber and D. Dallinger, *Angew. Chem. Int. Ed.*, 2013, 52, 1088-1094.
9. C. S. Cundy, *Collect. Czech. Chem. Commun.*, 1998, 63, 1699-1723.
10. G. A. Tompsett, W. C. Conner and K. S. Yngvesson, *ChemPhysChem*, 2006, 7, 296-319.
11. S. Kundu, L. Peng and H. Liang, *Inorg. Chem.*, 2008, 47, 6344-6352.
12. V. Polshettiwar, M. N. Nadagouda and R. S. Varma, *Aust. J. Chem.*, 2009, 62, 16-26.
13. M. Baghbanzadeh, L. Carbone, P. D. Cozzoli and C. O. Kappe, *Angew. Chem. Int. Ed.*, 2011, 50, 11312-11359.
14. C. J. Milios, A. Vinslava, A. G. Whittaker, S. Parsons, W. Wernsdorfer, G. Christou, S. P. Perlepes and E. K. Brechin, *Inorg. Chem.*, 2006, 45, 5272-5274.
15. A. Pons-Balagué, M. J. H. Ojea, M. Ledezma-Gairaud, D. R. Mañeru, S. J. Teat, J. S. Costa, G. Aromí and E. C. Sañudo, *Polyhedron*, 2013, 52, 781-787.
16. I. A. Gass, C. J. Milios, A. G. Whittaker, F. P. A. Fabiani, S. Parsons, M. Murrie, S. P. Perlepes and E. K. Brechin, *Inorg. Chem.*, 2006, 45, 5281-5283.
17. E. M. López-Vidal, V. Blanco, M. D. García, C. Peinador and J. M. Quintela, *Org. Lett.*, 2011, 14, 580-583.
18. O. Stefanczyk, T. Korzeniak, W. Nitek, M. Rams and B. Sieklucka, *Inorg. Chem.*, 2011, 50, 8808-8816.
19. N. Berg, S. M. Taylor, A. Prescimone, E. K. Brechin and L. F. Jones, *CrystEngComm*, 2012, 14, 2732-2738.
20. Z.-J. Lin, Z. Yang, T.-F. Liu, Y.-B. Huang and R. Cao, *Inorg. Chem.*, 2012, 51, 1813-1820.
21. S. M. F. Vilela, D. Ananias, A. C. Gomes, A. A. Valente, L. D. Carlos, J. A. S. Cavaleiro, J. Rocha, J. P. C. Tome and F. A. Almeida Paz, *J. Mater. Chem.*, 2012, 22, 18354-18371.
22. S. S. Zumdahl and S. A. Zumdahl, *Chemistry, Chapter 7*, Charles Hartford, United States, 8th edn., 2010.
23. P.-H. Lin, T. J. Burchell, R. Clérac and M. Murugesu, *Angew. Chem. Int. Ed.*, 2008, 47, 8848-8851.
24. P.-H. Lin, W.-B. Sun, M.-F. Yu, G.-M. Li, P.-F. Yan and M. Murugesu, *Chem. Commun.*, 2011, 47, 10993-10995.
25. Y.-N. Guo, X.-H. Chen, S. Xue and J. Tang, *Inorg. Chem.*, 2011, 50, 9705-9713.
26. F. Pointillart, Y. Le Gal, S. Golhen, O. Cador and L. Ouahab, *Chem. Euro. J.*, 2011, 17, 10397-10404.
27. J. Long, F. Habib, P.-H. Lin, I. Korobkov, G. Enright, L. Ungur, W. Wernsdorfer, L. F. Chibotaru and M. Murugesu, *J. Am. Chem. Soc.*, 2011, 133, 5319-5328.
28. X. Yi, K. Bernot, F. Pointillart, G. Poneti, G. Calvez, C. Daiguebonne, O. Guillou and R. Sessoli, *Chem. Euro. J.*, 2012, 18, 11379-11387.
29. L. Zou, L. Zhao, P. Chen, Y.-N. Guo, Y. Guo, Y.-H. Li and J. Tang, *Dalton Trans.*, 2012, 41, 2966-2971.

30. R. Liu, C. Zhang, L. Li, D. Liao and J.-P. Sutter, *Dalton Trans.*, 2012, 41, 12139-12144.
31. L. Bogani and W. Wernsdorfer, *Nature Mater.*, 2008, 7, 179-186.
32. G. Karotsis, M. Evangelisti, S. J. Dalgarno and E. K. Brechin, *Angew. Chem.*, 2009, 121, 10112-10115.
33. J. W. Sharples, Y.-Z. Zheng, F. Tuna, E. J. L. McInnes and D. Collison, *Chem. Commun.*, 2011, 47, 7650-7652.
34. S. K. Langley, N. F. Chilton, B. Moubaraki, T. Hooper, E. K. Brechin, M. Evangelisti and K. S. Murray, *Chem. Sci.*, 2011, 2, 1166-1169.
35. T. N. Hooper, J. Schnack, S. Piligkos, M. Evangelisti and E. K. Brechin, *Angew. Chem. Int. Ed.*, 2012, 51, 4633-4636.
36. M. Evangelisti, O. Roubeau, E. Palacios, A. Camón, T. N. Hooper, E. K. Brechin and J. J. Alonso, *Angew. Chem. Int. Ed.*, 2011, 50, 6606-6609.
37. S. T. Meally, G. Karotsis, E. K. Brechin, G. S. Papaefstathiou, P. W. Dunne, P. McArdle and L. F. Jones, *CrystEngComm*, 2010, 12, 59-63.
38. S. T. Meally, C. McDonald, G. Karotsis, G. S. Papaefstathiou, E. K. Brechin, P. W. Dunne, P. McArdle, N. P. Power and L. F. Jones, *Dalton Trans.*, 2010, 39, 4809-4816.
39. S. T. Meally, C. McDonald, P. Kealy, S. M. Taylor, E. K. Brechin and L. F. Jones, *Dalton Trans.*, 2012, 41, 5610-5616.
40. T. A. Manz, J. M. Caruthers, S. Sharma, K. Phomphrai, K. T. Thomson, W. N. Delgass and M. M. Abu-Omar, *Organometallics*, 2012, 31, 602-618.
41. Y. Obora and M. Tanaka, *J. Organomet. Chem.*, 2000, 595, 1-11.
42. M. A. T. Munoz, C. Urbaneja, M. Temprado, M. E. G. Mosquera and T. Cuenca, *Chem. Commun.*, 2011, 47, 11757-11759.
43. W. H. Press, S. A. Teukolsky, W. T. Vetterling and B. P. Flannery, *Numerical Recipes in C, 2nd edn.*, Cambridge University Press, Cambridge, 1992.
44. M. Nematirad, W. J. Gee, S. K. Langley, N. F. Chilton, B. Moubaraki, K. S. Murray and S. R. Batten, *Dalton Trans.*, 2012, 41, 13711-13715.
45. N. G. Naumov, M. S. Tarasenko, A. V. Virovets, Y. Kim, S.-J. Kim and V. E. Fedorov, *Eur. J. Inorg. Chem.*, 2006, 2006, 298-303.
46. P.-H. Lin, M. Leclere, J. Long, T. J. Burchell, I. Korobkov, R. Clerac and M. Murugesu, *Dalton Trans.*, 2010, 39, 5698-5704.
47. S. Liu, L. Gelmini, S. J. Rettig, R. C. Thompson and C. Orvig, *J. Am. Chem. Soc.*, 1992, 114, 6081-6087.
48. T. Rajeshkumar, S. K. Singh and G. Rajaraman, *Polyhedron*, 2013, 52, 1299-1305.
49. O. Kahn and B. Briat, *J. Chem. Soc. Faraday Trans.*, 1976, 72, 268-281.
50. O. Kahn and B. Briat, *J. Chem. Soc. Faraday Trans.*, 1976, 72, 1441-1446.
51. J. Paulovič, F. Cimpoesu, M. Ferbinteanu and K. Hirao, *J. Am. Chem. Soc.*, 2004, 126, 3321-3331.
52. Y.-N. Guo, G.-F. Xu, W. Wernsdorfer, L. Ungur, Y. Guo, J. Tang, H.-J. Zhang, L. F. Chibotaru and A. K. Powell, *J. Am. Chem. Soc.*, 2011, 133, 11948-11951.
53. R. A. Layfield, J. J. W. McDouall, S. A. Sulway, F. Tuna, D. Collison and R. E. P. Winpenny, *Chem. Euro. J.*, 2010, 16, 4442-4446.
54. R. Sessoli and A. K. Powell, *Coord. Chem. Rev.*, 2009, 253, 2328-2341.
55. P. Å. Malmqvist, B. O. Roos and B. Schimmelpfennig, *Chem. Phys. Lett.*, 2002, 357, 230-240.
56. K. Bernot, J. Luzon, L. Bogani, M. Etienne, C. Sangregorio, M. Shanmugam, A. Caneschi, R. Sessoli and D. Gatteschi, *J. Am. Chem. Soc.*, 2009, 131, 5573-5579.
57. K. Bernot, J. Luzon, A. Caneschi, D. Gatteschi, R. Sessoli, L. Bogani, A. Vindigni, A. Rettori and M. G. Pini, *Phys. Rev. B: Condens. Matter.*, 2009, 79, 134419.
58. J. Luzon, K. Bernot, I. J. Hewitt, C. E. Anson, A. K. Powell and R. Sessoli, *Phys. Rev. Lett.*, 2008, 100, 247205.
59. N. F. Chilton, R. P. Anderson, L. D. Turner, A. Soncini and K. S. Murray, *J. Comput. Chem.*, 2013, 34, 1164-1175.

60. A. Venugopal, F. Tuna, T. P. Spaniol, L. Ungur, L. F. Chibotaru, J. Okuda and R. A. Layfield, *Chem. Commun.*, 2013, 49, 901-903.
61. R. J. Blagg, L. Ungur, F. Tuna, J. Speak, P. Comar, D. Collison, W. Wernsdorfer, E. J. L. McInnes, L. F. Chibotaru and R. E. P. Winpenny, *Nature Chem.*, 2013, 5, 673-678.
62. M. Jeletic, P.-H. Lin, J. J. Le Roy, I. Korobkov, S. I. Gorelsky and M. Murugesu, *J. Am. Chem. Soc.*, 2011, 133, 19286-19289.
63. C. B. P. Finn, R. Orbach and W. P. Wolf, *Proc. Phys. Soc.*, 1961, 77, 261.
64. N. F. Chilton, D. Collison, E. J. L. McInnes, R. E. P. Winpenny and A. Soncini, *Nature Commun.*, 2013, 4.
65. G. Cucinotta, M. Perfetti, J. Luzon, M. Etienne, P.-E. Car, A. Caneschi, G. Calvez, K. Bernot and R. Sessoli, *Angew. Chem. Int. Ed.*, 2012, 51, 1606-1610.
66. V. Mereacre, A. Baniodeh, C. E. Anson and A. K. Powell, *J. Am. Chem. Soc.*, 2011, 133, 15335-15337.
67. L. Ungur and L. F. Chibotaru, *PCCP*, 2011, 13, 20086-20090.
68. E. Colacio, J. Ruiz-Sanchez, F. J. White and E. K. Brechin, *Inorg. Chem.*, 2011, 50, 7268-7273.
69. M. J. Frisch, G. W. Trucks, H. B. Schlegel, G. E. Scuseria, M. A. Robb, J. R. Cheeseman, G. Scalmani, V. Barone, B. Mennucci, G. A. Petersson, H. Nakatsuji, M. Caricato, X. Li, H. P. Hratchian, A. F. Izmaylov, J. Bloino, G. Zheng, J. L. Sonnenberg, M. Hada, M. Ehara, K. Toyota, R. Fukuda, J. Hasegawa, M. Ishida, T. Nakajima, Y. Honda, O. Kitao, H. Nakai, T. Vreven, J. A. Montgomery, Jr., J. E. Peralta, F. Ogliaro, M. Bearpark, J. J. Heyd, E. Brothers, K. N. Kudin, V. N. Staroverov, R. Kobayashi, J. Normand, K. Raghavachari, A. Rendell, J. C. Burant, S. S. Iyengar, J. Tomasi, M. Cossi, N. Rega, N. J. Millam, M. Klene, J. E. Knox, J. B. Cross, V. Bakken, C. Adamo, J. Jaramillo, R. Gomperts, R. E. Stratmann, O. Yazyev, A. J. Austin, R. Cammi, C. Pomelli, J. W. Ochterski, R. L. Martin, K. Morokuma, V. G. Zakrzewski, G. A. Voth, P. Salvador, J. J. Dannenberg, S. Dapprich, A. D. Daniels, Ö. Farkas, J. B. Foresman, J. V. Ortiz, J. Cioslowski and D. J. Fox, Gaussian Inc., Wallingford CT, GAUSSIAN 09 edn., 2009.
70. A. D. Becke, *J. Chem. Phys.*, 1993, 98, 5648-5652.
71. A. D. Becke, *J. Chem. Phys.*, 1993, 98, 1372-1377.
72. E. Ruiz, P. Alemany, S. Alvarez and J. Cano, *J. Am. Chem. Soc.*, 1997, 119, 1297-1303.
73. E. Ruiz, P. Alemany, S. Alvarez and J. Cano, *Inorg. Chem.*, 1997, 36, 3683-3688.
74. E. Ruiz, J. Cano, S. Alvarez and P. Alemany, *J. Am. Chem. Soc.*, 1998, 120, 11122-11129.
75. E. Ruiz, J. Cano, S. Alvarez and P. Alemany, *J. Comput. Chem.*, 1999, 20, 1391-1400.
76. E. Ruiz, A. Rodríguez-Fortea, P. Alemany and S. Alvarez, *Polyhedron*, 2001, 20, 1323-1327.
77. E. Ruiz, C. de Graaf, P. Alemany and S. Alvarez, *J. Phys. Chem. A*, 2002, 106, 4938-4941.
78. E. Ruiz, A. Rodríguez-Fortea, J. Cano, S. Alvarez and P. Alemany, *J. Comput. Chem.*, 2003, 24, 982-989.
79. E. Ruiz, J. Cano, S. Alvarez, A. Caneschi and D. Gatteschi, *J. Am. Chem. Soc.*, 2003, 125, 6791-6794.
80. A. Rodríguez-Fortea, P. Alemany, S. Alvarez and E. Ruiz, *Eur. J. Inorg. Chem.*, 2004, 2004, 143-153.
81. E. Ruiz, S. Alvarez, J. Cano and V. Polo, *J. Chem. Phys.*, 2005, 123, 164110.
82. L. Noodleman, *J. Chem. Phys.*, 1981, 74, 5737-5743.
83. T. R. Cundari and W. J. Stevens, *J. Chem. Phys.*, 1993, 98, 5555-5565.
84. A. Schäfer, C. Huber and R. Ahlrichs, *J. Chem. Phys.*, 1994, 100, 5829-5835.

85. F. Aquilante, L. De Vico, N. Ferré, G. Ghigo, P.-å. Malmqvist, P. Neogrády, T. B. Pedersen, M. Pitoňák, M. Reiher, B. O. Roos, L. Serrano-Andrés, M. Urban, V. Veryazov and R. Lindh, *J. Comput. Chem.*, 2010, 31, 224-247.
86. B. A. Heß, C. M. Marian, U. Wahlgren and O. Gropen, *Chem. Phys. Lett.*, 1996, 251, 365-371.
87. L. Chibotaru and L. Ungur, *University of Leuven,* 2006.
88. A. Abraham and B. Bleaney, *Electron Paramagnetic Resonance of Transition Ions; Oxford University Press: London, UK*, 1970, 186-208.

Chapter Six

Phenolic Ligands as Building Blocks in Discrete Cages and Extended Networks

6.1 Introduction

Previous experimental studies carried out by our group investigated the coordination chemistry of the Schiff base ligand 2-imino-methyl-6-methoxyphenol (immpH) and its analogues (Figure 159). To this end, a family of heptanuclear [M_7] (where M = Co(II/III), Ni(II), Zn(II)) pseudo metallocalix[6]arene disc like complexes were successfully synthesised. The paramagnetic analogues were found to be magnetically interesting, while it was also discovered that all siblings exhibited solid state host-guest properties, allowing for the encapsulation of a variety of small organic guest species (i.e. MeOH, MeCN and $MeNO_2$).[1-3] In addition, a family of homo- and heterometallic complexes were formed through the incorporation of the immp- bridging ligands in conjunction with a range of other transition metal salts. For instance the reaction of $Fe(NO_3)_3 \cdot 9H_2O$ in the presence of immpH and a suitable base gave rise to the formation of the heterometallic tetranuclear *butterfly* complex [$Na_2Fe(III)_2(OMe)_2(immp)_4(NO_3)_2$].[4] Furthermore, a homometallic 1D Mn(III) coordination polymer of formula [$Mn(III)(immp)_2(Cl)$]$_n$ was synthesised, where the chloride ions act as bridging moieties in the formation of a repeated chain.[4] In particular, this complex is of great relevance to the first section of results detailed in this chapter. More specifically, [$Mn(III)(immp)_2(Cl)$]$_n$ is a member of a family of seven Mn(III) chain analogues formed via the immp- bridging ligand by the Jones group to date (Figure 160).[5]

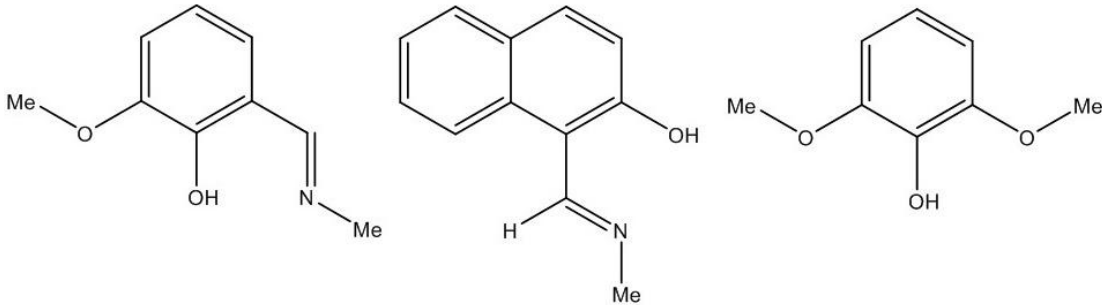

***Figure 159** - Structural representation of the Schiff base ligand 2-iminomethyl-6-methoxyphenol (immpH) (left) and the two ligands utilised in this chapter, 1-[(methylimino)methyl]-2-naphthol (L_7H) (middle) and 2,6-dimethoxyphenol (L_6H) (right).*

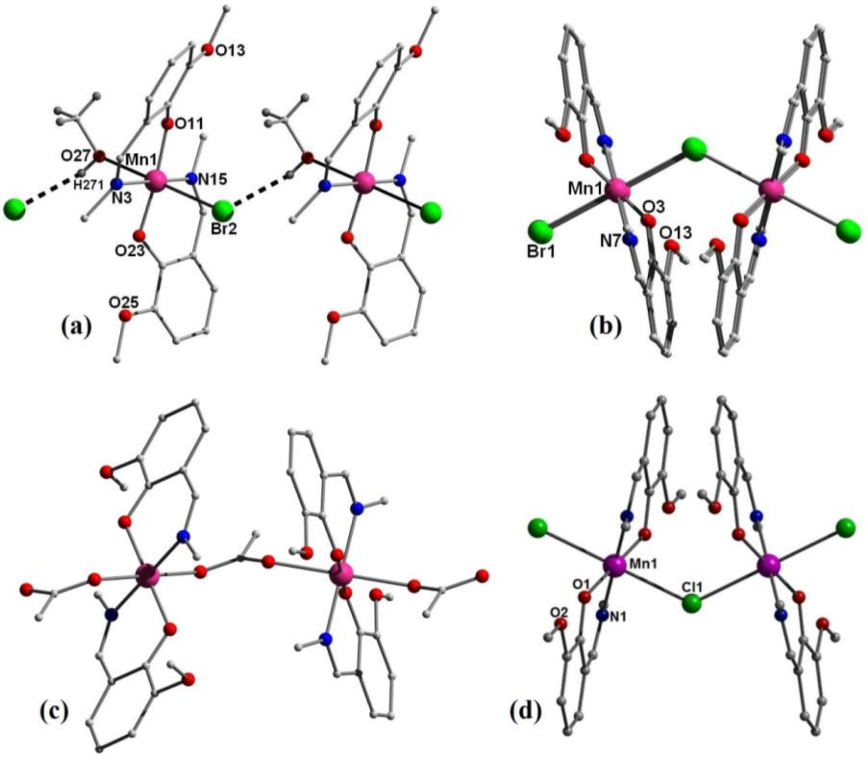

Figure 160 - *Crystal structures of four members of the Mn(III) 1D chain family. (a) $[Mn(immp)_2(MeOH)(Br)]_n$, (b) $[Mn(immp)_2(Br)]_n$, (c) $[Mn(immp)_2(OAc)]_n$ and (d) $[Mn(immp)_2(Cl)]_n$. Colour code: pink/purple (Mn), red (O), blue (N), green (Br or Cl) and grey (C). The majority of hydrogen atoms have been removed for clarity. Dashed lines in (a) represent hydrogen bonding interactions.*

The work detailed herein, concerns the coordination chemistry of the analogous ligands 1-[(methylimino)methyl]-2-naphthol (L_7H) and 2,6-dimethoxyphenol (L_6H) (Figure 159). Prior to our research, a Mn(IV) ($[Mn(IV)(L_7)_2(\mu\text{-}O)]_2$) and a Cu(II) ($[Cu(II)(L_7)_2]_2$) dimer along with a number of Cu(II) monomers had been synthesised using the L_7H ligand.[6-9] It was therefore clear that L_7H possesses an affinity for such coordination complexes and this piqued our interest. Furthermore, we discussed in Chapter 5 the vital role taken by the L_6H ligand in the production of a family of $[Ln(III)_2]$ dimeric complexes. This, coupled with the analogous nature of L_6H to the ligand immpH (Figure 159) encouraged us to probe further its coordination chemistry with various transition metal ions, the results of which are divulged in this chapter. It should be noted however that despite huge efforts, when 2,6-dimethoxyphenol (L_6H) was reacted with a 1st row transition metal (i.e. Cu(II), Mn(II) and Fe(II)), the predominant products were amorphous powders and semi-crystalline materials. Eventually, we succeeded at obtaining X-ray quality crystals through the use of $Co(ClO_4)_2 \cdot 6H_2O$ as our metal source (see section 6.4.2.7).

In recent years, the utilisation of Co(II) metal salts towards the synthesis of Single-Molecule Magnets (SMMs) (Section 1.9.1) have become more popular as a result of the large single ion anisotropy associated with the Co(II) centre.[10] Here, the zero-field splitting (ZFS) arises from first order spin-orbit coupling (SOC), therefore it can be extremely difficult to interpret the magnetic data for octahedral Co(II) polynuclear complexes. As a general approximation, only the lowest lying Kramer's doublet is populated at low temperatures; hence Co(II) centres are typically assigned an effective spin $s' = 1/2$.[11] The first Co(II) complex to display SMM behaviour was the [Co_4] cubic complex [$Co(II)_4(hmp)_4(MeOH)_4Cl_4$] (where hmp = hydroxymethylpyridine), synthesised by Yang et al.[12] Here, a ground spin state of $S = 6$ and a magnetoanisotropy D value of -4 K were observed. The out-of-phase ac susceptibility (χ'') measurements for this complex showed an increase in susceptibility as the temperature decreases towards 1.8 K which is consistent with slow magnetic relaxation. More recent investigations into the SMM behaviour of [Co(II)] cubic complexes have been carried out by Liu et al,[13] Murray et al[14, 15] and Galloway et al.[16] This chapter presents the synthesis and structure of a Mn(III) hydrogen bonded chain [$Mn(III)(L_7)_2(N_3)MeOH$] (**25**) and two Mn(III) 1D coordination polymers [$Mn(III)(L_7)_2(Cl)]_n$ (**26**) and [$Mn(III)(L_7)_2(N_3)]_n$ (**27**). The reaction of a Cu(II) metal salt with L_7H yielded a dinuclear Cu(II) metal complex of formula [$Cu(II)_2(L_7)$] (**28**). This Cu(II) dimeric complex was first synthesised by Clark et al,[7] however we synthesised complex **28** using a different reaction path. A linear ditopic secondary building unit (SBU) in the form of 4,4'-bipyridine was added to the reaction scheme for **28** with the aim of forming an extended network architecture. This proved to be successful with the formation of the 2D hydrogen bonded network [$Cu(II)_2(NO_3)_2(L_7)_2(MeOH)_2(4,4'\text{-bipy})$] (**29**). Additionally, we report the synthesis, structure and magnetic characterisation of a tetranuclear Co(II) cubic complex [$Co(II)_4(OMe)_4(L_6)_4(MeOH)_4$] (**30**).

6.2 Results and Discussion

6.2.1 Structural Descriptions

6.2.1.1 Transition from Mn(III) Hydrogen Bonded Chains to Mn(III) Coordination Polymer Analogues

We first discuss here the synthesis of the Mn(III) monomer [Mn(III)(L_7)$_2$(N_3)MeOH] (**25**) which was made via the methanolic reaction of $MnCl_2 \cdot 4H_2O$, 1-[(methylimino)methyl]-2-naphthol (L_7H), NaOH and NaN_3 (Figure 161). Complex **25** crystallises in the monoclinic *Cc* space group with unit cell parameters: a = 20.248(4) Å, b = 9.3995(19) Å, c = 13.106(3) Å, α = 90°, β = 117.20(3)°, γ = 90°. Complete single crystal X-ray diffraction data is given in Table 20 (Section 6.2.4). The monomeric unit in **25** comprises a single Mn(III) metal centre which displays distorted octahedral geometry. The L_7H ligands are singly deprotonated (L_7^-) and utilise a chelating η^1:η^1 coordination mode (Figure 161). The equatorial positions of the Mn(III) centre are occupied via imine nitrogen and phenolic oxygen atoms giving bond lengths of 1.865(2) Å (Mn1-O2), 1.873(2) Å (Mn1-O1), 2.019(3) Å (Mn1-N2) and 2.030(3) Å (Mn1-N1). Coordination at the Mn(III) centre is completed at the Jahn-Teller (JT) elongated axial positions via an N_3^- moiety and a terminal methanol solvent ligand with bond lengths of 2.182(3) Å (Mn1-N3) and 2.351(2) Å (Mn1-O3) respectively. Individual [Mn(III)] units form rows along the a axis and are linked via $\pi_{centroid}\cdots\pi_{centroid}$ stacking of neighbouring naphthalene rings ([C3-C12]$\cdots$[C15'-C24'] = 4.489 Å) (Figure 162).

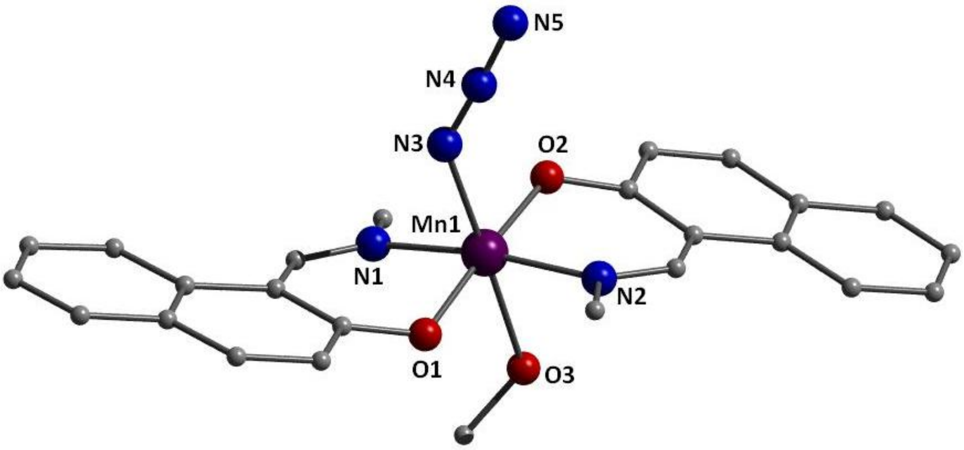

Figure 161 *- Crystal structure of the monomeric complex in* ***25****. Colour code: purple (Mn), red (O), blue (N) and grey (C). Hydrogen atoms have been omitted for clarity.*

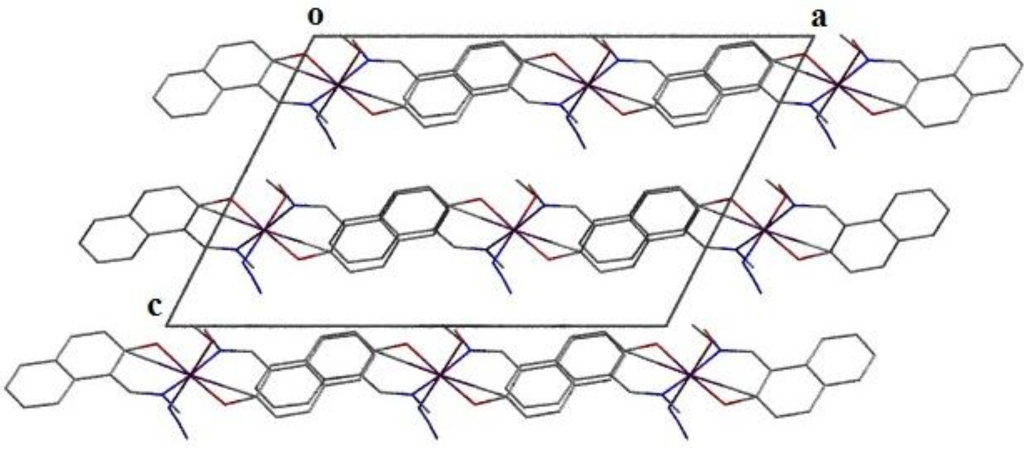

Figure 162 - *Crystal packing diagram for* ***25****, depicting the π-π stacking interactions between neighbouring naphthalene rings, as viewed along the b axis of the unit cell. Colour scheme as in Figure 161. Hydrogen atoms have been removed for clarity.*

Inter-molecular hydrogen bonding interactions occur between the individual [Mn(III)] moieties of perpendicularly arranged rows via the methanol solvent ligand and the azide group (i.e. O3(H3)$^{\cdots}$N5' = 2.123 Å; Figure 163), further enhancing the crystal packing arrangement of **25** and resulting in the formation of hydrogen bonded chains along the *c* axis of the unit cell. The crystal packing arrangement in Figure 164(left) illustrates the alternating perpendicular pattern of the individual 1D rows.

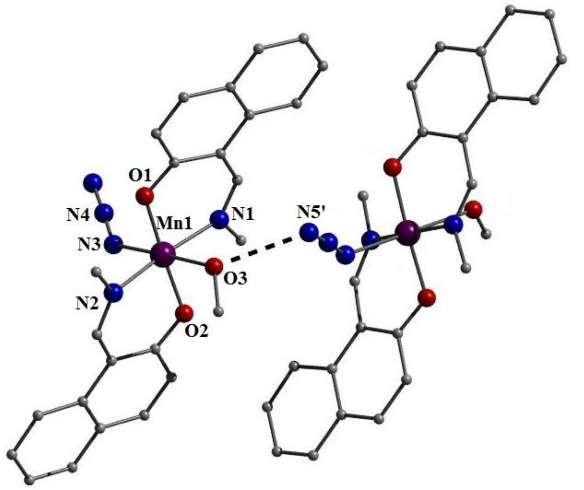

Figure 163 - *Illustration of the hydrogen bonding interaction (dashed lines) between the azide moiety of one Mn(III) monomeric unit and the MeOH solvent ligand of a perpendicular Mn(III) unit in* ***25****. Hydrogen atoms have been omitted for clarity.*

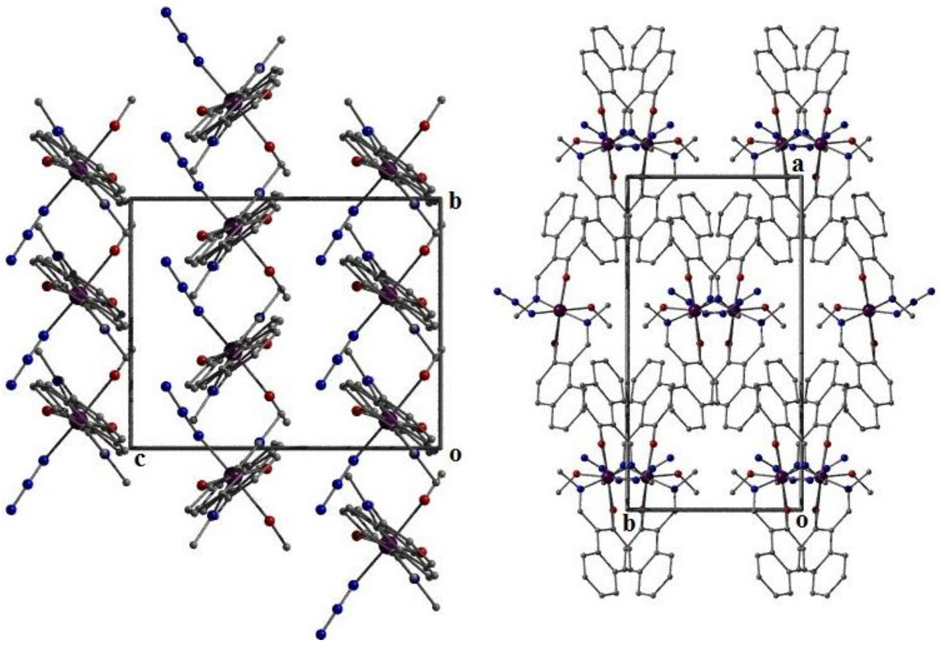

***Figure 164** - (Left) Crystal packing arrangement of **25** as viewed along the a axis, highlighting the perpendicular arrangement of individual and neighbouring [Mn(III)] 1D rows. (Right) Packing diagram for **25** as viewed down the c axis of the unit cell. Hydrogen atoms have been removed for clarity.*

Slight variations to the reaction scheme for **25** produced the two covalent 1D coordination polymers $[\mathrm{Mn(III)(L_7)_2(Cl)}]_n$ (**26**) and $[\mathrm{Mn(III)(L_7)_2(N_3)}]_n$ (**27**) (Figures 165 and 166). Complex **26** was synthesised in acetonitrile in the absence of sodium azide, while complex **27** was formed through the ethanolic reaction of $\mathrm{MnCl_2{\cdot}4H_2O}$, $\mathrm{L_7H}$, NaOMe and $\mathrm{NaN_3}$. Both complexes crystallise in the monoclinic $C2/c$ space group with unit cell parameters: a = 12.809(3) Å, b = 17.616(4) Å, c = 9.5233(19) Å, α = 90°, β = 109.75(3)°, γ = 90° for **26** and a = 22.424(5) Å, b = 6.5388(13) Å, c = 16.968(3) Å, α = 90°, β = 125.92(3)°, γ = 90°. Complete single crystal X-ray diffraction data for **26** and **27** can be seen in Table 20 (Section 6.2.4).

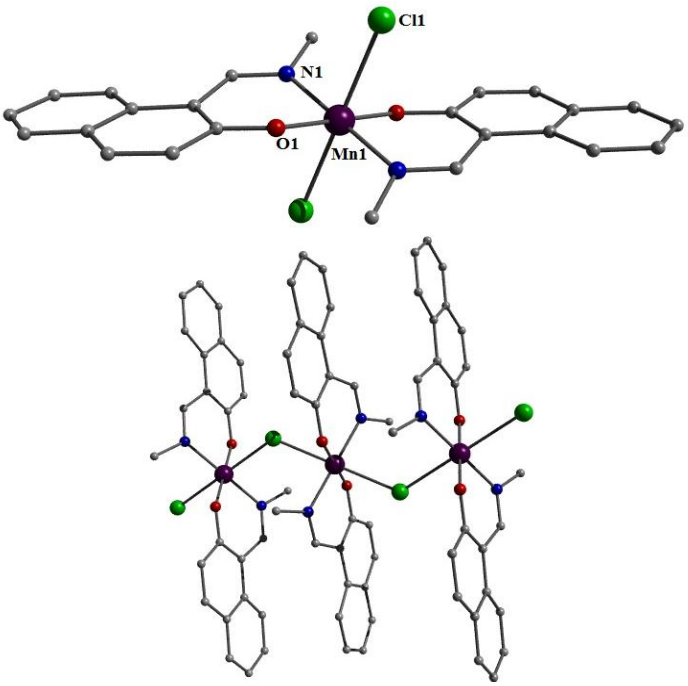

***Figure 165** - (Top) Crystal structure of one [Mn(III)(L_7)Cl]$_n$ unit in **26** (including the next bridging Cl moiety). (Bottom) The repeating 1D chain structure in **26** comprising three [Mn(III)(L_7)Cl]$_n$ units (Cl = lime green spheres). Hydrogen atoms have been omitted for clarity.*

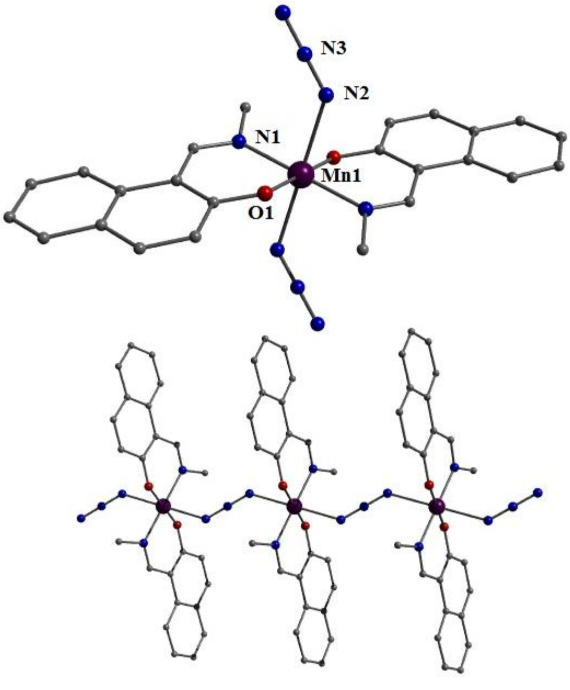

***Figure 166** - (Top) Crystal structure of one [Mn(III)(L_7)N_3]$_n$ unit in complex **27** (including the next azide connector ligand). (Bottom) Repeating 1D chain structure of **27** (composed of three [Mn(III)(L_7)N_3]$_n$ units) linked via nitrogen azide atoms. Hydrogen atoms have been removed for clarity.*

Once again, the equatorial positions of the Mn(III) centres in **26** and **27** are occupied by imine nitrogen and phenolic oxygen atoms of two chelating Schiff base ligands

(L_7^-). Coordination is completed at the JT elongated axial positions of **26** by a linker chloride ion (and its symmetric equivalent), with a bond length of 2.651(5) Å (Mn1-Cl1), resulting in the formation of 1D coordination polymers with an intra-chain Mn(III)···Mn(III)' distance of 4.762 Å. The individual [Mn(III)] units are further linked via inter-molecular hydrogen bonding interactions between phenolic oxygen atoms and aliphatic protons of the -NMe functional group with a bond length of 2.599 Å (O1'···(H1C)C1). The $[Mn(III)(L_7)Cl]_n$ chains propagate along the *c* axis of the unit cell in a zig-zag formation, while the individual rows in **26** pack in the space efficient brickwork motif (Figure 167).

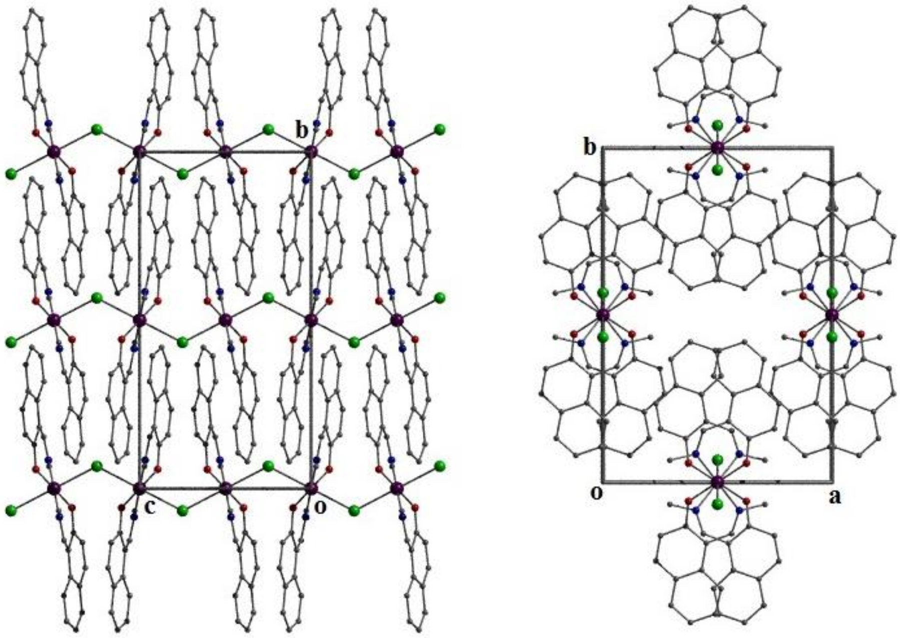

Figure 167 *- Crystal packing arrangements of* ***26*** *as viewed along the a (left) and c axis (right). Hydrogen atoms have been removed for clarity.*

The JT elongated axial positions in $[Mn(III)(L_7)N_3]_n$ (**27**) are occupied by connector azide (N_3^-) moieties (Mn1-N2 = 2.338(16) Å), resulting in the growth of chains along the *b* axis of the unit cell (Figure 168). Aromatic protons partake in inter-molecular hydrogen bonding interactions with phenolic oxygen atoms (e.g. O1'···(H3)C3 = 2.696 Å) and N_{azide} atoms (e.g. N2'···(H6)C6 = 2.650 Å). Furthermore, the individual [Mn(III)] units of the 1D coordination polymer in **27** stack in a superimposable manner with an intra-chain Mn(III)···Mn(III)' distance of 6.539 Å. The individual rows in **27** arrange themselves along the *c* axis in a space efficient brickwork pattern (Figure 169).

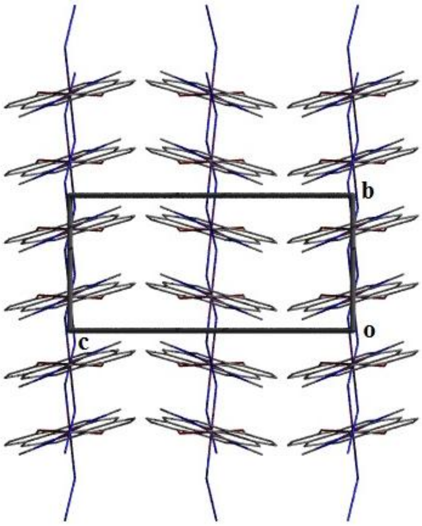

Figure 168 *- Crystal packing diagram (viewed along the a axis) illustrating the propagation of chains in* ***27*** *along the b axis of the unit cell. Hydrogen atoms have been omitted for clarity.*

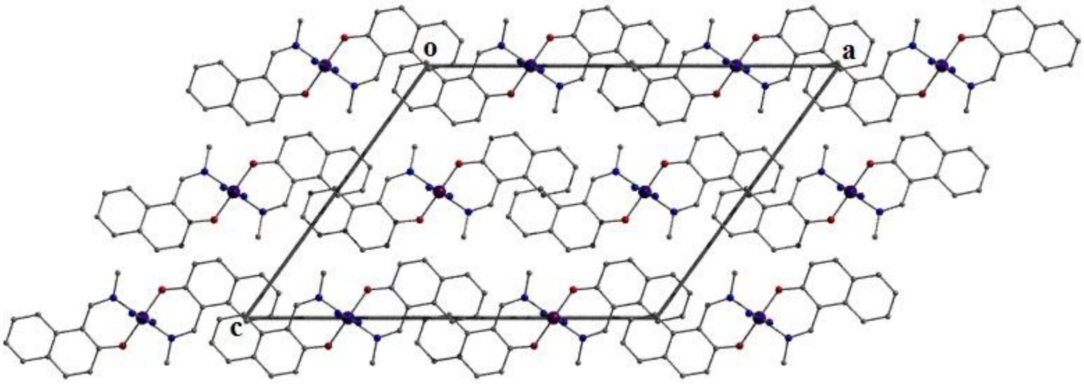

Figure 169 *- Illustration of the crystal packing arrangement in* ***27*** *as viewed along the b axis of the unit cell. The individual chains stack in a superimposable pattern down the b cell direction. All hydrogen atoms have been removed for clarity.*

To the best of our knowledge complexes **25**-**27** are the first Mn(III) chains to be synthesised using the L_7H ligand. The formation of these hydrogen bonded (**25**) and covalent chains (**26** and **27**) add to an existing family of analogous coordination polymers of general formula $[Mn(III)(L)_2(X)]_n$ (where L = 2-iminomethyl-6-methoxyphenol (immpH) or 1-[(methylimino)methyl]-2-naphthol and X = Cl^-, Br^-, OAc^-, N_3^-) previously synthesised in the Jones laboratory.

6.2.1.2 Construction of Cu(II) Dimers and Cu(II) 2D Networks

In order to further our investigations into the coordination chemistry of the 1-[(methylimino)methyl]-2-naphthol ligand (L_7H), we decided to probe its reactivity with the Cu(II) ion. To this end, the methanolic reaction of $Cu(ClO_4)_2 \cdot 6H_2O$, L_7H and NaOMe gave rise to the Cu dinuclear complex $[Cu(II)_2(L_7)_4]$ (**28**) (Figure 170).

Complex **28** crystallises in the monoclinic $P2_1/c$ space group with unit cell parameters: a = 10.509(2) Å, b = 14.584(3) Å, c 12.540(3) Å, α = 90°, β = 105.19(3)°, γ = 90°. Complete single crystal X-ray diffraction data can be seen in Table 21 (Section 6.2.4).

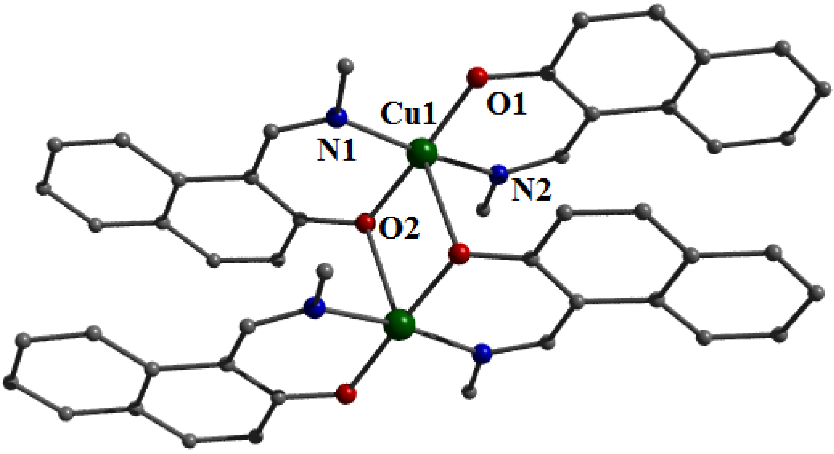

Figure 170 *- Crystal structure representation of the Cu(II) dimeric complex (**28**). Colour code: dark green (Cu), red (O), blue (N) and grey (C). Hydrogen atoms have been omitted for clarity.*

The core of complex **28** consists of two symmetrically equivalent five coordinate Cu(II) metal centres, related through an inversion centre. Here, a Cu(II)···Cu(II) distance of 3.350 Å and a Cu1-O2-Cu1' angle of 95.56° are observed. The Cu(II) centres exhibit distorted square based pyramidal geometries (τ = 0.116).[17] In this complex, the L_7^- ligands exhibit two coordination motifs as described below and shown in Figure 171.

1) $\eta^1:\eta^2$-μ: The Cu(II) centres are linked via the bridging phenoxy oxygen atoms (O2 and its symmetric equivalent (s.e.)) of two singly deprotonated L_7^- ligands at the equatorial (Cu1-O2 = 1.925(15) Å) and axial sites (Cu1-O2' = 2.561 Å). The $\eta^1:\eta^2$-μ binding mode is completed at the equatorial position via the Cu1-N2 bond (1.983(19) Å).

2) $\eta^1:\eta^1$: The remaining equatorial positions of the Cu(II) centres are occupied via O_{phen} atoms (O1 and s.e.) and nitrogen atoms (N1 and s.e.) of L_7^- with bond lengths of 1.901(16) (Cu1-O1) and 1.985(19) Å (Cu1-N1) respectively. The individual [Cu(II)$_2$] units in **28** stack in superimposable arrangements along both the a and c axes, forming a common brickwork pattern along the bc plane (Figure 172).

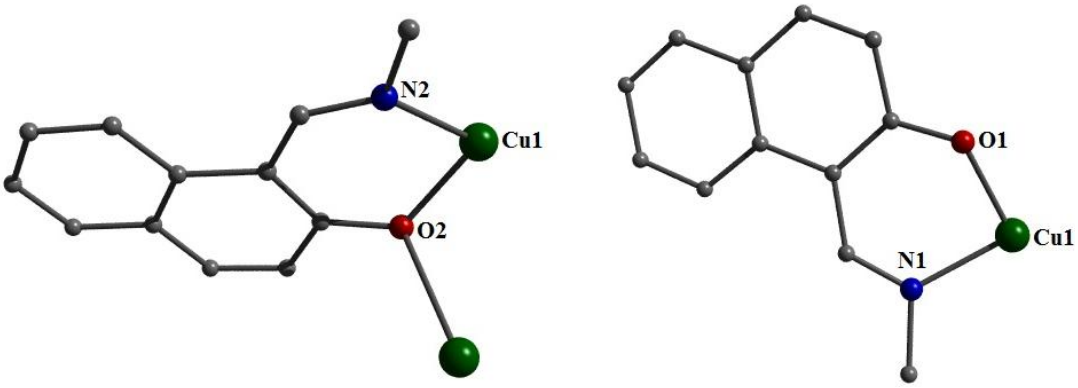

Figure 171 - *Illustration of the two coordination modes* $\eta^1:\eta^2\text{-}\mu$ *(left) and* $\eta^1:\eta^1$ *(right) utilised in* ***28****.*

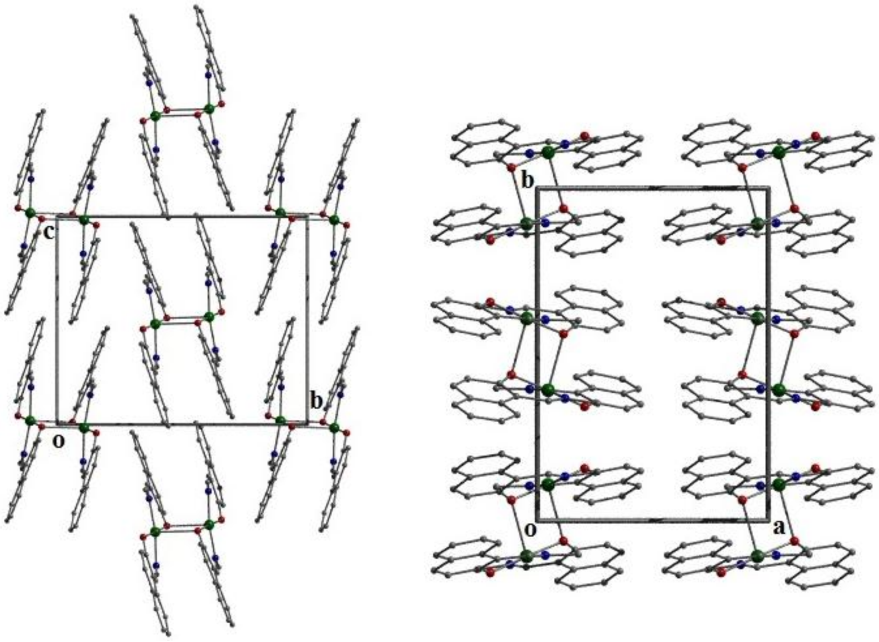

Figure 172 - *Crystal packing arrangements of* ***28*** *as viewed along the a (left) and c axis (right). Hydrogen atoms have been removed for clarity.*

The synthesis of complexes **25-28** showed that the self-assembly of $\{M(L_7)_2\}$ (M = Mn(III) or Cu(II)) units were reliably favourable. We therefore decided to add a linear ditopic SBU (secondary building unit) to the synthetic procedure for **28** towards the production of an extended architecture. We chose the ever reliable linker ligand 4,4'-bipyridine as it has proven to be suitable for the synthesis of extended networks in our group[18] and elsewhere.[19-30] The addition of a linker ligand to the reaction procedure for **28** resulted in the formation of the 2D hydrogen bonded network $[Cu(II)_2(NO_3)_2(L_7)_2(MeOH)_2(4,4'\text{-bipy})]_n$ (**29**), whereby a transformation from a $[Cu_2(L_7)_2]$ unit to a $[Cu(L_7)\text{-}X\text{-}Cu(L_7)]$ moiety (where X = 4,4'-bipyridine) is observed (Figure 173). Complex **29** crystallises in the triclinic *P*-1 space group with unit cell parameters: a = 9.2936(19) Å, b = 10.334(2) Å, c = 10.887(2) Å, α = 64.35(3)°, β = 86.86(3)°, γ = 68.37(3)°. Complete single crystal X-ray diffraction data is given in Table 21 (Section 6.2.4).

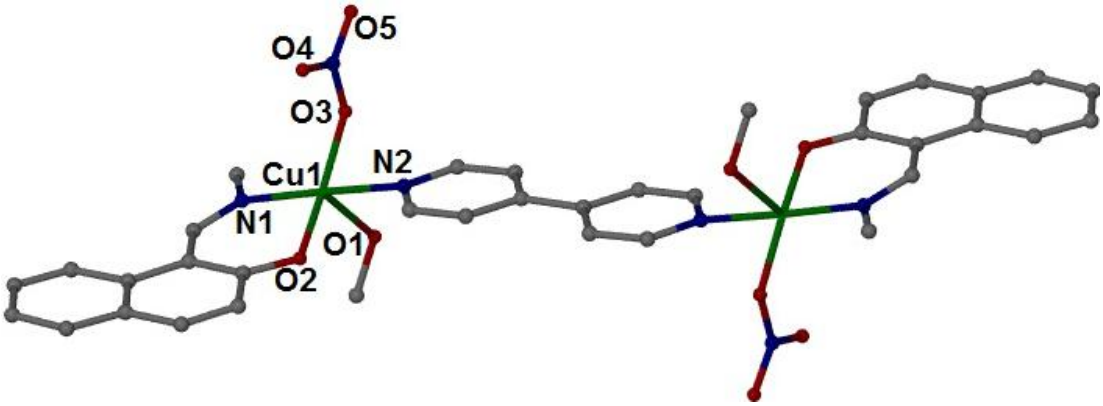

Figure 173 *- Crystal structure of one [Cu(L_7)-X-Cu(L_7)] (where X = 4,4'-bipyridine) unit in* ***29****, displaying an η^1:η^1 coordination motif. Hydrogen atoms have been removed for clarity.*

Each repeating unit in complex **29** comprises two symmetrically equivalent five coordinate Cu(II) centres, related by an inversion centre and linked via a 4,4'-bipyridine ligand. Each of the Cu(II) metal centres possesses distorted square based pyramidal geometries (τ = 0.1165).[17] The individual Cu(II) centres are coordinated at two of the equatorial sites via chelating L_7^- ligands, forming bond lengths of 1.897(2) Å (Cu1-O2) and 1.972(3) Å (Cu1-N1) respectively. The remaining two equatorial positions are occupied by a single 4,4'-bipy ligand via N2 (2.033(3) Å) and an $O_{nitrate}$ atom (O3), displaying a bond length of 2.032(3) Å (Cu1-O3). A pseudo sixth close contact is formed by the $O_{nitrate}$ atom (O4), lying at a Cu1-O4 distance of 2.764 Å (Figure 173). Coordination is completed at the axial position via a terminal methanol ligand with a Cu1-O1 bond length of 2.323(3) Å. The methanol ligands of one [Cu_2] unit partake in strong inter-molecular hydrogen bonding interactions with the nitrate moieties from a neighbouring [Cu_2] unit (e.g. O1'(H1')¨O5 = 2.006 Å) (Figure 174). Self-assembly is further enhanced via hydrogen bonding interactions between the alpha proton of a 4,4'-bipy moiety and the O3 atom of the nitrate group (C17(H17)¨O3' = 2.482 Å), forming zig-zag chains (Figure 174). In addition, these chains are further bridged via C-H¨O bonds and π-π interactions, leading to the formation of 2D layers in the crystal structure of **29**. More specifically, the alpha and beta protons of the 4,4'-bipy ligand (H13 and H14 respectively) interact with the second uncoordinated nitrate oxygen atom (i.e. C13(H13)¨O4' = 2.538 Å and

C14(H14)···O4' = 2.537 Å), while both of the pyridyl groups of the 4,4'-bipy ligand are sandwiched between two L_7^- ligands belonging to two neighbouring chains via their phenyl groups (i.e. [C13-C17-N2]···[C4'-C9'] = 3.624 Å and [C13-C17-N2]···[C3'-C4'-C9'-C12'] = 3.620 Å) (Figure 175 and 176).

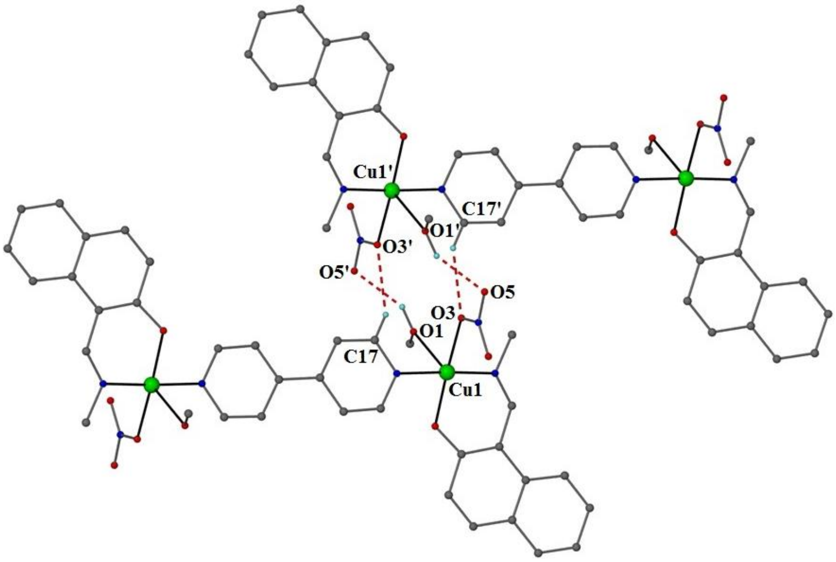

***Figure 174** - (Left) Depiction of the hydrogen bonding interactions (red dashed lines) between two [Cu$_2$] units. Colour code: light green (Cu), light blue (H). The majority of hydrogen atoms have been omitted for clarity.*

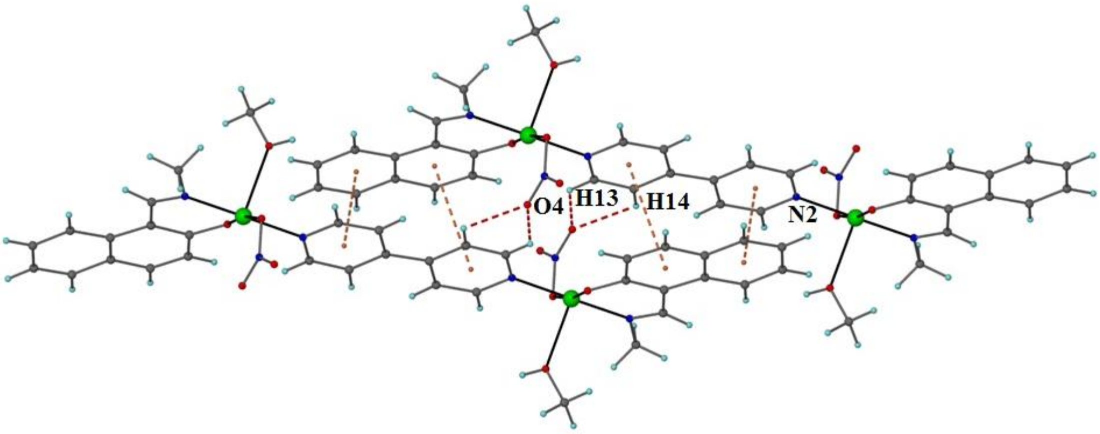

***Figure 175** - Schematic representation of C-H···O bond and π-π stacking interactions between [Cu$_2$] chains, resulting in the formation of 2D layers.*

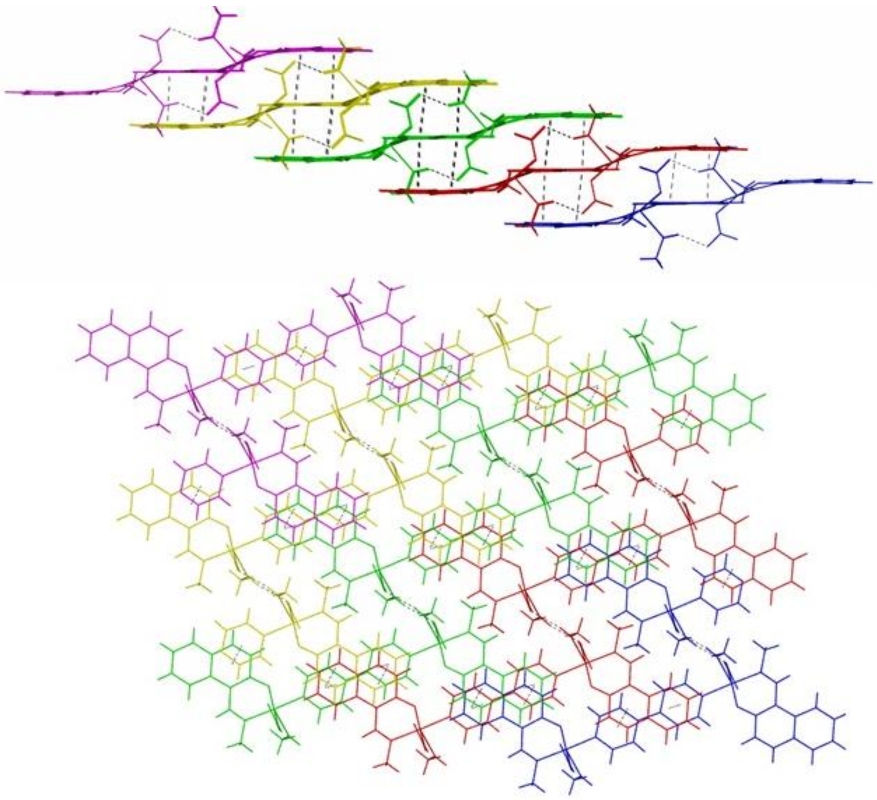

Figure 176 - *Representations of the 2D layer formed by five colour coded interacting [Cu_2] chains in* ***29****.*

Here, 2D layers connect via C-H$\cdots\pi$ interactions of methanol -CH_3 protons (H18C) and L_7^- phenyl rings ([C3-C4-C9-C12]) with bond lengths of 2.912 Å (Figure 177).

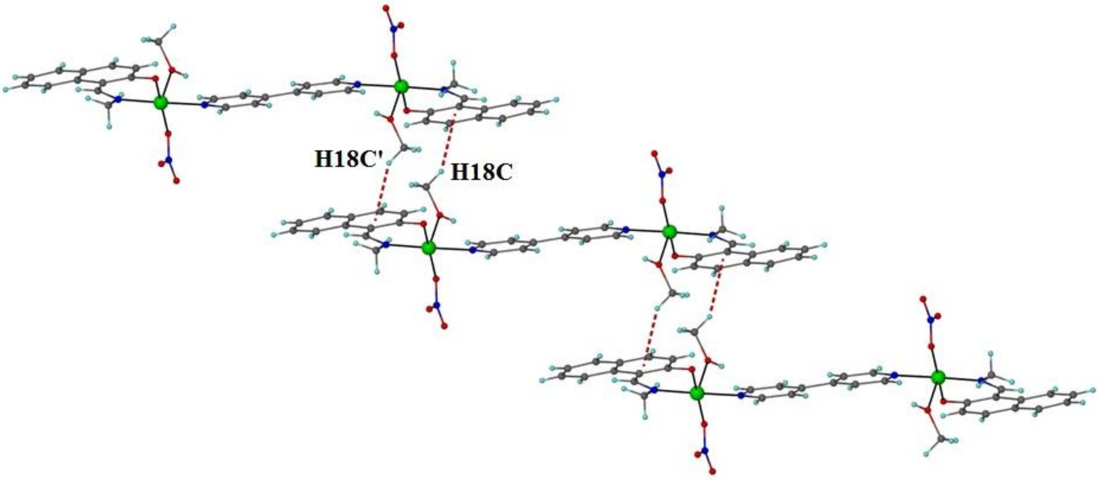

Figure 177 - *Depiction of the C-H$\cdots\pi$ interactions connecting the 2D layers in* ***29****.*

6.2.1.3 Expansion of our 2,6-dimethoxyphenol Studies Towards the Formation of Transition Metal Complexes

During our investigations into the coordination chemistry of the ligand 2,6-dimethoxyphenol (L_6H) with numerous transition metal ions, we struggled to obtain X-ray quality single crystals. Instead we formed a range of amorphous powders and semi-crystalline materials. However, one promising result came from the methanolic reaction of $Co(ClO_4)_2\cdot 6H_2O$, L_6H and $NEt_4(OH)$, giving a paltry return of 1-2 single crystals of an unknown material. We decided to slow down the crystallisation process by placing these reaction mixtures in the freezer and after one week X-ray quality crystals of the Co(II) cube complex $[Co(II)_4(OMe)_4(L_6)_4(MeOH)_4]$ (**30**) (Figure 178) were obtained. Complex **30** crystallises in the tetragonal $I4_1/a$ space group with unit cell parameters: a = 21.784(3) Å, b = 21.784(3) Å, c = 10.120(2) Å, α = 90°, β = 90°, γ = 90°. Complete single crystal X-ray diffraction can be seen in Table 21 (Section 6.2.4).

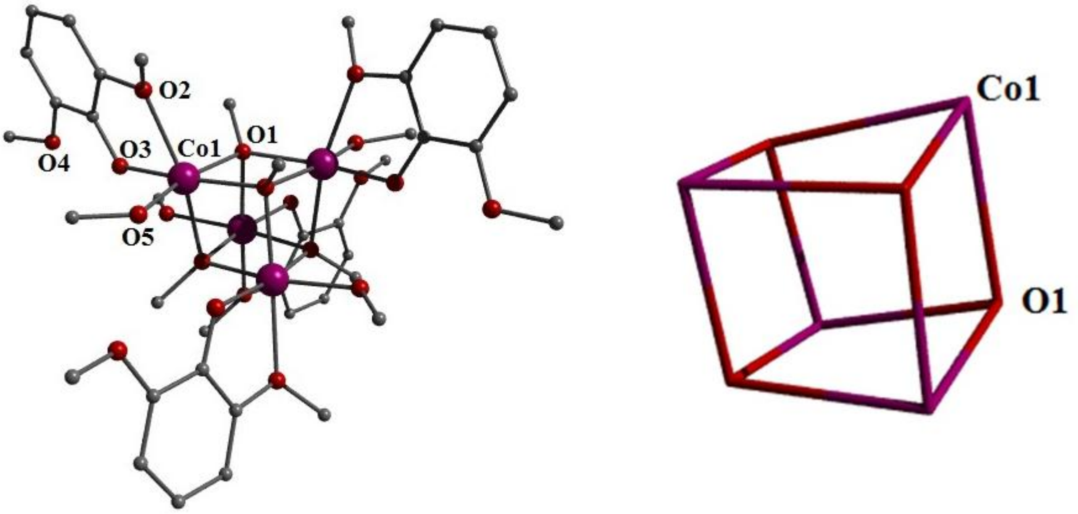

Figure 178 *- (Left) Crystal structure of complex* ***30*** *and (right) representation of the Co_4 core. Colour code: purple (Co). Hydrogen atoms have been omitted for clarity.*

The $[Co_4]$ core in **30** is composed of a tetragonal unit cell, whereby four-fold symmetry is observed. The composition of the corners of the cubic core alternates between Co(II) metal centres and O1 atoms (Figure 178). Each Co(II) metal centre displays distorted octahedral geometry, whereby two of the equatorial positions and one of the axial positions are occupied via bridging methoxide groups, resulting in bond lengths in the range of 2.065(16) and 2.120(16) Å (Co1-O1). In addition, all of the above methoxide groups are coordinated to another two Co(II) metal centres, completing the [Co_4] core. The remaining axial position is capped by a terminal MeOH ligand via O5 (Co1-O5 = 2.102(17) Å). The distorted octahedral coordination at Co1 is completed by a chelating L_6^- ligand (utilises a η^1:η^1 coordination motif) via a methoxide group and a phenolic oxygen atom with bond lengths of 2.259(17) Å (Co1-O2) and 1.994(17) Å (Co1-O3) respectively. The individual [Co_4] units are linked via inter-molecular C-H$^{\cdots}$O hydrogen bonding interactions between *1)* aromatic protons and methoxy oxygen atoms (e.g. O4$^{\cdots}$(H6')C6' = 2.628 Å) and *2)* methoxy protons and O_{phen} atoms (e.g. C9(H9A)$^{\cdots}$O3' = 2.703 Å). The individual [Co_4] units in **30** arrange in a space efficient pattern along the *a* unit cell direction as shown in Figure 179.

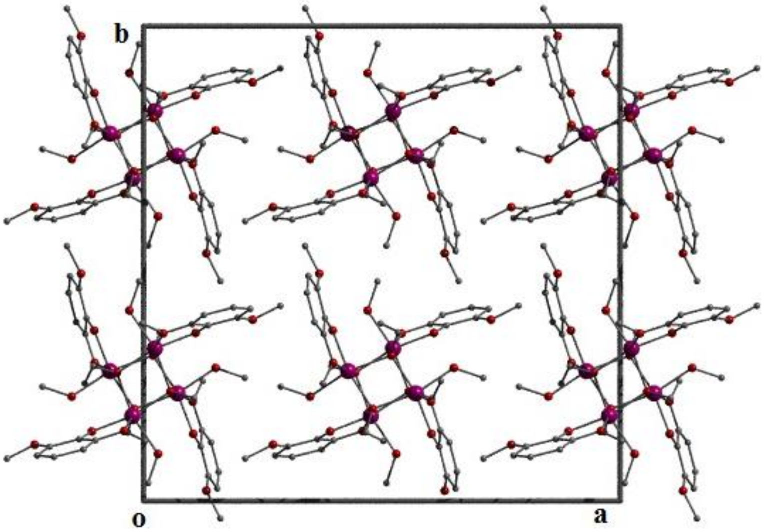

Figure 179 *- Crystal packing arrangement of individual [Co_4] units in* ***30*** *as viewed down the c axis of the unit cell. Hydrogen atoms have been removed for clarity.*

6.2.2 Magnetic Susceptibility Studies of [Co_4] (30)

Dc magnetic susceptibility measurements were performed on a powdered microcrystalline sample of [$Co(II)_4(OMe)_4(L_6)_4(MeOH)_4$] (**30**) in the 300-5 K temperature range, using an applied field of 0.1 T (Figure 180). Initially, as the temperature reduces a gradual decline in the $\chi_M T$ value is observed, while below 125 K a more steeper decrease in magnetic susceptibility is observed before reaching a $\chi_M T$ value of approximately 4.84 cm^3 K mol^{-1} at 16 K. Spin-orbit coupling interactions may be responsible for the decrease in magnetic susceptibility seen here. Next, a slight rise in the $\chi_M T$ value is observed reaching a value of approximately 5.31 cm^3 K mol^{-1}, before decreasing again to give a minimum $\chi_M T$ value of ~ 4.42 cm^3 K mol^{-1} at ~ 5 K. This type of behaviour is indicative of very weak ferromagnetic intra-molecular exchange interactions between Co(II) centres. The Co(II) core consists of Co-O-Co bridging angles ranging between 93.48 and 102.81°, where the angles towards the lower end of this window are typical of ferromagnetic exchange, while those at the higher end of the range tend to promote antiferromagnetic coupling. Therefore, it appears that the smaller more acute angles dominate the exchange interactions in **30**, resulting in overall weak ferromagnetic exchange interactions.

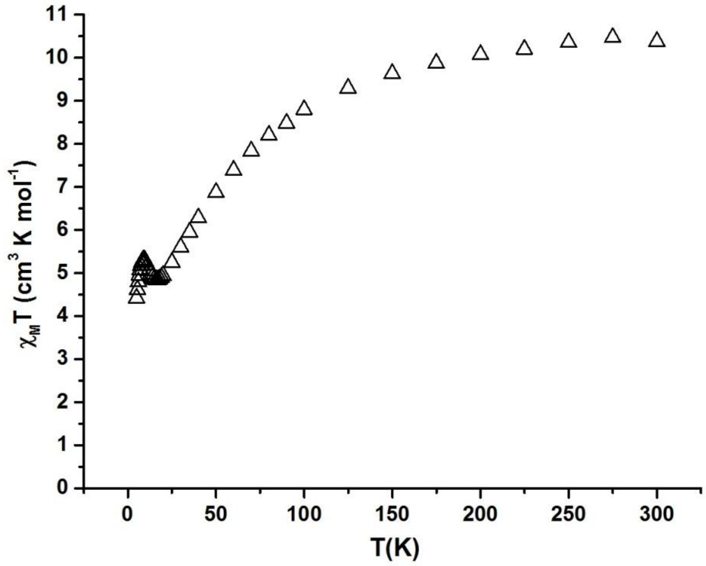

Figure 180 - *Plot of $\chi_M T$ vs. T obtained for complex **30** in the 300-5 K temperature range with an applied field of 0.1 T.*

In addition, we fitted the 1/χ vs. T plot for complex **30** to the Curie-Weiss law, resulting in a Curie-Weiss constant (θ) of -33.35 K (Figure 181). This would suggest that antiferromagnetic exchange interactions are occurring, however the Curie-Weiss law does not account for strong inter-molecular interactions, as observed in the crystal structure of **30**. No out-of-phase ac signals were observed upon measurement of **30**, thus ruling out SMM behaviour.

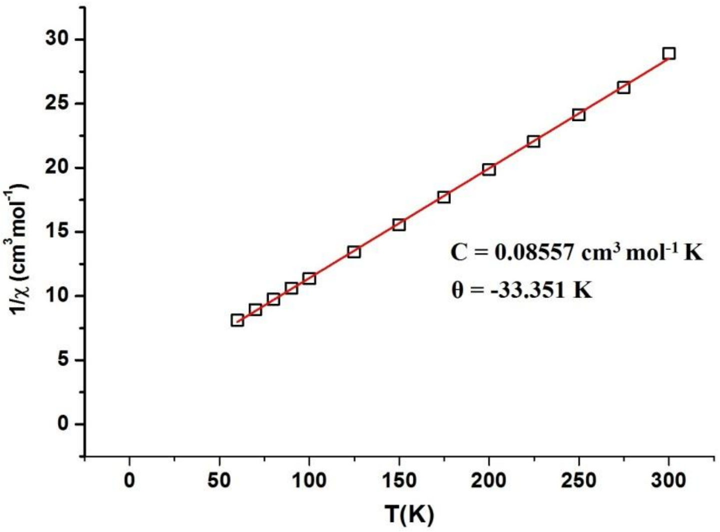

Figure 181 *- Curie-Weiss law plot of 1/χ vs. T for complex* ***30****. It must be noted that large inter-molecular interactions are not taken into account, resulting in an antiferromagnetic θ value of -33.351 K.*

6.2.3 Magnetisation versus Field Studies of [Co$_4$] (30)

Magnetisation (M) versus Field (H) studies were performed on a polycrystalline sample of [Co(II)$_4$(OMe)$_4$(L$_6$)$_4$(MeOH)$_4$] (**30**) in the 0.5-7 T magnetic field range (Figure 182). Large zero-field splitting effects result in non-superimposable magnetisation isotherms as expected for a Co(II) system. The magnetic saturation value at 7 T of 2.95 Nµß is indicative of an S = 2 ground spin state in **30**, thus corroborating previous magnetic susceptibility measurements.

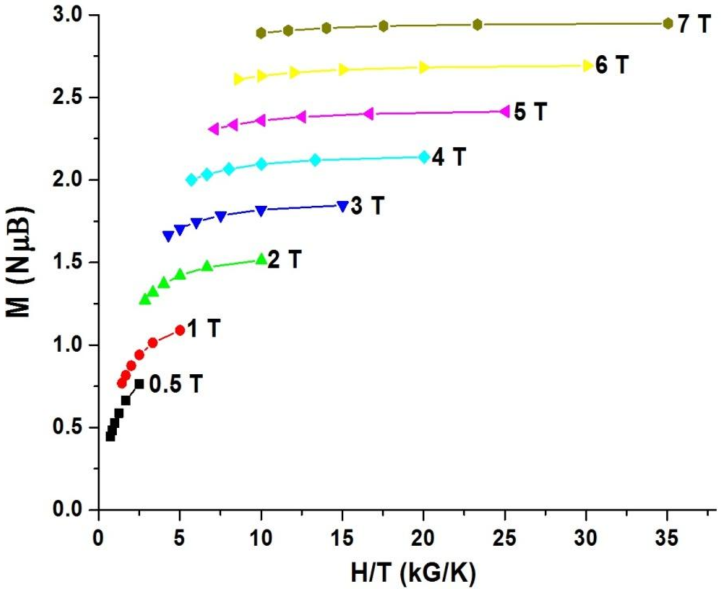

Figure 182 *- Reduced magnetisation (M/Nµ$_B$) vs. Field (H/T) data for complex* ***30*** *in the applied magnetic field range of 0.5-7 T. The solid lines act as a guide for the eye only.*

6.2.4 Crystallographic Data of Complexes 25-30

Table 20 *- Crystallographic data for complexes* ***25-27****.*

Complex	**25**	**26**	**27**
Formula[a]	$C_{25}H_{24}N_5O_3Mn_1$	$C_{24}H_{20}N_2O_2Cl_1Mn_1$	$C_{24}H_{20}N_5O_2Mn_1$
M_W	497.43	458.81	465.39
Crystal Appearance	Dark Brown Parallelepiped	Red-Brown Parallelepiped	Dark Brown Parallelepiped
Crystal System	Monoclinic	Monoclinic	Monoclinic
Space group	*Cc*	*C*2/*c*	*C*2/*c*
a/Å	20.248(4)	12.809(3)	22.424(5)
b/Å	9.3995(19)	17.616(4)	6.5388(13)
c/Å	13.106(3)	9.5233(19)	16.968(3)
α/°	90.00	90.00	90.00
β/°	117.20(3)	109.75(3)	125.92(3)
γ/°	90.00	90.00	90.00
V/Å^3	2218.4(8)	2022.4(7)	2014.9(7)
Z	4	4	4
T/K	150(2)	150(2)	150(2)
λ^b/Å	0.7107	0.7107	0.7107
D_c/g cm^{-3}	1.489	1.507	1.534
μ(Mo-Ka)/ mm^{-1}	0.634	0.809	0.689
Meas./indep., (R_{int}) refl.	2844/2687, (0.0223)	1852/1730, (0.0164)	1834/1606, (0.0180)
wR2 (all data)	0.0660	0.0640	0.0774
$R1^{d,e}$	0.0268	0.0235	0.0271
Goodness of fit (GOOF) on F^2	1.041	1.085	1.080

[a] Includes guest molecules. [b] Mo-Kα radiation, graphite monochromator. [c] $wR2= [\sum w(|F_o^2|- |F_c^2|)^2/ \sum w|F_o^2|^2]^{1/2}$. [d] For observed data. [e] $R1= \sum||F_o|- |F_c||/ \sum|F_o|$.

***Table 21** - Crystallographic data for complexes **28-30**.*

Complex	28	29	30
Formula[a]	$C_{48}H_{40}N_4O_4Cu_2$	$C_{36}H_{36}N_6O_{10}Cu_2$	$C_{40}H_{64}O_{20}Co_4$
M_W	863.92	839.79	1100.63
Crystal Appearance	Dark green Parallelepiped	Green Parallelepiped	Purple Cube
Crystal System	Monoclinic	Triclinic	Tetragonal
Space group	$P2_1/c$	P-1	$I4_1/a$
a/Å	10.509(2)	9.2936(19)	21.784(3)
b/Å	14.584(3)	10.334(2)	21.784(3)
c/Å	12.540(3)	10.887(2)	10.120(2)
$\alpha/^o$	90.00	64.35(3)	90.00
$\beta/^o$	105.19(3)	86.86(3)	90.00
$\gamma/^o$	90.00	68.37(3)	90.00
V/Å^3	1854.7(6)	869.3(3)	4802.1(14)
Z	2	1	4
T/K	150(2)	150(2)	150(2)
λ[b]/Å	0.7107	0.7107	0.7107
D_c/g cm^{-3}	1.547	1.604	1.522
μ(Mo-Ka)/ mm^{-1}	1.202	1.293	1.432
Meas./indep., (R_{int}) refl.	3390/2772, (0.0325)	3181/2526, (0.0346)	2201/1819, (0.0249)
wR2 (all data)	0.0778	0.1226	0.0735
$R1$[d,e]	0.0292	0.0480	0.0289
Goodness of fit (GOOF) on F^2	1.062	1.047	1.046

[a] Includes guest molecules. [b] Mo-Kα radiation, graphite monochromator. [c] $wR2= [\sum w(|F_o^2|- |F_c^2|)^2/ \sum w|F_o^2|^2]^{1/2}$. [d] For observed data. [e] $R1= \sum||F_o|- |F_c||/ \sum|F_o|$.

6.3 Conclusions and Observations

In this chapter, we have reported the synthesis of a Mn(III) hydrogen bonded chain [Mn(III)$(L_7)_2(N_3)$MeOH] (**25**) and two 1D coordination polymers [Mn(III)$(L_7)_2$(Cl)]$_n$ (**26**) and [Mn(III)$(L_7)_2(N_3)$]$_n$ (**27**), via the utilisation of the Schiff base ligand 1-[(methylimino)methyl]-2-naphthol (L_7H). The production of **25-27** adds to our family of Mn(III) 1D chains of general formulae [Mn(III)(L)$_2$(X)]$_n$ (where L = 2-iminomethyl-6-methoxyphenol (immpH) or 1-[(methylimino)methyl]-2-naphthol and X = connector ligands e.g. Cl^-, N_3^-, Br^-). We furthered our investigations into the coordination chemistry of the L_7H ligand via the use of Cu(II) transition metal salts, resulting in the formation of the dimeric complex [Cu(II)$_2(L_7)_4$] (**28**). As the synthesis of complexes **25-28** favoured the formation of [M$(L_7)_2$] units, we decided to introduce an N donor secondary building unit to the synthetic reaction scheme of **28** towards the construction of an extended network. We chose the ditopic ligand 4,4'-bipyridine, resulting in the construction of a [Cu(L_7)-X-Cu(L_7)] (where X = 4,4'-bipyridine) 2D hydrogen bonded extended network of formula [Cu(II)$_2$(NO$_3$)$_2$(L_7)$_2$(MeOH)$_2$(4,4'-bipy)] (**29**). The final section of this chapter investigated the coordination chemistry of 2,6-dimethoxyphenol (L_6H) leading to the synthesis of the Co(II) cubic complex [Co(II)$_4$(OMe)$_4$(L_6)$_4$(MeOH)$_4$] (**30**). Magnetic susceptibility and magnetisation vs. field studies carried out on **30** were indicative of an S = 2 ground spin state.

6.4 Experimental Section

6.4.1 Instrumentation

For details on instrumentation utilised in the analyses of complexes **25**-**30** see Chapter Two (Section 2.4.1).

6.4.1.1 Single Crystal X-ray Diffraction

The structures of **25**-**30** were collected on an Xcalibur S single crystal diffractometer (Oxford Diffraction) using an enhanced Mo source. Each data reduction was performed by the CrysAlisPro software package. The structures were solved by direct methods (SHELXS-97)[31] and refined by full matrix least squares using SHELXL-97.[32] SHELX operations were automated using the OSCAIL software package.[33] All hydrogen atoms in complexes **25**-**30** were placed in calculated positions while all non-hydrogen atoms were refined as anisotropic.

6.4.2 Syntheses

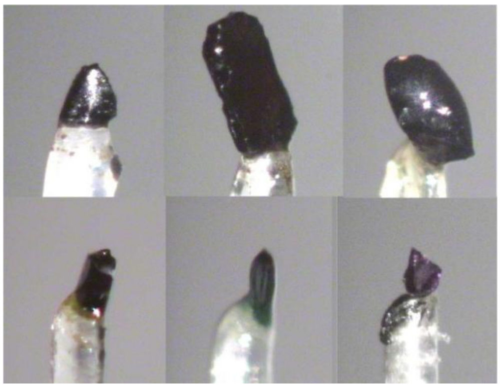

Figure 183 *- Single crystals of complexes* ***25-27*** *(top left to right) and complexes* ***28-30*** *(bottom left to right).*

6.4.2.1 Synthesis of 1-[(methylimino)methyl]-2-naphthol (L_7H)

Method A: $MeNH_2$ (0.361 g, 0.402 cm^3, 11.62 mmol) was added to a 40 cm^3 methanolic solution of 2-hydroxy-1-naphthaldehyde (1 g, 5.81 mmol) and refluxed for 4 h. Upon cooling, the solution was evaporated under reduced pressure to give a yellow/orange solid in 87% yield. L_7H was also synthesised via another procedure.

Method B: $MeNH_2$ (9.007 g, 10.04 cm^3, 290 mmol) was added to a 80 cm^3 methanolic solution of 2-hydroxy-1-naphthaldehyde (5 g, 29 mmol) and stirred for 4 h. The yellow solution was evaporated to dryness under reduced pressure to produce a yellow-orange solid in 80% yield.

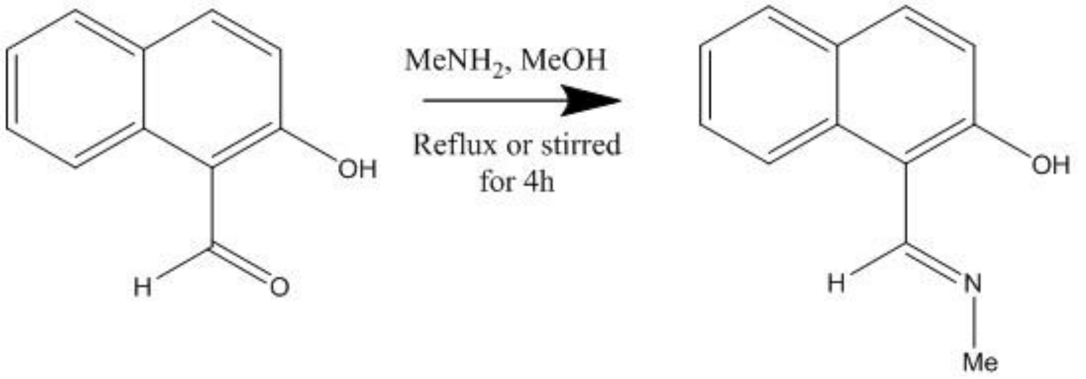

Scheme 5 *-Reaction scheme for the synthesis of 1-[(methylimino)methyl]-2-naphthol (L_7H).*

C, H, N Elemental Analysis

Calculated % for $C_{12}H_{11}O_1N_1$: C 77.81, H 5.99, N 7.56.

Found %: C 77.52, H 6.14, N 7.42.

FT-IR (cm^{-1}): 3050 (w), 1615 (m), 1539 (m), 1490 (m), 1447 (w), 1425 (w), 1396 (w), 1349 (m), 1313 (m), 1253 (m), 1213 (m), 1182 (m), 1167 (m), 1136 (m), 1007 (m), 953 (w), 882 (m), 856 (m), 828 (s), 776 (w), 741 (s).

TOF MS-ES (%) m/z (H_2O/MeCN): 186.0892 (100, L_7H +H).

^1H NMR (400 MHz, $CDCl_3$): δ 1.64 (s, H_2O), 3.44 (s, 3H, =N-CH_3), 6.91-7.86 (m, 6H, Ar-H), 7.26 ($CDCl_3$ residual solvent peak), 8.7 (s, 1H, N=CH).

6.4.2.2 Synthesis of Mn(III)(L_7)$_2$(N_3)MeOH (25)

$MnCl_2\cdot4H_2O$ (0.25 g, 1.26 mmol) was dissolved in a 40 cm^3 methanolic solution of 1-[(methylimino)methyl]-2-naphthol (L_7H) (0.23 g, 1.26 mmol). NaOH (0.05 g, 1.26

mmol) and NaN_3 (0.08 g, 1.26 mmol) were then added and the resultant solution left to stir for 3 h. The resultant dark brown solution obtained was filtered and X-ray quality crystals of **25** were obtained upon slow evaporation of the mother liquor after two days. Crystals of **25** were then collected and dried in air with to give a yield of 24%.

C, H, N Elemental Analysis

Calculated % as $[Mn(III)(L_7)_2(N_3)]\cdot 2H_2O$ ($C_{24}H_{24}N_5O_4Mn_1$): C 57.49, H 4.82, N 13.97.

Found %: C 57.75, H 4.61, N 13.6.

FT-IR (cm^{-1}): 2930 (w), 2042 (s), 1603 (s), 1541 (m), 1506 (w), 1452 (m), 1428 (m), 1388 (m), 1355 (w), 1339 (m), 1296 (m), 1252 (m), 1193 (s), 1170 (w), 1161 (w), 1147 (m), 1087 (w), 1029 (s), 962 (m), 941 (m), 860 (w), 832 (s), 782 (w), 752 (s).

6.4.2.3 Synthesis of $[Mn(III)(L_7)_2(Cl)]_n$ (26)

$MnCl_2\cdot 4H_2O$ (0.25 g, 1.26 mmol), (L_7H) (0.23 g, 1.26 mmol) and NaOH (0.05 g, 1.26 mmol) were dissolved in 40 cm^3 of MeCN and stirred for 1 h to give a red brown solution. This solution was then filtered and X-ray quality crystals of **26** were formed upon slow evaporation of the mother liquor after five days. The crystalline sample of **26** was then collected and air dried to give a yield of 11%.

C, H, N Elemental Analysis

Calculated % as $\{[Mn(III)(L_7)_2(Cl)]\cdot H_2O\}_n$ ($C_{24}H_{22}N_2O_3Cl_1Mn_1$): C 60.45, H 4.65, N 5.88.

Found %: C 60.32, H 4.39, N 6.21.

FT-IR (cm^{-1}): 3056 (w), 2912 (w), 1605 (s), 1541 (s), 1506 (m), 1450 (m), 1431 (m), 1389 (m), 1358 (m), 1338 (s), 1302 (m), 1254 (m), 1190 (s), 1160 (m), 1147 (m), 1087 (m), 1049 (w), 1033 (m), 982 (w), 960 (m), 942 (s), 862 (m), 824 (s), 775 (m), 762 (m), 740 (s).

6.4.2.4 Synthesis of $[Mn(III)(L_7)_2(N_3)]_n$ (27)

$MnCl_2\cdot 4H_2O$ (0.25 g, 1.26 mmol), (L_7H) (0.23 g, 1.26 mmol) and NaOMe (0.07 g, 1.26 mmol) were dissolved in 40 cm^3 of EtOH and stirred for 5 mins. NaN_3 (0.08 g, 1.26

mmol) was then added and the solution was left to stir for 3 h. The resultant dark brown solution was filtered and X-ray quality crystals of **27** were obtained upon slow evaporation within 24 h and were subsequently washed and air dried to give a yield of 22%.

C, H, N Elemental Analysis

Calculated % as $\{[Mn(III)(L_7)_2(N_3)]\cdot 2H_2O\}_n$ ($C_{24}H_{24}N_5O_4Mn$): C 57.49, H 4.82, N 13.97.

Found %: C 57.01, H 4.48, N 13.65.

FT-IR (cm^{-1}): 3054 (w), 2024 (m), 1603 (m), 1542 (m), 1507 (w), 1451 (m), 1428 (m), 1390 (m), 1359 (m), 1339 (m), 1300 (m), 1252 (m), 1193 (m), 1140 (m),1090 (m), 1048 (w),1031 (w), 958 (m), 942 (m), 860 (w), 824 (s), 754 (s).

6.4.2.5 Synthesis of [Cu(II)$_2$(L$_7$)$_4$] (28)

$Cu(ClO_4)_2\cdot 6H_2O$ (0.25 g, 0.68 mmol), (L_7H) (0.126 g, 0.68 mmol) and NaOMe (0.04 g, 0.68 mmol) were dissolved in 30 cm^3 of MeOH and the green mixture was stirred at ambient temperature for 2 h. The resultant solution was filtered and after a few days, X-ray quality crystals of **28** began to form and were subsequently collected and air dried to give a yield 12%.

C, H, N Elemental Analysis

Calculated % as $[Cu(II)_2(L_7)_4]\cdot H_2O$ ($C_{48}H_{42}N_4O_5Cu_2$): C 65.37, H 4.8, N 6.35.

Found %: C 65.54, H 4.64, N 6.04.

FT-IR (cm^{-1}): 3051 (w), 2972 (w), 2922 (w), 1606 (m), 1541 (m), 1506 (w), 1458 (m), 1431 (m), 1397 (s), 1366 (m), 1311 (w), 1254 (w), 1192 (s), 1166 (m), 1144 (m), 1133 (m), 1086 (w), 1024 (m), 967 (w), 952 (m), 858 (m), 831 (s), 776 (w), 744 (s).

6.4.2.6 Synthesis of [Cu(II)$_2$(NO$_3$)$_2$(L$_7$)$_2$(MeOH)$_2$(4,4'-bipy)] (29)

$Cu(NO_3)_2\cdot 3H_2O$ (0.025 g, 0.104 mmol), (L_7H) (0.02 g, 0.104 mmol) and NaOMe (0.006 g, 0.104 mmol) were dissolved in 15 cm^3 of MeOH and stirred for 1 h. The resultant green solution was filtered and was then layered with 4,4'-bipyridine (0.016 g, 0.104 mmol) in a 5 cm^3 MeOH solution. Upon slow evaporation, X-ray quality crystals of **29** formed within three days. These crystals were then collected and air dried to give a yield of 31%.

C, H, N Elemental Analysis

Calculated % for $C_{36}H_{36}N_6O_{10}Cu_2$: C 51.49, H 4.32, N 10.07.

Found %: C 51.31, H 4.09, N 9.98.

FT-IR (cm^{-1}): 3421 (w), 2913 (w), 1608 (s), 1575 (m), 1541 (m), 1506 (w), 1490 (w), 1456 (s), 1431 (m), 1416 (m), 1391 (s), 1362 (m), 1300 (s), 1252 (m), 1220 (m), 1186 (m), 1138 (m), 1083 (w), 1066 (m), 1022 (s), 985 (w), 968 (m), 949 (w), 855 (w), 827 (s), 810 (s), 774 (w), 743 (s), 722 (m), 685 (w), 675 (w).

6.4.2.7 Synthesis of [Co(II)$_4$(OMe)$_4$(L$_6$)$_4$(MeOH)$_4$] (30)

$Co(ClO_4)_2 \cdot 6H_2O$ (0.25 g, 0.683 mmol) was added to a 40 cm^3 methanolic solution of 2,6-dimethoxyphenol (L_6H) (0.105 g, 0.683 mmol). $NEt_4(OH)$ (1.5 cm^3, 1.53 g, 10.4 mmol) was subsequently added to the solution to give an orange-brown colour. The reaction mixture was stirred for 3 h at ambient temperature before being filtered and placed in the freezer. After a week, purple X-ray quality crystals of **30** began to form and were collected and air dried to give a yield of 9%.

C, H, N Elemental Analysis

Calculated % as $[Co_4(OMe)_4(L_6)_4(MeOH)_3] \cdot H_2O$ ($C_{39}H_{62}O_{20}Co_4$): C 43.11, H 5.75.

Found %: C 42.71, H 5.59.

FT-IR (cm^{-1}): 2938 (w), 2817 (w), 1584 (w), 1495 (m), 1472 (m), 1439 (m), 1295 (m), 1235 (m), 1190 (w), 1162 (w), 1096 (s), 1030 (s), 897 (w), 842 (m), 764 (m), 722 (s), 708 (m).

6.5 Bibliography

1. S. T. Meally, G. Karotsis, E. K. Brechin, G. S. Papaefstathiou, P. W. Dunne, P. McArdle and L. F. Jones, *CrystEngComm*, 2010, 12, 59-63.
2. S. T. Meally, C. McDonald, G. Karotsis, G. S. Papaefstathiou, E. K. Brechin, P. W. Dunne, P. McArdle, N. P. Power and L. F. Jones, *Dalton Trans.*, 2010, 39, 4809-4816.
3. S. T. Meally, C. McDonald, P. Kealy, S. M. Taylor, E. K. Brechin and L. F. Jones, *Dalton Trans.*, 2012, 41, 5610-5616.
4. S. T. Meally, S. M. Taylor, E. K. Brechin, S. Piligkos and L. F. Jones, *Dalton Trans.*, 2013, 42, 10315-10325.
5. S. T. Meally and L. F. Jones, *Unpublished Results*.
6. H. Torayama, H. Asada, M. Fujiwara and T. Matsushita, *Polyhedron*, 1998, 17, 3859-3874.
7. G. R. Clark, J. M. Waters, T. N. Waters and G. J. Williams, *J. Inorg. Nucl. Chem.*, 1977, 39, 1971-1975.
8. D. W. Martin and T. N. Waters, *J. Chem. Soc., Dalton Trans.*, 1973, 2440-2443.
9. M. Shiotsuka, Y. Okaue, N. Matsumoto, H. Okawa and T. Isobe, *J. Chem. Soc., Dalton Trans.*, 1994, 2065-2070.
10. M. Murrie, *Chem. Soc. Rev.*, 2010, 39, 1986-1995.
11. O. Kahn, *Molecular Magnetism*, Wiley, 1993.
12. E.-C. Yang, D. N. Hendrickson, W. Wernsdorfer, M. Nakano, L. N. Zakharov, R. D. Sommer, A. L. Rheingold, M. Ledezma-Gairaud and G. Christou, *J. Appl. Phys.*, 2002, 91, 7382-7384.
13. J. Liu, S. Datta, E. Bolin, J. Lawrence, C. C. Beedle, E.-C. Yang, P. Goy, D. N. Hendrickson and S. Hill, *Polyhedron*, 2009, 28, 1922-1926.
14. T. A. Hudson, K. J. Berry, B. Moubaraki, K. S. Murray and R. Robson, *Inorg. Chem.*, 2006, 45, 3549-3556.
15. B. Moubaraki, K. S. Murray, T. A. Hudson and R. Robson, *Eur. J. Inorg. Chem.*, 2008, 2008, 4525-4529.
16. K. W. Galloway, A. M. Whyte, W. Wernsdorfer, J. Sanchez-Benitez, K. V. Kamenev, A. Parkin, R. D. Peacock and M. Murrie, *Inorg. Chem.*, 2008, 47, 7438-7442.
17. A. W. Addison, T. N. Rao, J. Reedijk, J. van Rijn and G. C. Verschoor, *J. Chem. Soc., Dalton Trans.*, 1984, 1349-1356.
18. C. McDonald, T. Whyte, S. M. Taylor, S. Sanz, E. K. Brechin, D. Gaynor and L. F. Jones, *CrystEngComm*, 2013, 15, 6672-6681.
19. M. Fujita, Y. J. Kwon, S. Washizu and K. Ogura, *J. Am. Chem. Soc.*, 1994, 116, 1151-1152.
20. S.-i. Noro, S. Kitagawa, M. Kondo and K. Seki, *Angew. Chem. Int. Ed.*, 2000, 39, 2081-2084.
21. E. Suresh, K. Boopalan, R. V. Jasra and M. M. Bhadbhade, *Inorg. Chem.*, 2001, 40, 4078-4080.
22. B. Rather and M. J. Zaworotko, *Chem. Commun.*, 2003, 830-831.
23. Y. Lu, Y. Xu, E. Wang, J. Lü, C. Hu and L. Xu, *Crys. Growth Des.*, 2004, 5, 257-260.
24. O. Ohmori and M. Fujita, *Chem. Commun.*, 2004, 1586-1587.
25. K. Biradha, M. Sarkar and L. Rajput, *Chem. Commun.*, 2006, 4169-4179.
26. D. Tanaka, A. Henke, K. Albrecht, M. Moeller, K. Nakagawa, S. Kitagawa and J. Groll, *Nature Chem.*, 2010, 2, 410-416.
27. S.-T. Zheng and G.-Y. Yang, *Dalton Trans.*, 2010, 39, 700-703.
28. S.-L. Cai, S.-R. Zheng, J.-B. Tan, M. Pan, J. Fan and W.-G. Zhang, *CrystEngComm*, 2011, 13, 6345-6348.

29. S. D. Burd, S. Ma, J. A. Perman, B. J. Sikora, R. Q. Snurr, P. K. Thallapally, J. Tian, L. Wojtas and M. J. Zaworotko, *J. Am. Chem. Soc.*, 2012, 134, 3663-3666.
30. G.-Y. Wang, L.-L. Yang, Y. Li, H. Song, W.-J. Ruan, Z. Chang and X.-H. Bu, *Dalton Trans.*, 2013, 42, 12865-12868.
31. G. M. Sheldrick, *Acta Crystallogr. Sect. A: Found. Crystallogr.*, 1990, 46, 467-473.
32. G. M. Sheldrick, *SHELXL-97, A computer program for crystal structure determination*, 1997.
33. P. McArdle, P. Daly and D. Cunningham, *J. Appl. Crystallogr.*, 2002, 35, 378.

Chapter Seven

Conclusions and Observations

7.1 Conclusions and Observations

This thesis presents a range of thirty metal complexes comprising the metal ions: Cu(II), Ni(II), Mn(III), Co(II) or Ln(III) (where Ln = La(III), Ce(III), Gd(III), Tb(III) and Dy(III)) and whose structures have been built using a variety of related ligands (seven in total; Scheme 6). These complexes have been utilised in structural and magnetic studies presented in Chapters 2-6.

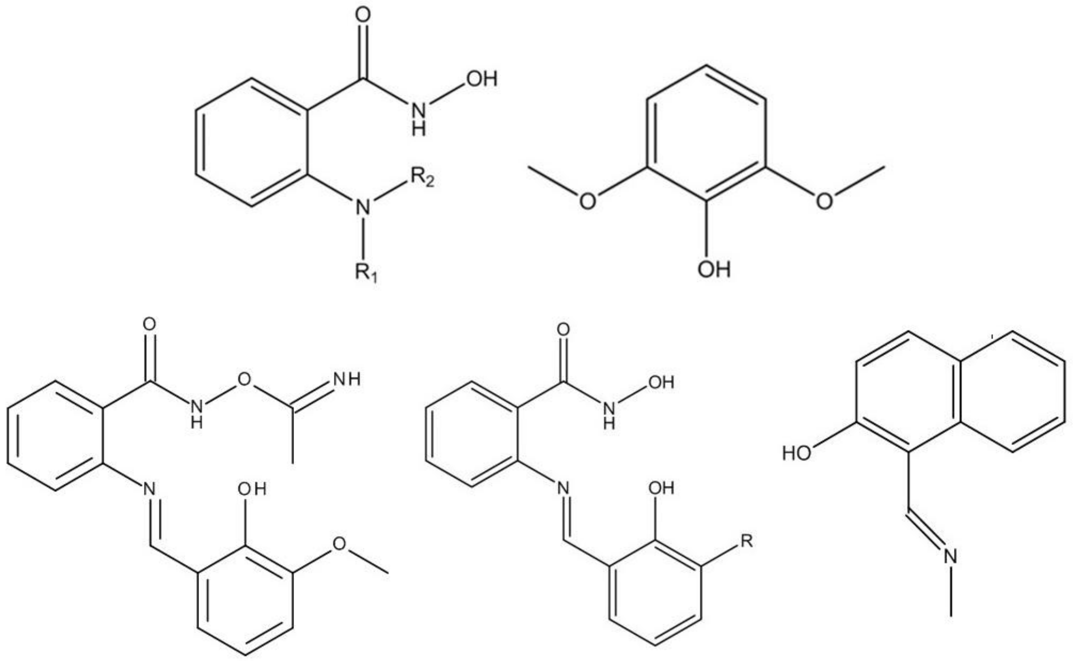

Scheme 6 - *Structure representation of ligands used in this thesis. (Top left) Hydroxamic acid ligands L_xH_2 where $R_1 = R_2 = Me$; L_1H_2 and $R_1 = R_2 = H$; L_2H_2 and (top right) 2,6-dimethoxyphenol (L_6H). (Bottom left to middle) In-situ formed Schiff base ligands L_4H_2 and L_XH_3 (where x = 3, R = OMe; x = 5, R = H) and (bottom right) Schiff base ligand L_7H.*

In Chapter 2 we reported the synthesis, structural and magnetic characterisation of a family of seven 12-$MC_{Cu(II)}$-4 metallacrown complexes via the utilisation of the hydroxamic acid ligands 2-(dimethylamino)phenylhydroxamic acid (L_1H_2) or 2-(amino)phenylhydroxamic acid (L_2H_2) (Scheme 6). Our first 12-$MC_{Cu(II)}$-4 metallacrown was $[Cu(II)_5(L_1)_4(MeOH)_4](ClO_4)_2$ (**1**) and from this prototype we demonstrated that we could exploit the coordinatively unsaturated nature of its Cu(II) centres by progressively introducing N-donor ligands at the vacant axial sites, resulting in the formation of the discrete [Cu_5] analogues $[Cu(II)_5(L_1)_4(py)_2](ClO_4)_2{\cdot}py$ (**2**) and $[Cu(II)_5(L_1)_4(py)_6](ClO_4)_2$ (**3**). This work was then expanded by successfully incorporating ditopic N-donor connector ligands in order to produce the pre-meditated 1D and 2D extended architectures: $\{[Cu(II)_5(L_1)_4(4,4'\text{-bipy})_3](ClO_4)_2\cdot H_2O\}_n$ (**4**), $\{[Cu(II)_5(L_1)_4(4,4'\text{-azp})_2(MeOH)_2](ClO_4)_2\}_n$ (**5**) and $\{[Cu(II)_5(L_2)_4(pz)_2(MeOH)](ClO_4)_2\cdot 3MeOH\}_n$ (**6**). Electrospray mass spectrometry and UV-vis analysis illustrated the solution stability of the $\{Cu_5(L_x)_4\}^{2+}$ (x = 1, 2) cores, which is further highlighted by our ability to manipulate these moieties in solution, resulting in the construction of the 1-2D extended networks **4-6**. Magnetic susceptibility measurements performed on **1**, **4** and **6** displayed strong antiferromagnetic exchange interactions between the Cu(II) ions and an isolated S = 1/2 ground spin value in all cases.

For the purposes of extending our family of 12-MC-4 metallacrowns, we investigated the coordination chemistry of Ni(II) metal salts with the hydroxamic acid ligands L_1H_2 and L_2H_2. In Chapter 3 we presented our findings in the form of a family of five Ni(II) cages ranging from penta- to nonanuclear topologies. The simple addition of pyridine to the synthetic procedure for the pentametallic founding member $[Ni(II)_5(L_1)_4(MeOH)_4](ClO_4)_2\cdot 2MeOH$ (**8**) yielded a 12-$MC_{Ni(II)}$-4 metallacrown analogue in the form of $[Ni(II)_5(L_1)_4(pyr)_5](ClO_4)_2\cdot 1H_2O$ (**9**). Pyridine ligands occupy the axial positions at selected Ni(II) metal centres, resulting in the conversion of square planar sites to square-based pyramidal/octahedral sites, thus magnetically 'switching on' additional superexchange pathways within our $[Ni_5]$ metallacrowns. DFT calculations performed on **8** and **9** yielded triplet S = 1 ground states for both complexes. Simple alterations to the synthetic schemes for **8** and **9** produced non-metallacrown conformations comprising hepta- and nonametallic cages of formulae $[Ni(II)_7(L_1H)_8(L_1)_2(H_2O)_6](SO_4)\cdot 15H_2O$ (**10**), $[Ni(II)_9(\mu\text{-}H_2O)_2(L_2)_6(L_2H)_4(H_2O)_2](SO_4)\cdot 29H_2O$ (**11**) and $[Ni(II)_9(\mu\text{-}H_2O)_2(L_2)_6(L_2H)_4(H_2O)_2](ClO_4)_2\cdot 2MeOH\cdot 18H_2O$ (**12**). These complexes form metallic skeletons comprising two bicapped, face sharing tetrahedra in **10** and two annexed tetrahedra in **11** and **12**. Magnetic susceptibility measurements performed on complexes **8**, **9** and **12** indicated the presence of dominant antiferromagnetic exchange interactions with S = 1 ground spin states. Complex **10** displays competing ferro- and antiferromagnetic exchange pathways between the seven Ni(II) centres, yielding an intermediate S = 3 ground spin state. DFT analysis were carried out on **8** and **9** to ascertain the ground spin configurations (s = 0 vs. s = 1) of all Ni(II) centres, producing three and four paramagnetic (s = 1) Ni(II) centres in **8** and **9** respectively.

DFT computed magnetic exchange interactions nicely reflect our experimental data. Furthermore, overlap between the magnetic orbitals observed in DFT computed calculations were employed to rationalise the nature and magnitude of the interactions.

In Chapter 4 we reported the in-situ formation and subsequent Cu(II) ligation of the polydentate ligands *o*-[(*E*)-(2-Hydroxy-3-methoxyphenyl)methylideneamino]benzohydroxamic acid (L_3H_3), [[2-[(E)-(2-hydroxy-3-methoxy-phenyl)methyleneamino]benzoyl]amino]ethanimidate (L_4H_2) and *o*-[(*E*)-(*o*-Hydroxyphenyl)methylideneamino]benzohydroxamic acid (L_5H_3) (Scheme 6) via the Schiff base condensation reactions of precursors 2-(amino)phenylhydroxamic acid (L_2H_2) and either 2-hydroxy-3-methoxybenzaldehyde or 2-hydroxybenzaldehyde, respectively. By varying reaction conditions and synthetic methodologies the family of Cu(II) cages $[Cu_{10}(L_3)_4(L_2)_2(H_2O)_2](ClO_4)_4\cdot5MeOH\cdot H_2O$ (**13**), $[Cu_{14}(L_3)_8(MeOH)_3(H_2O)_5](NO_3)_4\cdot2MeOH\cdot3H_2O$ (**15**), $[Cu_{14}(L_5)_8(MeOH)_6(NO_3)_4(H_2O)_2]\cdot6MeOH\cdot10H_2O$ (**16**) and $[Cu_{30}(O)_1(OH)_4(OMe)_2(L_3)_{16}(MeOH)_4(H_2O)_2](ClO_4)_4\cdot2MeOH\cdot27H_2O$ (**17**) were successfully synthesised. Furthermore, simple modifications to the reaction scheme employed in the production of **13** resulted in the formation of the entirely different 1D coordination polymer $\{[Cu(II)(L_4)]\cdot H_2O\}_n$ (**14**) (where L_4^{2-} = [[2-[(E)-(2-hydroxy-3-methoxy-phenyl)methyleneamino]benzoyl]amino]ethanimidate).

The work described in Chapter 5 detailed the microwave assisted synthesis of a family of seven $[Ln(III)_2]$ dinuclear complexes of general formula: $[Ln(III)_2(L_6)_2(ROH)_x(H_2O)_y(NO_3)_4]\cdot zEtOH$; where Ln = La, R = Et, $x = 4$, $y = 0$, $z = 0$ (**18**); Ln = Ce, R = Et, $x = 4$, $y = 0$, $z = 0$ (**19**); Ln = Gd, $x = 0$, $y = 2$, $z = 2$ (**20**); Ln = Gd, R = Me, $x = 2$, $y = 0$, $z = 0$ (**21**); Ln = Tb, R = Et, $x = 2$, $y = 0$, $z = 1$ (**22**); Ln = Tb, R = Me, $x = 2$, $y = 0$, $z = 0$ (**23**); Ln = Dy, $x = 0$, $y = 2$, $z = 2$ (**24**). These complexes are either unobtainable or exhibit extremely poor yields via ambient bench and reflux conditions. This illustrates the importance of microwave technology towards obtaining shorter reaction times, a wider range of reaction conditions, along with larger yields. In addition, we showed that through simple solvent selection we could control the number of $\{Ln(III)_2\}$ moieties (1 versus 2) in the asymmetric unit, thus allowing for their legitimate magnetic characterisation. Dc magnetic susceptibility measurements performed on [Ce(III)$_2$(L$_6$)$_2$(EtOH)$_4$(NO$_3$)$_4$] (**19**), [Gd(III)$_2$(L$_6$)$_2$(MeOH)$_2$(NO$_3$)$_4$] (**21**), [Tb(III)$_2$(L$_6$)$_2$(MeOH)$_2$(NO$_3$)$_4$] (**23**) and [Dy(III)$_2$(L$_6$)$_2$(H$_2$O)$_2$(NO$_3$)$_4$]·2EtOH (**24**) displayed weak antiferromagnetic exchange pathways in all complexes. Fitting of the data for complex **21** yielded a *J* value of -0.05 cm^{-1} with a ground spin state of S = 7/2. In complexes **19**, **21**, **23** and **24** magnetic saturation was observed at 7 T, confirming very weak exchange which can be easily overcome by an applied magnetic field. Ac magnetisation studies indicated no frequency dependence signals for all members; therefore SMM properties at temperatures above 2 K were ruled out. DFT and *ab initio* calculations were successfully performed on complexes **19**, **21**, **23** and **24**. The DFT computed magnetic exchange interactions are in agreement with those obtained experimentally. DFT and *ab initio* calculations were successfully performed on complexes **19**, **21**, **23** and **24** towards the investigation of the mechanisms responsible for the exchange interactions in these complexes.

Finally, in Chapter 6 we reported the synthesis of a Mn(III) hydrogen bonded chain [Mn(III)(L$_7$)$_2$(N$_3$)MeOH] (**25**) and two Mn(III) 1D coordination polymers [Mn(III)(L$_7$)$_2$(Cl)]$_n$ (**26**) and [Mn(III)(L$_7$)$_2$(N$_3$)]$_n$ (**27**), using the Schiff base ligand 1-[(methylimino)methyl]-2-naphthol (L$_7$H) (Scheme 6). The production of **25**-**27** adds to our family of Mn(III) 1D chains of general formulae [Mn(III)(L)$_2$(X)]$_n$ (where L = 2-iminomethyl-6-methoxyphenol or 1-[(methylimino)methyl]-2-naphthol and X = connector ligands e.g. Cl^-, N_3^-, Br^-). We furthered our investigations into the coordination chemistry of L$_7$H in conjunction with Cu(II) transition metal salts, resulting in the formation of the dimeric complex [Cu(II)$_2$(L$_7$)$_4$] (**28**). As the synthesis of complexes **25**-**28** favoured the formation of [M(L$_7$)$_2$] units (M = Mn(III) (**25**-**27**) and Cu(II) (**28**)), we decided to introduce an N-donor secondary building unit into the synthetic procedure of **28** towards the construction of an extended network. We chose the ditopic ligand 4,4'-bipyridine, resulting in the construction of the hydrogen bonded 2D extended network [Cu(II)$_2$(NO$_3$)$_2$(L$_7$)$_2$(MeOH)$_2$(4,4'-bipy)]$_n$ (**29**). The final section of this chapter investigated the coordination chemistry of 2,6-dimethoxyphenol (L$_6$H) (Scheme 6) with transition metal salts. Unfortunately, for the most part, only amorphous powders and semi-crystalline products were obtained. However, we did successfully synthesise one transition metal complex in the form of the Co(II) cubic complex [Co(II)$_4$(OMe)$_4$(L$_6$)$_4$(MeOH)$_4$] (**30**). Magnetic susceptibility and magnetisation vs. field studies carried out on **30** were indicative of an effective S' = 2 ground spin state.

7.2 Future work

In terms of our future work, we would like to attempt to synthesise heterometallic 3d-4f dimeric complexes[1] via the general synthetic procedure described in Chapter 5. This would enable us to further examine the magnitude and nature of the resultant exchange interactions towards the development of a more detailed magneto-structural correlation study. We would also like to expand our research into the formation of the Schiff base polydentate ligands L_xH_y (where x = 3, y = 3; x = 4, y = 2; x = 5, y = 3) (Scheme 6) via alternative synthetic routes such as click chemistry[2] in the hopes of minimising our dependence on the reversible Schiff base condensation reaction and thus improving our yields. It should also be noted that the presence of H_2O in our synthetic schemes drives the reaction in the opposite direction and therefore produces metal ligated complexes with low yields. Therefore, investigations into alternative synthetic routes for the construction of these Schiff base super-ligands, whereby H_2O interference is controlled is of the utmost importance.

7.3 Bibliography

1. E. Colacio, J. Ruiz-Sanchez, F. J. White and E. K. Brechin, *Inorg. Chem.*, 2011, 50, 7268-7273.
2. H. C. Kolb, M. G. Finn and K. B. Sharpless, *Angew. Chem. Int. Ed.*, 2001, 40, 2004-2021.